Dissertation

submitted to the
Combined Faculties for the Natural Sciences and for Mathematics
of the Ruperto-Carola University of Heidelberg, Germany
for the degree of
Doctor of Natural Sciences

Presented by
Dipl.–Phys. Bettina Fischer
Born in Kronstadt

Oral examination: 23.06.2010

Time resolved studies of H_2^+ dissociation with phase-stabilized laser pulses

Referees: **Priv.-Doz. Dr. Robert Moshammer**
Prof. Dr. Selim Jochim

Summary:

In the course of this thesis, experimental studies on the dissociation of H_2^+ ($H_2^+ \rightarrow p + H$) in ultrashort laser pulses with a stabilized carrier-envelope phase (CEP) were carried out. In single-pulse measurements, the ability to control the emission direction of low energetic protons, i.e. the localization of the bound electron at one of the nuclei after dissociation, by the CEP was demonstrated. The coincident detection of the emitted protons and electrons and the measurement of their three-dimensional momentum vectors with a reaction microscope allowed to clarify the localization mechanism. Further control was achieved by a pump-control scheme with two time-delayed CEP-stabilized laser pulses. Here the neutral H_2 molecule was ionized in the first pulse and dissociation was induced by the second pulse. Electron localization was shown to depend on the properties of the bound nuclear wave packet in H_2^+ at the time the control pulse is applied, demonstrating the ability to use the shape and dynamics of the nuclear wave packet as control parameters. Wave packet simulations were performed reproducing qualitatively the experimental results of the single and the two-pulse measurements. For both control schemes, intuitive models are presented, which qualitatively explain the main features of the obtained results.

Zusammenfassung:

Im Rahmen dieser Arbeit wurden experimentelle Untersuchungen zur Dissoziation von H_2^+ ($H_2^+ \rightarrow p + H$) in ultrakurzen Laserpulsen mit einer stabilisierten Träger-Einhüllenden-Phase (CEP) durchgeführt. In Einzelpulsmessungen konnte gezeigt werden, dass die Emissionsrichtung der niederenergetischen Protonen, das heißt die Lokalisierung des gebundenen Elektrons an einem der Kerne nach der Dissoziation, mit der CEP kontrolliert werden kann. Aufgrund der koinzidenten Detektion der emittierten Protonen und Elektronen, sowie der Bestimmung der dreidimensionalen Impulsvektoren mit Hilfe eines Reaktionsmikroskops, konnte der Lokalisierungsmechanismus geklärt werden. Die Kontrolle wurde durch ein Pump-Kontrolle-Schema mit zwei zeitversetzten CEP-stabilisierten Pulsen erweitert. Dabei wurde das neutrale H_2 Molekül in dem ersten Puls ionisiert und die Dissoziation wurde im zweiten Puls eingeleitet. Es konnte gezeigt werden, daß die Elektronenlokalisierung von den Eigenschaften des gebundenen Kernwellenpaketes in H_2^+ zur Zeit des Kontrollpulses abhängt. Es ist also möglich, die Form und Dynamik des Kernwellenpaketes als Kontrollparameter zu benutzen. Wellenpaket-Simulationen wurden durchgeführt, welche die experimentellen Ergebnisse qualitativ reproduzieren. Für beide Kontroll-Schemata werden anschauliche Modelle vorgestellt, die eine qualitative Erklärung der wesentlichen Ergebnisse ermöglichten.

Contents

Introduction

In 1999 the Time magazine claimed: 'Ring farewell to the century of physics, the one in which we split the atom and turned silicon into computing power. It's time to ring in the century of biotechnology.' [Isa11]. Indeed, biotechnology and biological sciences in general have undergone tremendous progress in the last years. For this progress, the development of improved methods to study biological as well as the underlying chemical processes played a major role. With such methods it became possible to analyze, for example, the structure of DNA or the folding of proteins. Meanwhile, increasing interest is payed to the role of molecular dynamics as it turned out to often comprise the actual function. For instance, molecular motion plays an important role for the activity of enzymes or pharmaceutical or in the synthesis of new materials. For the understanding of chemical reactions, knowledge of the dynamics of atoms and molecules is of profound importance as it is elementary for the formation and breakage of molecular bonds or changes of the molecular configuration.

The time scales for molecular motion spans a wide range. Complex dynamics, like protein folding or the synthesis of DNA, need milliseconds to seconds. For more elementary dynamics and reactions, the time scales are on the order of femtoseconds ($10^{-15}\,fs$). For example, several hundred femtoseconds for the rotation of molecules and $10-100\,fs$ for simple chemical reactions or vibrations. The tracing of molecular motion not only provides a deeper understanding of such processes, but also opens the possibility to control them in real time. For a time resolved investigation of motion, one has to take 'snapshots' of the motion at different times. Thereby, the 'exposure time' has to be shorter than the timescale of the motion. The shorter it is, the better the temporal resolution.

Temporal investigations of molecular motion became possible with the progress in the technology of pulsed lasers aiming for shorter and shorter pulses. First, the pulses were generated by Q-switching, which allowed for pulse durations of nanoseconds down to picoseconds. With the development of Titanium:Sapphire lasers in the 1980s, in which the pulses are generated by a mechanism called Kerr-lens mode locking [FGS81, VFG85], pulse durations in the femtosecond regime at a wavelength of about $800\,nm$ were achieved. These lasers could be improved to provide pulses of less than $10\,fs$, which corresponds to only two or three optical cycles. For applications in molecular and atomic physics, the intensity of the pulses had to be increased, which became possible with the development of a new amplification technique, the so-called chirped pulse amplification [SM85]. Nowadays, table top laser systems providing pulses of less than $10\,fs$ with peak intensities of $10^{15}\,W/cm^2$ are available.

The development of laser pulses in the femtosecond regime enabled the investigation of the dynamics of molecules and chemical reactions, which is referred to as femtochemistry [Zew88, Zew91, Zew95, Zew96, Zew00a] and was later extended to femtobiology [MWZ06, MWWZ07].

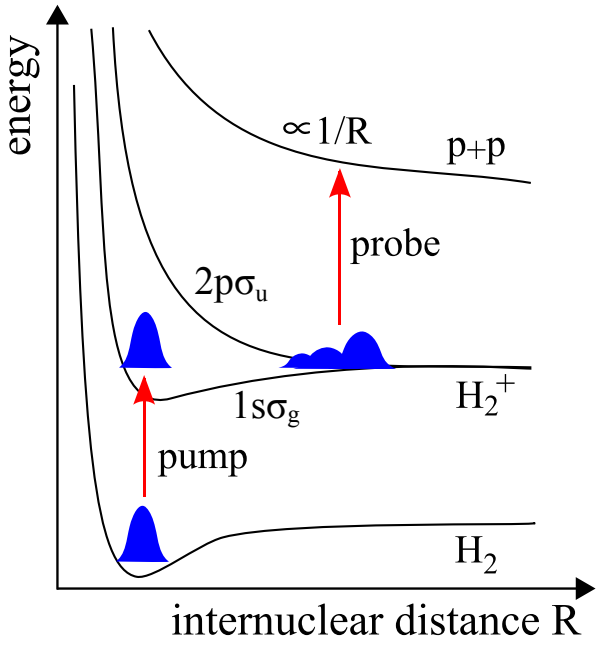

Figure 1: Schematic illustration of the pump-probe scheme for the potential energy curves of H_2 and H_2^+. The pump pulse ionizes the H_2 molecule, which leads to the creation of a wave packet in H_2^+. The second pulse probes the wave packet evolution by further ionizing the H_2^+ ion after some variable time delay.

The first time resolved studies were performed by Ahmed Zewail, who was awarded the Nobel price for his pioneering work in 1999 [Zew00b].
Time resolved studies of the vibrational motion of the fastest molecular system H_2 were for a long time not possible as the short vibrational periods of 17 fs for H_2^+ and 11 fs for H_2 imposed challenging requirements on the pulse duration. The first time resolved mapping of the vibrational dynamics of H_2^+ was therefore achieved not until 2005 [ERF$^+$05, ERF$^+$06a, ERF$^+$06b]. In these experiments, 6 fs laser pulses were used and allowed for an unprecedented time-resolution of the motion of this most simple and basic molecular system.
By regarding the progress in chemistry and biology, one might ask why it should be interesting to study such a simple system like H_2. Actually, it is just this simplicity which makes H_2 so interesting. An interpretation of measurements on complex molecules is often difficult and theoretical simulations are very challenging. By contrast, for H_2 theoretical calculations are feasible and often it is possible to develop simple and intuitive models of the physical processes. Thus, H_2 serves as a benchmark system for understanding bigger molecules.
For describing chemical reactions and molecular motion, in quantum mechanics often the concept of a nuclear wave packet[1], propagating on a so-called potential energy surface (PES) is used. The potential energy surface, or curve in the one-dimensional case, thereby represents the total energy of the rigid molecular system dependent on the relative position of the atoms. The dynamics of a molecule or chemical reaction is described by the motion of a nuclear wave packet on such a

[1] A wave packet represents a probability distribution, which has a significant amplitude only in a small spatial area.

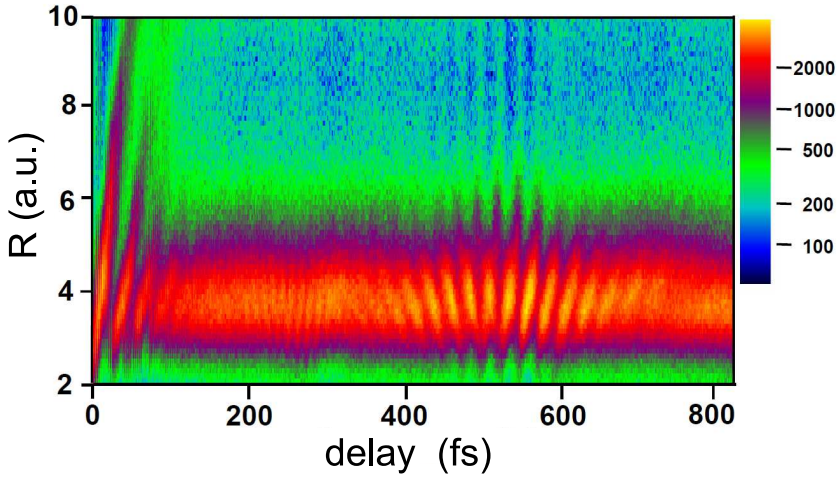

Figure 2: Result of a pump-probe measurement on D_2 [ERF$^+$06a, ERF$^+$05]. The internuclear distance of the wave packet was reconstructed from the energy spectrum of the deuterons and is shown as a function of the time delay between the two laser pulses. At small time delays, a line reaching to high internuclear distances can be observed, which corresponds to the dissociating part of the wave packet. The red stripe between 2 and $6\,a.u.$ corresponds to the bound part of the wave packet. One can clearly see the oscillatory motion of the wave packet at small delays, the dephasing after about $100\,fs$ as well as the revival after about $500\,fs$.

surface. The relevant potential curves of H_2 and H_2^+ are shown in figure 1.
For time resolved measurements of the wave packet evolution, usually a pump-probe technique is used, which is illustrated in figure 1. The first pulse ionizes the H_2 molecule and thereby induces the dynamical process in H_2^+. This corresponds to the creation of a bound nuclear wave packet, which can propagate on the ground state potential curve $1s\sigma_g$ of H_2^+. A second pulse is used to probe the wave packet after a variable time delay. The most common probe technique is Coulomb explosion imaging. Here the second pulse further ionizes the H_2^+ ion leading to the creation of two protons, which separate from each other due to Coulomb repulsion. This corresponds to a projection onto the Coulomb curve as illustrated in figure 1. The result of such a pump-probe measurement of the vibration of D_2^+ is shown in figure 2, where the proton count rate, which corresponds approximately to the probability density of the D_2^+ wave packet, is shown dependent on the internuclear distance and the time delay between the two pulses. Between $0\,fs$ and $100\,fs$ a clear time dependence in the internuclear distance of the wave packet can be observed. Here the wave packet has a small spatial spread, i.e. it is well localized, and oscillates in the potential well. The anharmonicity of the potential introduces dispersion, which leads to a broadening of the wave packet with time until it is spread over the potential well. Due to this so-called dephasing the structures in figure 2 wash out with time and finally vanish. After some time, however, the spreading reverses itself until the initial shape of the wave packet is recovered. In this revival, which can be seen at around $500\,fs$ in figure 2, the oscillatory motion of the wave packet can be observed again.
The final goal of understanding molecular dynamics is the manipulation and control of chemical

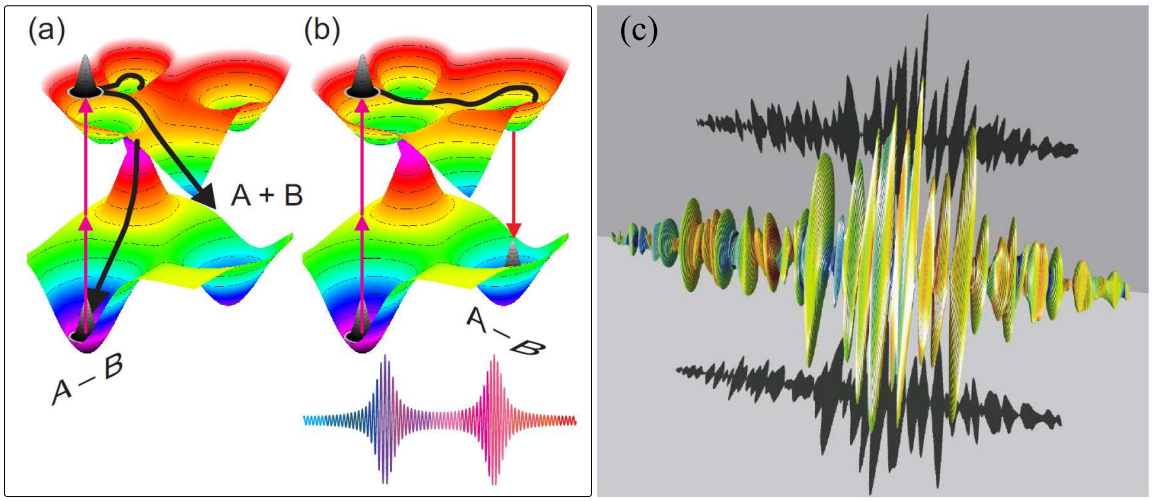

Figure 3: Illustration of coherent control in terms of potential energy surfaces [WBK+07]. a) A wave packet created in the excited potential energy surface (PES) can evolve along different pathways. b) With intense laser pulses the potential energy surface can be modified, so that new reaction pathways are created. c) Example of a tailored laser pulse optimized to enhance a certain reaction pathway. For this pulse, the momentary frequency (denoted by the color scale), the momentary field amplitude and the ellipticity was optimized by pulse shaping [BKP+04].

reactions. Manipulating chemical reactions by macroscopic variables, such as temperature or pressure, leads only to a shift of the chemical equilibrium, but the actual pathway of the reaction i.e. the evolution of the wave packet, does not change. A coherent steering of the wave packet evolution, by contrast, allows for changing selectively the outcome of a chemical reaction. This opens the possibility to synthesize specific chemical substances or to avoid the creation of undesired by-products.

Coherent control deals with such a coherent manipulation of chemical reactions. Already in the 1980s, several schemes were proposed for the control of quantum mechanical systems by laser radiation. In these schemes, a single parameter of the laser field is used as control knob, like the relative phase of two laser fields in the Brumer-Shapiro scheme [BS86] or the delay between two laser pulses [TKR86]. All these schemes have in common that they are based on the interference of possible reaction pathways [Bri03]. For simple systems, the functioning of these methods could be verified experimentally. For the manipulation of complex systems, however, they are not sufficient as optimal control requires the modulation of more than one parameter of the laser field. This can be done by so-called pulse shapers, which were originally developed for telecommunication purposes. With such devices the amplitude, phase and polarization of the single frequency components of laser pulses can be altered. Due to the large spectral bandwidth of ultrashort pulses, almost arbitrary pulse shapes can be created. An example of such a so-called tailored pulse is shown in figure 3 (c). It reveals a temporal variation of the momentary frequency, amplitude and polarization.

For finding the appropriate pulse shape for enhancing a certain reaction channel, learning opti-

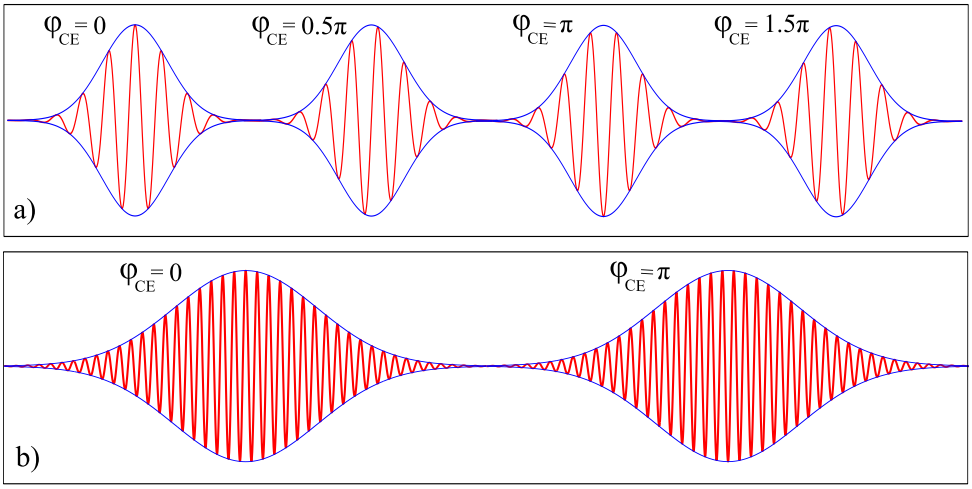

Figure 4: a) Schematic illustration of the electric field of ultrashort laser pulses ($4\,fs$, $800\,nm$) for different values of the carrier-envelope phase φ_{CE}. b) For pulses of $20\,fs$ duration, the carrier-envelope phase has no significant influence on the shape of the electric field.

mization loops are used. Hereby, the parameters of the pulse are varied and the resulting change of the reaction products is measured and used as feedback. In this way, so-called evolutionary algorithms optimize the pulse such that the yield of the desired reaction product is maximized [BPG+05, WEB05].

The working principle of coherent control is illustrated in figure 3, where a chemical reaction is illustrated in terms of potential energy surfaces. A wave packet is created in the excited potential surface, which can then evolve along different pathways. Such pathways can correspond, for example, to dissociation or relaxation. By coherent control, one of the available reaction pathways can be selected by changing the initial position and momentum of the wave packet in the excited potential surface (figure 3 (a)). By using high intensity laser pulses, the shape of the potential energy surface can be changed (figure 3 (b)). In this way, new reaction channels can be created, which are not accessible otherwise.

Using tailored laser pulses for controlling chemical reactions has become very successful. The question why a certain optimized pulse shape leads to a certain reaction product is an area of intense research, as it provides information on the molecular potential surface and the reaction mechanism. Due to its complexity a general solution for this inversion problem has not yet been found, so that deducing information from the pulse shape remains a very difficult task. Therefore, basic research providing information on the interaction of molecules with intense laser fields and the influence of certain pulse parameters is still of great importance.

For infrared laser pulses (wavelength about $800\,nm$) with a pulse length below $10\,fs$, the so-called carrier-envelope phase (CEP) becomes an important pulse parameter. The CEP is the relative phase between the maximum of the pulse envelope and the highest maximum of the electric field. For long pulses containing many optical cycles, this phase does not play a role (see figure 4 (b)). For pulse durations below $10\,fs$, the electric field varies on the same timescale as the pulse envelope. The shape of the electric field now strongly depends on the CEP, as can be seen in

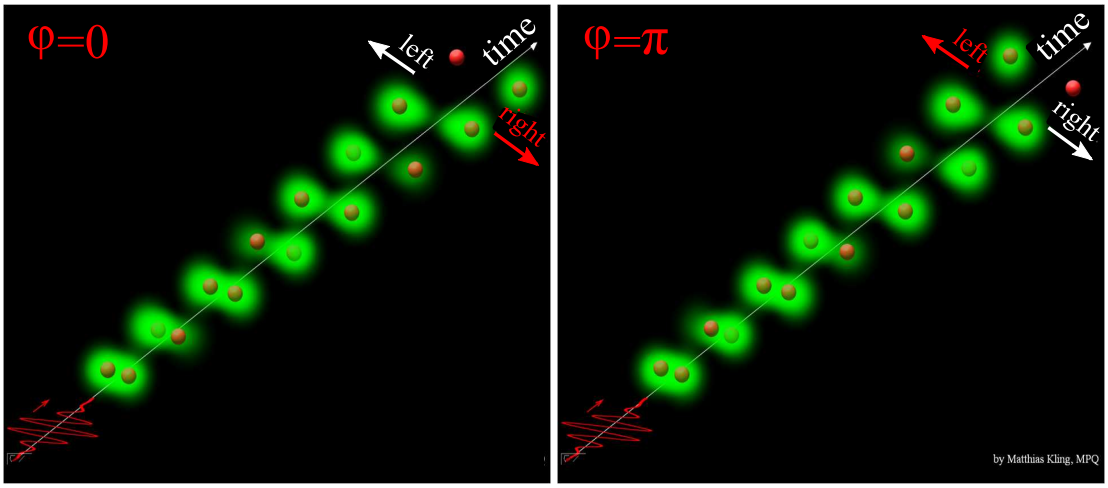

Figure 5: Illustration of the electron localization mechanism presented in [KSV+06]. The laser pulse ionizes the neutral D_2 molecule and induces the dissociation of the molecular ion. The remaining electron is driven back and forth between the two nuclei. When the distance between the two nuclei has become too large for the electron to tunnel, it remains localized at one of them. At which it remains localized depends on the carrier-envelope phase of the pulse. Image with permission of M. Kling.

figure 4 (a). The CEP can thus be used as a control parameter for processes which depend on the instantaneous electric field of the pulse.

The carrier-envelope phase of pulses emitted from laser systems is generally not constant, but varies from pulse to pulse. The development of techniques for measuring and stabilizing the phase were an important step in frequency metrology [Hän06]. With the extension of phase stabilization to amplified laser systems by Baltuska et al. [BUU+03] phase-stable laser pulses became also an important tool in strong field physics. The CEP was shown to influence processes like non-sequential double ionization [LRE+04] or emission of terahertz radiation [KLT+06]. The application of phase stable laser pulses in high harmonic generation allowed for the creation of isolated attosecond pulses [SBC+06]. Attosecond physics, however, becomes already accessible with phase-stable laser pulses as the electric field is controlled with attosecond precision. This allows for experiments on effects related to the attosecond time-scale with CEP-stabilized laser pulses [GSM+09, KGU+04].

In an important experiment on D_2 molecules by Kling et al. [KSV+06], it was shown that electron localization in dissociating molecules can be achieved. This was the first demonstration of direct light-field control of a chemical reaction via the steering of electronic motion. The localization process is schematically illustrated in figure 5. The neutral D_2 molecule is ionized in the laser pulse and dissociation is induced. The deuterons thus move apart from each other whereby the remaining electron is driven back and forth between them. With increasing distance between the deuterons, a potential barrier between them emerges, which increases with the internuclear separation. When the potential barrier has become so high, that the electron cannot tunnel through anymore, the electron remains localized at one of the deuterons. At which of the deuterons it remains predominantly localized depends on the carrier-envelope phase of the pulse. The deuteron

and the neutral deuterium atom emerging from the dissociation are emitted opposite to each other. For non-phase-stabilized laser pulses, the deuteron is emitted with equal probability to the left or to the right along the laser polarization axis. Electron localization in phase stable laser pulses leads to a CEP dependent asymmetry in the emission direction of the deuteron. Like for other coherent control schemes, the control mechanism can be also understood in terms of interfering reaction pathways, here different pathways of dissociation.
In the experiment of Kling et al., an asymmetry was observed for high energetic deuterons emerging from a recollision process. Here the electron emitted by ionization of D_2 in the laser pulse is driven back to the D_2^+ ion by the laser electric field and induces its dissociation by an inelastic scattering process. For low energetic deuterons, for which recollision is not involved in the dissociation mechanism, only a very weak asymmetry was observed. An asymmetry in this regime was however predicted by theory [RE07b, HE09].
In this thesis, measurements are presented, in which an asymmetry in this low energetic regime was observed for H_2 [KFF$^+$09]. The measurements were carried out by using a reaction microscope as detector, which has several advantages compared to the velocity-map-imaging-spectrometer (VMI) [EP97] used in the measurements of Kling. With a reaction microscope the full three-dimensional momentum vectors of all charged fragmentation products can be determined, which makes kinematically complete experiments possible. Another advantage is that particles can be detected in coincidence so that different reaction channels can be separated from each other.
In this measurement, it could be shown that the asymmetry is dependent on the relative angle between the molecular axis and the polarization axis of the laser pulse. By detecting the emitted electron in coincidence with the dissociating proton, the role of the first ionization step for the asymmetry could be investigated. The experimental results could be well reproduced by a time dependent Schrödinger equation (TDSE) calculation, and were in good agreement with a simple model developed to explain the asymmetry.
These experimental results provided new and important insights into the control of electron localization by the CEP. But still some interesting questions remain open. What is the role of coherence, that means what difference does it make for the asymmetry if the vibrational states in the H_2^+ ion are populated coherently and form a localized nuclear wave packet or if the vibrational states are populated incoherently. How does the asymmetry depend on the dynamics of the wave packet, i.e. does it play a role in which direction the wave packet moves or what momentum it has? Is it possible to enhance the asymmetry by choosing such parameters appropriately?
In order to shed light onto these questions, a two-pulse scheme can be used. With the first pulse H_2 is ionized and a nuclear wave packet is created in the H_2^+ potential well. A second pulse is used to induce electron localization after some time delay. In this way. the asymmetry dependent on the wave packet evolution shown in figure 2 can be analyzed. In the revival, the dependence of the asymmetry on the position and momentum of the wave packet can be studied. By comparing the asymmetry in the revival to the asymmetry in the dephasing region, the role of coherence can be investigated.

This thesis is structured as follows: The first chapter deals with the theoretical basis of the interaction of atoms and molecules with strong laser fields. The possible ionization mechanisms are presented and dissociation of H_2 is discussed in terms of the Floquet representation. Besides that, the evolution of a bound wave packet with its relevant time scales is described. In the second

chapter, the basic properties of ultrashort laser pulses are presented followed by a description of the laser system used to generate such laser pulses. A general description of the carrier-envelope phase is provided in chapter 3. Techniques to measure and stabilize the phase are discussed in general followed by a description of the experimental realization and the achieved stabilization quality. Chapter 4 deals with the reaction microscope used for detection of the reaction fragments and the reconstruction of the momenta and energies of the fragments. Single-pulse measurements on electron localization in H_2 and D_2 in the bond-softening regime are presented in chapter 5, which were carried out in the framework of [Kre09] and this thesis. A model developed for explaining electron localization is discussed and compared to the localization mechanism including recollision. A TDSE calculation based on this model is described and its results are compared to the experimental data. In chapter 6, two-pulse measurements are presented, in which electron localization is studied in different regimes of the wave packet evolution. The experimental data are compared to the results of a wave packet simulation. The results are discussed and models for their description are explained. The thesis ends with a conclusion and an outlook to future experiments.

Chapter 1

Atoms and molecules in intense laser fields

In this chapter, basic theoretical concepts for the description of atoms and molecules in intense laser fields are presented. Some elements are thereby common to atoms and molecules, like for example mechanisms for single and double ionization. They are described in the first part of this chapter using the example of rare-gas-atom-laser interactions.
The rest of the chapter deals mainly with H_2 in strong laser fields. First single ionization is discussed, which leads to the coherent population of several vibrational states in the ground state of H_2^+. The Franck-Condon principle, which was first used for calculating the population of these states, is described. Afterwards, the dependence of the ionization probability on the internuclear distance, which was shown to play an important role for the population of the vibrational states, is discussed.
After single ionization, the created H_2^+ ion can dissociate in the laser field. Dissociation phenomena can be well understood within the Floquet representation, in which the interaction of the H_2^+ with the laser field is described in terms of light induced states. The theoretical concepts of this model are introduced in section 1.4 and important dissociation phenomena are presented. The next section deals with the dynamics of the wave packets which remain bound in the H_2^+ ion. The temporal evolution of the wave packet is described and the relevant time scales are derived. Further possible fragmentation pathways of H_2 in intense laser fields are discussed in the last section of this chapter.

1.1 Single ionization

For single ionization in intense laser fields, two mechanisms can be distinguished, multiphoton and tunneling ionization. Which of the two models is applicable is determined by the so-called Keldysh parameter [Kel64]

$$\gamma = \sqrt{\frac{I_p}{2U_p}}\,, \tag{1.1}$$

where I_p is the ionization potential and $U_p = \frac{I}{4\omega^2}$ the ponderomotive energy[1] of an electron in a laser field with the frequency ω and the intensity I. For a fixed laser frequency and ionization potential, as is the case in the experiments presented in this thesis, γ is only determined by the laser intensity.
The Keldysh parameter can be also expressed in terms of the ratio between the laser frequency and the tunneling rate ω_t

$$\gamma = \frac{\omega}{\omega_t}. \tag{1.2}$$

At high intensities ($\gamma \ll 1$), the period of the laser field is longer than the tunneling time of the electron and tunneling ionization is dominant. At small intensities ($\gamma \gg 1$), the change of the electric field is faster than the tunneling time so that the electron does not have enough time to tunnel. Here the ionization is described by the absorption of n photons, which is referred to as multiphoton ionization.

1.1.1 Multiphoton ionization

In the multiphoton regime, single ionization occurs due to the simultaneous absorption of n photons with $n\,\hbar\omega \geq I_p$. The ionization rate is given by [FPAC82]

$$\upsilon_n = \sigma_n I^n, \tag{1.3}$$

where σ_n is a generalized n-photon cross section. Due to the interaction with the Coulomb potential of the ion, the electron can also absorb more photons than required for ionization (see figure 1.1). The ionization rate is then given by

$$\upsilon_{n+s} = \sigma_n I^{n+s}, \tag{1.4}$$

where s is the number of additionally absorbed photons. Characteristic for this process, which is referred to as above threshold ionization (ATI), are discrete peaks in the electron energy spectra separated by the photon energy [AFM$^+$79].
Since a free electron in a laser field has the ponderomotive energy U_p, for ionization this energy has to be given to the electron in addition to I_p. Thus, the energy of the freed electron is

$$E_{el} = (n+s)\hbar\omega - I_p^*, \tag{1.5}$$

with the modified ionization potential $I_p^* \approx I_p + U_p$.
Generally, the electric field of the laser introduces an intensity dependent shift of the atomic levels (AC-Stark shift) so that multiphoton transitions can become resonant with atomic levels. At such Freeman resonances, the ionization rate can be enhanced by orders of magnitude [FBM$^+$87, MBT$^+$92, MBT$^+$93]. As the intensity in the laser focus changes temporally as well as spatially, for understanding the photo-electron spectra, the intensity dependence of the ionization potential and the occurrence of resonances have to be considered. A detailed discussion of this processes can be found, for example, in [Zro05] and [Sta05].

[1] The ponderomotive energy is the mean quiver energy of a charged particle in the laser field.

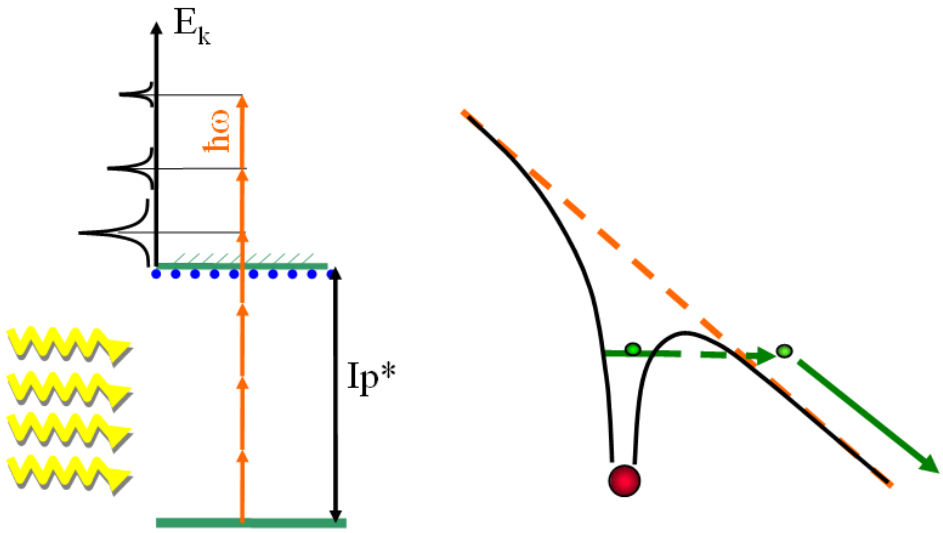

Figure 1.1: Schematic illustration of the ionization mechanisms in intense laser fields. Left: In the multiphoton regime, the ionization is described by the absorption of n photons. The electron can also absorb more photons than required for ionization which is referred to as above threshold ionization. Right: In the tunneling regime, the atomic potential is deformed by the laser field. Thereby, a potential barrier is formed, through which the electron can tunnel.

1.1.2 Tunnel ionization

For high intensities, where $\gamma \ll 1$, the electric field of the pulse can be treated classically. It introduces a bending of the atomic or molecular potential so that a potential barrier is built, through which the electron can tunnel (see figure 1.1). The ionization rate is obtained from the ADK-theory [ADK86, DK91]. For the ionization of atoms, it is given by

$$w_T(t) = \frac{4(2I_P)^{5/2}}{\mathcal{E}(t)} e^{-\frac{2(2I_P)^{2/3}}{3\mathcal{E}(t)}}, \tag{1.6}$$

with the electric field strength $\mathcal{E}(t)$ of the laser.
The measurements presented in this thesis are in the tunneling regime as $\gamma \approx 0.1$. The transition between tunneling and multiphoton regime is, however, smooth so that the two regions can be clearly separated only for $\gamma \ll 1$ and $\gamma \gg 1$, respectively.
Directly after tunneling, the electron has approximately zero energy. Its further dynamics is determined by the electric field of the laser, which can be written as $\mathcal{E}(t) = \mathcal{E}_0(t)\cos(\omega t)$, with the frequency ω and the pulse envelope $\mathcal{E}_0(t)$. For linearly polarized laser pulses, only the motion of the electron parallel to the polarization axis is affected by the laser field. The motion of the electron is composed of an oscillation in the laser field and a drift motion. When the laser pulse passes by, only the drift energy remains[2]. The drift energy thereby depends on the phase $\phi_0 = \omega t_0$

[2]This is the case for ultrashort laser pulses. In long laser pulses, the electron gains additionally the ponderomotive energy as kinetic energy.

the electron is set into the laser field [FMU00] and is given by

$$E_{drift}(t_0) = 2U_p \sin^2(\omega t_0). \tag{1.7}$$

If the electron is set into the laser field at a maximum of the electric field, no drift momentum is gained. The drift energy is maximal at a zero crossing of the field, where it has a value of $2U_p$.

1.1.3 Recollision

For linearly polarized laser pulses, the electron energy distribution reveals a plateau above $2U_p$, which vanishes in the case of elliptical polarization [PBNW94]. The occurrence of this high energetic electrons can be explained by a recollision mechanism [Kuc87, SYDK93]: After tunneling, the electron is accelerated in the laser field. When the laser field changes its sign, the electron is decelerated and then reverses its direction. It can return to the parent ion if the phase, at which it tunnels, lies in the range $m\,\pi/2 < \phi_0 < (m+1)\pi/2$ for odd m. If the electron is elastically scattered at the ion potential in backward direction, it is further accelerated in the subsequent half-cycle of the laser field thereby gaining energies up to $10\,U_p$.
In a so-called stereo-ATI spectrometer, this process is used for measuring the carrier-envelope phase of laser pulses as explained in section 3.4. A recollision scenario also provides an explanation for other important processes in intense laser fields, like for example high harmonic generation[Cor93][Kuc87][TGB99] or non-sequential multiple ionization [BDM05][DWW$^+$02].

1.2 Double and multiple ionization

At high intensities, double ionization can be explained by two sequential tunneling ionization steps, which occur independently from each other. In figure 1.2, the intensity dependent double ionization rate of neon is shown. At high intensities, the experimental data is in good agreement with the theoretical prediction for sequential ionization. At low intensities, however, the double ionization rate is underestimated by this model by several orders of magnitude [WSD$^+$94, LTC98]. This discrepancy indicates that at low intensities a process involving electron-electron correlation becomes important. Several such non-sequential processes were suggested, like shake off [BJ67, SJD$^+$95, PSR03], two-step-one [Khe01, Sam90] and a recollision model [Cor93, DWW$^+$02]. Differential measurements of the electron momentum distribution, which became possible by the development of COLTRIMS and reaction microscopes [FMU00, MFS$^+$00, WGW$^+$00, WWS$^+$00a, WWS$^+$00b], provided evidence that the recollision mechanism dominates.
As described in the previous section, the electron can be driven back to the parent ion by the laser field. When it returns to the ion, it can inelastically scatter and thereby remove a further electron from the ion. Since recollision takes place close to the zero crossing of the electric field, the electrons gain a high drift momentum. The sum momentum of the electrons is balanced by the momentum of the ion so that the ion also obtains a high momentum. This leads to a double hump structure in the momentum distribution of the doubly charged ion parallel to the laser polarization axis (see figure 1.2). This structure disappears if the polarization of the laser field is elliptic as then the electron cannot return to the ion. The other suggested mechanisms for non-sequential double ionization were ruled out as they would lead to a momentum distribution

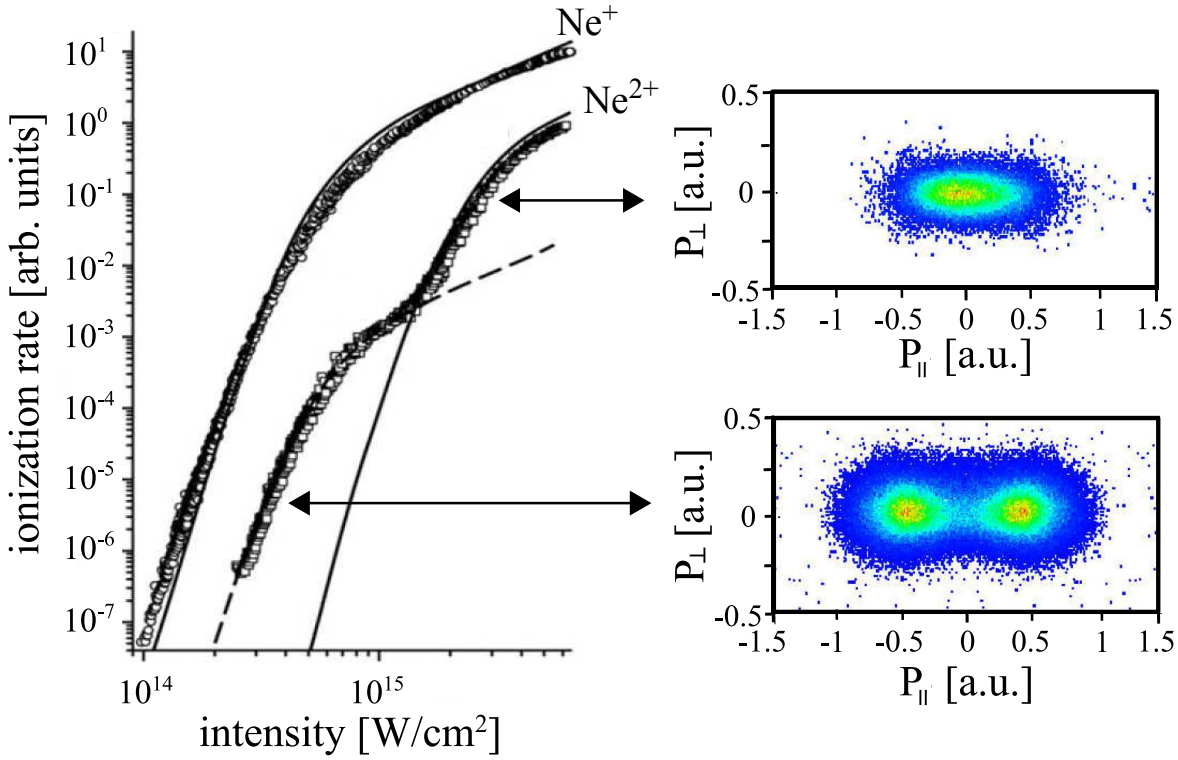

Figure 1.2: In the left image, the intensity dependent ionization yield for single and double ionization of neon in 25 fs laser pulses is shown. At high intensities, double ionization is well described by a sequential model, whereas for low intensities double ionization is dominated by a recollision process. The momentum distributions of the Ne^{2+} ions for sequential and non-sequential double ionization are shown in the right images. Here $P_{\parallel}$ is the momentum component parallel and $P_{\perp}$ the momentum component perpendicular to the polarization axis.

centered around zero.
The measured momentum distribution of doubly-ionized neon could be well explained with direct ionization in the recollision process as described above. For other atomic species, like argon, however, the double-hump structure is less pronounced than predicted by this model. It was shown that this discrepancy can be explained by a non-sequential process called RESI[3] [FMF+01]. Here the recollision process leads to excitation of the bound electron followed by tunneling in a subsequent maximum of the laser field. As for ionization near the field maximum the drift momentum is small, the RESI-mechanism leads to a filling of the gap of the double-hump structure. The probability for this process to occur, depends on the excitation cross section and thus on the atomic structure [dJFZ+06].

[3] **R**ecollision **e**xcitation with **s**ubsequent field **i**onization

1.3 Single ionization of H_2

Due to their much lower mass, the motion of the electrons in a molecule is much faster than that of the nuclei so that the electron distribution adapts instantaneously to a change of the nuclear configuration. Therefore, the nuclear and the electronic motion can be regarded separately, which is known as the Born-Oppenheimer approximation. The potential curves of the molecule are determined by keeping the internuclear distance $\mathbf{R}$ at a fixed value and calculating the total energy V of the system, which is composed of the total potential energy of the electrons and the nuclei and the average kinetic energy of the electrons. One thereby obtains the potential curves $V(\mathbf{R})$, on which the nuclei can move. For H_2^+ in ultrashort laser pulses, the relevant potential curves belong to the electronic states $1s\sigma_g$ and $2p\sigma_u$.
Single ionization of H_2 mainly leads to a population of the electronic ground state $1s\sigma_g$ of H_2^+. The population of excited electronic states can be neglected due to their significantly higher potential energy. The resulting distribution of the vibrational states in this potential curve is discussed in the following subsection.

1.3.1 Franck-Condon principle

Assuming that the single ionization step happens so fast, that the internuclear distance and the velocity of the nuclei almost does not change during this process, single ionization corresponds to a vertical transition between the H_2 potential curve and the $1s\sigma_g$ state of H_2^+. This is referred to as the Franck-Condon principle. The ionization step can be regarded as a projection of the initial wave function Ψ_{H_2} via the dipole transition matrix element $\mathbf{D}$ onto the wave function $\Psi_{H_2^+}$ of H_2^+, whereby the transition probability is assumed to be independent of $\mathbf{R}$. The transition matrix element $\mathbf{D}$ thus depends only on the electronic coordinates $\mathbf{r_1}$ and $\mathbf{r_2}$ and not on $\mathbf{R}$.
By neglecting the spin and the rotation, the total wave function Ψ in the Born-Oppenheimer approximation can be written as a product of the electronic ϕ_{el} and the vibronic wave function ψ_ν

$$\Psi_{H_2} = \phi_{el_{H_2}}(\mathbf{r_1}, \mathbf{r_2}) \cdot \psi_{\nu_{H_2}}(\mathbf{R}) \tag{1.8}$$

$$\Psi_{H_2^+} = \phi_{el_{H_2^+}}(\mathbf{r_1}) \cdot \psi_{\nu_{H_2^+}}(\mathbf{R}). \tag{1.9}$$

The transition amplitude is then given by

$$\left\langle \Psi_{H_2} \left| \mathbf{D} \right| \Psi_{H_2^+} \right\rangle = \left\langle \phi_{el_{H_2}} \left| \mathbf{D} \right| \phi_{el_{H_2^+}} \right\rangle \left\langle \psi_{\nu_{H_2}} \middle| \psi_{\nu_{H_2^+}} \right\rangle. \tag{1.10}$$

The first integral of equation (1.10) contains the dipole selection rules. The second integral is the so-called Franck-Condon factor, which determines the occupation of the vibrational states in H_2^+.
The occupation of the vibrational states in H_2^+ is well described by the Franck-Condon principle if H_2 is ionized by high energetic protons or by collisions with electrons (see figure 1.4 (c)). In these cases, the assumption of an R independent ionization probability is well fulfilled. For ionization in ultrashort laser pulses, the vibrational distribution differs from the one predicted by the Franck-Condon principle [UFSC$^+$04, vBD72]. This discrepancy can be attributed to the dependence of the ionization rate on the internuclear distance, which is discussed in the following.

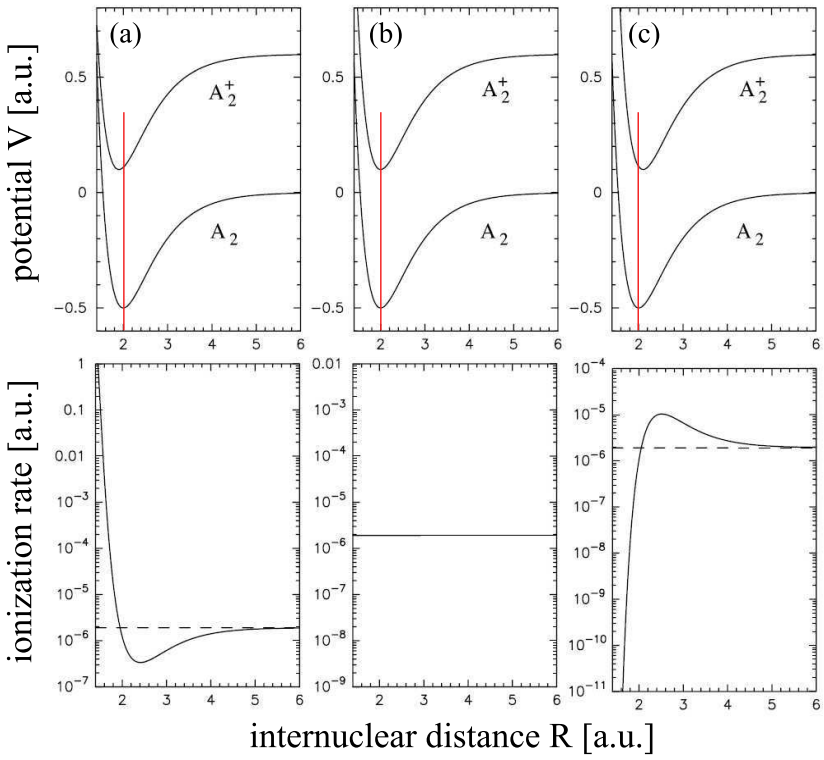

Figure 1.3: Illustration of the R dependence of the ionization potential of diatomic molecules. The potential curves for the ground states of the neutral and the ionized molecule are shown for three different cases. In (a), the equilibrium distance R_0 of the ionized state is smaller than in the neutral molecule, in (b) it is equal and in (c) it is larger. The corresponding ionization probabilities calculated with the ADK-theory are shown in the images below [Sae00].

1.3.2 R dependence of the ionization probability

The ADK-formula (1.6), which determines the ionization rate in the tunneling regime, reveals a strongly nonlinear dependence on the intensity and on the ionization potential I_p. The ionization potential for a diatomic molecule at a certain internuclear distance $\mathbf{R}$ is given by the energy difference between the potential of the neutral (A_2) and the potential of the ionized molecule (A_2^+)

$$I_p(\mathbf{R}) = E_{A_2^+}(\mathbf{R}) - E_{A_2}(\mathbf{R}). \tag{1.11}$$

In figure 1.3, the ionization rates for three different diatomic molecules are shown. If the ionized state has the same equilibrium distance as the potential of the neutral molecule, as illustrated in figure 1.3 (b), I_p is independent of $\mathbf{R}$. The corresponding ionization rate, which is shown as a function of $\mathbf{R}$ in the image below, is thus constant. In case the equilibrium distance of the ionized state is shifted as illustrated in figure 1.3 (a) and (c), the ionization potential depends on $\mathbf{R}$. Here the corresponding ionization rate varies with the internuclear distance by several orders of magnitude. The transition matrix element $\mathbf{D}$ therefore depends on $\mathbf{R}$ and the Franck-Condon

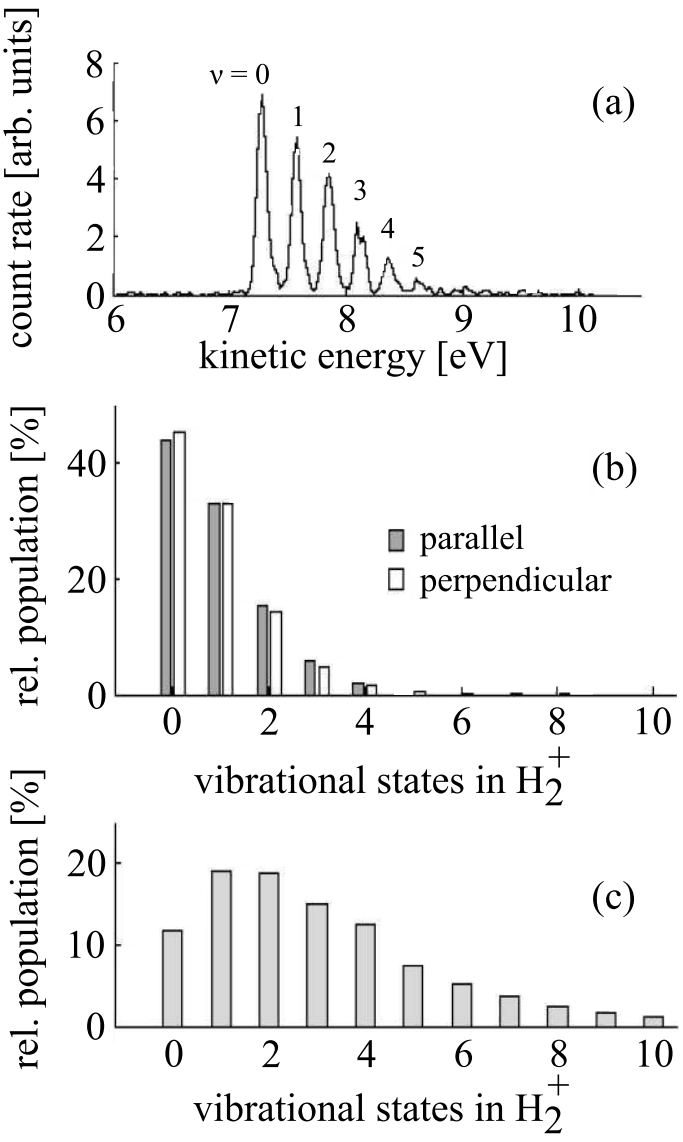

Figure 1.4: Population of the vibrational states in H_2^+. In (a), the measured relative population of the vibrational states after ionization of H_2 by a $45\,fs$ laser pulse with a peak intensity of $3 \cdot 10^{13}\,W/cm^2$ is shown. The result of a calculation for the same pulse parameters as in (a) is shown in (b). Here the dependence of the ionization rate on the internuclear distance (see figure 1.3) was taken into account. The results for the polarization axis of the laser pulse being parallel (gray) and perpendicular (white) to the molecular axis are depicted. (c) Measured population distribution after ionization by electron impact ($100\,eV$ electrons). In this case, the distribution is in good agreement with the Franck-Condon principle [UFSC+04].

principle is not valid anymore [Sae00]. Then the Franck-Condon factor in equation (1.10) has to be replaced by

$$\left\langle \psi_{\nu_{H_2}} \left| \mathbf{D} \right| \psi_{\nu_{H_2^+}} \right\rangle. \tag{1.12}$$

In H_2^+, the equilibrium distance R_0 is larger than in H_2 (see figure 1.3 (c)) so that the parts of the ground state wave function in H_2 above R_0 have a higher transition probability. The population of the vibrational states in the H_2^+ ground state therefore differs from the Franck-Condon distribution, whereby lower vibrational states are populated more strongly [UFSC$^+$04]. This can be seen in figure 1.4 (a), where the measured occupation of the vibrational states is shown. It is in good agreement with the results of a calculation, in which the R dependence of the ionization probability was considered (figure 1.4(b)).

1.4 Floquet representation

Different theoretical models for describing molecules in strong laser fields were developed. One of the most descriptive ones is the Floquet representation [Shi65, Chu81], which provides, for instance, intuitive insight into the dissociation of H_2^+. The basic concepts of the Floquet approach are presented in this section based on the representation in [Pav04, Erg06].
The Schrödinger equation of an H_2^+ molecule in a monochromatic, linearly polarized and periodic electric field $\mathcal{E}(t) = \mathcal{E}_\mathbf{0} \cos \omega t$ is given by

$$\hat{\mathcal{H}}(\mathbf{r}, \mathbf{R}, t)\Psi(\mathbf{r}, \mathbf{R}, t) = i\hbar \frac{\partial}{\partial t}\Psi(\mathbf{r}, \mathbf{R}, t). \tag{1.13}$$

Here $\mathbf{r}$ is the position vector of the electron in the center of mass system of the ion and $\mathbf{R}$ is the internuclear distance. The total Hamiltonian can be separated into a field-free Hamiltonian $\hat{\mathcal{H}}_0$, which is time independent, and an interaction Hamiltonian $\hat{\mathcal{V}}(\mathbf{r}, t)$ characterizing the interaction with the laser field

$$\hat{\mathcal{H}}(\mathbf{r}, \mathbf{R}, t) = \hat{\mathcal{H}}_0(\mathbf{r}, \mathbf{R}) + \hat{\mathcal{V}}(\mathbf{r}, t). \tag{1.14}$$

The field free Hamiltonian is given by

$$\hat{\mathcal{H}}_0(\mathbf{r}, \mathbf{R}) = \hat{\mathcal{T}}_K + \hat{\mathcal{H}}_{el}(\mathbf{r}, \mathbf{R}), \tag{1.15}$$

where $\hat{\mathcal{T}}_K$ is the kinetic energy of the nuclei and $\hat{\mathcal{H}}_{el}(\mathbf{r}, \mathbf{R})$ the Hamiltonian of the electron.

The interaction with a linearly polarized laser field in the dipole approximation is given by

$$\hat{\mathcal{V}}(\mathbf{r}, t) = -e\mathbf{r} \cdot \mathcal{E}(t), \tag{1.16}$$

with the dipole moment $e\mathbf{r}$. If the molecular axis is parallel to the polarization axis z, one obtains

$$\hat{\mathcal{V}}(\mathbf{r}, t) = -\frac{e\mathcal{E}_0 z}{2}\left(e^{i\omega t} + e^{-i\omega t}\right) = \mathcal{V}_- e^{i\omega t} + \mathcal{V}_+ e^{-i\omega t}. \tag{1.17}$$

The interaction term $\hat{\mathcal{V}}(\mathbf{r}, t)$ has a temporal periodicity of $T = 2\pi/\omega$. As it contains the only time dependence of the system, the total Hamiltonian is also periodic in time

$$\hat{\mathcal{H}}(\mathbf{r}, \mathbf{R}, t) = \hat{\mathcal{H}}(\mathbf{r}, \mathbf{R}, t + T). \tag{1.18}$$

If the Hamilton operator is periodic in space or time, the Floquet-theory can be applied. Thereby, for the wave function $\Psi(\mathbf{r},\mathbf{R},t)$ one makes the ansatz

$$\Psi(\mathbf{r},\mathbf{R},t) = e^{iEt/\hbar}\Phi(\mathbf{r},\mathbf{R},t), \tag{1.19}$$

where E is the so-called quasi energy and $\Phi(\mathbf{r},\mathbf{R},t) = \Phi(\mathbf{r},\mathbf{R},t+T)$ is periodic in T. Due to the periodicity of $\Phi(\mathbf{r},\mathbf{R},t)$ a discrete Fourier expansion can be applied

$$\Phi(\mathbf{r},\mathbf{R},t) = \sum_{n=-\infty}^{\infty} e^{-in\omega t}\Phi_n(\mathbf{r},\mathbf{R}) \tag{1.20}$$

so that the wave function is given by

$$\Psi(\mathbf{r},\mathbf{R},t) = e^{iEt/\hbar}\sum_{n=-\infty}^{\infty} e^{-in\omega t}\Phi_n(\mathbf{r},\mathbf{R}). \tag{1.21}$$

By inserting this expression into the Schrödinger equation and making use of (1.14) and (1.17), the time dependent Schrödinger equation is transformed into a set of time independent coupled differential equations

$$\left[E + n\hbar\omega - \hat{\mathcal{T}}_K + \hat{\mathcal{H}}_{el}(\mathbf{r},\mathbf{R})\right]\Phi_n(\mathbf{r},\mathbf{R}) = \mathcal{V}_+\Phi_{n-1}(\mathbf{r},\mathbf{R}) + \mathcal{V}_-\Phi_{n+1}(\mathbf{r},\mathbf{R}), \tag{1.22}$$

where neighboring Fourier components are coupled to each other. The functions $\Phi_n(\mathbf{r},\mathbf{R})$ are solutions of the field free Hamiltonian $\hat{\mathcal{H}}_0$, which are embedded in the laser field by the phase factor $e^{-in\omega t}$ and are referred to as dressed states [AT55, Lau77, BZ77].
For H_2^+, the $\Phi_n(\mathbf{r},\mathbf{R})$ correspond to the gerade and the ungerade wave functions $\phi_g(\mathbf{r},\mathbf{R})$ and $\phi_u(\mathbf{r},\mathbf{R})$ of the two electronic states $1s\sigma_g$ und $2p\sigma_u$. Their eigenvalue equations are given by

$$\begin{aligned}\hat{\mathcal{H}}_{el}(\mathbf{r},\mathbf{R})\,|\phi_{g,n}(\mathbf{r},\mathbf{R})\rangle &= V_g(\mathbf{R})\,|\phi_{g,n}(\mathbf{r},\mathbf{R})\rangle \\ \hat{\mathcal{H}}_{el}(\mathbf{r},\mathbf{R})\,|\phi_{u,n}(\mathbf{r},\mathbf{R})\rangle &= V_u(\mathbf{R})\,|\phi_{u,n}(\mathbf{r},\mathbf{R})\rangle\,,\end{aligned} \tag{1.23}$$

where $V_g(\mathbf{R})$ and $V_u(\mathbf{R})$ are the energy eigenvalues corresponding to the potential curves of the $1s\sigma_g$ and the $2p\sigma_u$ state, respectively.
As can be seen from equation (1.21), there are identical solutions for energies $E = n\hbar\omega$ with $n = 0, 1, 2, ...$ so that the field free states $\phi_g(\mathbf{r},\mathbf{R})$ and $\phi_u(\mathbf{r},\mathbf{R})$ can be regarded as dressed with n photons as denoted by the index n in equation (1.23). The operators in (1.17) can thereby be interpreted as ladder operators for absorption ($\mathcal{V}_+$) and emission ($\mathcal{V}_-$) of one photon. Due to selection rules only states with different symmetry can couple (here gerade and ungerade) so that functions with neighboring indices (n and $n \pm 1$) must correspond to different electronic states. Equation 1.22 then becomes

$$\begin{aligned}[E + n\hbar\omega - V_g(\mathbf{R})]\,|\phi_{g,n}(\mathbf{r},\mathbf{R})\rangle &= \mathcal{V}_+\,|\phi_{u,n-1}(\mathbf{r},\mathbf{R})\rangle + \mathcal{V}_-\,|\phi_{u,n+1}(\mathbf{r},\mathbf{R})\rangle \\ [E + (n+1)\hbar\omega - V_u(\mathbf{R})]\,|\phi_{u,n+1}(\mathbf{r},\mathbf{R})\rangle &= \mathcal{V}_+\,|\phi_{g,n}(\mathbf{r},\mathbf{R})\rangle + \mathcal{V}_-\,|\phi_{g,n+2}(\mathbf{r},\mathbf{R})\rangle\,.\end{aligned} \tag{1.24}$$

This infinite set of differential equations can be also written as an infinitely-dimensional matrix, from which the energies can be calculated by diagonalization. The matrix can be brought to a tridiagonal form, where the elements of the main diagonal are given by $V_g(\mathbf{R})$ and $V_u(\mathbf{R})$ shifted

by n, $n \pm 1$, $n \pm 2, ...$ photons, which are referred to as diabatic potential curves. The upper and the lower diagonal are given by the matrix elements

$$V_{ug}(\mathbf{R}) = V_{gu}(\mathbf{R}) \equiv \langle 2p\sigma_u | \, \mathcal{V}_{\pm} \, | 1s\sigma_g \rangle = \frac{\mathcal{E}_0}{2} \langle 2p\sigma_u | \, ez \, | 1s\sigma_g \rangle = \frac{\hbar \, \omega_R}{2}, \tag{1.25}$$

which denote the dipole coupling between neighboring states. Here ω_R is the Rabi frequency.
For practical calculations, the dimension of the matrix has to be reduced. The simplest case is a 2x2 Floquet-block. The energy eigenvalues can then be obtained by solving the equation

$$\begin{vmatrix} V_g(\mathbf{R}) - E & V_{ug}(\mathbf{R}) \\ V_{gu}(\mathbf{R}) & V_u(\mathbf{R}) - E - \hbar\omega \end{vmatrix} = 0, \tag{1.26}$$

where for simplicity n was assumed to be zero. The eigenvalues are the so-called adiabatic potential curves

$$E_{\pm}(\mathbf{R}) = \frac{V_g(\mathbf{R}) + V_u(\mathbf{R}) - \hbar\omega}{2} \pm \frac{1}{2}\sqrt{\left(V_g(\mathbf{R}) + \hbar\omega - V_u(\mathbf{R})\right)^2 + \left(\hbar\omega_R\right)^2}. \tag{1.27}$$

For describing the system appropriately, however, more than one Floquet-block has to be taken into account.
In case the intensity of the field is zero, the off-diagonal matrix elements of the Floquet blocks vanish and the diabatic potential curves are obtained. As mentioned above, they correspond to the potential curves of the gerade and the ungerade electronic state shifted by n, $n \pm 1$, $n \pm 2, ...$ photons and are illustrated in figure 1.5. The laser wavelength is assumed to be $800\,nm$, which corresponds approximately to the center wavelength of the laser pulses used in the experiments presented in this thesis. The corresponding photon energy is about $1.5\,eV$. Crossings of the diabatic states occur at an internuclear distance $R = X_1$, at which the energy difference between V_g and V_u corresponds to the photon energy ($X_1 = 4.8\,a.u.$). For a non-vanishing intensity, the laser field couples neighboring states, which leads to the formation of the so-called adiabatic potential curves. The adiabatic curves calculated by considering 20 Floquet blocks are shown in figure 1.5. At X_1, a so-called avoided crossing is formed, which means that an energy gap between the adiabatic curves evolves. The width of the gap is thereby proportional to the strength of the electric field.
The crossing at X_1 is referred to as the $1\,\omega$ crossing. Passing this gap along the lower adiabatic curve from $R < X_1$ to $R > X_1$ corresponds to the absorption of one photon. As can be seen from figure 1.5, at high intensities additional avoided crossings emerge. For intensities above $10^{14} W/cm^2$, at $R = X_2$ ($X_2 = 3.3\,a.u.$) an avoided crossing occurs due to the coupling of the diabatic curves $V_{g,n}$ and $V_{u,n-3}$. Passing this $3\,\omega$ crossing corresponds to the absorption of 3 photons.
The dissociation of molecules in intense laser fields can be explained by considering the nuclear motion in the adiabatic potential curves, which are also called light induced states. Two of the most important mechanisms are bond-softening and bond-hardening, which are presented in the following subsections.

1.4.1 Bond-softening

In absence of a laser field, the H_2^+ potential curves are unpertubed. In the Floquet picture, the system is then described by the diabatic potential curves shown in figure 1.5. With the

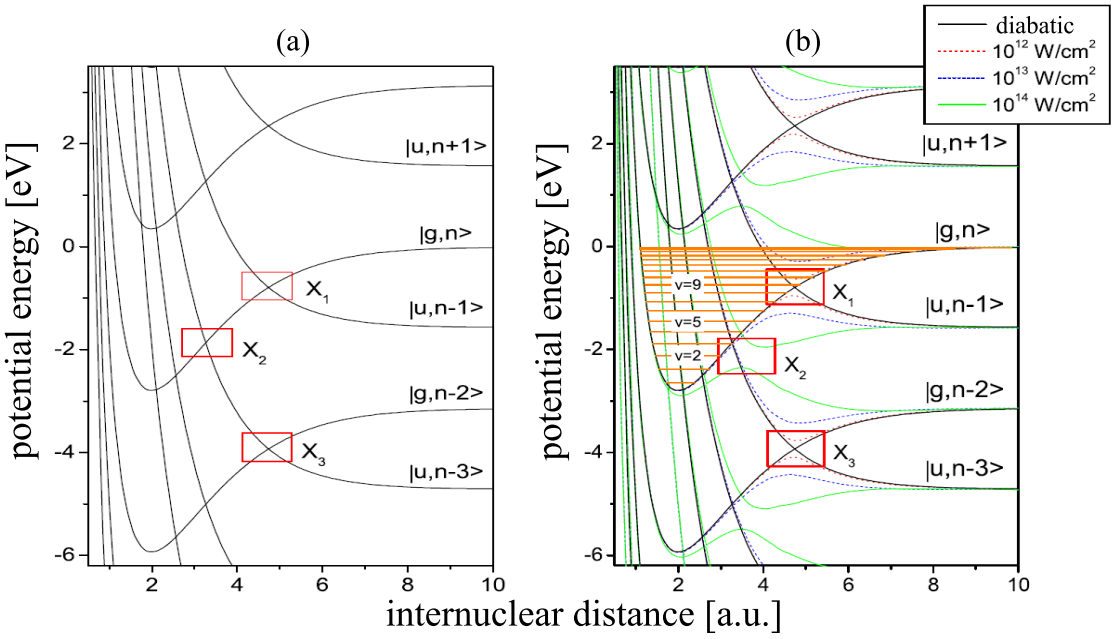

Figure 1.5: Illustration of the Floquet model for H_2^+ [Pav04]. a) For vanishing laser intensity, the molecule can be described by diabatic potential curves, which correspond to the potential curves of the $1s\sigma_g$ and the $2p\sigma_u$ state shifted by $n = 1, 2, 3, ...$ photons. The relevant crossings are marked with red rectangles. b) For a finite intensity, avoided crossings occur at the crossing points due to the coupling of the gerade and the ungerade state by the laser field and the so-called adiabatic potential curves are formed. The adiabatic potential curves for $10^{12}\,W/cm^2$ (red), $10^{13}\,W/cm^2$ (blue) and $10^{14}\,W/cm^2$ (green) were calculated by using 20 Floquet blocks.

presence of a laser field, the diabatic curves evolve into the adiabatic ones and the $1\,\omega$ avoided crossing opens. By passing this crossing, the potential changes from a binding one for $R < X_1$ to a repulsive one for $R > X_1$. The potential barrier which is formed is thereby lowered with increasing intensity. Vibrational states which lie above the potential barrier become unbound and can dissociate. Dissociation can also emerge from lower vibrational states by tunneling through the potential barrier. As the asymptotic energy of the final state $|u, n-1\rangle$ is lower than the energy of the $\nu = 5$ vibrational state, all vibrational states with $\nu \geq 5$ can dissociate.
With increasing intensity more and more vibrational states become unbound and at intensities above $10^{14}\,W/cm^2$ the $3\,\omega$ crossing opens. At somewhat higher internuclear distance, the $2\,\omega$ crossing is located, which emerges due to the coupling of the $|u, n-3\rangle$ and the $|g, n-2\rangle$ potential curve. Dissociation now occurs by passing the $3\,\omega$ crossing via the absorption of 3 photons and then the $2\,\omega$ crossing by the emission of one photon so that in total two photons are absorbed. At these intensities, basically all vibrational states are unstable and can dissociate.
This lowering of the binding potential by the laser field is referred to as bond softening [ZBMS90, BZMS90, GSMD$^+$95]. The energy of the dissociating proton is thereby determined by the energy of the vibrational state E_ν and the number of absorbed photons n (multiphoton dissociation)

[ESW$^+$06]

$$E_{diss} = \frac{1}{2}\left(n\hbar\omega - |E_\nu|\right). \tag{1.28}$$

In the experiments presented in this thesis, the influence of the carrier-envelope phase on the dissociation of H_2^+ and D_2^+ is studied. The focus lies on low energetic protons and deuterons, for which the dissociation mechanism is bond softening (see chapter 5 and 6). In these experiments, ultrashort laser pulses with a duration of only $6\,fs$ are used. Such ultrashort laser pulses have a large spectral bandwidth (see section 2.1) so that absorption and emission of photons can occur across the whole frequency spectrum. Thus, there is not only a certain internuclear distance, at which the transition between the gerade and the ungerade state of H_2^+ is resonant, but rather a range of distances.

1.4.2 Bond-hardening

At the avoided crossings, not only a lowering of the potential barrier occurs, but also the creation of a potential well above the energy gap (see figure 1.5). During the opening of the avoided crossings in the rising edge of the laser pulse, high vibrational states can be trapped in such a potential well. This phenomenon is referred to as bond hardening or population trapping [AS91, ZB93, FPPC99]. When the intensity decreases in the falling edge of the pulse, these states can move back to the $1s\sigma_g$ state or dissociate with almost zero energy.

1.4.3 Validity for ultrashort laser pulses

The Floquet formalism describes the interaction of a molecule with an infinitely long monochromatic wave. Therefore, the question arises whether it is also applicable for ultrashort pulses containing only a few optical cycles. In [RE07a], it was shown that this is indeed the case as ultrashort laser pulses are composed of many spectral components, each of which can be regarded as a monochromatic plane wave. The Floquet model can thus be applied for each of the frequency components. For describing the interaction with a laser pulse, one could add the results obtained for all spectral components coherently.
As discussed in subsection 1.4.1, the shape of the adiabatic potential curves depends on the intensity of the laser field, and thus changes with the envelope of the pulse. The Floquet picture is well suited in case the pulse envelope changes slowly compared to the nuclear dynamics. For ultrashort laser pulses, however, the envelope can change on a shorter timescale than the wave packet dynamics, which has to be taken into account when considering the dynamics of the wave packet on the adiabatic curves. This can be illustrated by means of the dissociation probability by net absorption of 2 or 3 photons [MSA$^+$08]. If the laser pulses are long, dissociation along the 3ω crossing via absorption of 3 photons is followed by the emission of 1 photon at the 2ω crossing, resulting in the net absorption of 2 photons. For $7\,fs$ pulses, however, the pulse intensity has already significantly decreased when the nuclear wave packet reaches the 2ω crossing, so that the re-emisson of one photon is less probable. Therefore, for $7\,fs$ pulses, dissociation via the net absorption of 3 photons is significantly enhanced compared to pulses longer than $10\,fs$.
This example illustrates that the Floquet representation can be helpful to gain insight into the dissociation dynamics also for ultrashort pulses, but one has to be careful when using it.

1.4.4 Three-dimensional potential curves

The potential curves shown in figure 1.5 were calculated for the special case of the molecular axis being parallel to the polarization axis. For the general case of an angle α between polarization axis and molecular axis, the dipole coupling terms are given by

$$V_{ug}(\mathbf{R}) = \frac{\mathcal{E}_0}{2} cos\,(\alpha)\ \langle 2p\sigma_u |\, ez\, | 1s\sigma_g \rangle\,. \tag{1.29}$$

The coupling is maximal for parallel orientation ($\alpha = 0°$) and vanishes for perpendicular orientation ($\alpha = 90°$). The potential barrier at the avoided crossings is therefore minimal for parallel orientation and increases with increasing angle. This leads to a strong angular dependence of the dissociation probability. Therefore, predominantly molecules with the molecular axis being parallel to the polarization axis dissociate, whereas there is almost no dissociation for molecules being oriented perpendicular to the polarization axis. This is referred to geometric alignment [Pos04]. The angle dependence of the light induced states is described in theory by three-dimensional potential curves [ZBMS90].

1.5 Temporal evolution of a bound wave packet

By single ionization of H_2, a wave packet is created in the electronic ground state of H_2^+. The wave packet $\psi(R,t)_{H_2^+}$ can be written as a superposition of the vibrational eigenfunctions ψ_ν

$$\psi(\mathbf{R},t)_{H_2^+} = \sum_\nu a_\nu \psi_\nu e^{-iE_\nu t/\hbar} = \sum_\nu a_\nu \psi_\nu e^{-i\omega_\nu t}, \tag{1.30}$$

with the energy eigenvalues E_ν. The factors a_ν denote the occupation of the vibrational states. The further evolution of the wave packet is determined by the eigenfunctions and energy eigenvalues. The time dependent probability density of the wave packet can be written as [CBNW09]

$$\left|\psi(\mathbf{R},t)_{H_2^+}\right|^2 = \sum_\nu |a_\nu|^2 |\psi_\nu|^2 + \sum_{\nu,\,\nu'\neq\nu} a_{\nu'} a_\nu^* \psi_{\nu'} \psi_\nu^* exp\left\{-i(\omega_{\nu'} - \omega_\nu)t\right\}. \tag{1.31}$$

The first term of this equation is just a sum of standing waves, which is time independent. The time dependence of the wave packet is provided by the second term. For $t = 0$, its value is unity, but for later times the time evolution is determined by the level spacings $\omega_{\nu'} - \omega_\nu$. In order to obtain an intuitive picture of the time evolution, it is useful to regard equation (1.31) for $\nu - \nu' = 1$. In case the level spacing is independent of ν, also the phase factor in equation (1.31) is independent of ν. Thus, the vibrations are in phase with each other. If the level spacing depends on ν, as is the case for molecular potentials, the vibrations get out of phase with time. The wave packet thus starts to spread and the motion gets delocalized. After some time, the vibrational states or a fraction of them re-phase again. In such a revival, the wave packet motion is again localized. In reality, also higher order contributions with $\nu' - \nu = 2, 3, ...$ occur.
For obtaining the time scales of the wave packet evolution, it is useful to consider the case, where the wave packet is composed of many vibrational states which are spread around a large central vibrational quantum number ν_0 so that $\nu_0 \gg \Delta\nu \gg 1$ [Rob04]. In this case, the energy

eigenvalues can be expanded by a Taylor series around this value

$$\begin{aligned} E(\nu) &\approx E(\nu_0) + \left.\frac{\partial E}{\partial \nu}\right|_{\nu_0} (\nu-\nu_0) + \frac{1}{2}\left.\frac{\partial^2 E}{\partial \nu^2}\right|_{\nu_0} (\nu-\nu_0)^2 + \frac{1}{6}\left.\frac{\partial^3 E}{\partial \nu^3}\right|_{\nu_0} (\nu-\nu_0)^3 + ... \\ &= E(\nu_0) + E'(\nu_0)\,(\nu-\nu_0) + \frac{E''(\nu_0)}{2}\,(\nu-\nu_0)^2 + \frac{E'''(\nu_0)}{6}\,(\nu-\nu_0)^3 + ... \end{aligned} \tag{1.32}$$

The time dependence of each eigenstate is then given by

$$e^{-iE_\nu t/\hbar} = \exp\left(-i\omega_0 t - 2\pi i\frac{\nu-\nu_0}{T_{cl}}t - 2\pi i\frac{(\nu-\nu_0)^2}{T_{rev}}t^2 - \dots\right), \tag{1.33}$$

with the characteristic timescales

$$T_{cl} = \frac{2\pi\hbar}{|E'(\nu_0)|} \quad \text{and} \quad T_{rev} = \frac{2\pi\hbar}{|E''(\nu_0)|/2}, \tag{1.34}$$

where T_{cl} is the classical oscillation period and T_{rev} is the revival time. The first term in the expansion drops out for $|\psi|^2$ and has therefore no observable effect.

1.5.1 Harmonic potential

The time T_{cl} is associated with the classical oscillation period in the bound state. In case of a harmonic oscillator, the energy eigenvalues are given by

$$E_\nu = \left(\nu + \frac{1}{2}\right)\hbar\omega_0. \tag{1.35}$$

The oscillation period of the eigenstates are harmonics of ω_0 on thus the level spacing of the vibrational states is constant. Therefore, the relative phase between the eigenstates remains preserved and thus also the shape of the wave packet. T_{cl} is given by

$$T_{cl} = \frac{2\pi}{\omega_0} \tag{1.36}$$

and denotes the oscillation period of the centroid of the wave packet. As higher order derivatives vanish, there are no longer time scales than T_{cl}.

1.5.2 Anharmonic potential

The electronic ground state of H_2^+ can be well approximated by a Morse potential with the energy eigenvalues

$$E_\nu = \hbar\omega_0\left[\left(\nu+\frac{1}{2}\right) - \alpha\left(\nu+\frac{1}{2}\right)^2\right], \tag{1.37}$$

where α is the anharmonicity constant. The first derivative of the energy is given by $|E'(\nu_0)| = (1-\alpha-2\alpha\nu_0)\,\hbar\omega_0$ leading to the classical period

$$T_{cl} = \frac{2\pi}{(1-\alpha-2\alpha\nu_0)\,\omega_0}, \tag{1.38}$$

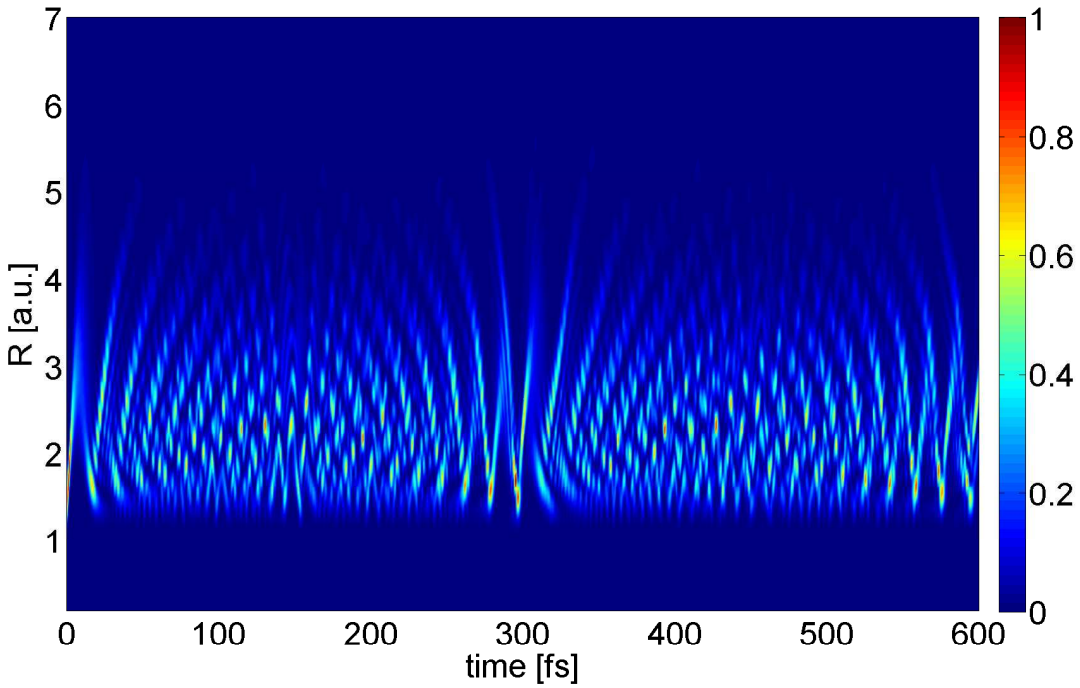

Figure 1.6: Temporal evolution of the bound wave packet in H_2^+. The probability density is shown as a function of time and internuclear distance. The oscillation of the wave packet as well as its dephasing and revivals can be observed.

which is larger than in case of a harmonic potential. As the second derivative $|E''(\nu_0)| = 2\alpha\hbar\omega_0$ does not vanish, one obtains a finite revival time

$$T_{rev} = \frac{2\pi}{\alpha\omega_0}, \tag{1.39}$$

which is much larger than the classical period (for $\alpha \ll 1$).
The temporal evolution of the H_2^+ wave packet obtained from a wave packet simulation (see also chapter 6 and appendix B) is shown in figure 1.6. Here the calculated probability distribution of the bound wave packet is shown as a function of time and internuclear distance. After its creation, the wave packet is localized and oscillates with its classical period. As the level spacings of the vibrational states are not equidistant, the oscillations of the eigenstates get more and more out of phase [Rob04]. Due to this dephasing the wave packet broadens and after some time the classical oscillation is not observable anymore. After T_{rev}, the phase term $exp(i2\pi\,(\nu-\nu_0)^2\;t/T_{rev})$ becomes one so that $\psi(\mathbf{R}, T_{rev}) = \psi(\mathbf{R}, t = 0)$. The wave packet is thus reformed and oscillates again with its classical period [VVU93, VVS96]. For H_2^+, the revival occurs at about $600\,fs$.
A reconstruction of the wave packet does not only occur after T_{rev}, but also at the times

$$\frac{t}{T_{rev}} = \frac{p}{q}, \quad \text{with} \quad p, q \in \mathbb{N}, \quad p/q \quad \text{irreducible.} \tag{1.40}$$

One of these so-called fractional revivals is the half-revival at $T_{rev}/2$. Here the initial wave packet is reconstructed completely, but it has a phase shift of π relative to $\psi(\mathbf{R}, t = 0)$. For H_2, the

half-revival is around $300\,fs$ as can be seen in figure 1.6.
At the quarter-revival near $T_{rev}/4$, the wave packet consists of two copies of the initial wave packet, which oscillate with a phase shift of π relative to each other. It can be seen in figure 1.6 at about $150\,fs$. As each of the wave packets passes the same location in phase space twice during each classical period, an oscillation with twice the classical frequency is observed.
For a potential, for which the energy dependence on the vibrational quantum number is quadratic, the fractional and full revivals will repeat indefinitely on the time scale of T_{rev}. This is usually not the case for realistic systems, where the energy dependence generally contains higher order terms so that also other timescales than T_{rev} start to play a role. Another effect of these terms is that the wave packet evolution is not symmetric with respect to the center of the revival as can be seen in figure 1.6 for the half-revival.
The temporal evolution of the H_2^+ wave packet was studied by pump-probe experiments with ultrashort laser pulses in [Erg06, ERF+06a, ERF+05] as discussed in more detail in chapter 6.

1.6 Double ionization of H_2

Single ionization of H_2 leads to the creation of a bound wave packet in H_2^+, which propagates in the $1s\sigma_g$ potential curve. The wave packet can dissociate in the laser field as explained in section 1.4.1, or it can be further ionized. Double ionization of H_2 leads to a vertical transition to the Coulomb potential curve as shown in figure 1.7. The wave packet then slides down the Coulomb potential curve, which corresponds to the repulsion of the unshielded nuclei and is referred to as Coulomb explosion. The energy the wave packet gains is inversely proportional to the internuclear distance R, at which the ionization step took place $E \propto 1/R$. Each of the protons thereby obtains half of the Coulomb energy.
As already discussed in section 1.2, double ionization can be described either by a sequential or a non-sequential process. For sequential double ionization, a resonance process called CREI[4] [ZB95, PM96, PDMT03] leads to an enhancement of the ionization rate of H_2^+ at $R = 6\,a.u.$ and $R = 10\,a.u.$ [Erg06].
In the case of non-sequential double ionization, the recolliding electron can either directly ionize the H_2^+ ion, or it can excite the ion to the $2p\sigma_u$ state along which it starts to dissociate[5]. As the electron recollides quite early after ionization (approximately 3/4 of the laser cycle), the transition to the $2p\sigma_u$ or the Coulomb curve occurs at small $\mathbf{R}$ so that the protons gain a high energy of several eV.

[4] **C**harge-**r**esonant **e**nhanced **i**onization

[5] The ion in the $2p\sigma_u$ state can also be ionized in a subsequent field maximum (RESI), as described in section 1.2, before the second electron is removed by tunneling ionization.

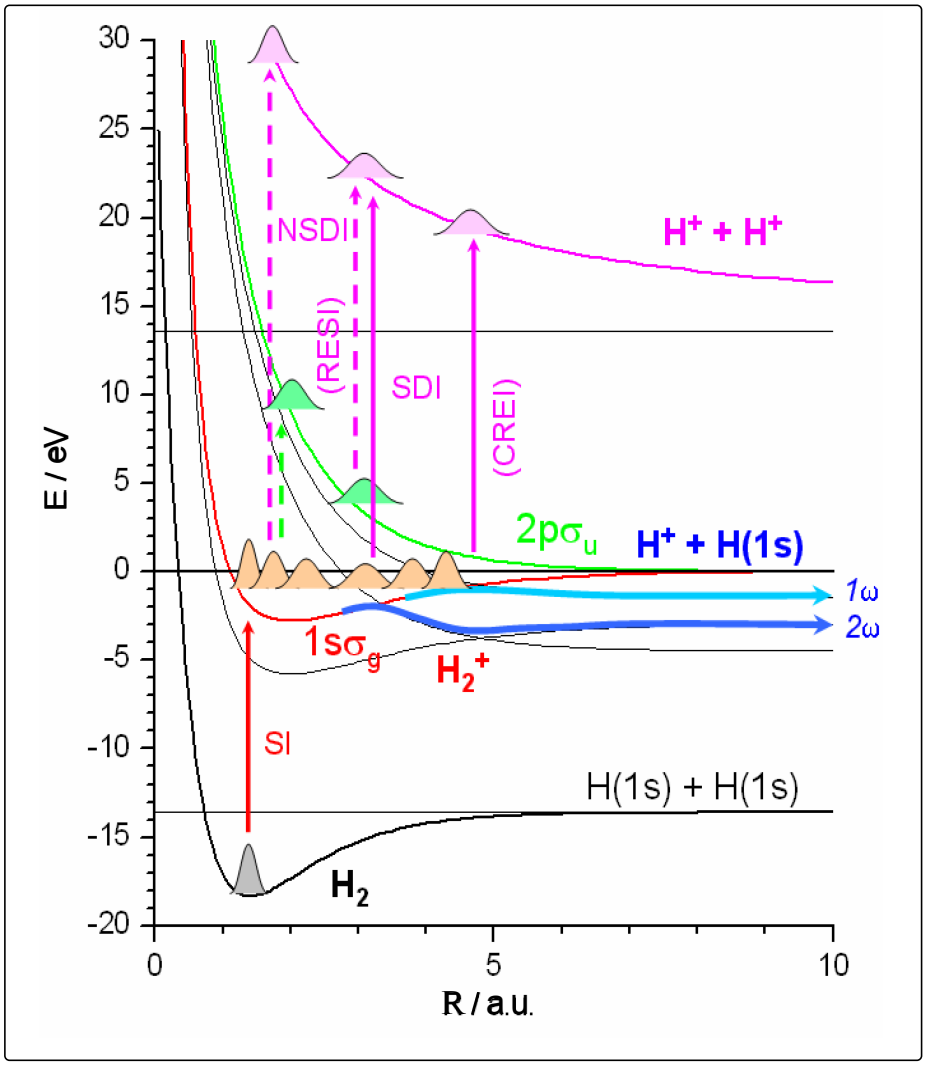

Figure 1.7: Illustration of the ionization channels of H_2. The potential curves of H_2 and H_2^+ in an intense laser pulse of 800 nm wavelength are shown. The vertical arrows denote the fragmentation channels and are located at the internuclear distances, at which the ionization processes occur predominantly. SI: Sequential ionization, SDI: Sequential double ionization, NSDI: Non-sequential double ionization, CREI: Charge resonance enhanced ionization.

Chapter 2

Generation of ultrashort laser pulses

For laser pulses having a length of only a few optical cycles, the relative phase between the maximum of the pulse envelope and the nearest maximum of the electric field, the so-called carrier-envelope phase (CEP), plays a crucial role. The shape of the electric field depends strongly on the CEP and reveals a spatial asymmetry for different phase values as becomes apparent from figure 4 in the introduction. Processes in atoms and molecules, which depend on the instantaneous electric field can be influenced or even controlled by varying the CEP. The asymmetry of the field, however, decreases rapidly with the number of optical cycles in the laser pulse. For a wavelength of $800\,nm$, it almost vanishes for a pulse length of more than $10\,fs$. Therefore, ultrashort pulses are a prerequisite for observing phase effects.
In this chapter, first the basic properties of ultrashort laser pulses are explained. The laser system used for the generation of the pulses as well as the Mach-Zehnder interferometer, which is used for the two-pulse measurements presented in chapter 6, is described. The last part of this chapter deals with two techniques to characterize the laser pulses, autocorrelation and SPIDER.

2.1 Properties of ultrashort laser pulses

Laser pulses in the femtosecond regime are created by a superposition of different longitudinal modes of a laser resonator. If they have a fixed phase relation [KS08], they interfere in such a way that a pulse train is emitted. The electric field of a pulse at a fixed position in space can be obtained by a Fourier transform of the frequency spectrum

$$\mathcal{E}(t) = Re \int S(\omega) e^{i(\omega t + \varphi(\omega))} d\omega, \tag{2.1}$$

where $I(\omega) = |S(\omega)|^2$ is the spectral intensity and $\varphi(\omega)$ the spectral phase. Thus, there is a relation between the pulse length τ_0[1] and the width of the spectrum $\Delta\omega$. The broader the frequency spectrum, the shorter is the minimal pulse length that can be achieved. For a Gaussian pulse envelope, the relation between τ_0 and $\Delta\omega$ is given by [DR06a]

$$\Delta\omega\,\tau_0 \leq c_B \qquad c_B = 0.441. \tag{2.2}$$

[1]The pulse length τ_0 is generally defined as the full width at half maximum (FWHM) of the intensity profile of the pulse. For a pulse with a Gaussian envelope of the form $A(t) = A_0 exp\left\{-(t/\tau_G)^2\right\}$, with the intensity profile $I(t) \propto |A(t)|^2$, one obtains $\tau_0 = \tau_G\sqrt{2ln2}$.

A pulse, for which the equal sign holds, is called transform limited or Fourier limited. Such a pulse has the shortest possible length for a given spectral width $\Delta\omega$.

2.1.1 Dispersion

In optical materials, the frequency components of the laser pulse propagate with different phase velocities $v_{ph} = c/n(\omega)$ due to the frequency dependence of the refractive index $n(\omega)$. This so-called dispersion can also be expressed in terms of a frequency dependent wave vector $k(\omega) = \frac{\omega n(\omega)}{c}$. A pulse propagating in z-direction can be written as

$$\mathcal{E}(z,t) = \int \tilde{S}(z,\omega)e^{i\omega t}d\omega = \int S(0,\omega)e^{i\varphi(z,\omega)}e^{i\omega t}d\omega. \tag{2.3}$$

The phase $\varphi(z,\omega)$ thereby describes the effect of the dispersive material on the pulse. Due to the dispersion, the spectral phase of the pulse changes during propagation through a medium, whereas the spectral intensity remains unchanged. A Taylor expansion of the phase around the center frequency ω_0 yields

$$\begin{aligned}\varphi(z,\omega) &= \varphi(\omega_0) + \left.\frac{\partial\varphi}{\partial\omega}\right|_{\omega_0}(\omega-\omega_0) + \frac{1}{2}\left.\frac{\partial\varphi^2}{\partial^2\omega}\right|_{\omega_0}(\omega-\omega_0)^2 + ... \\ &= \varphi(\omega_0) + GD|_{\omega_0}(\omega-\omega_0) + \frac{1}{2}GDD|_{\omega_0}(\omega-\omega_0)^2 + ... \\ &= \varphi_0 + \omega_0 z\, n(\omega_0)/c + k_1|_{\omega_0} z\,(\omega-\omega_0) + \frac{1}{2}k_2|_{\omega_0} z\,(\omega-\omega_0)^2 ...\end{aligned} \tag{2.4}$$

The values of the dispersion coefficients k_i are characteristic for the dispersive medium. The influence of dispersion on the pulse is described in the following.
The group delay ($GD = k_1 z = \frac{z}{v_g}$) causes a difference between the velocity of the carrier of the pulse (phase velocity v_{ph}) and the velocity of the pulse envelope (group velocity v_g). This leads to a change of the carrier-envelope phase of the pulse, which is discussed in more detail in chapter 3.
Contrary to the group delay, which has no effect on the shape of the pulse, the group delay dispersion ($GDD = k_2 z$) changes the temporal profile of the pulse. If the corresponding coefficient is nonzero, the frequency components of the pulse propagate with different phase velocities so that they shift relative to each other in the time domain. Therefore, the pulse envelope broadens and the carrier frequency changes along the pulse. The pulse obtains a so-called chirp. Higher order terms of the dispersion have an even more complicated effect on the pulse shape and can lead to the formation of satellite pulses.
Due to their large bandwidth, ultrashort laser pulses are much more effected by dispersion than longer ones. A pulse of $6\,fs$ duration is stretched to $25\,fs$ after propagation through $1\,mm$ of glass (BK7), whereas a $25\,fs$ pulse is stretched to $25.5\,fs$ after passing the same amount of glass. Therefore, the compensation of dispersion plays a crucial role in the generation of ultrashort pulses, whereby the dispersion up to third order (TOD) has to be taken into account.

2.1.2 Self-phase modulation

The temporal profile of a laser pulse can be expressed in terms of its carrier frequency ω_0, which generally corresponds to the center frequency of the spectrum

$$\mathcal{E}(z,t) = A(z,t)e^{i(\omega_0 t - k(\omega_0)z)}e^{i\varphi_{CE}}, \tag{2.5}$$

where $A(z,t)$ is the envelope of the pulse and φ_{CE} is the carrier-envelope phase, which determines the position of the carrier relative to the envelope. As the pulse shape is not influenced by the nonlinear phase, this frequency modulation leads to a broadening of the spectrum. Thus, by compression a shorter pulse can be obtained. A method to broaden the frequency spectrum of laser pulses and thus reduce their Fourier limit is to make use of an effect called self-phase modulation. This effect is based on the nonlinearity of the refractive index at high intensities [DR06a]. The refractive index then depends on the intensity I of the pulse

$$n = n_0(\omega) + n_2 I(t), \tag{2.6}$$

where n_2 is the nonlinear refractive index. Inserting equation (2.6) into (2.5) leads to the expression

$$\mathcal{E}(z,t) = A(z,t)e^{i\left(\omega_0 t - k_0(\omega_0)z - \frac{\omega_0}{c}n_2 I(t)z\right)}. \tag{2.7}$$

The pulse has then a nonlinear phase depending on the nonlinear refractive index n_2

$$\varphi(z,t) = \frac{\omega_0}{c}n_2 I(t)z, \tag{2.8}$$

which causes an intensity dependent frequency change

$$\Delta\omega = \frac{d\varphi}{dt} \propto \frac{\omega_0}{c}n_2\frac{I_0}{\tau_0}z, \tag{2.9}$$

where τ_0 is the pulse length and I_0 the peak intensity. Hereby, the frequency at the rising edge is reduced whereas it is increased at the falling edge of the pulse.

2.2 The laser system

The laser pulses are generated and amplified in a commercial laser system[2], which is schematically illustrated in figure 2.1. It provides pulses of about 25 fs with a pulse energy of about 1 mJ. The pulse length is then further reduced to 6 fs by a fiber compressor. In the following subsections, the components of the laser system are described. The Mach-Zehnder interferometer, which is used to generate two identical pulses for autocorrelation measurements and pump-probe experiments (chapter 6), is presented afterwards.

[2]Femtopower Compact Pro of the company FEMTOLASERS Produktions GmbH, Fernkorngasse 10, 1100 Wien, Österreich

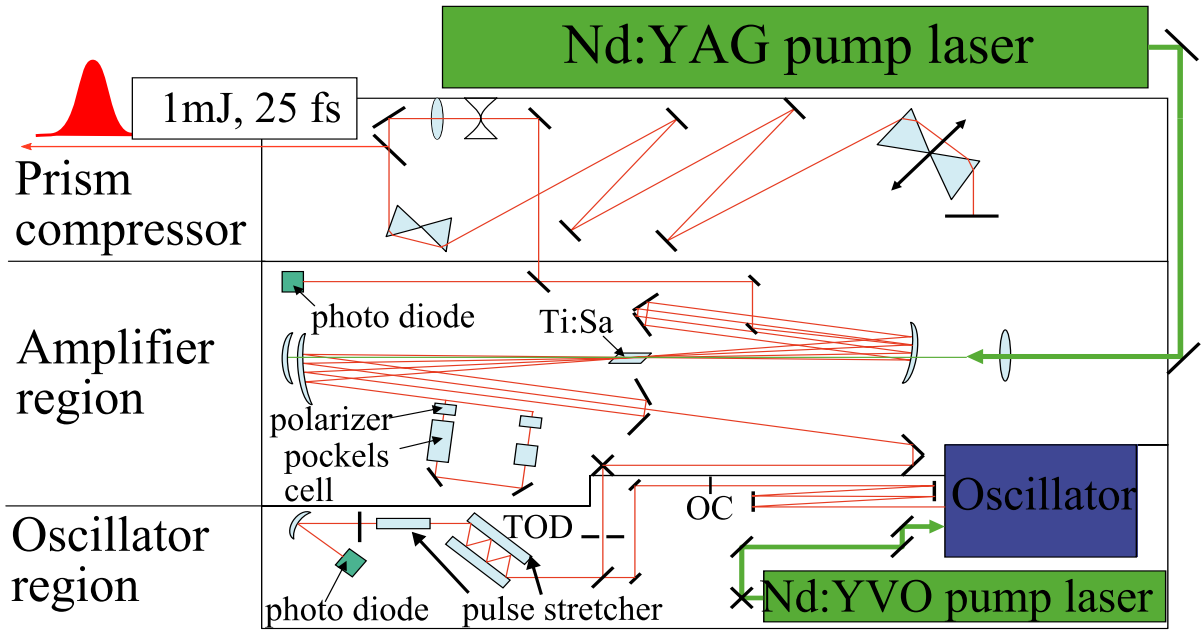

Figure 2.1: Schematic representation of the laser system. The pulses are created in a Ti:sapphire oscillator and amplified in a multipass amplifier by chirped pulse amplification. The chirp of the pulses is then compensated by a prism compressor.

2.2.1 The oscillator

The pulses are created by a mechanism called Kerr-lens-mode-locking which is again based on the intensity dependence of the refractive index at high intensities. A nonlinear medium acts like a lens for a laser beam with a Gaussian intensity profile transversal to the propagation direction. This so-called Kerr effect leads to an intensity dependent focusing of the beam, whereby higher intensities are better focused than lower ones.
The oscillator is designed in such a way that those parts of the beam, which are strongly focused, have a better overlap with the pump beam than the less focused ones and thus have a higher gain. Therefore, in the time domain the edges of the pulse obtain a smaller gain than the center, which leads to a shortening of the pulse. This effect corresponds to a locking of the relative phases of the frequency components in the time domain.
Pulse generation can be started by introducing an intensity fluctuation in the continuous wave mode of the oscillator, which is then transformed into a laser pulse by the mode locking process. The positive dispersion of the laser crystal and the air inside the cavity is compensated by chirped mirrors[3] [SFSK94]. Those are dielectric mirrors consisting of multiple layers of materials with different thickness and refractive index such that long wavelengths are reflected at deeper layers than shorter ones. This introduces a time delay of the red components relative to the blue ones and thus negative dispersion.
A Titanium:Sapphire crystal is used as gain medium because it has a large bandwidth (235 nm FWHM). It is pumped by a Nd:YVO laser with a pump power of about 3 W. The oscillator

[3]Oscillators, in which the dispersion is compensated by chirped mirrors, are called mirror dispersion controlled.

provides laser pulses with a duration of approximately $6\,fs$ at a center wavelength of $800\,nm$. The pulse energy is about $2.5\,nJ$ at a repetition rate of $80\,MHz$. A more detailed description of the oscillator design can be found in [SLS+95].

2.2.2 The amplifier and prism compressor

The laser pulses provided by the oscillator are too weak to be used in the experiments presented here and hence have to be amplified. In order to achieve a high amplification factor (here about 10^6), the concept of chirped pulse amplification [SM85] is applied. Hereby, the pulses are stretched in time before they enter the amplifier such that their peak intensity does not reach the damage threshold of the gain medium despite a strong amplification. This is done by a thick glass block and chirped mirrors so that the pulses have a length of a few picoseconds when they enter the amplifier. The amplifier is built up in a multipass configuration, in which the laser pulses pass the gain medium nine times (see figure 2.1). As a gain medium a Titanium:sapphire crystal is used that is pumped by a pulsed Nd:YAG laser (pulse duration $\approx 120\,ns$, pulse energy $\approx 10\,mJ$) with a repetition rate of $3\,kHz$. To get a train of pulses having the same energy, only one laser pulse per pump pulse is picked out by a Pockels cell after the fourth pass and then further amplified. Pulses with an energy of approximately $1\,mJ$ at a repetition rate of $3\,kHz$ are obtained. After the amplification, the chirp of the pulses is compensated by a prism compressor [FMG84]. Chirped mirrors in the compressor compensate third order dispersion. However, the pulses can be compressed only to a pulse length of about $25\,fs$ as their bandwidth is reduced during the amplification process by gain narrowing [DR06a]. The pulse duration therefore has to be further reduced by a fiber compressor, which is described in the following subsection.

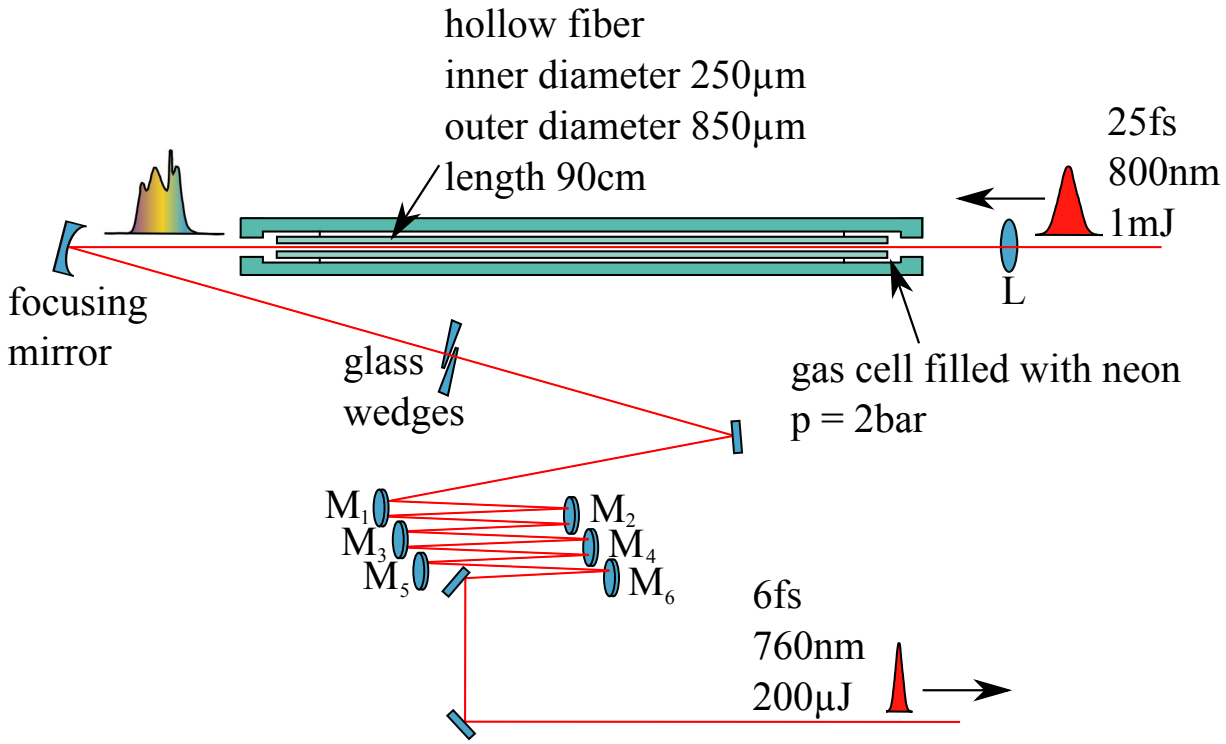

Figure 2.2: Setup of the fiber compressor. The pulses are focused into a hollow fiber filled with neon, in which self-phase modulation leads to a broadening of the pulse spectrum. The chirp of the pulse and the dispersion on the way to the reaction microscope are compensated by six chirped mirrors. A fine tuning of the dispersion can be done by two glass wedges.

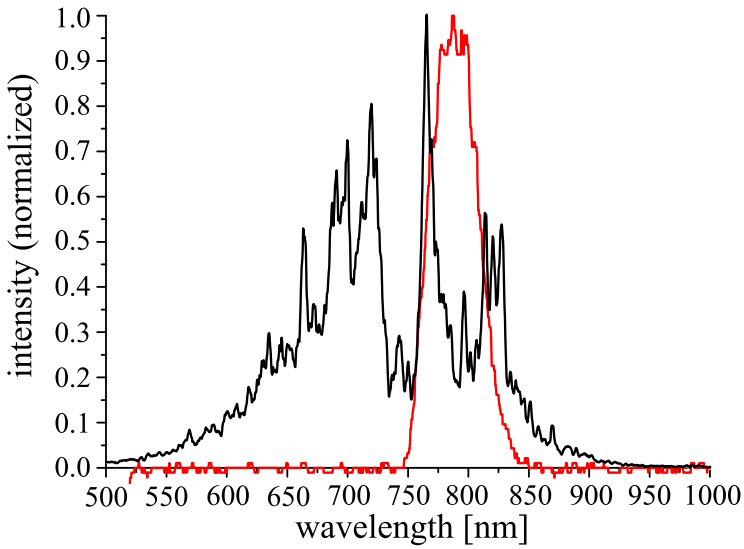

Figure 2.3: Spectrum before (red) and after (black) spectral broadening in the hollow fiber. Due to self-steepening, the center frequency of the broadened pulse is shifted to a shorter wavelength ($760\,nm$) with respect to the center frequency of the initial spectrum ($800\,nm$).

2.2.3 The fiber compressor

To obtain a pulse length of only $6\,fs$, the Fourier limit has to be reduced again. This means that the bandwidth of the pulses has to be broadened. As described in section 2.1.2, this is done by self-phase modulation in a nonlinear medium. For a strong broadening effect, a high intensity and a large interaction length in the nonlinear medium is required. These conditions are well fulfilled by a hollow fiber filled with a noble gas [Zro05][NDSS96], whereby the noble gas acts as a nonlinear medium.
The setup of the fiber compressor is shown in figure 2.2. A glass fiber with an inner diameter of $250\,\mu m$ and $90\,cm$ length is mounted in a chamber filled with neon at a pressure between 2.0 and $2.5\,bar$. The laser beam is focused into the fiber by a convex lens with a focus length of $1.5\,m$. The beam propagates through the fiber as a Gaussian mode. Due to its small diameter, during propagation a high intensity throughout the whole length of the fiber is obtained. The parameters of this setup were chosen to provide efficient self-phase modulation at minimal losses [Zro05].
A typical spectrum is shown in figure 2.3 together with the spectrum before propagation through the fiber. Its Fourier limit supports pulses of about $5\,fs$. By comparing the two spectra, one can see that the broadened one has a blue shift compared to the original one. The reason is that the temporal center of the pulse propagates slower through the fiber than the edges due to its higher refractive index. The pulse is therefore steepened at its back and flattened at the front (self-steepening). As the short wavelengths are generated at the back of the pulse, an asymmetric broadening relative to the center frequency occurs, which leads to a shift of the center frequency to about $760\,nm$.
A mirror compressor consisting of six chirped mirrors is used to compress the pulses after the

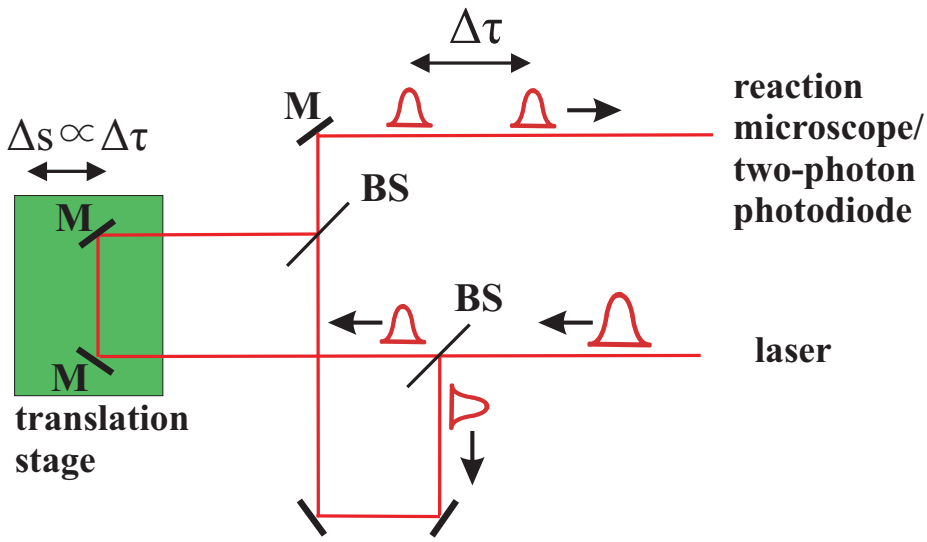

Figure 2.4: Mach-Zehnder interferometer. Two identical laser pulses are created by splitting the initial pulse with two beam splitters (BS). The time delay $\Delta\tau$ between the two pulses can be adjusted with high accuracy by changing the length of one interferometer arm via a translation stage.

spectral broadening. As the pulses have to be short in the reaction microscope, where the experiments take place, the positive dispersion of the air and glass on the way to the reaction chamber is pre-compensated by the mirror compressor. Fine tuning of the pulse length can be done by changing the amount of positive dispersion via two glass wedges.

2.3 The Mach-Zehnder interferometer

For the two-pulse measurements described in chapter 6 as well as for measuring the autocorrelation as shown in subsection 2.4.1, two identical copies of the laser pulse are required. This is realized by a Mach-Zehnder interferometer, which was built up within the framework of [Erg06]. The schematic of the interferometer is shown in figure 2.4. At the first beam splitter, the laser beam is half reflected and half transmitted. The two reflecting mirrors of one interferometer arm are mounted on a translation stage so that the relative length of the interferometer arms can be varied with high accuracy. The beams are overlapped again by a second beam splitter so that each of the two beams was once transmitted and once reflected. As the two beam splitters are identical in construction, the amount of dispersion in both arms is the same and the two pulses are identical.
For measurements with ultrashort laser pulses, the beam splitters in the interferometer have to withstand high intensities, support a broad spectral range and introduce only little dispersion. For this purpose, thin (500 μm, coating: six Si_2/TiO_2 layers) dielectric beam splitters were de-

signed[4] having a bandwidth of 520 to 1150 nm and supporting intensities up to 10 GW/cm^2. The two-pulse measurements presented here and in [Erg06] require a delay range of several 100 fs between the two pulses and a good resolution for interferometric measurements. Additionally, a good long-term stability of the interferometer and the laser system is required as long measurement times are needed in order to obtain good statistics. It was shown in [Erg06] that these requirements are well fulfilled by the present setup.

2.4 Pulse characterization

As mentioned above, the spectrum after broadening in the hollow fiber has a Fourier limit of about 5 fs. To reach this limit in the reaction microscope, the chirp due to the self-phase modulation process as well as due to the dispersion on the way to the reaction chamber has to be compensated properly. Furthermore, not only the pulse length, but also the existence and shape of pre- and post-pulses is of importance. In the following subsections, two different methods to characterize the laser pulses are presented and the results are compared to each other.

2.4.1 Autocorrelation

For measuring the interferometric autocorrelation, the Mach-Zehnder interferometer described above is used. The two identical pulse copies are overlapped collinearly and the interference signal of the pulses is measured as a function of the temporal delay between the pulses. In order to get information on the pulse shape, a higher order process is required to detect the signal. One then obtains the autocorrelation signal of order n dependent on the delay τ [DR06a]

$$I(\tau) = \int \left\{ |\mathcal{E}(t-\tau) - \mathcal{E}(t)|^2 \right\}^n dt. \tag{2.10}$$

The autocorrelation signal was detected with a photo diode which absorbs two photons so that the autocorrelation is of second order. A characteristic feature of a second order autocorrelation is that for a pulse without chirp the ratio of the peak to the background is 8 : 1. In case of a chirped pulse of the same length, the delay region, in which interference fringes can be observed, is shortened and the background next to the interference signal is raised. The background level at the delay, at which the interference signal starts, is a measure for the linear chirp of the pulse [SKS91][DR06a].
As the pulse length in the reaction microscope is of interest, a delay stage was built containing the same amount of air and glass the pulse would pass through on its way to the reaction chamber. The result of such an autocorrelation measurement is shown in the left image of figure 2.5. To estimate the pulse length, a Gaussian laser pulse was simulated and its autocorrelation was calculated. The simulated autocorrelation was fit to the measured one (least square fit), whereby the pulse length, the chirp of second order as well as the relative carrier-envelope phase[5] were

[4] Beam splitters designed in a collaboration with Uwe Morgner, University of Hannover.

[5] The autocorrelation of two identical pulses has a maximum at zero delay. In the measured autocorrelations, the position of the fringes was shifted, indicating that the carrier-envelope phase of the two pulse copies differ [XSP+96]. This is probably caused by a small difference in the dispersion the pulses experience (see chapter 3) in the two interferometer arms. Already a difference of a few microns of fused-silica glass, for example, leads to a significant difference in the CEP.

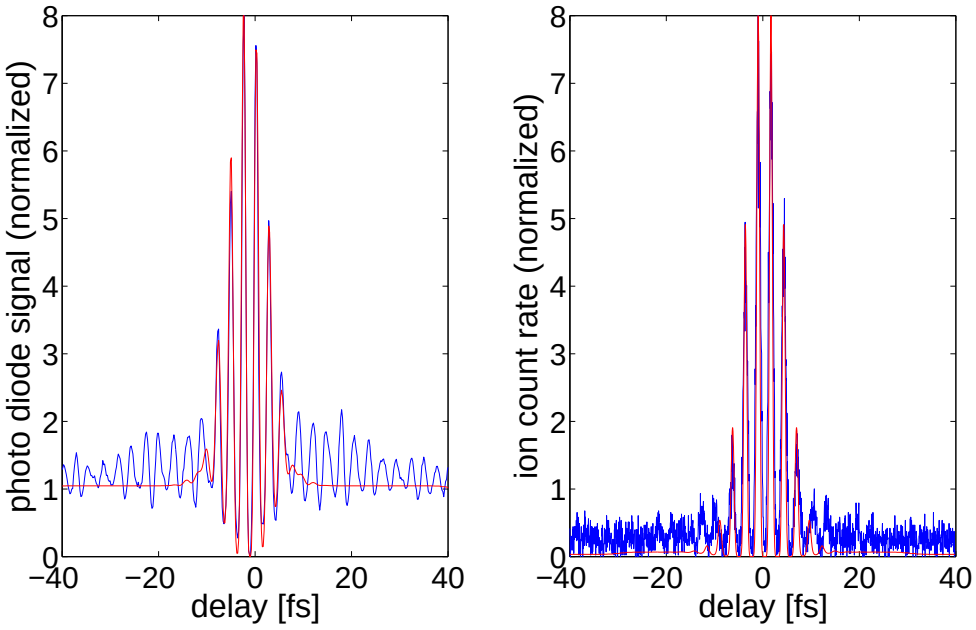

Figure 2.5: Left: Autocorrelation of second order measured with a two-photon photo diode. In red a least-square fit is shown, which assumes the pulse shape to be a Gaussian. Deviations from the measured autocorrelation occur as the shape of the real pulse is not an ideal Gaussian and has satellite pulses. Right: Autocorrelation measured with single ionization of argon in the reaction microscope and fitted fourth-order autocorrelation (red). The fits reveal a pulse length of approximately 6 fs for both autocorrelations.

used as fit parameters. The result of the fit is shown in figure 2.5 in red and revealed a pulse length of approximately 6 fs with only little chirp (second order chirp 0.03 fs^2). The simulated autocorrelation does not entirely reproduce the measured one as an ideal pulse shape is assumed. The envelope of the real pulse, however, deviates from a Gaussian and contains pre- and post-pulses, which give rise to the modulations on the sides of the main interference signal. They occur as a result of the modulation of the spectrum after propagation through the fiber, which would lead to satellite pulses even in case of optimal compression. They can also be caused by an insufficient compensation of dispersion of third or higher order.

As the autocorrelation is always symmetric, it contains no information on asymmetries of the pulse shape as, for example, if there is a pre- or a post-pulse. Besides that, the autocorrelation signals of very different pulse shapes can be very similar. Hence, no unambiguous determination of the pulse shape is possible.

The detection of the autocorrelation with the photo diode has the disadvantage that errors due to a discrepancy in the dispersion on the way to the photo diode and the way to the reaction microscope might occur. Therefore, the autocorrelation was also directly measured in the reaction microscope, where the ionization rate of argon was used as nonlinear process. An example of such an autocorrelation can be seen in the right image of figure 2.5. The autocorrelation was fit with

the method mentioned above, whereby the order[6] of the process was chosen to be $n = 4$. The pulse length was estimated to be $6\,fs$.
A shortcoming of the autocorrelation measured in the reaction microscope is that the order of the nonlinear process is not exactly known as the intensity dependence of the ionization cross section changes strongly between the multiphoton, the tunneling regime and the regime of saturation [Zro05]. For the experimental conditions described here, the ionization is in an intermediate regime between multiphoton and tunneling ionization so that the intensity dependence is not exactly known. Besides that, as the intensity changes with the delay due to the interference of the pulses, the intensity dependence of the signal may also change. Therefore, it is difficult to estimate the pulse length from this autocorrelation in a reliable way.
The autocorrelation measurement revealed a pulse length, which is close to the Fourier limit of the spectrum. But as explained above it allows only a qualitative estimation of the pulse shape. A more accurate method to measure the pulse shape is presented in the next section.

[6]Order of the autocorrelation chosen such, that the fringe pattern of the simulated autocorrelation agrees well with the measured one.

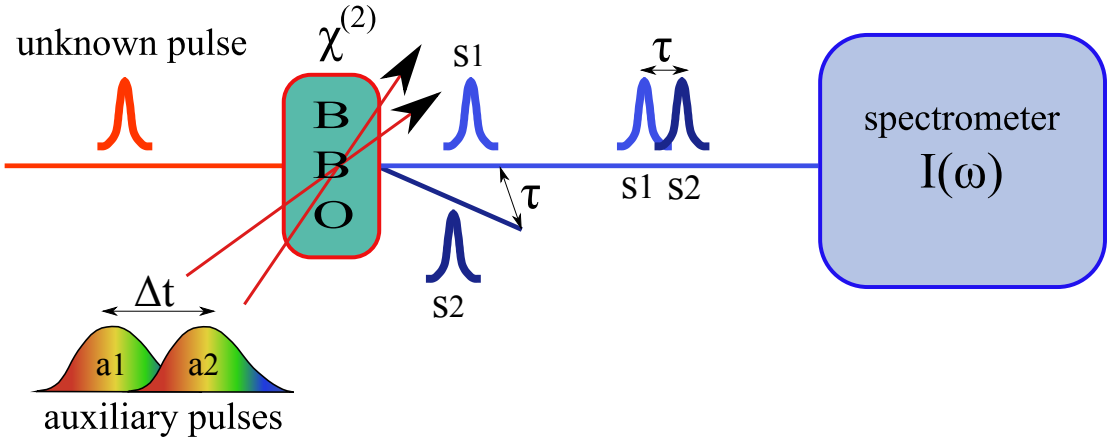

Figure 2.6: Principle of the ZAP-SPIDER. The unknown pulse is overlapped with two strongly chirped auxiliary pulses in a BBO. As the auxiliary pulses are temporally shifted versus each other, the resulting sum frequency signals have a spectral shear of Ω. They are brought to interference in a spectrometer with a time delay τ. From the interference pattern the spectral phase can be reconstructed up to an unknown constant.

2.4.2 The ZAP-SPIDER

There are several methods to determine the pulse shape unambiguously, like the so-called FROG[7] [WT96] [TDF+97] and SPIDER[8] [IW98]. Both techniques are self-referencing. This means that no reference pulse with known properties is required, but the pulse is used as its own reference. In this section, a ZAP-SPIDER[9] [BLR04] [BR05], which was built up in the framework of [Tar07], is described. Its working principle is illustrated in figure 2.6. The laser pulse to be characterized (unknown pulse) is overlapped with two auxiliary pulses in a BBO crystal, where sum frequency generation of the overlapping pulses occurs. To generate the auxiliary pulses a fraction of the $25\,fs$ laser pulse is branched off with a beam splitter before the fiber compressor. The obtained pulse is then stretched to several picoseconds by passing a few times through a thick ($70\,mm$) block of high dispersive glass (SF57). Afterwards, a beam splitter is used to produce two identical copies of the pulse, which are further referred to as $a1$ and $a2$. The two auxiliary pulses are then temporally shifted by a time delay Δt versus each other as illustrated in figure 2.6. In the BBO crystal, the sum frequency of the unknown pulse with $a1$ and the sum frequency of the unknown pulse with $a2$ is generated. As the auxiliary pulses are much longer than the unknown pulse, the unknown pulse interacts only with a single frequency component of the auxiliary pulses, respectively. This means, the unknown pulse interacts with the frequency component ω_1 of $a1$, resulting in the sum frequency signal $s1$, and it interacts with $\omega_2 = \omega_1 + \Omega$ of $a2$, resulting in the sum frequency signal $s2$. The frequency difference Ω is determined by the time delay Δt between the auxiliary pulses. Therefore, $s1$ differs from $s2$ by the frequency Ω, whereby Ω is referred to as spectral shear. The spectral shear is essential for the reconstruction of the spectral phase. The two pulses $s1$ and $s2$ are then delayed in time by τ and overlapped in a spectrometer. Due to

[7] **F**requency **r**esolved **o**ptical **g**ating
[8] **S**pectral **p**hase **i**nterferometry for **d**irect **e**lectric field **r**econstruction
[9] Zero additional phase-SPIDER

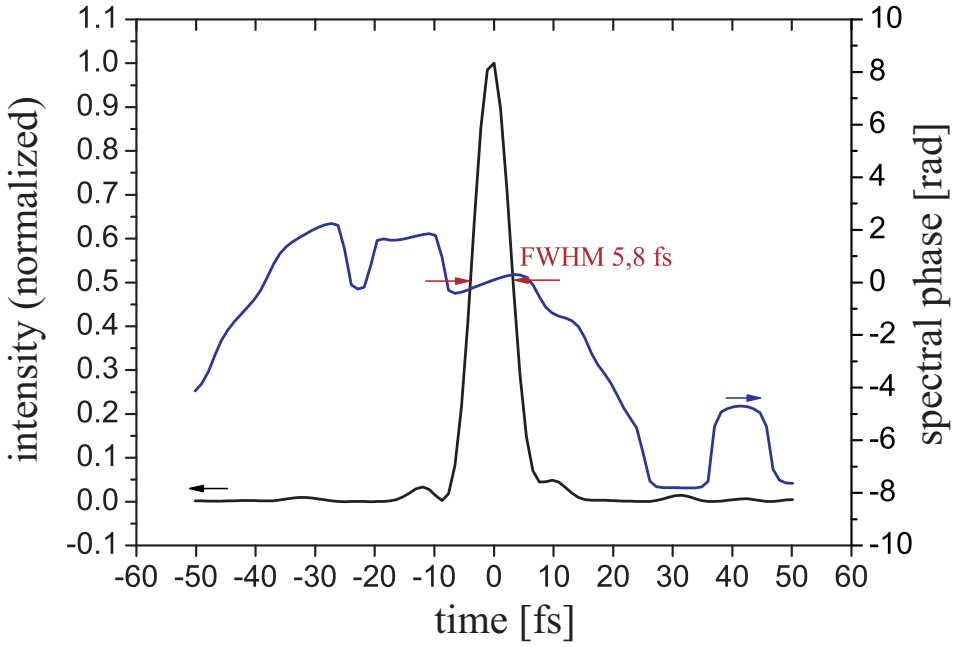

Figure 2.7: Temporal intensity profile (black) and phase (blue) of the laser pulses measured with the ZAP-SPIDER. The phase has a small upward slope along the pulse profile, indicating that the pulses are not entirely Fourier limited.

interference of the two pulses, the obtained spectrum is modulated with $\omega = \frac{2\pi}{\tau}$ in case of $\Omega = 0$. If Ω is nonzero, the maxima and minima are not equidistant anymore. From the distance of the fringes it is then possible to retrieve the spectral phase of the pulse up to an unknown constant [TIK82]. The spectral intensity is obtained by measuring the spectrum of the unknown pulse with a second spectrometer. From the spectral amplitude and phase the temporal shape and phase of the pulse can be reconstructed (see equation (2.1)).
The result is shown in figure 2.7, where the intensity profile (black) as well as the temporal phase (blue) are plotted. The FWHM of the intensity profile is about $6\,fs$ and in good agreement with the pulse length obtained from the autocorrelation measurements. The satellite pulses, which are observed, are quite small, which means that the pulse shape is rather clean. The second order autocorrelation of the pulse shape measured with SPIDER was calculated and is in good agreement with the measured autocorrelation signal.
Note that SPIDER and FROG do not allow the determination of the carrier-envelope phase. Techniques to measure and stabilize the CEP are presented in the following chapter.

Chapter 3

Phase stabilization

The carrier-envelope phase (CEP) of laser pulses provided by femtosecond lasers varies randomly from pulse to pulse. Thus, for performing CEP dependent measurements the phase has to be actively stabilized. The phase stabilization of the laser system described in the previous chapter was accomplished during this thesis and in [Kre09].
In this chapter, first general properties of the carrier-envelope phase are described. After that, the principles of the f-0f and of the f-2f interferometer, used for phase stabilization of the oscillator and the amplifier, respectively, are explained. The experimental realization of the phase stabilization is shown afterwards. The stereo-ATI spectrometer is presented, which provides an independent monitoring of the CEP evolution. Finally the achieved stability of the phase locking is discussed.

3.1 Definition and properties of the carrier-envelope phase

In the time domain, a laser pulse can be described by equation (2.5), where φ_{CE} is the carrier-envelope phase. It denotes the position of the most pronounced maximum of the electric field with respect to the maximum of the pulse envelope as illustrated in figure 3.1. As already mentioned, the phase plays only a role if the field strength of neighboring maxima of the electric field differs significantly, which is only the case for pulses containing few optical cycles.
The difference between phase and group velocity in dispersive media leads to a shift of the electric field through the envelope so that the CEP changes continuously during propagation through a medium (see also section 2.1). Even an ideal oscillator would generally not emit pulses of the same phase as the resonator contains dispersive elements.
The temporal evolution of the carrier-envelope phase is also manifested in the frequency domain. An isolated laser pulse has a continuous frequency spectrum. An oscillator, however, emits a train of laser pulses. The pulses are separated by the round trip time $T = 2L/c$, where L is the resonator length and c the speed of light. The spectrum of such a train of equally spaced pulses, which is referred to as a frequency comb, is schematically illustrated in figure 3.2. It consists of discrete frequency components[1], which are separated by the repetition rate of the laser $\nu_{rep} = \frac{1}{T}$.

[1] An isolated laser pulse has a continuous frequency spectrum. The carrier-envelope phase then corresponds to a frequency independent offset of the spectral phase.

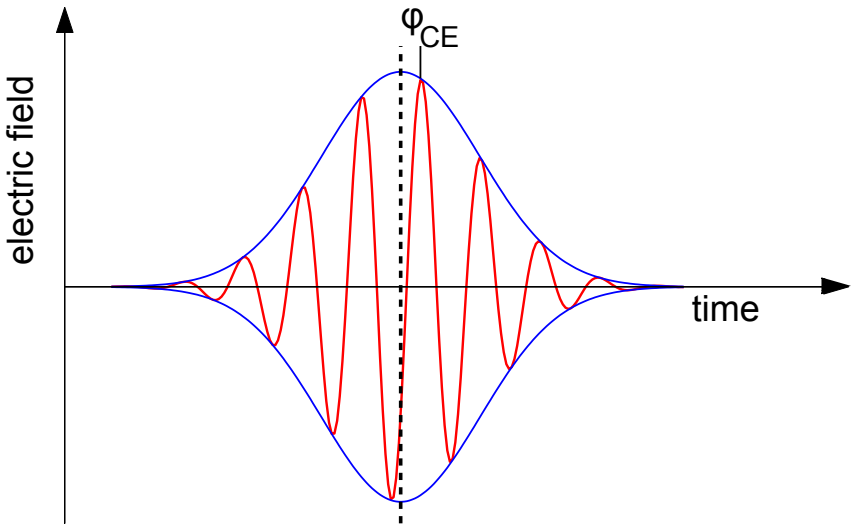

Figure 3.1: Definition of the carrier-envelope phase. The carrier-envelope phase is the relative phase between the maximum of the electric field and the maximum of the pulse envelope. For ultrashort laser pulses, it determines the shape of the electric field.

The difference between group and phase velocity introduces an offset ν_{CE} to the frequency comb, the so-called carrier-envelope offset frequency ν_{CE}. The frequencies of the laser modes are then given by the equation [YC05]

$$\nu_n = n\,\nu_{rep} + \nu_{CE}. \tag{3.1}$$

The carrier-envelope phase of consecutively emitted laser pulses is determined by the ratio of ν_{CE} and ν_{rep} and is given by

$$\delta\varphi_{CE} = 2\pi\frac{\nu_{CE}}{\nu_{rep}}. \tag{3.2}$$

If the repetition frequency is an integer multiple of the offset frequency $\nu_{rep} = n\,\nu_{CE}$, every n-th pulse has the same phase. Thus, by picking out every n-th pulse, one obtains a train of pulses with identical phase.
For a stable frequency comb, active phase stabilization is required as in a realistic oscillator instabilities lead to a jitter of the offset frequency. For example, vibrations or air currents can occur, causing pointing instabilities inside the laser cavity, which can lead to a change of the dispersion. The development of techniques for measuring and actively stabilizing the carrier-envelope phase revolutionized the field of frequency metrology. If ν_{CE} is stable, the modes of the frequency comb remain fixed so that the comb can be used similar to a ruler for measuring frequencies with unprecedented precision. For the development of this technique, the Nobel prize was awarded to John L. Hall [Hal06] and Theodor W. Hänsch [Hän06] in 2005.
For experiments with intense laser pulses, phase stabilization of the oscillator is not sufficient as the pulses have to be further amplified and compressed and phase drifts also occur during propagation through the amplification and compression stage. Phase drifts can be caused by beam pointing instabilities, which can lead to a change of the amount of dispersion the pulses propagate through. Additionally, nonlinear processes, like self-phase modulation, influence the

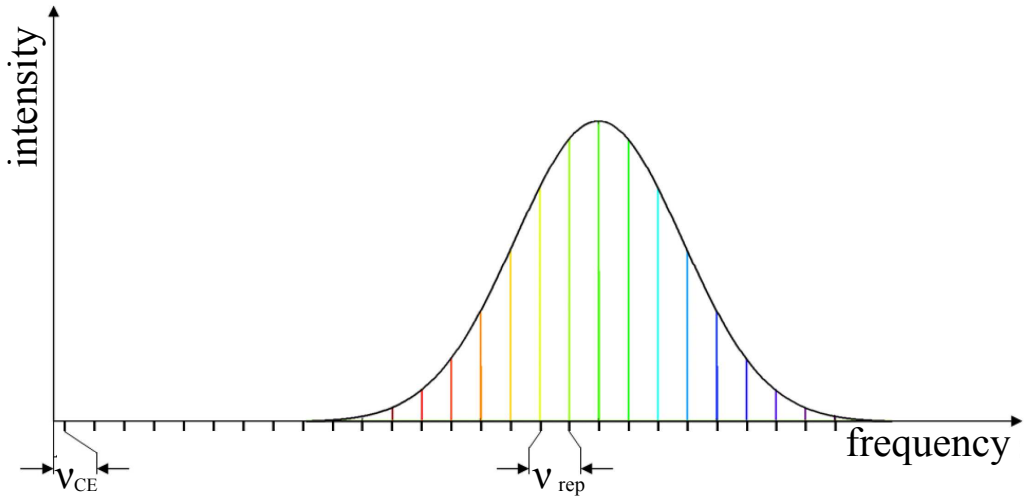

Figure 3.2: Schematic illustration of a frequency comb. The spectrum of a train of equally spaced pulses consists of discrete frequency modes, which are separated by the repetition frequency ν_{rep}. The offset ν_{CE} (carrier-envelope offset frequency) determines how much the carrier-envelope phase changes from pulse to pulse.

phase, whereby the nonlinear phase accumulated during the self-phase modulation process adds up to the CEP (see equation (2.7)). This effect is utilized for the phase stabilization of the oscillator. However, due to this effect, intensity fluctuations in the amplifier and the hollow fiber, where self-phase modulation occurs, result in fluctuations of the CEP.

3.2 Measurement of the carrier-envelope phase

The methods for pulse characterization described in 2.4 reveal only information on the envelope of the pulse, but not on its carrier-envelope phase. The cross-correlation of two pulses with different phase contains information about the relative phase between the two pulses [XSP+96][JDR+00], but not on the CEP of each single pulse (see also section 2.4.1).
A standard technique for measuring the phase is the so-called f-2f (or f-0f) interferometry, which is a purely optical method. The f-2f interferometer relies on the interference of a high and a frequency doubled low frequency component of the pulse spectrum. If these frequency components overlap spectrally, a beat signal is created, which contains information about ν_{CE}. For a spectral overlap, the low and the high frequency component must differ by one harmonic order, which means that the fundamental spectrum has to span an octave. The beat signal can be detected either in the time or in the frequency domain.

3.2.1 F-2f interferometer in the time domain

In an f-2f interferometer in the time domain, the fundamental spectrum is frequency doubled so that a second frequency comb is generated as shown in figure 3.3 (a). Additionally, the fundamental spectrum is broadened by self-phase modulation so that the high frequency wing of

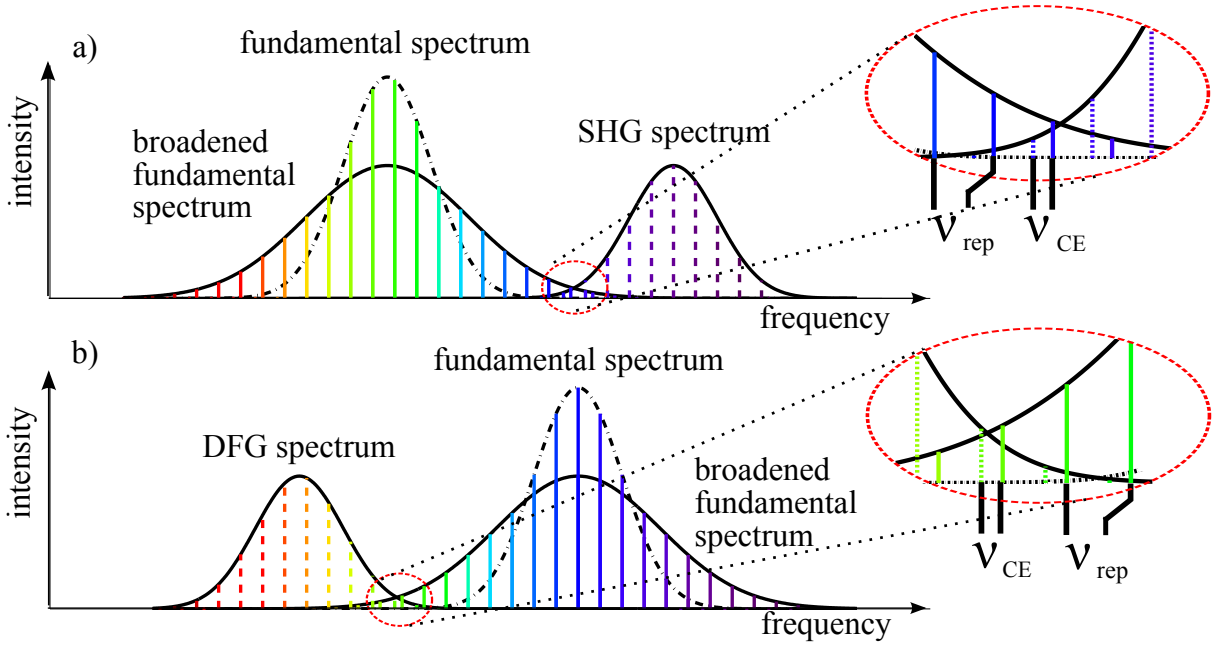

Figure 3.3: a) Schematic illustration of the working principle of an f-2f interferometer. The fundamental spectrum of the oscillator pulses is broadened in a nonlinear medium such that it spans an octave. At the same time, a second frequency comb is created by second harmonic generation (SHG) of the fundamental spectrum. The two frequency combs partially overlap and produce a beat signal corresponding to the carrier-envelope offset frequency ν_{CE}. b) In an f-0f interferometer, a difference frequency signal (DFG) of the high frequency and the low frequency part of the fundamental spectrum is generated. The overlap of the generated spectrum and the broadened fundamental spectrum provides ν_{CE}.

this spectrum $(m \cdot \nu_{rep} + \nu_{CE})$ overlaps with the low frequency wing of the frequency doubled spectrum $2(n \cdot \nu_{rep} + \nu_{CE})$. The condition for spectral overlap is thereby $2n = m$. If it is fulfilled, a beat signal is obtained

$$\begin{aligned} \nu_{f-2f} &= 2(n \cdot \nu_{rep} + \nu_{CE}) - (m \cdot \nu_{rep} + \nu_{CE}) \\ &= (2n - m) \cdot \nu_{rep} + \nu_{CE} \\ &\underset{2n=m}{=} \nu_{CE}, \qquad n, m \in \mathbb{N}^0, \end{aligned} \tag{3.3}$$

which corresponds to the carrier-envelope offset frequency. As ν_{CE} lies in the radio frequency regime, it can be detected easily .
The f-0f interferometer is based on the same principle as the f-2f interferometer. Here the difference frequency signal ν_{DFG} of the high and the low frequency part of the fundamental spectrum is generated. Its high frequency side overlaps with the low frequency wing of the broadened

fundamental spectrum (see figure 3.3 (b))

$$\begin{aligned}\nu_{f-0f} &= k\cdot\nu_{rep}+\nu_{CE}-\nu_{DFG}\\ &= k\cdot\nu_{rep}+\nu_{CE}-[(l\cdot\nu_{rep}+\nu_{CE})-(m\cdot\nu_{rep}+\nu_{CE})]\\ &= k\cdot\nu_{rep}+\nu_{CE}-(l-m)\nu_{rep}\\ &\underset{k=l-m}{=} \nu_{CE}, \qquad k,l,m\in\mathbb{N}^0. \end{aligned} \tag{3.4}$$

An f-2f or f-0f interferometer in the time domain detects only a narrow range of the frequency spectrum of the pulse. It is well suited for stabilization of the carrier-envelope offset frequency of oscillators, which have a repetition rate of tens of megahertz. Pulses emitted from the amplifier have a much lower repetition rate of only several kilohertz so that the modes in the frequency comb lie much closer to each other, which complicates the measurement of the CEO-frequency with this scheme. The f-2f interferometer in the frequency domain is better suited for this purpose.

3.2.2 F-2f interferometer in the frequency domain

The measurement of the carrier-envelope phase in the frequency domain is based on spectral interferometry [KTK+01] [SZW+08]. As for the detection in the time domain, the spectrum of the pulse must be octave broad.
The blue part of the fundamental spectrum is overlapped in a spectrometer with the frequency doubled red part. If the fundamental spectrum is octave broad, the frequency components of the blue and the frequency doubled red wing overlap spectrally so that they interfere with each other. The interfering frequency components arrive at the spectrometer with a time delay $\tau = (t_2 - t_1)$ if the pulse was chirped before frequency doubling. Information on the phase can be obtained because a frequency component of the fundamental spectrum contains the carrier-envelope phase once and its frequency doubled signal contains φ_{CE} twice. The measured interference spectrum is given by [YC05]

$$\begin{aligned} I(\omega) &= I_f(\omega)+I_{SH}(\omega)+\sqrt{I_f(\omega)I_{SH}(\omega)}cos\left[(\omega t_2+2\varphi_{CE})-(\omega t_1+\varphi_{CE})+\theta(\omega)\right]\\ &= I_f(\omega)+I_{SH}(\omega)+\sqrt{I_f(\omega)I_{SH}(\omega)}cos\left[\omega\tau+\varphi_{CE}+\theta(\omega)\right], \end{aligned} \tag{3.5}$$

where $I_f(\omega)$ is the intensity of the fundamental spectrum and $I_{SH}(\omega)$ the intensity of the frequency doubled spectrum. Here $\theta(\omega)$ contains contributions to the phase arising from the second harmonic generation process. It also contains contributions from an initial chirp of the pulse. The position of the interference fringes is determined by the carrier-envelope phase. A change of the phase can therefore be detected by the shift of the interference pattern [BUU+03]. However, the absolute phase cannot be measured with this method as in practice the value of θ is not known. A change of this value due to intensity fluctuations or mechanical instabilities can therefore lead to measurement errors.
As for the measurement only the blue and red wing of the spectrum are used, the phase evolution can only be traced appropriately if the spectral phase of the pulse does not change. Otherwise, the phase of the wings can change relative to the CEP, which is defined at the center frequency. This gives rise to a systematic measurement error [DAL+04]. This problem occurs if the phase is stabilized by changing the amount of glass in the beam path.

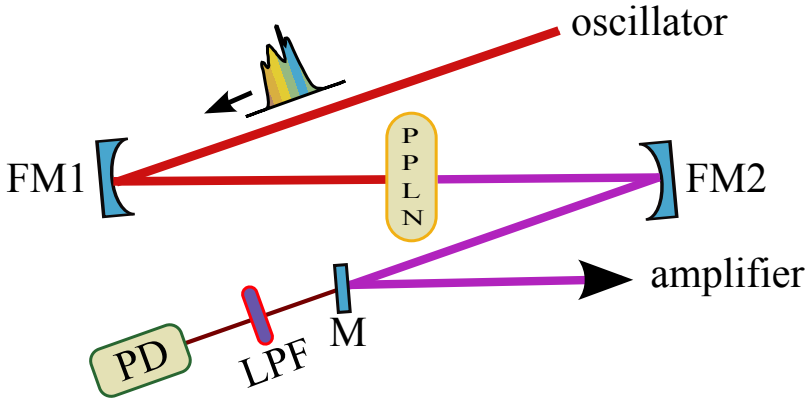

Figure 3.4: Setup of the f-0f interferometer used for phase stabilization of the oscillator. The laser beam coming from the oscillator is focused by a concave silver mirror (FM1, $f = 60\,mm$) into a PPLN crystal, in which the difference frequency signal of a low and a high frequency component of the frequency comb is generated. The divergence of the beam is corrected with a second silver mirror (FM2). The low frequency part of the spectrum, which passes through a mirror (M) and a long pass filter (LPF, $\lambda = 1300\,nm$), is detected with a photo diode (PD). The other part of the beam is used for seeding the amplifier.

The carrier-envelope phase changes by $\Delta\varphi_{CE}$ after propagating through a certain type of glass of thickness ΔL. This phase change is caused by the different propagation velocities of the carrier v_{ph} and the envelope v_g and is given by

$$\Delta\varphi_{CE} = \frac{\omega_0}{2\pi}\Delta L\left(\frac{1}{v_g} - \frac{1}{v_{ph}(\omega_0)}\right), \tag{3.6}$$

where ω_0 is the center frequency of the pulse. By making use of the first order Taylor expansion of $\frac{1}{v_g}$, one obtains[2]

$$\Delta\varphi_{CE} = 2\pi\Delta L\left.\frac{\partial n}{\partial\lambda}\right|_{\lambda_0}. \tag{3.7}$$

The f-2f measures a phase change of $\Delta\varphi_{f-2f}$ as the red (frequency ω) and the blue (frequency 2ω) wing of the spectrum have different travel times through a glass plate, which are $t_\omega = \Delta L n(\omega)/c$ and $t_{2\omega} = \Delta L n(2\omega)/c$. The change of the measured phase is then given by

$$\Delta\varphi_{f-2f} = 2\omega\left(t_\omega - t_{2\omega}\right) = 2\omega\Delta L\left(n(\omega) - n(2\omega)\right), \tag{3.8}$$

which is generally different from the change of the carrier-envelope phase $\Delta\varphi_{CE}$ in equation (3.6) [PLW+05].

3.3 Phase stabilization of the laser system

In the present setup, an f-0f interferometer in the time domain is used for phase stabilization of the oscillator and an f-2f interferometer in the frequency domain for stabilization of the pulses

[2]Here one makes use of $v_{ph} = \frac{c}{n}$ and $v_g = \frac{c}{n} + \frac{c\lambda}{n^2}\frac{\partial n}{\partial\lambda}$.

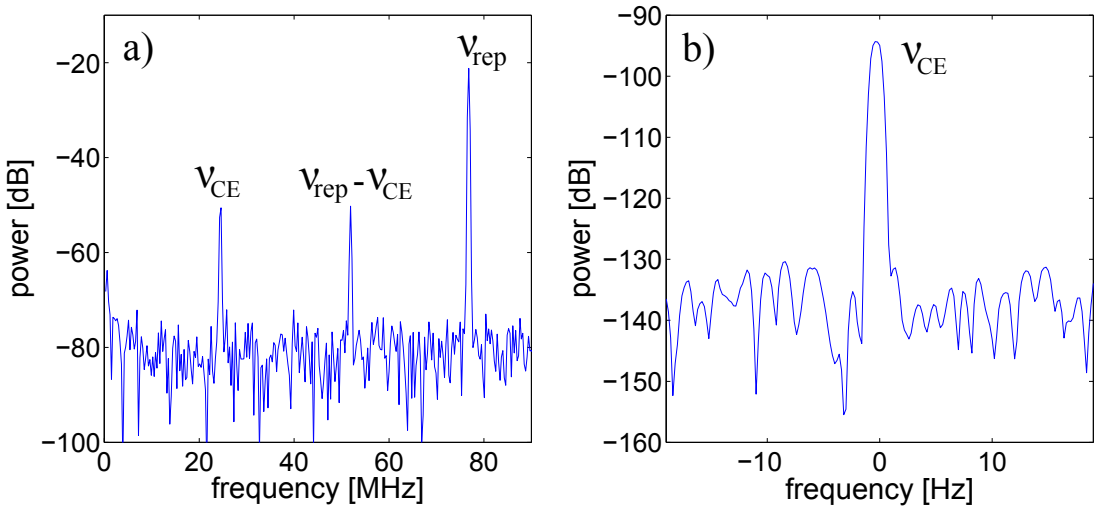

Figure 3.5: a) Frequency spectrum of the signal of the photo diode used in the $f-0f$ interferometer. A signal can be observed at the repetition rate of the oscillator ν_{rep}, the carrier-envelope offset frequency ν_{CE} as well as at $\nu_{rep}-\nu_{CE}$. (Resolution bandwidth $0.3\,MHz$) b) Peak at ν_{CE} measured with a resolution bandwidth of $1\,Hz$.

after the fiber compressor. With the stereo-ATI spectrometer, which is explained in section 3.4, an independent measurement of the phase is performed so that systematic measurement errors of the f-2f can be detected and corrected.

3.3.1 Phase stabilization of the oscillator

The setup of the f-0f interferometer for stabilization of the oscillator is illustrated in figure 3.4. The pulses emitted by the oscillator used in this setup have a nearly octave broad spectrum. The pulses are focused by a concave mirror (FM1) onto a nonlinear crystal (PPLN), where a further broadening takes place such that the spectrum becomes octave broad. The orientation of the PPLN is chosen such that the difference frequency ν_{DFG} of the high and the low frequency part of the spectrum is generated [FRA+05]. A small fraction of the laser beam, which now contains the fundamental spectrum and the difference frequency components, is transmitted through a mirror (M) and passes through a filter (LPF), which transmits only the long wavelength part of the spectrum above $1300\,nm$. This low frequency components are then focused onto a photo diode (PD). The signal of the photo diode corresponds to a train of pulses with a repetition frequency of ν_{rep}, whereby the amplitude of the pulses is modulated with ν_{CE}. By a Fourier transform of the photo diode signal to the frequency domain, a peak at the repetition rate ν_{rep} and at ν_{CE} is obtained as shown in figure 3.5. The offset frequency is stabilized to one quarter of the repetition rate by a feedback loop[3]. This is done by a modulation of the pump laser intensity

[3]As the change of the carrier-envelope phase depends on the ratio of ν_{CE} and ν_{rep}, noise of the repetition frequency is canceled out if ν_{CE} is stabilized to a fraction of ν_{rep}. Then ν_{CE} is equal to ν_{rep}/n so that every n-th pulse has the same phase.

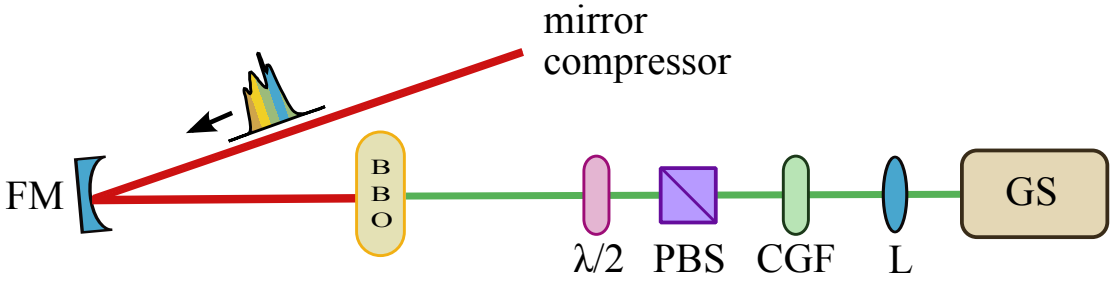

Figure 3.6: Setup of the f-2f interferometer for phase stabilization of the amplified pulses. The beam transmitted through the first mirror of the mirror compressor is focused by a silver focusing mirror (FM) onto a BBO crystal (thickness: $300\mu\,m$), where the second harmonic of the low frequency part of the pulse spectrum is generated. With a half-wave plate ($\lambda/2$) and a polarizing beam splitter (PBS) the second harmonic and the high frequency part of the fundamental spectrum are projected onto the same polarization axis and focused by a lens (L) into a grid spectrometer (GS). A saturation of the spectrometer is avoided by colored glass filters (CGF), which filter out the irrelevant frequency components.

via an acousto-optic modulator[4], which changes the nonlinear phase the pulses obtain due to self-phase modulation in the Ti:sapphire crystal (see equation (2.7)).
This stabilization scheme can compensate fast fluctuations of the phase efficiently, but is not well suited to compensate long term drifts. Such drifts can be compensated by a second feedback loop, which detects long term drifts by monitoring the voltage signal applied to the AOM. These drifts are then compensated by changing the amount of glass and thus the amount of dispersion inside the laser cavity, which is done by moving glass wedges. With this second stabilization loop the long term stability could be significantly enhanced by a factor of three to five.

An advantage of the presented setup is that no photonic crystal fiber is required for broadening of the spectrum as is the case for oscillators operating at a narrower spectral width. Therefore, instabilities occurring due to the sensitive incoupling of the laser beam into a fiber are avoided so that a better long term stability is achieved. Besides that, in case a fiber is used, a part of the beam has to be branched off for the f-2f interferometer. This part of the beam can generally not be re-compressed to a short pulse as the f-2f setup introduces strong dispersion. Furthermore, phase fluctuations between the main beam and the beam used for the phase measurement can occur, which reduce the achievable phase stability. This problem is avoided in the setup presented here as the phase is directly measured in the beam, which is then further used for seeding the amplifier. Furthermore, as the entire beam is focused into the PPLN, its full power is available for inducing nonlinear processes so that a high beat signal can be obtained[5]. The introduced dispersion is moderate and can be compensated so that almost the entire power remains available for further applications [TFJRG+05].

[4]An acousto-optic modulator diffracts light by using sound waves. In this way, the intensity in the non-diffracted part of the laser beam can be modulated.

[5]Generally a beat signal between 40 and $45\,dB$ is achieved, whereby at least $35\,dB$ are required for a good performance of the locking electronics.

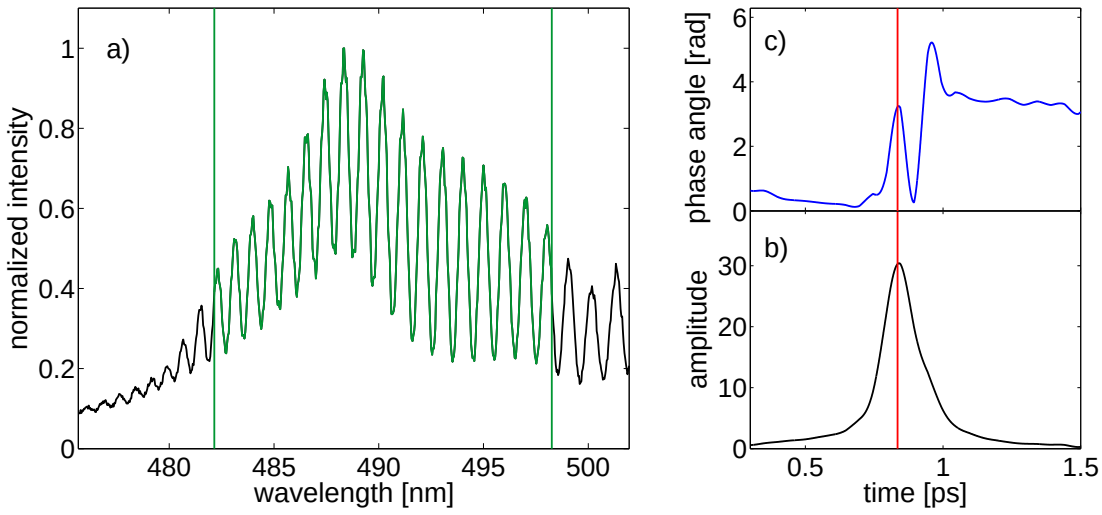

Figure 3.7: a) Interference spectrum of the f-2f interferometer. A change of the CEP results in a shift of the interference pattern. b) Absolute value of the Fourier transform of the interference spectrum. The peak position corresponds to the time delay between the two interfering pulses. c) Phase angle of the Fourier transform. The value of the phase angle at the peak maximum of the Fourier spectrum reveals the carrier-envelope phase up to an unknown constant.

3.3.2 Phase stabilization of the amplified pulses

As the carrier-envelope offset frequency is stabilized to one quarter of the repetition rate, every fourth pulse emitted from the oscillator has the same phase. The Pockels cell, which reduces the repetition rate in the amplifier, is triggered such that it reduces the repetition rate by a multiple of four so that only pulses having the same phase are picked out for further amplification.
During propagation through the amplification stage and the hollow fiber, instabilities in the laser system result in a drift of the carrier-envelope phase. These fluctuations occur on a relatively long time scale compared to the drifts in the oscillator and can be detected by an f-2f interferometer in the frequency domain, which is placed after the hollow fiber.
The setup is illustrated in figure 3.6. The light which is transmitted through the first chirped mirror of the mirror compressor is used for measuring the phase. It is focused into a BBO crystal, in which second harmonic generation occurs. The second harmonic signal and the fundamental spectrum are projected onto the same polarization axis by a half-wave plate ($\lambda/2$) and a polarizing beam splitter (PBS). They are focused by a lens (L) into a grid spectrometer (GS). A saturation of the spectrometer is avoided by a filter (CGF), which transmits only the relevant high frequency components of the spectrum. For the phase measurement, the obtained interference signal is transformed into the time domain as shown in figure 3.7. The Fourier spectrum has a peak at a time corresponding to the time delay between the interfering signals. The carrier-envelope phase up to an unknown constant is given by the phase angle of the Fourier transform at the maximum of the peak[6].

[6]A shift of the time delay τ also results in a shift of the interference pattern. It can be distinguished from a shift of the CEP as it additionally changes the distance of the interference fringes and thus the

Drifts of the phase are compensated by moving a glass wedge in and out of the laser beam, which changes the amount of dispersion. The glass wedges can also be used to drive a phase ramp, which was done in the experiments presented here. The amount of glass required for changing the phase by $4\,\pi$ is only about $100\,\mu m$ so that the pulse shape is not significantly affected. However, as already explained above, a systematic measurement error is introduced. By comparing the phase change detected with the f-2f interferometer with the one measured by the stereo-ATI spectrometer [Hof09], the systematic error was found to be about 20 % in good agreement with the predictions by [Gim06].
This f-2f interferometer is well suited for measuring and compensating the slow phase drifts of the amplified and compressed pulses. Note that a prerequisite for observing the interference pattern is the phase stabilization of the oscillator. If the oscillator is not phase stabilized, the phase varies more or less randomly from pulse to pulse. As during the integration time of the spectrometer the spectrum is averaged over many laser shots, the interference pattern gets washed out in this case.

3.4 The stereo-ATI spectrometer

A stereo-ATI spectrometer is a device to measure the carrier-envelope phase, which is based on the ionization of noble gases. Contrary to the f-2f interferometer, it allows in principle the determination of the absolute phase of the pulses [WHH+09] and can be used for an independent monitoring of the phase.
In a stereo-ATI spectrometer one makes use of the strong CEP dependence of electrons emerging from a rescattering process (see also section 1.1.3). The electric field of the laser pulse can tilt the atomic potential such that an electron can tunnel out. The energy of the electron after tunneling can be assumed to be zero. The electron is accelerated in the laser field of the pulse, whereby its trajectory and the energy it gains is strongly dependent on the time of tunneling. The maximal energy an electron can gain without further interaction with the ion is $2\,U_p$, where $U_p = \frac{I}{4\omega_0^2}$ is the ponderomotive energy, I the intensity and ω_0 the carrier frequency. An electron, which tunnels out slightly after the maximum of the field, can be driven back to the ion when the field changes its sign. If the electron is then scattered at the ion potential in backward direction, it can be further accelerated in the next field cycle thereby gaining high energies up to $10\,U_p$. The electrons are mainly emitted parallel to the polarization direction of the electric field.

Whether such high energetic electrons are mainly emitted to the left or to the right strongly depends on the CEP of the laser pulses. The reason is that the rescattered electrons gain a high energy only if the field strength in the laser cycle following the rescattering event is large. Additionally, the field strength at the field maximum, at which the electron tunnels, must be sufficiently high for obtaining a large tunneling rate. The tunneling time and the time of rescattering differ by about three quarter of a laser cycle. For ultrashort laser pulses, whether both conditions are fulfilled for one of the two emission directions depends strongly on the shape of the electric field and hence on the CEP. The phase dependent asymmetry of the electric field thus leads to a phase dependent asymmetry in the emission direction of the electrons. The magnitude of the asymmetry depends strongly on the pulse length.

A schematic illustration of the stereo-ATI spectrometer built in the framework of [Hof09] is

position of the peak of the Fourier transform.

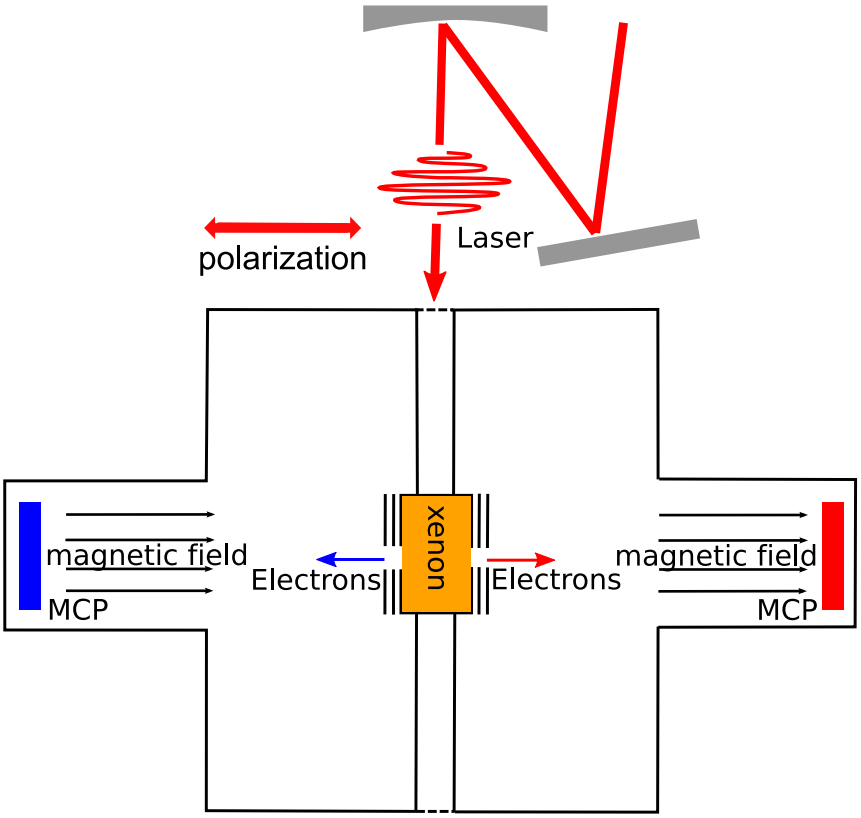

Figure 3.8: Schematic of the stereo-ATI spectrometer. The laser pulses are focused into a chamber filled with xenon ($10^{-3}\,mbar$). The electrons are emitted mainly parallel to the polarization direction and leave the chamber through two holes. Before the electrons reach the MCP detectors placed behind the holes, they pass through a drift tube so that their energy can be determined from their time of flight. A magnetic field along the drift tubes compensates the effect of the earth magnetic field.

shown in figure 3.8. A fraction of the laser beam after the fiber compressor is focused into a gas cell filled with xenon (pressure about $10^{-3}\,mbar$). In the direction of the polarization axis, the gas cell has a hole on each side, through which the emitted electrons can escape into a vacuum chamber ($10^{-6}\,mbar$). For the detection of the electrons, multi channel plates (MCPs) are placed behind the hole on the left and the right side, respectively. As only the high energetic electrons are of interest, the low energetic ones can be blocked by applying a voltage at a repeller, which is placed behind each hole. To characterize the asymmetry, one can define an asymmetry parameter

$$A = \frac{N_L - N_R}{N_L + N_R}, \tag{3.9}$$

where N_L (N_R) is the number of electrons emitted to the left (right). From the asymmetry the relative phase can be determined by

$$\varphi = arcsin\left(b\,\frac{N_L - N_R}{N_L + N_R}\right). \tag{3.10}$$

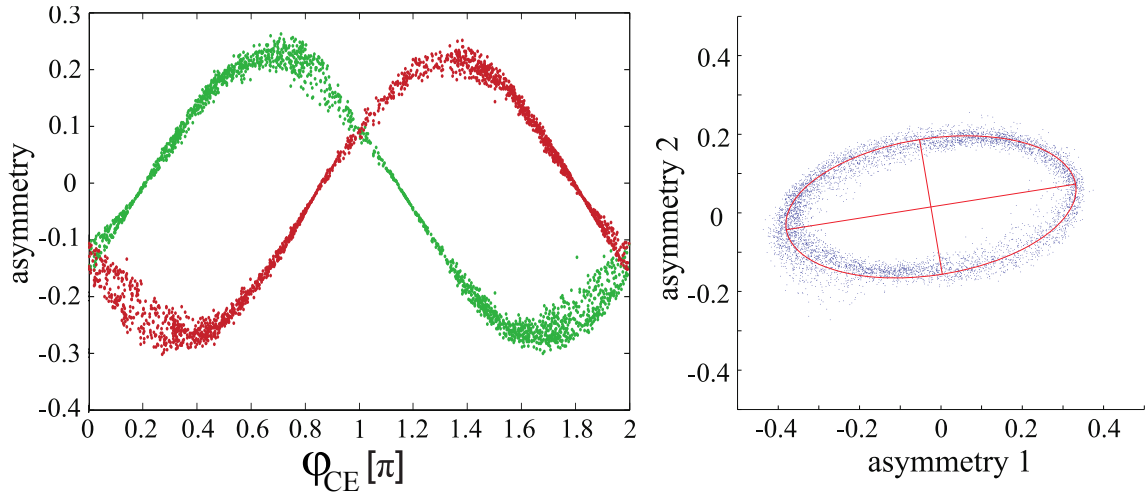

Figure 3.9: Phase ellipse. Left: CEP dependent asymmetry parameter for two different electron energy ranges (red $45-65\,eV$, green $65-85\,eV$) measured with the stereo-ATI spectrometer. Right: By plotting the asymmetry parameters for two different energy ranges versus each other, one obtains an ellipse. Each point on the ellipse corresponds to a certain CEP value.

Here b is a scaling factor, which is chosen such that the argument of the arcsin function ranges from -1 to 1. The phase can, however, be determined only with an ambiguity of π.
To determine the phase without ambiguity, one can make use of the energy dependence of the asymmetry [PLW+03]. For this purpose, the distance between the gas cell and the MCPs was made so large, that the energy of the electrons can be easily determined from their time of flight. A magnetic field was applied along the drift tubes to compensate the influence of the earth magnetic field. To determine the phase, the asymmetry is measured for two different energy regions [WHH+09]. The obtained asymmetry values are plotted versus each other as shown in figure 3.9. Due to the sinusodial dependence of the asymmetry on the phase, an ellipse is obtained by scanning the phase from zero to $2\,\pi$. Each point on the ellipse thereby corresponds to a certain CEP value[7].
For the measurements carried out with the reaction microscope, the absolute phase measured by the stereo-ATI spectrometer is not of interest as it differs from the one in the reaction microscope. In the present setup, the stereo-ATI spectrometer is mainly used to trace the phase evolution so that phase shifts, which may occur during the measurement, can be recognized and corrected.

[7]For a determination of the absolute phase for each point of the phase ellipse, the experimental data has to be compared to theoretical simulations, like for example TDSE-calculations [WHH+09].

3.5 Characterization of the phase stability

For characterizing the phase stabilization, two quantities are of importance, the phase noise and the long term stability. As a measure of the first the standard deviation of the f-2f signal can be used. It is smaller than 100 $mrad$ in the current setup, which is comparable or even better than the values reported by other groups [Ver06]. However, as the f-2f is used for both, measuring and stabilizing the phase, the standard deviation does not reveal the real phase noise, but rather the stability of the feedback loop. For an accurate determination of the real phase noise, an independent out-of loop measurement is required [Rau07]. This can be done either by a second f-2f interferometer or by the stereo-ATI spectrometer. For the measurements presented in this thesis, the stereo-ATI spectrometer was not well suited for this purpose as its signal-to-noise ratio was too low.
For achieving good statistics for measurements with the reaction microscope, a good long term stability of the phase stabilization is required. A significant improvement of the stability was achieved by a better climate control of the laboratory, the second feedback loop of the oscillator and an improved setup of the f-2f interferometer. For the oscillator, a long term stability of up to 12 hours was achieved. After loss of the phase stability of the oscillator and re-locking, the pulses picked out by the Pockels cell generally have another absolute phase. However, as the f-2f interferometer after the hollow fiber determines the phase value up to an unknown constant, this phase change can be compensated as long as the value of the unknown constant does not change. This could be verified by a stereo-ATI spectrometer measurement to hold for most of the cases the oscillator has to be re-locked. The phase stability is therefore mainly limited by intensity and beam pointing instabilities occurring in the laser system or the f-2f interferometer itself.
As the phase measured by the f-2f interferometer is intensity dependent due to the nonlinear processes involved, intensity fluctuations can also lead to measurement errors. Measurement errors can also occur if a change of dispersion leads to a change of the spectral phase of the pulse, which can be caused by beam pointing instabilities. Such instabilities were detected in the prism compressor, in which only a slight drift of the beam leads to a large change of the dispersion.
Measurement errors of the f-2f interferometer are probably the reason for sudden phase jumps, which are observed from time to time in the stereo-ATI spectrometer as well as in the reaction microscope measurements. By measuring the phase evolution with the stereo-ATI spectrometer, such phase changes can be corrected as long as the relative phase between the stereo-ATI spectrometer and the reaction microscope does not change.
With the present setup phase dependent measurements up to one day could be performed. An improvement of this stability can be achieved by a stabilization of the beam pointing, which is currently under construction for the prism compressor. An increase of the signal-to-noise ratio of the stereo-ATI spectrometer such that single shot measurement of the phase become possible, would even make a phase stabilization obsolete. This would significantly facilitate phase dependent measurements.

Chapter 4

The reaction microscope

The experimental data presented in this thesis were obtained by using a reaction microscope [UMD+03][US03] to detect the charged particles created by the interaction of laser pulses with molecules. A reaction microscope is composed of a COLTRIMS[1] [DMJ+00] and an electron spectrometer. The laser beam is focused into a cold and collimated supersonic gas jet of atoms or molecules. The charged particles created are guided by weak magnetic and electric fields dependent on their charge either to an electron or an ion detector. In this way, all charged particles emerging from the reaction can be detected and their three-dimensional momentum vectors can be determined with a high resolution. Furthermore, a coincident detection of the particles is possible so that different reaction channels can be separated.
In this chapter, first the design of the reaction microscope and its properties are described and in the following section the reconstruction of the momentum and energy of the charged particles is explained. The last section deals with the resolution and momentum acceptance that can be achieved.

4.1 Design of the reaction microscope

The design of the reaction microscope is illustrated schematically in figure 4.1. The laser beam is focused by a spherical gold mirror into a cold ($1\,K$) and collimated supersonic gas jet of atoms or molecules in an ultra high vacuum (UHV) chamber ($10^{-11} mbar$). A weak homogeneous electric field is applied parallel to the spectrometer axis, that guides the charged particles towards an ion and an electron detector, which are placed opposite to each other. This acceleration region is generally followed by a field free drift region, which the particles pass before reaching the detectors (see section 4.2).
The momentum of the electrons is usually comparable to that of the ions. Due to their small mass, they have a much larger energy than the ions so that in a moderate electric field most of them would miss the detector. Increasing the electric field, however, leads to a reduction of the momentum resolution as shown in section 4.4. Therefore, a weak magnetic field parallel to the spectrometer axis is applied by external Helmholtz coils, which forces the electrons onto spiral trajectories and thus confines their motion in space. By this means, all emitted electrons can be

[1] Sometimes reaction microscopes are referred to as COLTRIMS (**Col**d **t**arget **r**ecoil **i**on **m**omentum **s**pectrometer)

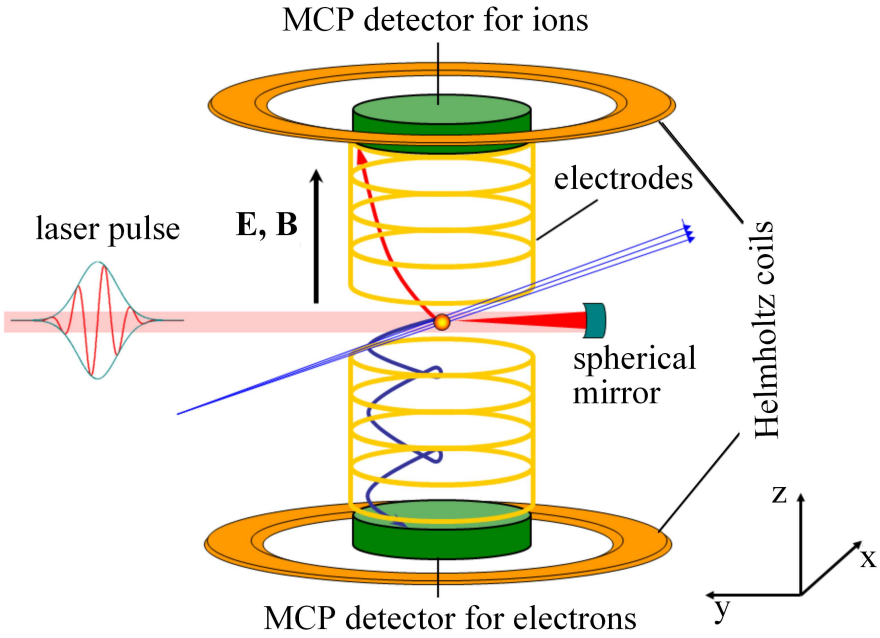

Figure 4.1: Schematic representation of the reaction microscope. The laser beam is focused onto a cold ($T \approx 1\,K$) and collimated supersonic gas jet of atoms or molecules. The charged fragments are guided by weak electric ($E \approx 2\,V/cm$) and magnetic fields ($B \approx 1\,mT$) to an ion ($\varnothing 127\,mm$) and an electron detector ($\varnothing 86\,mm$), each consisting of multichannel plates (MCPs) and a delay line anode placed behind [US03]. From the time and position information the full three dinemsional momentum vectors can be obtained.

detected and at the same time a good momentum resolution of the ions is maintained.
Each of the detectors consists of multichannel plates (MCPs) and a delay line anode for the position measurement. The time measurement is started by the laser trigger signal and is stopped when the particle hits the detector. From the time and position information the momentum vectors can be reconstructed as explained in section 4.3.
In order to gain a high momentum resolution, the initial thermal momentum spread of the atoms and molecules has to be very small and the reaction volume has to be well localized. This is achieved by the use of a supersonic gas jet [Mil88] which is created by the expansion of the target gas at high pressure through a small nozzle (diameter $30\,\mu m$) into a vacuum chamber. The conversion of internal motion into a directional one causes an effective cooling of the gas down to about $1K$. The jet is collimated by two skimmers ($d = 200\,\mu m$ and $400\,\mu m$) which are placed behind the nozzle. Furthermore, the skimmers block particles, which have a large momentum component perpendicular to the jet propagation direction, thereby further lowering the effective temperature in transversal direction. The distance of the nozzle to the laser focus is chosen such that the target density is reduced to about 10^8 to 10^9 particles per cm^3 so that on average less than one particle is in the focus during the duration of one laser pulse. This ensures that all fragments detected per laser shot are originating from the same atom or molecule, which is a prerequisite for coincidence measurements. A good vacuum in the reaction chamber is maintained

by differential pumping stages between the skimmers and the reaction chamber. A more detailed description of the reaction microscope design can be found in [dJRF+04].

4.2 Properties and advantages

Reaction microscopes are widely used to study the interaction of atoms and molecules with laser pulses as well as electron or ion beams as they allow a large insight into the reaction dynamics. The fragmentation channels can be easily distinguished as fragments with different mass to charge ratio appear as separated peaks at different times in the time of flight spectrum. From the width of the peaks together with the position information the three-dimensional momentum vectors can be reconstructed. The information on the momentum in all three dimensions together with the high momentum resolution makes it possible to observe features of the reaction dynamics not accessible by other detection techniques. Further insight is provided by the possibility to separate different reaction channels. Channels, which lead to different energies of the fragments, can be distinguished in the energy spectrum. Other channels can be separated by suited coincidence conditions. To reach a high momentum resolution, the time of flight of the particles must be determined with high precision. In reactions, in which ions or electrons are used as projectiles, the reaction volume is large, which imposes a major limit on the achievable resolution. This uncertainty can, however, be compensated by time and position focusing [UMD+03]. Position focusing is achieved by inserting an electrostatic lens in the acceleration region. For time focusing, the particles pass a field free drift region before they reach the detector, which is twice as long as the acceleration length.
Due to the small focal volume (focus diameter $\leq 7\,\mu m$), time and position focusing is not required in experiments with laser beams. The acceleration voltage can be applied over the whole flight region such that a high acceptance can be reached by maintaining a good resolution. This makes experiments with fragments of high mass and energy possible.

In experiments investigating the influence of the carrier-envelope phase of laser pulses, the so-called Gouy effect [Gou90] has to be considered. A laser beam, which propagates through a focus, obtains a phase shift of π, which is denoted as the Gouy phase shift (see figure 4.2 (a)). The Gouy phase shift for a beam propagating in z direction is given by

$$\phi = -arctan\left(\frac{z}{z_R(\lambda)}\right), \tag{4.1}$$

where z_R is the Rayleigh length[2], which depends on the wavelength λ. For an ultrashort laser pulse, which has a broad spectral bandwidth, the length scale of the Gouy phase shift differs for the different wavelength components. This leads to a difference between group and phase velocity and thus to a change of the carrier-envelope phase. The Gouy effect introduces a shift of the carrier-envelope phase by $\pi/2$ throughout the Rayleigh length [LPW+04] as shown in figure 4.2 (a).
In the experiments presented here, the Rayleigh length is only $150\,\mu m$ and thus smaller than the diameter of the gas jet. Therefore, the Gouy effect causes an averaging of the data over

[2]The Rayleigh length denotes the distance between the waist of a focused beam and the point, where the diameter of the beam corresponds to twice the diameter at the waist.

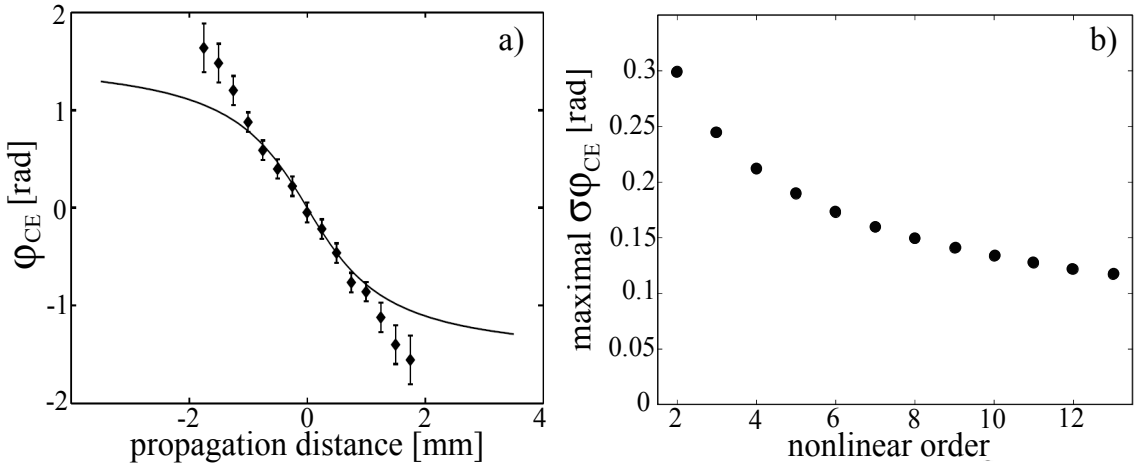

Figure 4.2: Influence of the Gouy phase shift on carrier-envelope phase effects. a) Experimental data from [LPW+04], where the evolution of the carrier-envelope phase throughout the laser focus was measured with a stereo-ATI spectrometer (see section 3.4). In this measurement, the Rayleigh length was $1\,mm$. The solid line represents the Gouy phase of a cw Gaussian beam. b) Weighted standard deviation of the phase without restriction of the reaction volume as a function of the nonlinear oder of the phase dependent process [Gim06].

different CEP values. This averaging can be reduced by localizing the reaction volume along the propagation direction to a fraction of the Rayleigh length by using a slit [Kre09]. The influence of the slit width and position was calculated in [Gim06]. The calculation revealed that the scatter of the carrier-envelope phase is proportional to the count rate.

For nonlinear processes, that means for processes, which have a nonlinear dependence on the laser intensity, the influence of the Gouy phase depends on the order of the process as shown in figure 4.2(b). For a second order process, the phase is averaged by $\pm 0.3\,rad$ and for a tenth order process by only about $\pm 0.15\,rad$.

In the single-pulse measurements carried out in the course of this work, the ion count rate was reduced to one third by positioning the slit outside the center of the focus. The two-pulse measurements, however, require long measurement times and thus a long term stability of the phase stabilization. This is difficult to achieve, making a reduction of the count rate disadvantageous. Therefore, the contrast of the phase effects in dissociation of H_2 with and without reduction of the reaction volume was compared. The contrast was shown to decrease when the reaction volume was not reduced. But this effect was small, which is probably due to the dependence of the phase averaging on the nonlinear order. Therefore, in the two pulse measurements the reaction volume was not reduced such that good statistics over relatively large delay ranges could be achieved at the expense of only a slight loss in the contrast of the phase effects.

4.3 Calculation of momentum and energy

The momenta in all three spacial directions can be reconstructed by using the equations of motion of charged particles in electric and magnetic fields. Before the interaction with the laser pulses, the initial momentum of the atoms or molecules in the coordinate system moving with the jet velocity is approximately zero

$$\mathbf{p_A} \approx \mathbf{0}. \tag{4.2}$$

The momentum of the absorbed photons in experiments with laser pulses is small compared to the momenta of the created ions and electrons and can be neglected. Therefore, in case a molecule is fragmented into K electrons and L ions, the sum momentum of the electrons $\sum_{i=1}^{K} \mathbf{p_{e_i}}$ is balanced by the sum momentum of the ions $\sum_{j=1}^{L} \mathbf{p_{r_j}}$

$$\sum_{i=1}^{K} \mathbf{p_{e_i}} = -\sum_{j=1}^{L} \mathbf{p_{r_j}}. \tag{4.3}$$

For single ionization, the momentum distribution of the ion equals the one of the emitted electron.

4.3.1 Ion momenta

The longitudinal momentum component, that is the component parallel to the spectrometer axis, can be calculated from the time of flight of the fragments. A particle with mass m acquires the momentum $p_{||}$ and the energy $E_{||} = \frac{p_{||}^2}{2m}$ during interaction with the laser. During acceleration in the homogeneous extraction field, it gains the additional energy qU, where U is the extraction voltage and q the charge of the particle. The time of flight as a function of the initial longitudinal energy is given by

$$t_{\pm}(E_{||}) = f \cdot \sqrt{m} \left[\frac{2a}{\sqrt{E_{||} + qU} \pm \sqrt{E_{||}}} + \frac{d}{\sqrt{E_{||} + qU}} \right], \tag{4.4}$$

where a is the acceleration length and d the length of the drift region. The plus sign holds for particles, which are emitted in the direction of the detector, and the minus sign for particles, which are emitted in the opposite direction. The factor $f = 719.9 \, \frac{ns}{cm} \sqrt{\frac{eV}{amu}}$ is chosen such that t is expressed in ns, m in amu, the distances a and d in cm and $E_{||}$ in eV.
For $d = 0$, as is the case for ions, the energy $p_{r_{||}} = \sqrt{2mE_{||}}$ can be calculated from (4.4) analytically. A simpler formula to calculate $p_{r_{||}}$ than the analytical one can be used in case the initial energy $E_{||}$ is much smaller than the energy gained during acceleration in the field qU. Then a Taylor expansion can be performed which yields

$$p_{r_{||}} = 8.04 \, \frac{a.u.\, cm}{eV\, ns} \cdot 10^{-3} \, \frac{qU}{a} \Delta t \tag{4.5}$$

for ions arriving with a time delay Δt with respect to ions with zero initial energy.
The transverse momentum of the ions can be determined from their time of flight and the position on the detector. Ions with zero transverse momentum arrive at the center of the position distribution. An ion with the perpendicular momentum component $p_{r_\perp}$ hits the detector at a

displacement R relative to the center. The transverse momentum component can be calculated from

$$p_{r_\perp} = 833.3\sqrt{\frac{ns\ a.u.}{cm\ amu}}\ \frac{Rm}{t}, \tag{4.6}$$

which yields the momentum in *a.u.*.
As the time of flight of the ions is much larger than their cyclotron period, the influence of the magnetic field can be neglected. It causes only an overall rotation of the detector image which can be easily corrected.

4.3.2 Electron momenta

The momenta of electrons can also be reconstructed from the time of flight and position information. As the longitudinal motion is not affected by the magnetic field, equation (4.4) is also valid for electrons. However, as the drift length is nonzero, $E_{\|}$ has to be calculated numerically. The electrons travel on spiral trajectories on the way to the detector, whereby the cyclotron frequency is determined by the magnetic field [Dür06b]

$$\omega_c = \frac{qB}{m_e}. \tag{4.7}$$

The radius of the spiral depends on the initial transverse momentum of the electron $p_\perp$ and is given by

$$r = \frac{p_{e_\perp}}{qB}. \tag{4.8}$$

The transverse momentum can be calculated from the time of flight t and displacement R relative to the center of the position distribution on the detector using equation

$$p_{e_\perp} = \left(8.04 \cdot 10^{-3} \frac{a.u.}{mm\,Gauss}\right) \frac{RB}{2\left|sin(\frac{1}{2}\omega_c t)\right|}. \tag{4.9}$$

Electrons with a time of flight, which is a full integer of the cyclotron period $T = \frac{2\pi}{\omega_c}$, arrive all at the same spot on the detector independent of their initial transverse momentum. A spectrum, in which the radius on the detector is plotted versus the time of flight as shown in figure 4.3, therefore exhibits nodal points. From the distance between the nodal points, which corresponds to the cyclotron period, the magnetic field can be determined. Furthermore, such a spectrum can be used to calibrate the time of flight of the electrons as electrons with $t = 0$ would hit the detector in a nodal point. If important information on the transverse momentum is required at times of flight coinciding with the nodal points, the nodal points can be shifted by slightly changing the strength of the magnetic field.

4.4 Resolution and momentum acceptance

The acceptance of the reaction microscope is defined as the direction dependent maximal momentum or energy a particle can have for being detected. The acceptance is mainly limited by the size of the detectors as well as the strength of the extraction fields. Particles emitted towards the

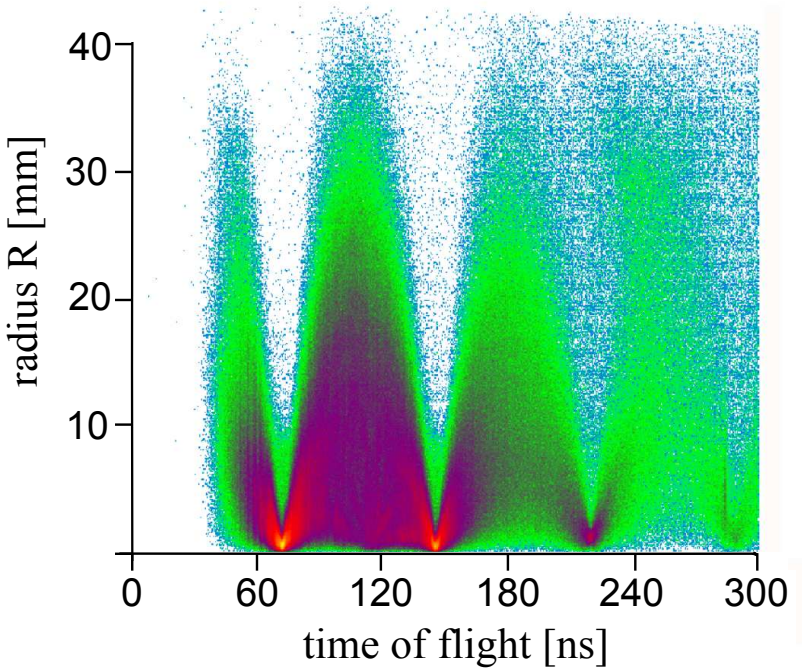

Figure 4.3: Displacement R of the electrons relative to the center of the position distribution on the detector dependent on the time of flight. At times corresponding to a full integer of the cyclotron frequency, all electrons hit the detector at the same spot independent of their initial transverse momentum. The nodal points can be used to determine the magnetic field and to calibrate the time of flight.

detector can be detected unrestrictedly. For ions or electrons emitted in the opposite direction, the acceptance is limited by the extraction voltage to

$$p_{r,e_\parallel}^{max} \leq \sqrt{2mqU}. \tag{4.10}$$

The maximal ion momentum perpendicular to the spectrometer axis, which can be detected, is given by the detector size R_{max} and the extraction voltage

$$p_{r_\perp}^{max} \leq R_{max}\frac{\sqrt{2mqU}}{2a}. \tag{4.11}$$

In the experiments performed with hydrogen and deuterium, the extraction voltage was $2\,V/cm$, which is sufficient as only low energetic ions emerging from dissociation were analyzed. With this extraction voltage a momentum acceptance for protons of $p_\parallel^{max} = 92.3\,a.u.$ and $p_\perp^{max} = 9.3\,a.u.$ was achieved. In figure 4.4, the detectable proton energy dependent on the angle relative to the spectrometer axis is shown. As only the protons emitted parallel to the laser spectrometer axis are of interest in the presented experiments, the low energy acceptance of $0.6\,eV$ for protons emitted at an angle of 90° is not relevant. For the detection of heavier ions, like for example methane [Wie07] or carbon dioxide [Sch09], the extraction field can be increased up to $40\,V/cm$.

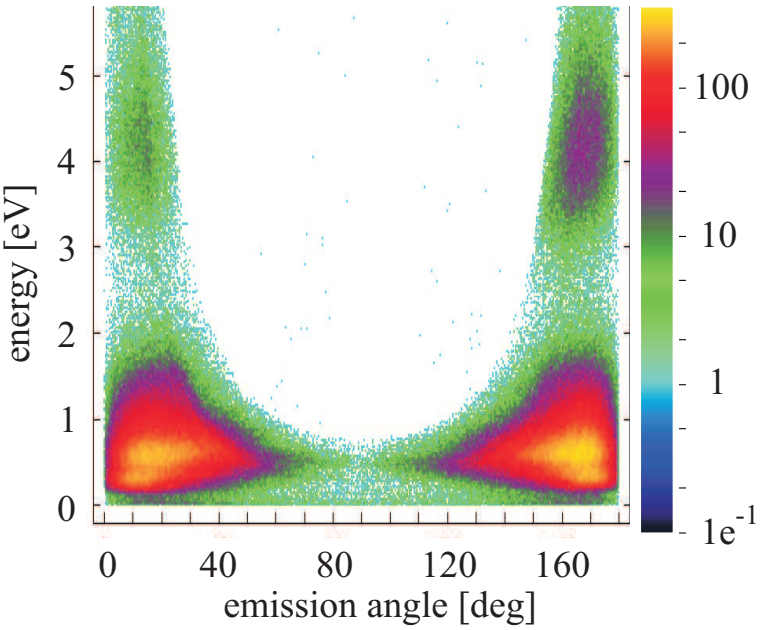

Figure 4.4: Energy acceptance of the ion detector. The proton spectrum emerging from the fragmentation of H_2 is shown as a function of the proton energy and the emission angle relative to the spectrometer axis for an extraction field of $2\,V/cm$. The laser pulses were polarized parallel to the spectrometer axis and had a peak intensity of about $0.4\,PW/cm^2$.

The maximal detectable transverse momentum of electrons is restricted by the detector size and the strength of the magnetic field

$$p_{e\perp}^{max} \leq qBR_{max}, \tag{4.12}$$

where R_{max} is the size of the detector. For a field of $10\,Gauss$, $p_{e\perp}^{max}$ is $2.4\,a.u.$, which corresponds to an energy of about $78\,eV$.
As follows from equation (4.5), the momentum resolution in longitudinal direction decreases with increasing extraction voltage. It is mainly limited by the accuracy of the time of flight measurement, which is about $0.5\,ns$. The transverse momentum resolution is additionally determined by the position resolution of the delay line anode, which is about $100\,\mu m$.
A further limitation of the ion momentum resolution is set by the temperature of the jet. In the direction parallel to the propagation direction of the jet, the temperature is higher than in the perpendicular direction such that the resolutions in the two transverse directions differ. The resolution parallel to the jet is $\Delta p_{r_\perp} \approx 0.1\,a.u.$ and perpendicular to the jet $\Delta p_{r\perp} \approx 0.05\,a.u.$. The best resolution of $\Delta p_{r_\parallel} < 0.01\,a.u.$ is achieved in the longitudinal direction.
For electrons, the jet temperature has no influence on the resolution as due to their low mass, the momentum uncertainty due to thermal motion is very small. Contrary to the ions, the longitudinal momentum resolution is not constant, but decreases with momentum. In transverse direction, it is maximal in the center between two nodal points, whereas there is no resolution at all in the nodal points (compare figure 4.3). A detailed discussion of the electron momentum resolution can be found in [Fis03].

Chapter 5

Single-pulse measurements on H_2 and D_2

It was first demonstrated in an experiment by M. Kling et al. [KSV$^+$06] that the emission direction of the D^+ ion emerging from dissociation of D_2 can be controlled by ultrashort carrier-envelope phase-stabilized laser pulses. Here the CEP determines at which of the deuterons the electron remains predominantly localized, which leads to a CEP dependent asymmetry in the emission direction of the D^+ ion. Such an asymmetry was observed for high energetic ions (KER: 6-16 eV) emerging from a recollision process.
The experiment of Kling et al. demonstrates the ability to control electronic motion in molecules via the carrier-envelope phase. However, some interesting questions could not be investigated with the detection technique used in those experiments: Does the first ionization step play a role for the asymmetry? Does the asymmetry depend on the molecular orientation relative to the polarization axis of the laser field? Why is almost no asymmetry observed in the low energetic deuterons, although predicted by theory [RE07b]?
In order to answer these questions, the CEP dependence of dissociating H_2^+ and D_2^+ was studied with a reaction microscope. This allowed one to investigate the influence of molecular orientation. Furthermore, the emitted electron could be detected in coincidence with the proton so that the correlation between the electron emission and the emission of the proton could be analyzed.
In the course of the present work and that of [Kre09], electron localization was for the first time observed for low energetic protons with a KER between 0 and 3 eV [KFF$^+$09]. These protons emerge from bond softening and the mechanism leading to the asymmetry differs from the one in [KSV$^+$06]. The obtained results are presented in this chapter together with measurements on D_2 and measurements, in which the dependence of the asymmetry on the pulse parameters was studied. The results are compared to wave packet calculations and a simple model for their explanation is provided.

5.1 Experimental results

The experimental results presented in this thesis were obtained by using laser pulses of about 6 fs, which were linearly polarized parallel to the spectrometer axis. The laser pulses were phase-stabilized as described in chapter 3. During the measurements the phase was scanned over a

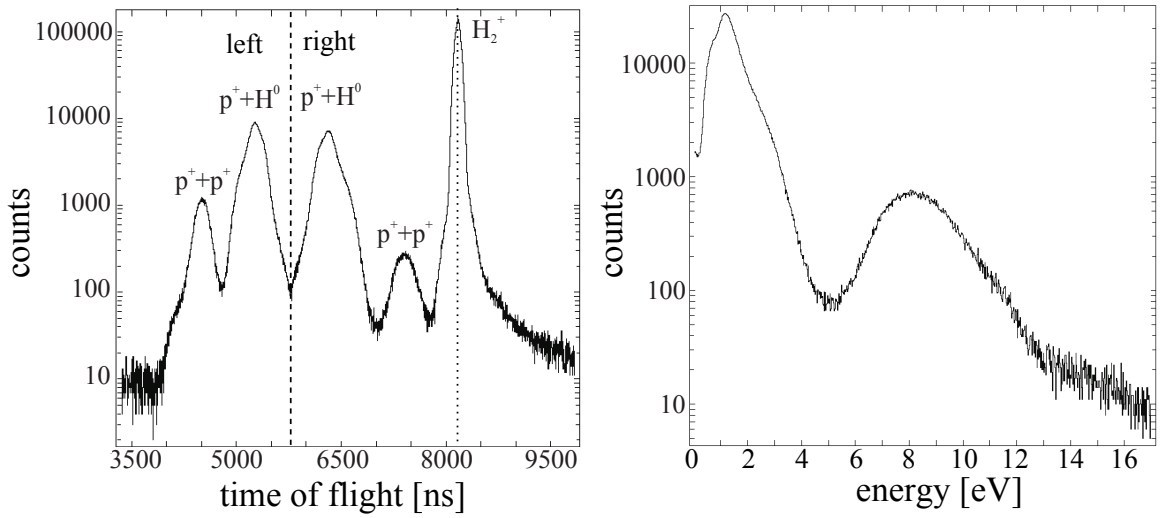

Figure 5.1: Left: Time of flight spectrum of H_2 obtained by laser pulses with a duration of $6\,fs$ and an intensity of about $0.44\,PW/cm^2$ for an extraction field of $2\,V/cm$. The peak centered at $8170\,ns$ corresponds to H_2^+, the other four peaks centered at $5800\,ns$ are protons emitted towards (left) and away from (right) the ion detector. The two inner peaks thereby stem from dissociation and the outer ones from Coulomb explosion. Right: Energy spectrum of the protons. The protons between $0-4\,eV$ emerge from dissociation due to bond softening (see section 1.4.1) and between $5-12\,eV$ from Coulomb explosion.

CEP range of $4\,\pi$ by moving a glass wedge in and out of the beam (see chapter 3.3.2). In the single-pulse measurements, the reaction volume was reduced with a slit in order to lower averaging over different phase values due to the Gouy effect (see chapter 4.2). The pulse intensity could be adjusted with an aperture and was chosen to be about $0.4\,PW/cm^2$. For such an intensity, Coulomb explosion, which is a competing fragmentation channel, is suppressed.
A time of flight spectrum of the reaction fragments of H_2 is shown in figure 5.1. The peak at $8170\,ns$ corresponds to single ionization of H_2, which is the dominating reaction channel. The proton spectrum consists of four peaks centered around $5800\,ns$, which corresponds to the time of flight of protons with zero initial momentum parallel to the spectrometer axis. The two inner peaks correspond to low energetic protons emerging from dissociation, whereas the high energetic outer peaks are protons from Coulomb explosion. Both fragmentation channels consist of two peaks as the protons are emitted predominantly parallel to the polarization axis and thus parallel to the spectrometer axis (see chapter 1.4.4). The two peaks on the right are the protons, which are emitted opposite to the ion detector. They first move away from the detector until their direction is reversed by the electric field of the spectrometer. Thus, they have a longer time of flight than the ions emitted towards the ion detector, which form the two peaks on the left (see equation (4.4)).
The energy spectrum of the protons is shown in the right image of figure 5.1. The protons with energies between 0 and $4\,eV$ result from dissociation. This low energetic part consists of the $1\,\omega$ and the $2\,\omega$ dissociation channel, corresponding to net absorption of 1 and 2 photons, respectively. As discussed in section 1.4.1, the energy of these two dissociation channels is determined by the

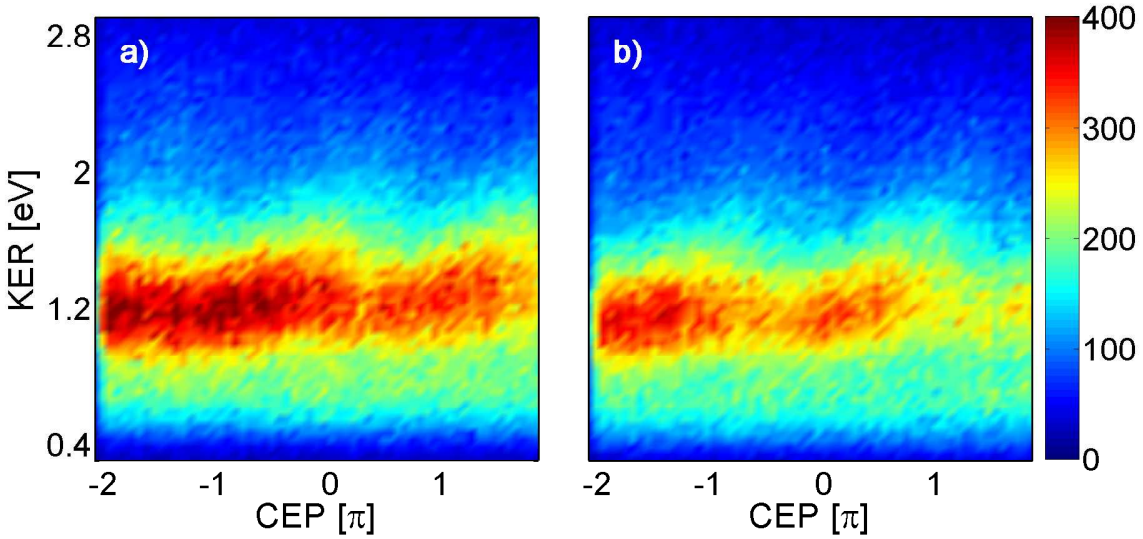

Figure 5.2: Proton count rate dependent on the KER and the carrier-envelope phase integrated over an emission angle relative to the polarization axis α between 0° and 30° for a) protons emitted towards the ion detector and b) in the opposite direction.

number of absorbed photons as well as the energy of the dissociating vibrational states. Besides that, a broadening of the energy spectrum due to the large bandwidth of the laser pulses occurs. The energy ranges of the two dissociation channels therefore overlap. Whether the peaks of the two channels can be well distinguished or are almost not separable as in the measurement shown here, depends strongly on the details of the pulse shape.
The protons with energies between 5 and 12 eV are the ones emerging from Coulomb explosion. Above 13 eV a weakly pronounced plateau is visible. Those are the protons created by non-sequential double ionization and recollision induced dissociation. For the latter mechanism, electron localization was observed by M. Kling [KSV$^+$06]. This channel can be separated from Coulomb explosion by a coincidence condition. However, as the count rate in this channel is very small in the measurements presented here, only the low energetic dissociation fragments are further considered.

5.1.1 Electron localization in H_2^+

In this section, a measurement on electron localization in dissociating H_2^+ is presented, in which the asymmetry of the proton and the electron emission was studied [KFF$^+$09]. Note that the phase scale in the measurements is not absolute as the CEP could be determined only up to an unknown constant. In the measurement presented in the following, the phase scale was chosen such that the experimental results are in agreement with the simulations presented in section 5.4.

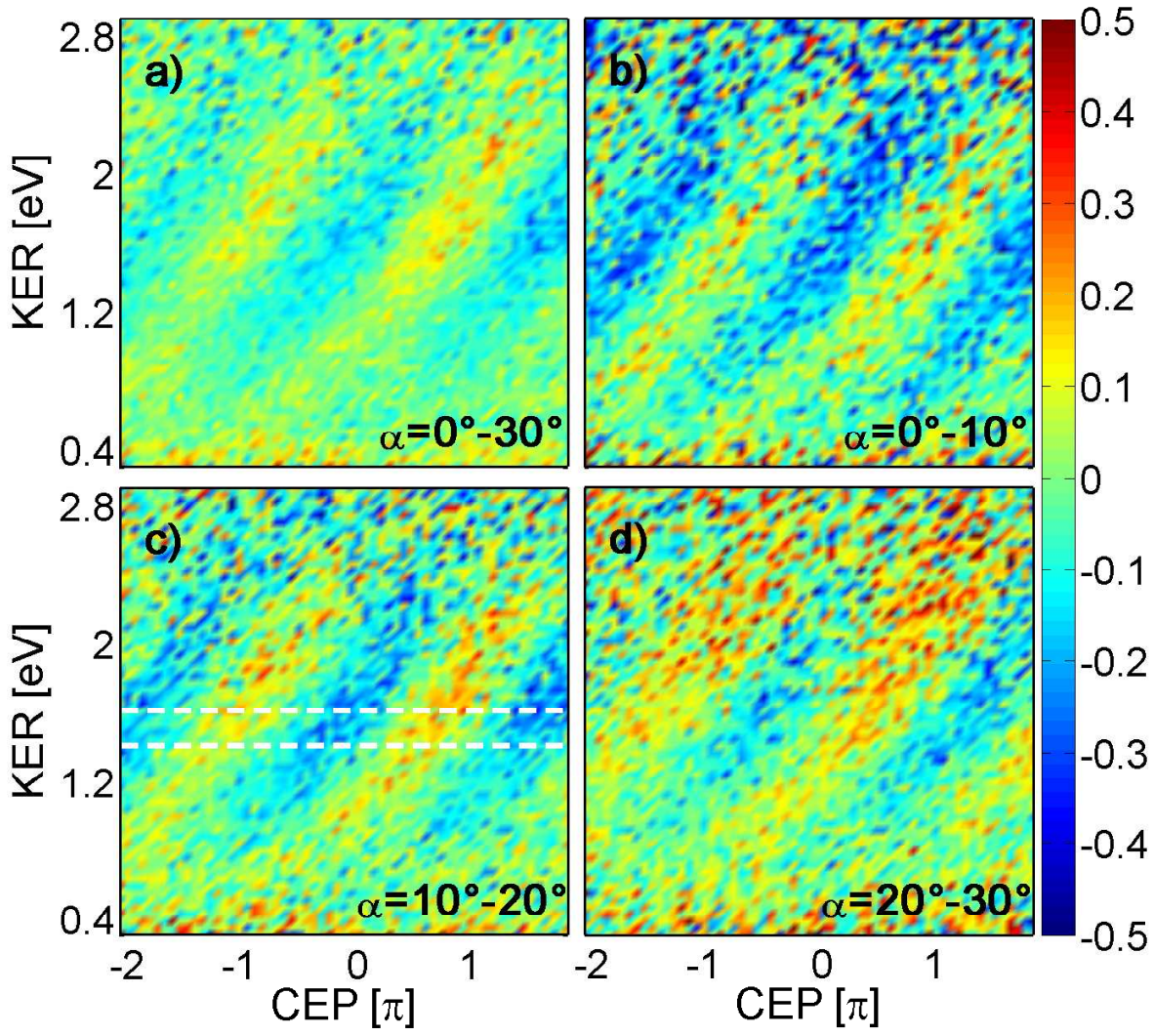

Figure 5.3: Asymmetry parameter dependent on KER and CEP for an emission angle α of a) 0° - 30°, b) 0° - 10°, c) 10° - 20° and d) 20° - 30°. A shift of the asymmetry stripes dependent on the angle between the molecular and the laser polarization axis is observed (see also figure 5.20).

Asymmetry in the proton emission

In figure 5.2, the count rate of the protons emitted towards the ion detector and in the opposite direction is shown as a function of the carrier-envelope phase and the kinetic energy release. The count rate was integrated over an emission angle relative to the spectrometer axis α between 0° and 30°. As can be seen in the figure, the proton emission at low energies between 0 and $3\,eV$ reveals a clear left-right asymmetry assuming that the spectrometer axis is horizontal, which depends on the carrier-envelope phase. This means that dependent on the CEP the bound electron of the dissociating H_2^+ ion remains predominantly localized at either the left or the right proton.
To quantify this asymmetry, it is useful to define an asymmetry parameter

$$A(KER, CEP) = \frac{N_l(KER, CEP) - N_r(KER, CEP)}{N_l(KER, CEP) + N_r(KER, CEP)}, \tag{5.1}$$

where N_l (N_r) is the number of counts emitted to the left (right). The asymmetry parameter calculated from the count rate in figure 5.2 is shown in figure 5.3 (a). The blue shaded areas correspond to the case, where the protons are emitted predominantly to the right, and the red ones to the case, where the protons are emitted predominantly to the left. The asymmetry ranges up to about 20% and has a $2\,\pi$ periodicity. Contrary to the measurements by Kling et al., the asymmetry stripes are tilted, which means that the asymmetry is energy dependent.

Dependence on the molecular orientation

The dissociation mechanism of the low energetic protons regarded here is bond softening. As shown in section 1.4.4, this mechanism strongly depends on the angle between the molecular axis and the polarization axis of the laser field. Thus, the question arises if the asymmetry is also angle dependent.
The asymmetry for protons emitted between 0° and 10° relative to the polarization axis is shown in figure 5.3 (b). It reveals a higher contrast than the asymmetry for the proton count rate being integrated from 0° to 30° shown in figure 5.3 (a). The reason for that becomes apparent from the images 5.3 (c) and (d), in which the asymmetry is shown for protons emitted between $10° - 20°$ and $20° - 30°$, respectively. One can see that the asymmetry stripes shift with the angle, whereas their shape does not change significantly. The shift can be also seen in figure 5.20, where the asymmetry parameter integrated over a KER range between 1.4 and $1.6\,eV$ (marked in figure 5.3 (a) with white lines) is shown for the different angles. The shift becomes larger with increasing angle, whereby the asymmetry decreases slightly. This result indicates that the coupling strength plays an important role for the asymmetry.

Asymmetry of the emitted electron

In the experiment of Kling et al., the emitted electron returns to the H_2^+ ion and induces the dissociation process. For bond softening, the electron leaves the H_2^+ ion after ionization and does not further interact with the ion. Hence, the question arises if there is a correlation between the emitted electron and the localization of the electron, which remains bound.
In order to answer this question, the CEP dependence of the emitted electron was analyzed. The electrons emitted together with the protons from dissociation were selected by setting a

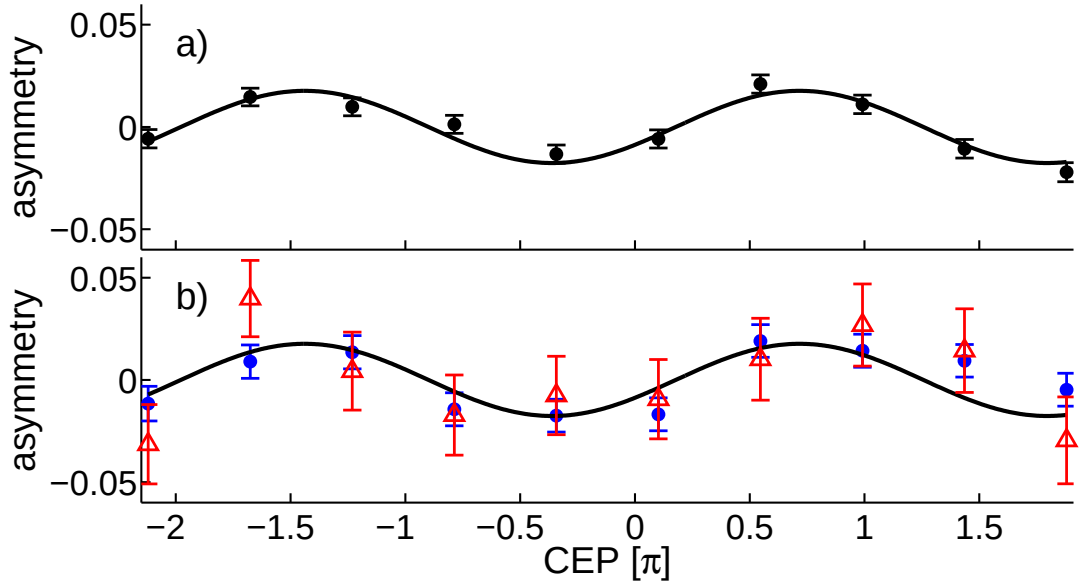

Figure 5.4: a) Asymmetry of the electrons emitted in coincidence with the protons (shown in figure 5.3) b) Electrons detected in coincidence with protons with a KER of 1.4 to 2.0 eV (red triangles) and 2.6 to 3.2 eV (blue dots). In both images, the electron count rate was integrated over the whole electron energy range as there is no energy dependence of the asymmetry.

coincidence condition on the time of flight of the protons. The asymmetry parameter of these electrons is shown in figure 5.4 (a). The asymmetry reveals also a CEP dependence with a periodicity of $2\,\pi$. However, the asymmetry is about one order of magnitude smaller than that of the protons. It is not dependent on the electron energy so that in figure 5.4 the electron count rate was integrated over the total energy range. To analyze if there is a correlation between electron and proton emission, coincidence conditions were set to protons of different energies. As can be seen by comparing the electron asymmetry for different proton energies, as shown in figure 5.4 (b), no dependence of the electron asymmetry on the proton energy could be found.
These results demonstrate that there is no obvious correlation between the emitted electron and the proton emission. This indicates that the emission direction of the removed electron does not play a significant role for the localization of the electron, which remains bound.

5.1.2 Dependence on the pulse properties

In order to investigate the influence of different pulse parameters, further measurements were carried out. Figure 5.5 (a) shows a measurement of the asymmetry in the proton emission for similar pulse parameters, i.e. for similar intensity and pulse length, as for the measurement shown in figure 5.3, but after a realignment of the laser system. One can see that the contrast of the asymmetry is higher and also the shape of the asymmetry stripes differs slightly from the measurement shown in figure 5.3.
Generally, the magnitude of the asymmetry may change after a realignment of the laser system

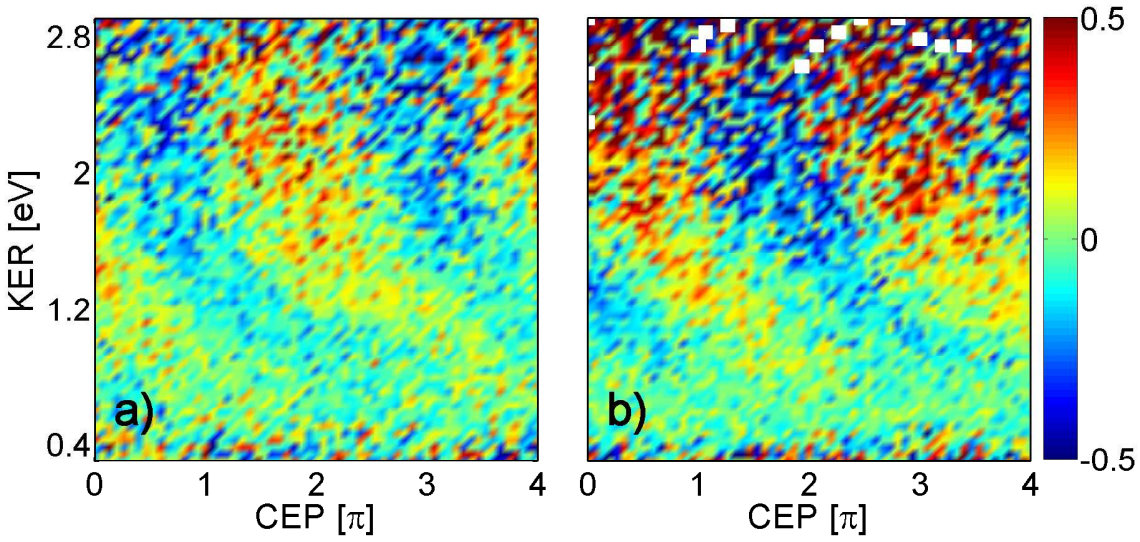

Figure 5.5: Asymmetry parameter for an intensity of a) about $0.42\,PW/cm^2$ and b) about $0.35\,PW/cm^2$. The phase scale is the same for both images.

as details of the pulse shape, like the exact pulse length or the intensity of satellite pulses, can change. In experiments [KSZ+08] as well as in theoretical simulations [Nie07], it was shown that the details of the pulse properties influence the obtained results. The reason for changes of the pulse properties is that the exact shape of the laser pulses is very sensitive to small variations in the amount of dispersion or variations in nonlinear processes, like for example self-phase modulation in the hollow fiber (see chapter 2). Therefore, even small changes of parameters, like for example beam pointing, the amount of dispersive material or the intensity, can significantly influence the details of the pulse shape. Due to the complexity of femtosecond laser systems, such small variations cannot be entirely avoided. An exact determination of the pulse properties is also difficult. As described in section 2.4.1, by measuring the autocorrelation, the pulse shape can be determined only qualitatively. A more accurate measurement is possible by using the SPIDER technique (see section 2.4.2). This method is, however, time consuming and thus not well suited for using it on a regular basis. For these reasons, if the laser system has to be realigned between two measurements, the magnitude of the asymmetry or fine details of its shape may change.
As can be seen in figure 5.5 also the direction of the asymmetry stripes changes between the measurements in figures 5.3 and 5.5. Such a change of the direction was observed several times and can be probably attributed either to variations of the pulse properties or to some systematic measurement errors of the f-2f interferometer, which lead to a change in the direction of the phase axis. This issue will be clarified in future measurements by monitoring the CEP with the stereo-ATI spectrometer.
In figure 5.5 (b), the asymmetry is shown for the same laser alignment (the phase scale is therefore also the same), but for another intensity. The shape and magnitude of the asymmetry does not change significantly, but the asymmetry stripes shift. However, the shape of the pulse might also change slightly if the beam has some spatial chirp. Therefore, the magnitude of the shift cannot

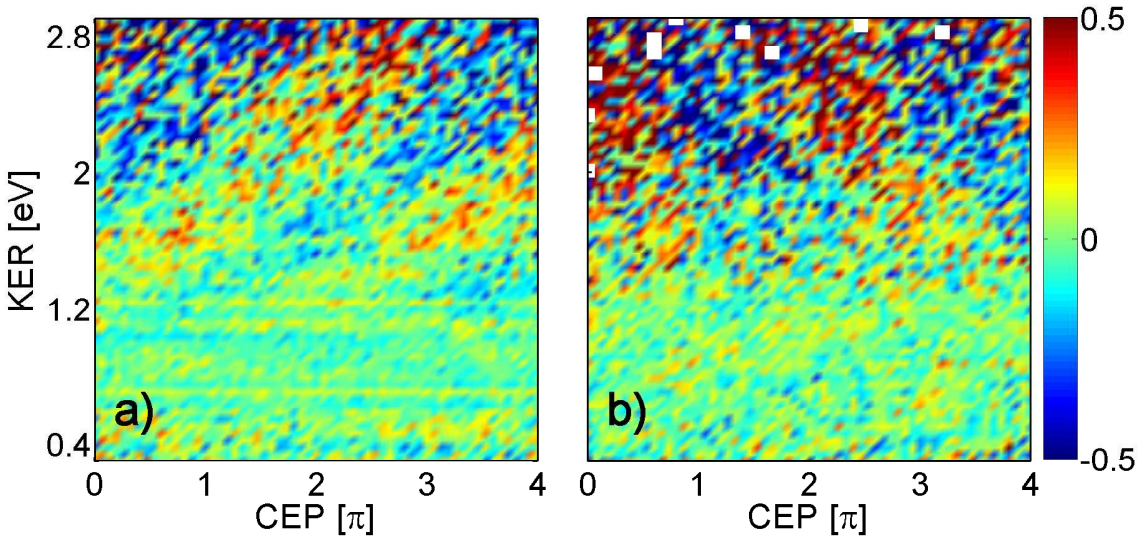

Figure 5.6: Asymmetry parameter of deuterons emerging from the dissociation of D_2^+. In a) and b), two different measurements are shown so that the phase scales differ from each other.

be regarded absolutely, but it provides qualitative information on the influence of the intensity. Although the magnitude of the asymmetry and details of the asymmetry stripes change for different measurements as described above, the main features of the experimental results are preserved and can be compared with theory.

5.1.3 Electron localization in D_2

As deuterium has a larger mass than hydrogen, the dissociation process of D_2^+ is slower than that of H_2^+. To investigate the influence of this difference on electron localization, the CEP dependence of the emission of deuterons emerging from bond softening of deuterium molecules was analyzed. The pulse parameters, i.e. the intensity and the pulse length, were similar as for the H_2 measurements.
The result of a measurement on D_2 is shown in figure 5.6 (a). The asymmetry is well pronounced for the high energetic part of the spectrum above $1.5\,eV$ and almost vanishes at lower energies. In image 5.6 (b), the deuteron asymmetry is shown for another measurement for the same laser parameters. It shows that for D_2 the direction of the asymmetry stripes depends on the pulse shape, too. However, the low contrast of the asymmetry at small KERs is a general feature.

5.1.4 Comparison with earlier measurements

As already mentioned, electron localization of dissociating D_2^+ was first observed by Kling et al., but the observed asymmetry differs from the results presented above. Those experiments were performed with $5\,fs$ linearly polarized phase-stable laser pulses at an intensity of $0.1\,PW/cm^2$

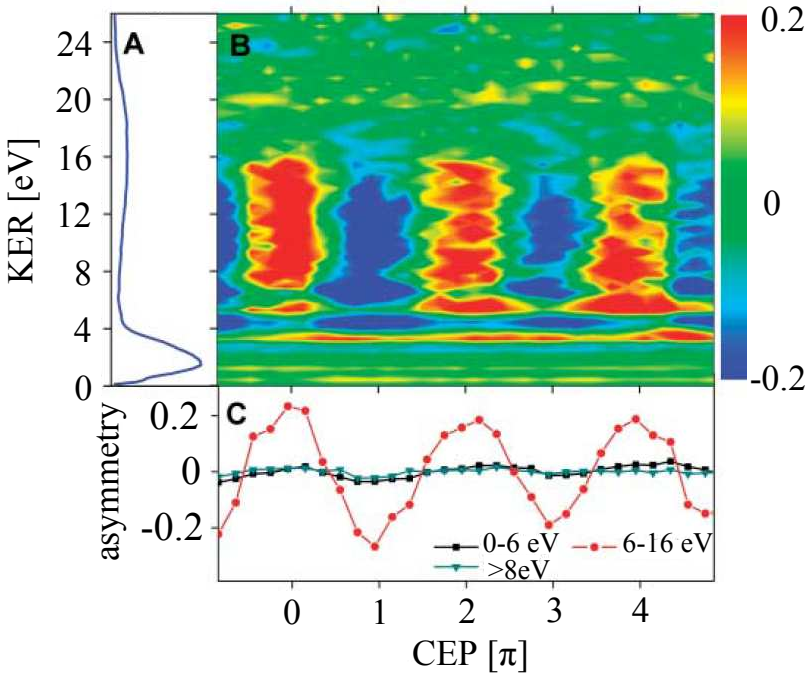

Figure 5.7: Experimental results from [KSV+06]. The asymmetry parameter of deuterons dependent on the KER and the CEP is shown. An asymmetry is mainly observed in the energy range between 6 and 16 eV, which is explained with a recollision model presented in section 5.2.1. Only a small asymmetry can be observed in the bond softening regime. In the left image, the energy spectrum of the deuterons is shown. The lower image shows the asymmetry integrated over different energy ranges.

[KSV+06]. In figure 5.7, the asymmetry parameter of deuterons dependent on the KER and the carrier-envelope phase is shown. A pronounced asymmetry is observed between 6 and 16 eV, which shows no dependence on the KER in this energy range. These deuterons emerge from recollision induced dissociation as was verified by comparing the energy spectrum of linearly and circularly polarized pulses [KSZ+08]. In the bond-softening regime, a CEP dependent asymmetry is observed between 2 eV and 4 eV, which is shifted by $\pi/2$ with respect to the asymmetry in the high energy range. The asymmetry is, however, very weak. Details of its shape and its KER dependence cannot be resolved.

5.2 Electron localization mechanisms

For electron localization, a coupling between a gerade and an ungerade electronic state is required. This becomes clear from figure 5.8, where the electronic wave functions of the $1s\sigma_g$ state and the $2p\sigma_u$ state of H_2^+ are illustrated. A coherent superposition of these wave functions leads to a wave function localized at either the left or the right nucleus. Two localized states can therefore be defined as a coherent superposition of the gerade and the ungerade state. The state localized

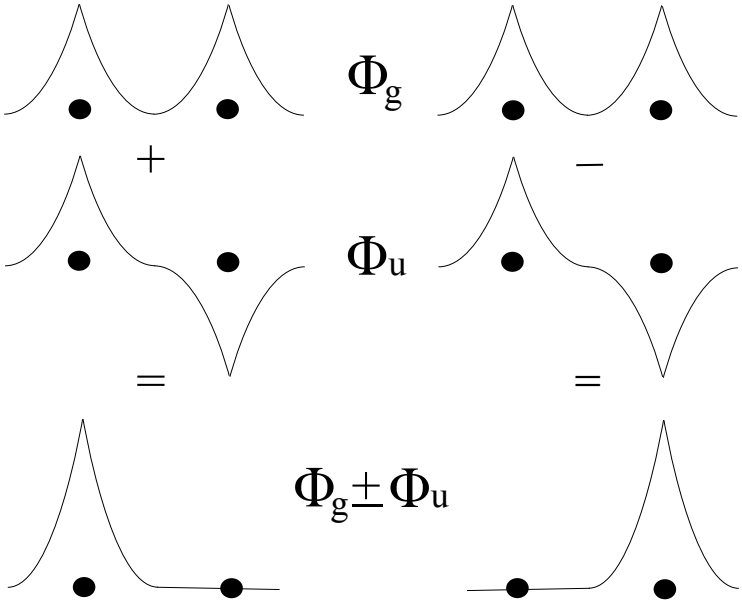

Figure 5.8: Schematic illustration of the electronic wave function of the gerade $1s\sigma_g$ state and the ungerade $2p\sigma_u$ state. A coherent superposition of these wave functions leads to the electron density being localized either at the left or the right nucleus.

at the left proton is then

$$|l\rangle = \frac{|1s\sigma_g\rangle + |2p\sigma_u\rangle}{\sqrt{2}} \tag{5.2}$$

and the state localized at the right proton

$$|r\rangle = \frac{|1s\sigma_g\rangle - |2p\sigma_u\rangle}{\sqrt{2}}. \tag{5.3}$$

By a projection onto these states, the corresponding nuclear wave functions are obtained

$$\Psi_{l,r}(R,t) = \frac{1}{\sqrt{2}}\left(\Psi_g(R,t) \pm \Psi_u(R,t)\right). \tag{5.4}$$

The probability of the electron to remain on either the left or the right nucleus is then given by

$$P_{l,r}(R,t) = \frac{1}{2}\left|\Psi_g(R,t) \pm \Psi_u(R,t)\right|^2 \tag{5.5}$$

and a localization parameter can be defined as

$$L = \frac{\int \left(P_l(R,t) - P_r(R,t)\right) dR}{\int \left(P_l(R,t) + P_r(R,t)\right) dR}, \tag{5.6}$$

which corresponds to the asymmetry parameter (5.1) used in the measurements. From these equations one can see that the probability of the electron for being localized at either the left or the right nucleus depends on the population of the gerade $1s\sigma_g$ and the ungerade $2p\sigma_u$ state.

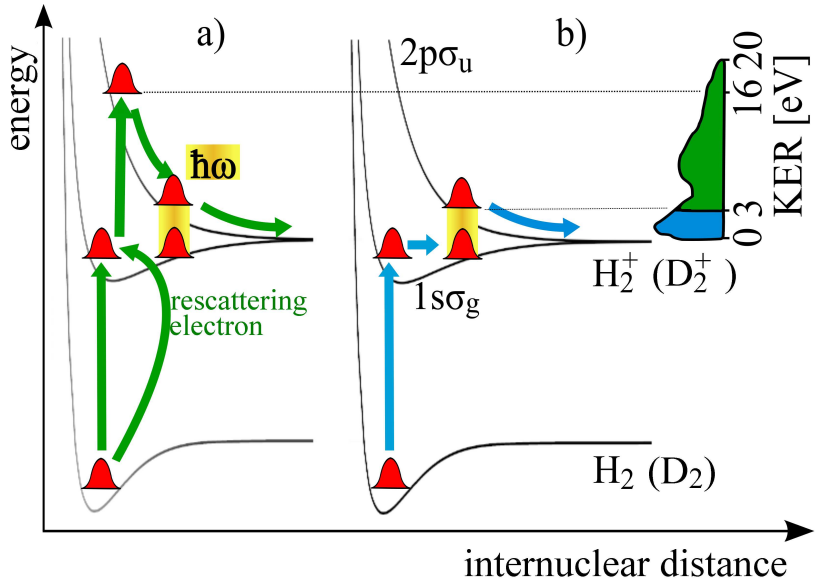

Figure 5.9: Simple models for the electron localization mechanisms for H_2 (D_2). In a) the model used to explain the electron localization for high energetic protons from recollision induced dissociation observed in [KSV+06] is illustrated. In b) the model developed for dissociation in the bond softening regime is shown. In both models, the localization is based on the coupling between the $1s\sigma_g$ and the $2p\sigma_u$ state by the laser field, which is symbolized by the yellow shaded area.

Higher excited states can be neglected for the experimental parameters of the measurements presented in this chapter.
The mechanisms which lead to the electron localization in the experiment of Kling et al. and the experiment presented here are explained in the following subsections.

5.2.1 Localization for recollision induced dissociation

In figure 5.9 (a), the recollision mechanism leading to the asymmetry observed in [KSV+06] is illustrated. The process starts with single ionization of D_2 in its vibrational ground state by tunnel ionization in the laser pulse. This way several vibrational states of the electronic ground state $1s\sigma_g$ of D_2^+ are populated coherently so that a wave packet is created. This wave packet is free to move in the potential curve and starts propagating towards a higher internuclear distance. When the sign of the electric field changes, the emitted electron is driven back to its parent ion. It recollides with the D_2^+ about $1.7\,fs$ after it was liberated. Thereby, it can transfer enough energy to shuffle population from the $1s\sigma_g$ state to the first electronically excited state $2p\sigma_u$. In [KSZ+08] and [KSV+06], it is assumed that no population remains in the $1s\sigma_g$ state. As the recollision process occurs relatively fast after ionization, the population transfer takes place at a small internuclear distance, where the $2p\sigma_u$ potential curve has a high energy. The wave packet dissociating along this curve thus gains a high KER. It slides down the potential curve in about $5\,fs$.

For electron localization, a coupling between the gerade and the ungerade state is required. Such a coupling is introduced by the remaining laser field of the pulse when the wave packet has reached an internuclear distance, where the energy gap between the $1s\sigma_g$ and the $2p\sigma_u$ corresponds approximately to the photon energy. Then the dipole coupling between the two states is sufficiently strong to transfer a part of the population from the $2p\sigma_u$ state back to the $1s\sigma_g$ state. Localization is achieved for a certain KER if a part of the wave packet emerging from the $2p\sigma_u$ dissociation channel contributes to the same KER as a part of the wave packet from the $1s\sigma_g$ channel. As the fraction of the wave packet, which is transferred back to the $1s\sigma_g$ state, has gained a high energy by sliding down the $2p\sigma_u$ curve, it can dissociate from the $1s\sigma_g$ state with a high KER and interfere with the wave packet dissociating from the $2p\sigma_u$ curve.
For the asymmetry at low energies, the low-energy tail of the wave packet dissociating along the excited state interferes with a wave packet, which was transfered from the $2p\sigma_u$ to the $1s\sigma_g$ relatively early after recollision. At high KERs, the transition to the $1s\sigma_g$ state occurs relatively late. Then the wave packet has gained a high kinetic energy by sliding down the $2p\sigma_u$ and thus can dissociate from the $1s\sigma_g$ state with a high energy. This simple model was shown to well describe the experimental results in the high energy regime between 6 and 16 eV.

5.2.2 Localization for bond softening

The model developed to explain the asymmetries in the low energy range for the measurements presented in this chapter is illustrated in figure 5.9 (b) [KFF+09]. The process also starts by single ionization from the ground state of H_2 or D_2 and the creation of a wave packet in the electronic ground state of the molecular ion. The energy gap to the $2p\sigma_u$ state at small internuclear distances is so large, that the laser field cannot couple the two states. However, when the wave packet reaches the area, where the distance of the two states approaches the photon energy, the electric field of the pulse can couple them efficiently. A part of the wave packet is then transferred to the $2p\sigma_u$ state and can dissociate by gaining a KER of up to 3 eV. For electron localization, the wave packet dissociating along the $2p\sigma_u$ has to interfere with a wave packet dissociating along the $1s\sigma_g$ state. The wave packet which remains on the $1s\sigma_g$ cannot overcome the potential barrier. However, the laser field can also transfer population back from the $2p\sigma_u$ state to the electronic ground state. This part of the wave packet has gained energy by sliding down the $2p\sigma_u$ curve and thus can dissociate along the $1s\sigma_g$ potential. The parts of the wave packet from the $2p\sigma_u$ state, which have the same KER as parts of the wave packet dissociating along the $1s\sigma_g$ state, interfere with each other leading to the observed asymmetry.

For a calculation of the CEP dependent asymmetry, the nuclear wave function is propagated on the $1s\sigma_g$ and the $2p\sigma_u$ and the coupling between these two states is considered. The ansatz for the calculation is to expand the total wave function $\Psi(R, r, t)$ dependent on the internuclear distance R and the electronic coordinate r in terms of the electronic states $1s\sigma_g$ (denoted by $|g\rangle$) and $2p\sigma_u$ ($|u\rangle$)

$$\Psi(R, r, t) = |g\rangle\, \Psi_g(R, t) + |u\rangle\, \Psi_u(R, t), \tag{5.7}$$

where $\Psi_g(R, t)$ is the nuclear wave packet in the gerade and $\Psi_u(R, t)$ is the nuclear wave packet in the ungerade state. By inserting this ansatz into the Schrödinger equation, one obtains two coupled equations, which can be written as

$$i\frac{\partial}{\partial t}\begin{pmatrix} \Psi_g(R,t) \\ \Psi_u(R,t) \end{pmatrix} = \begin{bmatrix} -\frac{1}{2\mu}\frac{\partial^2}{\partial R^2} + V_g(R) & V_{gu}(R) \\ V_{ug}(R) & -\frac{1}{2\mu}\frac{\partial^2}{\partial R^2} + V_u(R) \end{bmatrix} \begin{pmatrix} \Psi_g(R,t) \\ \Psi_u(R,t) \end{pmatrix}. \tag{5.8}$$

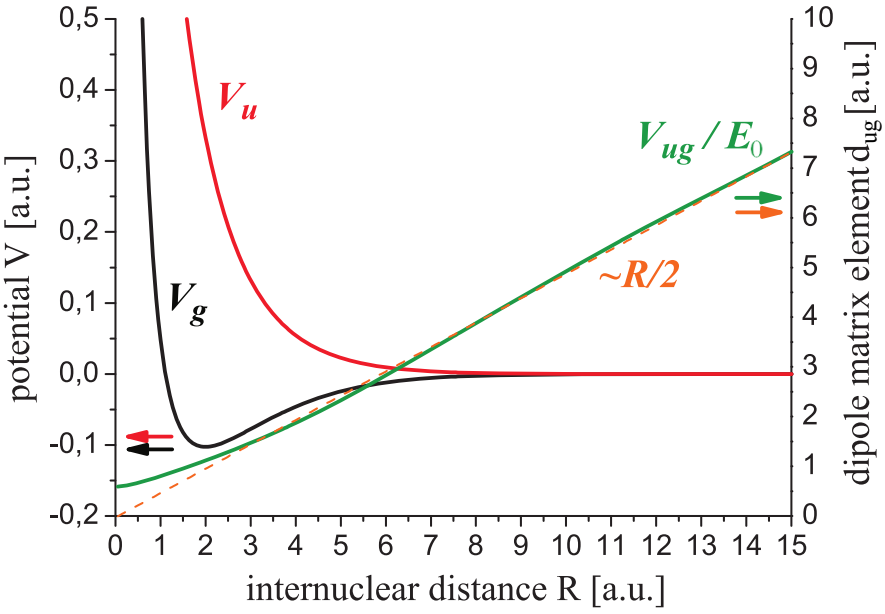

Figure 5.10: Illustration of the matrix elements in the Schrödinger equation used in the wave packet simulations. The red and the black curve represent the diagonal matrix elements V_g and V_u, which correspond to the $1s\sigma_g$ and the $2p\sigma_u$ potential curves. The dipole coupling d_{ug} for a constant electric field E_0 is plotted in green. The orange dashed line is a fit to the dipole coupling, which represents its asymptotic behavior.

Here V_g is the potential of the gerade and V_u the potential of the ungerade state

$$V_g(R) = \underbrace{\left\langle g \left| \hat{H}_e(R,r) \right| g \right\rangle}_{=I_P^g(R)} + \frac{1}{R} \tag{5.9}$$

and

$$V_u(R) = \underbrace{\left\langle u \left| \hat{H}_e(R,r) \right| u \right\rangle}_{=I_P^u(R)} + \frac{1}{R}\,. \tag{5.10}$$

The non-diagonal terms describe the dipole coupling between the two states and are given by

$$V_{gu} = \mathcal{E}(t)\, cos(\alpha)\, \underbrace{\langle g \,|e \cdot z|\, u\rangle}_{d_{gu}} \tag{5.11}$$

and

$$V_{ug} = \mathcal{E}(t)\, cos(\alpha)\, \underbrace{\langle u \,|e \cdot z|\, g\rangle}_{d_{ug}}, \tag{5.12}$$

where $\mathcal{E}(t)\, cos(\alpha)$ is the projection of the electric field onto the molecular axis, and d_{ug} and d_{gu} are the dipole matrix elements.
To illustrate the properties of the dipole coupling, it is useful to regard the dipole matrix element

at a large internuclear distance ($R \gg R_0$). The electronic wave functions can then be expressed in terms of the atomic 1s-orbitals Φ_{1s}

$$|1s\sigma_g\rangle = \frac{\Phi_{1s}(z - R/2) + \Phi_{1s}(z + R/2)}{\sqrt{2}} \tag{5.13}$$

$$|2p\sigma_u\rangle = \frac{\Phi_{1s}(z - R/2) - \Phi_{1s}(z + R/2)}{\sqrt{2}}. \tag{5.14}$$

The transition matrix element for large R is then given by

$$\begin{aligned} d_{ug} &= \frac{1}{2}\langle \Phi_{1s}(z - R/2) - \Phi_{1s}(z + R/2)\,|e \cdot z|\,\Phi_{1s}(z - R/2) + \Phi_{1s}(z + R/2)\rangle \\ &= \frac{1}{2}\underbrace{\langle \Phi_{1s}(z - R/2)\,|e \cdot z|\,\Phi_{1s}(z - R/2)\rangle}_{=R/2} - \frac{1}{2}\underbrace{\langle \Phi_{1s}(z + R/2)\,|e \cdot z|\,\Phi_{1s}(z + R/2)\rangle}_{=-R/2} \\ &+ \frac{1}{2}\underbrace{\langle \Phi_{1s}(z - R/2)\,|e \cdot z|\,\Phi_{1s}(z + R/2)\rangle}_{=0} - \frac{1}{2}\underbrace{\langle \Phi_{1s}(z + R/2)\,|e \cdot z|\,\Phi_{1s}(z - R/2)\rangle}_{=0} \\ &= R/2 \end{aligned} \tag{5.15}$$

as illustrated in figure 5.10.

5.3 Theoretical predictions

A phase dependent asymmetry in the bond softening regime was already predicted by theory. In [RE07b], the phase dependence in the dissociation of HD^+ ions was calculated by numerically solving the time dependent Schrödinger equation. This method was also used to study the asymmetry and its dependence on the nuclear mass for H_2^+, D_2^+ and T_2^+ ions in [HE09]. In this section, the main results presented in these two papers are summarized. Although they are not directly comparable to our experimental results as their basic assumptions differ from our experimental conditions, they provide important insight into the localization mechanism.
The calculation is performed for an H_2^+ target as provided by an ion source. In such a source, the ions are created by fast ionization of the ground state of H_2, which leads to a coherent Franck-Condon distribution for the vibrational states in the $1s\sigma_g$ state of H_2^+ (see chapter 1.3.1). The time the ions need to reach the interaction region with the laser beam has a spread, which is on the order of nanoseconds. It is much larger than the vibrational period of H_2^+ so that the ions interact with the laser pulse at different times of the wave packet evolution (see chapter 1.5). Thus, for each internuclear distance R there are always some ions, for which the wave packet is located around this R value or has dephased over the potential well at the time of interaction with the laser. On average, the wave packet is therefore spread over the whole range of internuclear distances, which effectively converts the distribution of vibrational states into an incoherent one. The total probability distribution is then obtained by an incoherent summation of the wave functions of all initial vibrational states

$$\Psi_{tot} = \sum_{i=1}^{n} a_i^{FC}\,|\Psi_i|^2 \tag{5.16}$$

weighted by their Franck-Condon factors a_i^{FC}.
Therefore, in the calculations the observables were added incoherently over all vibrational states weighted by the Franck-Condon factors. In the calculation, the molecular axis was fixed parallel to the polarization axis of the linearly polarized laser field ($\alpha = 0$) and the Born-Oppenheimer approximation was used. The time dependent Schrödinger equation for the nuclear wave functions was written analogous to equation (5.8). Only the bond softening process was considered and no recollision was included in the model.
In order to gain more insight into the physical mechanism of electron localization, the asymmetry was additionally analyzed analytically within the framework of a Floquet representation [HE09]. Thereby, $\mathbf{\Psi}(R,t)$, which is the column vector containing the nuclear wave functions on the gerade and the ungerade electronic state

$$\mathbf{\Psi}(R,t) = \begin{pmatrix} \Psi_g(R,t) \\ \Psi_u(R,t) \end{pmatrix}, \tag{5.17}$$

is expanded in a discrete Fourier transform in terms of the carrier-envelope phase φ_{CE}. This can be done as the Schrödinger equation is periodic in φ_{CE} due to the periodicity of the electric field $\mathcal{E}(t) = \mathcal{E}_0(t)cos(\omega t + \varphi_{CE})$. The wave function is then written as

$$\mathbf{\Psi}(R,t) = \sum_{n=-\infty}^{n=\infty} e^{in\varphi_{CE}} \mathbf{\Psi_n}(R,t). \tag{5.18}$$

The amplitudes $\mathbf{\Psi_n}(R,t)$ can be rewritten as

$$\mathbf{\Psi_n}(R,t) = e^{-in\omega t}\mathbf{G_n}(R,t). \tag{5.19}$$

By inserting these expressions into the Schrödinger equation, one obtains

$$i\frac{\partial}{\partial t}\mathbf{G_n} = \left(\left(-\frac{1}{2\mu}\frac{\partial^2}{\partial R^2} - n\omega\right)\mathbf{I} + \begin{bmatrix} -\frac{1}{2\mu}\frac{\partial^2}{\partial R^2} + V_g(R) & 0 \\ 0 & -\frac{1}{2\mu}\frac{\partial^2}{\partial R^2} + V_u(R) \end{bmatrix}\right)\mathbf{G_n} \tag{5.20}$$

$$- \frac{1}{2}\begin{bmatrix} 0 & d_{gu} \\ d_{ug} & 0 \end{bmatrix}\mathcal{E}_0(t)\left(\mathbf{G_{n-1}} + \mathbf{G_{n+1}}\right), \tag{5.21}$$

where $\mathbf{I}$ is the unit matrix. As this equation is independent of φ_{CE}, it is sufficient to solve it only once to get the whole CEP dependence. The amplitudes $\mathbf{G_n}$ can be interpreted as n-photon amplitudes as they are associated with $e^{-in\omega t}$.
The asymmetry for a certain kinetic energy release E_k is determined by the probability amplitudes of the channels $p+H$ labeled as $|l, E_k\rangle$ and $H+p$ labeled as $|r, E_k\rangle$, which correspond to the proton being emitted to the left and to the right with the asymptotic energy E_k, respectively. These channels can be obtained from a superposition of the outgoing continuum wavefunctions $|g, E_k\rangle$ on the gerade $1s\sigma_g$ state and $|u, E_k\rangle$ on the ungerade $2p\sigma_u$ state, which have the asymptotic kinetic energy E_k. The localized states are obtained from the equation

$$|(l,r), E_k\rangle = \frac{1}{\sqrt{2}}\left(e^{-i\delta_g}|g, E_k\rangle \pm e^{-i\delta_u}|u, E_k\rangle\right). \tag{5.22}$$

Here $\delta_{g,u}$ are the energy dependent phase shifts, that the interfering nuclear wave functions accumulate on the two potential curves. The probability for $p + H$ and $H + p$ can be obtained

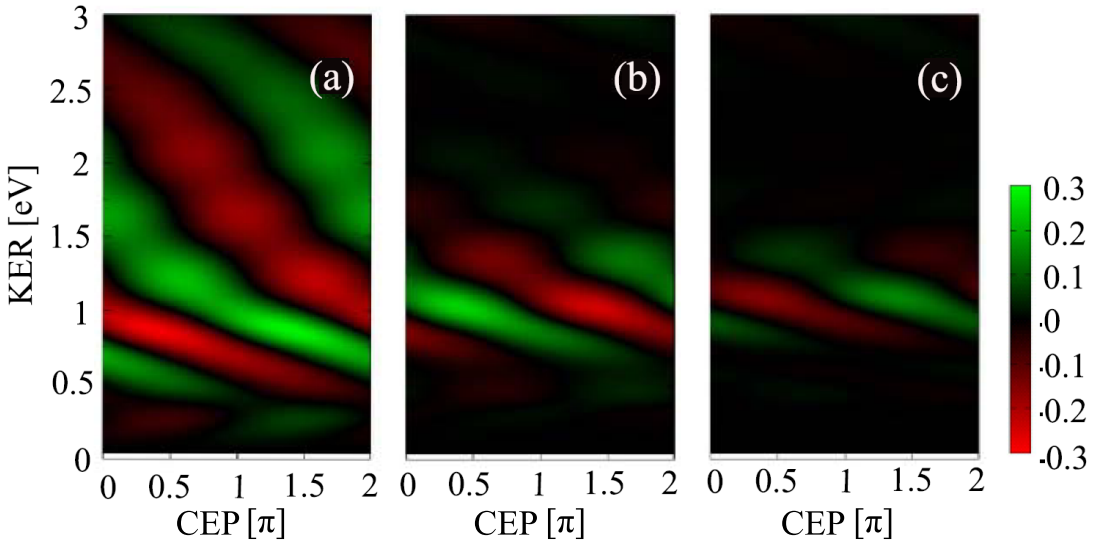

Figure 5.11: Theoretical predictions from [HE09] for the CEP dependent asymmetry in the dissociation of a) H_2^+ b) D_2^+ and c) T_2^+, calculated for a pulse length of 5.9 fs and an intensity of 0.1 PW/cm^2.

by projecting the wave function onto the localized states

$$P_{l,r},(E_k) = |\langle (l,r)E_k|\Psi\rangle|^2 = \frac{1}{2}\left|\sum_{n\,even} e^{in\varphi_{CE}}e^{i\delta_g}\,\langle g\,E_k|\Psi_n\rangle \pm \sum_{n\,odd} e^{in\varphi_{CE}}e^{i\delta_u}\,\langle u\,E_k|\Psi_n\rangle\right|^2 . \quad (5.23)$$

Note that here the gerade state is associated with the net absorption of an even number of photons and the ungerade state with the net absorption of an odd number of photons. This can be understood by considering the fact that due to the dipole selection rules, the state $1s\sigma_g$ with $n = 0$ can couple only to the $2p\sigma_u$ state with $n = \pm 1$ and not to $2p\sigma_u$ with $n = 0$ or $1s\sigma_g$ with $n = \pm 1$. Therefore, the first three states can be treated separately from the last three states. As the initial state is $1s\sigma_g$ with $n = 0$, one can associate the $1s\sigma_g$ state with even photon numbers n, and the $2p\sigma_u$ state with odd n.
The energy dependent asymmetry is then obtained from

$$A(E_k) = P_l(E_k) - P_r(E_k) = 2\sum_{\substack{n\,even\\ n'\,odd}} Re\left(e^{i(n-n')\varphi_{CE}}e^{i(\delta_g-\delta_u)}\,\langle g, E_k|\Psi_n\rangle\,\langle u, E_k|\Psi_{n'}\rangle^*\right). \quad (5.24)$$

From equation (5.24) one can see that for a CEP dependent asymmetry to occur the amplitudes $\langle (g,u), E_k|\Psi_n\rangle$, which differ in the photon numbers n and in the molecular channels (here $1s\sigma_g$ and $2p\sigma_u$), must contribute to the same energy. Thereby, for one of the interfering dissociation channels the net number n of absorbed photons must be even and for the other dissociation channel it must be odd. Therefore, in equation (5.24) $n - n'$ is an even number so that the CEP dependence of the asymmetry contains only contributions with a periodicity of $2\pi/(2m-1)\,(m = 1, 2, 3, ...)$. The energy dependent phase shifts $\delta_{g,u}$ also contribute by an energy dependent phase shift $\delta_g - \delta_u$

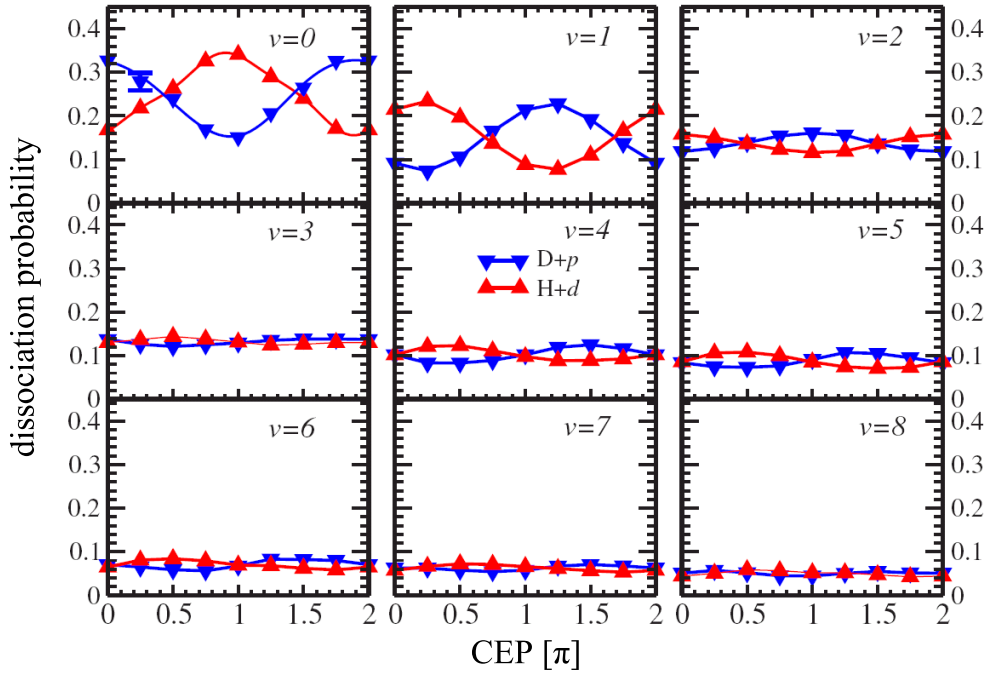

Figure 5.12: CEP dependent dissociation probability of aligned and oriented HD^+ into $H+d$ and $D+p$ for different vibrational states. The calculation was performed by Roudnev et al. [RE07b] for laser pulses with a duration of 7.1 fs and a peak intensity of 0.7 PW/cm^2.

of the asymmetry.

The results of Hua et al. show that the asymmetry is created by the interference of dissociation channels, which differ in the molecular channels and additionally in the net number of photons that were absorbed. An example is the interference of $2p\sigma_u$ with $n = 3$ and $1s\sigma_g$ with $n = 2$. In this case, population is transferred by the absorption of three photons from the $1s\sigma_g$ to the $2p\sigma_u$ state, from which it can dissociate. A part of the population is shuffled back to the $1s\sigma_g$ state by the emission of one photon and dissociates along this potential curve.

The numerically calculated asymmetry for H_2^+, D_2^+ and T_2^+ is displayed in figure 5.11. For protons above 0.3 eV, tilted asymmetry stripes with a periodicity of 2π are observed, which are similar to the ones observed in the experiment. At about 0.3 eV, a phase jump of the asymmetry occurs. Below that energy value only a weak asymmetry is observed. For D_2^+, a significant asymmetry is only observed above about 0.7 eV, below 0.5 eV it vanishes completely.

The theoretical predictions agree qualitatively well with the experimental findings presented above. They show a similar dependence on the KER and also similar differences between H_2^+ and D_2^+. A comparison of the contrast of the asymmetry is, however, not possible as no focal volume averaging was performed in the calculation. In [RE07b], it was shown that the asymmetry shifts with the intensity of the laser pulse and is strongly reduced if the intensity distribution in the focus is taken into account. Besides that, a normalization different from that in equation (5.1) was used to calculate the asymmetry. Furthermore, the calculation was performed for a smaller intensity than the intensity in the experiments.

Although the theoretical predictions of Hua et al. [HE09] are similar to the experimental find-

ings, there are important differences between the system regarded in the simulations and the experimental one. The simulations start already with H_2^+ so that the first ionization step is not taken into account and the molecular ion experiences the whole laser pulse. In the experiment, however, the neutral H_2 molecule is ionized during the pulse so that the first ionization step might play a role for the CEP dependence and the H_2^+ ion is affected only by a part of the pulse. Another important issue is the role of coherence. In the calculations of Esry, an incoherent population of the vibrational states is assumed. Therefore, the CEP dependent dissociation probabilities for each vibrational state are calculated and summed up incoherently weighted by their Franck-Condon factors. The different vibrational states thereby reveal a different dependence on the CEP. This is illustrated in figure 5.12, where for aligned and oriented HD the CEP dependent probability is shown for the electron remaining localized at the hydrogen, so that the dissociation fragments are a neutral H atom and a deuteron d, and for the electron remaining localized at the deuteron, leading to a proton p and a neutral deuterium atom D. Averaging over the vibrational states thus reduces the total asymmetry [RE07b].
By contrast, in the measurements shown here, the vibrational states are populated coherently so that a wave packet is created. One might thus expect a stronger CEP effect for that case.

5.4 Wave packet simulations

In order to test the validity of the localization model presented in section 5.2.2, simulations of the wave packet dynamics were performed. They are based on a simulation program developed by Uwe Thumm, Thomas Niederhausen and Bernold Feuerstein [FER+07, TNF08, NT08], in which the time dependent Schrödinger equation (TDSE) is solved by the Crank-Nicholson split-operator method. For more details of the simulations, see appendix B.

5.4.1 Calculation of the wave packet dynamics

The simulations start with the calculation of the ground state of the neutral H_2 molecule by assuming an arbitrary wave function and propagating it in imaginary time by solving the time dependent Schrödinger equation (B.1). The Schrödinger equation then has the form of a diffusion equation so that the wave function approaches the lowest energy value and thus the ground state of the potential [LTE07]. The molecular axis is assumed to be fixed parallel to the polarization axis z of the electric field. The calculation is reduced to one dimension, i.e. the axis of the molecule.
The wave function is then set into the electronic ground state of H_2^+ in an instantaneous step. In this so-called sudden approximation, the wave function is initially not an eigenfunction of the potential, but it has to adapt to the potential. It can therefore have an overlap with the continuum, which leads to ground state dissociation. Ground state dissociation is not only an artifact of the calculations, but occurs also in the experiment. The reason is that the equilibrium distance of the H_2^+ ground state potential is located at a larger internuclear distance R_0 as compared to the H_2 potential equilibrium distance. A part of the wave function at small R is projected onto a high energy part of the H_2^+ ground state and gains enough energy to escape from the potential. It dissociates with a small KER below $100\,meV$.

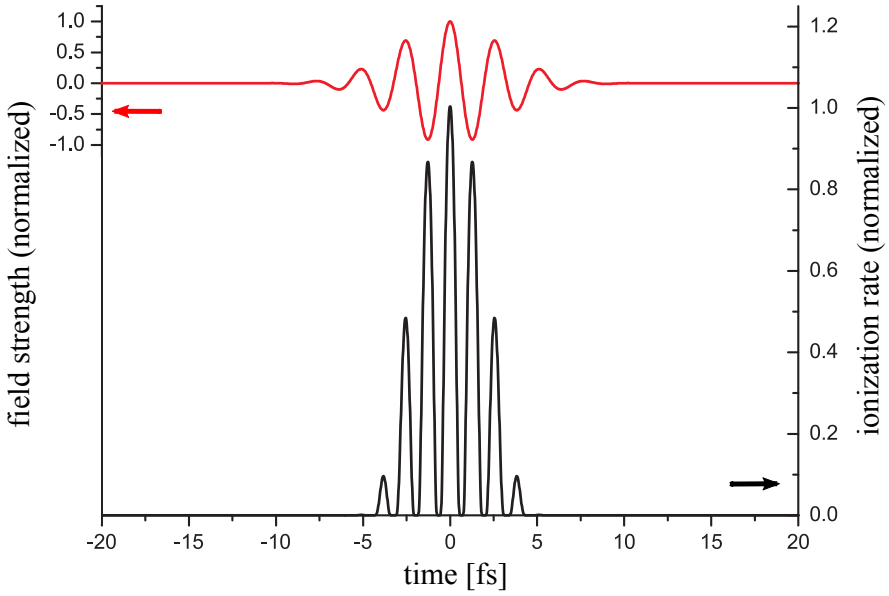

Figure 5.13: ADK ionization probability (black) calculated for the electric field of a Gaussian laser pulse (red) with a pulse duration of 6 fs.

As the wave function is set instantaneously into the H_2^+ ground state, the vibrational states are populated coherently and a nuclear wave packet is formed. The nuclear wave packet is then propagated in the electronic potential curves using equation (5.8). The matrix elements as well as the potential curves in the Schrödinger equation were already determined in earlier calculations and are read from external files.
The ionization of the neutral molecule can occur at any time during the laser pulse, where the field strength is strong enough for ionization. The wave packet created in H_2^+ then interacts only with the rest of the laser pulse. Hence, the laser field, which the wave packet experiences, depends on the time of ionization. Therefore, in order to describe the interaction with the pulse correctly, different ionization times have to be considered. Taking into account all possible ionization times, which would correspond to the blue shaded area in the time-phase diagram in figure 5.14, is, however, not possible with the available computation capacities. Ionization was therefore assumed to occur only at the maxima of the laser field. In figure 5.13, the ADK-ionization-rate (see also chapter 1.1.2)

$$\omega_{ADK}(t) = \frac{4(2I_P)^{5/2}}{\mathcal{E}(t)} e^{-\frac{2(2I_P)^{2/3}}{3\mathcal{E}(t)}} \tag{5.25}$$

calculated for a Gaussian laser pulse with a duration of 6 fs is shown. Only the five most intense field maxima contribute significantly to the ionization rate, the contribution of the other maxima is very small and hence can be neglected. The calculation is thus reduced to the five lines in the time-phase diagram in figure 5.14. For each of the five maxima, the CEP is varied between 0° and 180°[1] in steps of 30°, whereby the start time of the calculation is shifted together with the position of the respective field maximum.

[1]The asymmetry for the other phase values is reconstructed by symmetry considerations.

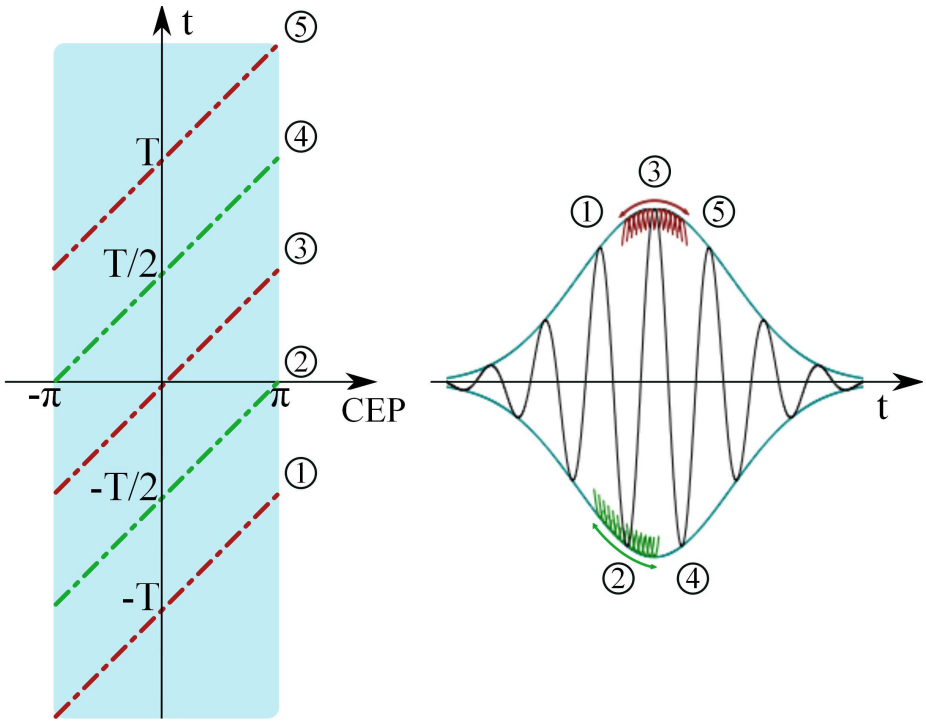

Figure 5.14: Ideally, the wave packet simulations should be performed for all possible CEP values and possible ionization times (blue shades area in left image), which however exceeds the computational capacities. Therefore, only ionization at the five most intense field maxima was considered, reducing the calculation to the red and green lines. The corresponding ionization times dependent on the CEP are illustrated in the right image for maximum 2 and 3 in green and red, respectively.

5.4.2 Results

The localized wave functions $\Psi_l(R,t)$ and $\Psi_r(R,t)$ are calculated from $\Psi_g(R,t)$ and $\Psi_u(R,t)$ using equation (5.4). In order to obtain the KER dependent asymmetry, $\Psi_l(R)$ and $\Psi_r(R)$ are transformed into momentum space by a fast Fourier transform. The KER dependent wave functions are obtained by

$$\Psi_{l,r}(KER, CEP) = \frac{\Psi_{l,r}(p, CEP)}{p}\mu, \tag{5.26}$$

where μ is the reduced mass of the hydrogen molecule and p the momentum. The asymmetry parameter is determined by

$$A(KER, CEP) = \frac{|\Psi_l(KER, CEP)|^2 - |\Psi_r(KER, CEP)|^2}{|\Psi_l(KER, CEP)|^2 + |\Psi_r(KER, CEP)|^2}. \tag{5.27}$$

The KER and CEP dependent probability density $P_{l,r} = |\Psi_{l,r}|^2$ weighted by the ADK-rate for each of the five maxima of the laser field calculated for an intensity of $0.44\,PW/cm^2$ and a pulse duration of $6\,fs$ is shown in figure 5.15 for H_2 and in 5.16 for D_2. One can see that mainly the first

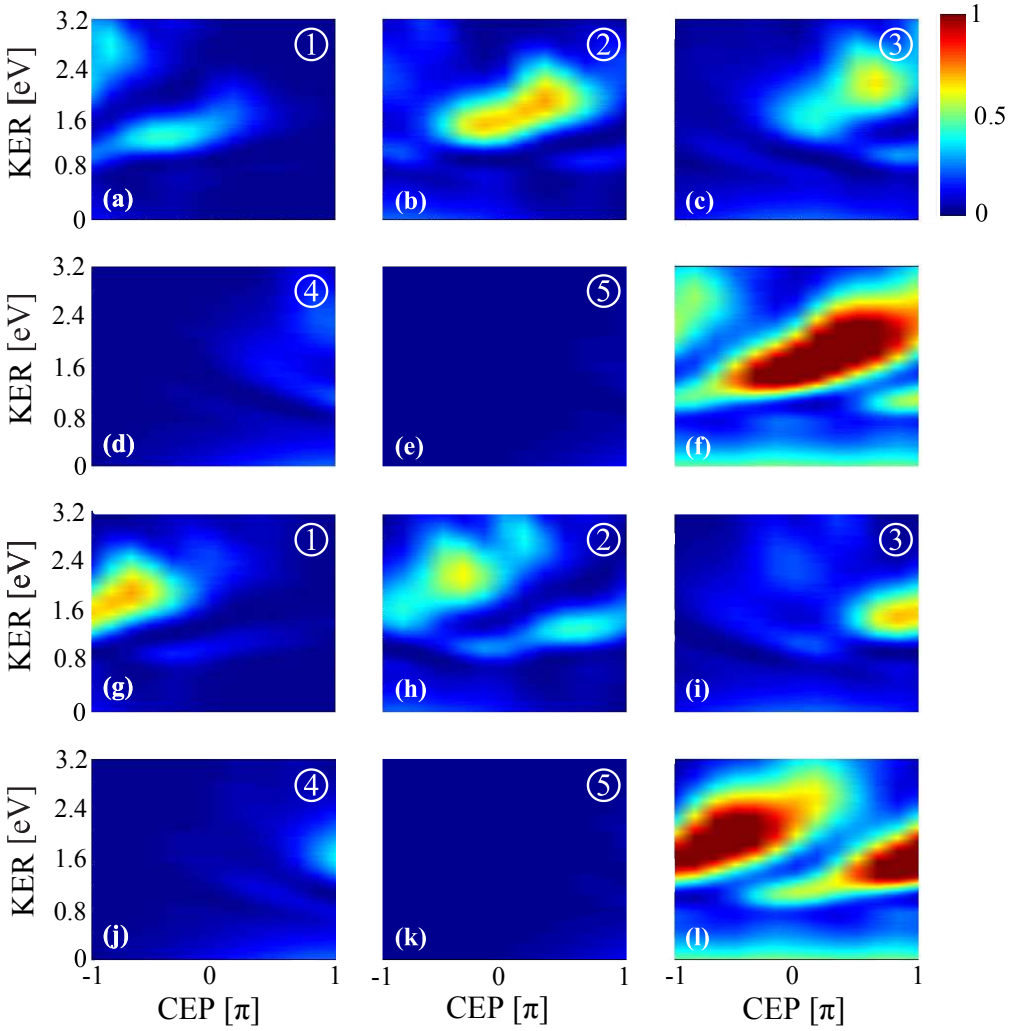

Figure 5.15: For each of the five field maxima of the pulse considered in the calculation, the ADK-weighted probability for the proton to be emitted to the left (image a-e) and to the right (image g-k) is shown. The total probability obtained by adding up incoherently the probabilities of the five field maxima for emission to the left and to the right is shown in images f and l, respectively.

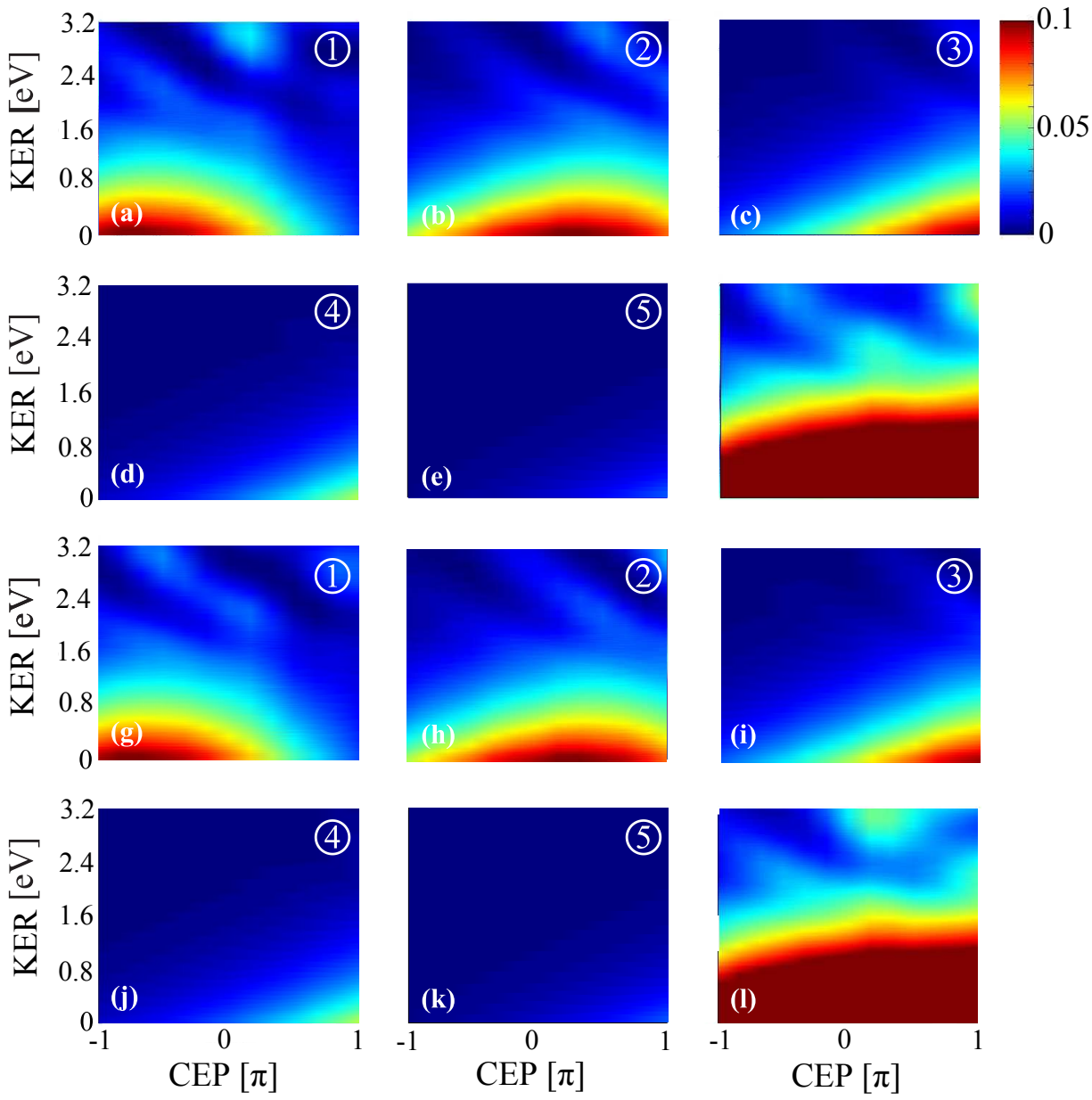

Figure 5.16: Results of the wave packet simulations for the same laser parameters as in figure 5.15 for D_2. The ADK-weighted probability for the deuteron to be emitted to the left is shown in image a-e and to the right in image g-k for the five field maxima. The total probability for the deuteron being emitted to the left or right is shown images f and l, respectively. Compared to H_2 the dissociation due to bond softening is significantly reduced and ground state dissociation, which has a peak at zero energy, dominates.

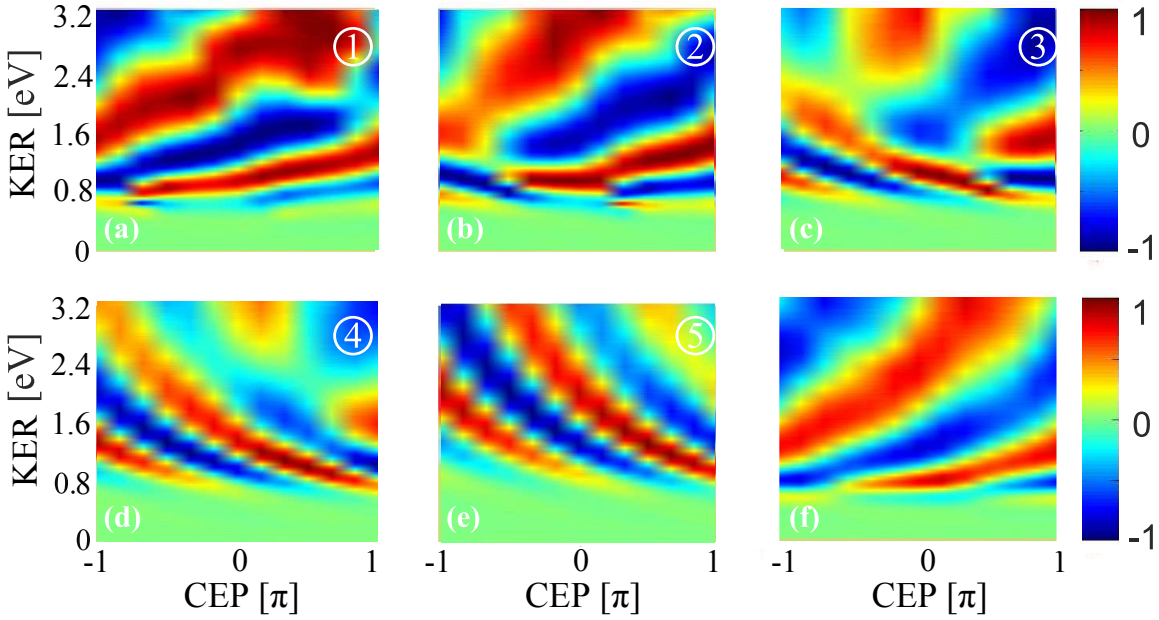

Figure 5.17: The phase and energy dependent asymmetry parameter for each of the five field maxima considered in the wave packet simulations, calculated from the probability distributions shown in figure 5.15 images (a-e) and (g-k). In image (f), the asymmetry parameter for the total dissociation probability is shown (calculated from figure 5.15 images (f) and (l)).

three maxima contribute to the total dissociation yield. One reason is the strong dependence of the ionization rate on the electric field strength taken into account by the ADK-weighting, which lowers the contribution from the outer maxima of the electric field. For asymmetric dissociation to occur, a coupling between the gerade and the ungerade electronic state is required (see chapter 5.2.2). The coupling strength depends on the strength of the electric field at the time the wave packet is in the region, where the energy gap between the electronic states is on the order of the photon energy. For a wave packet starting in field maximum number 1, the field strength in this strong coupling region is still rather high, whereas for field maximum number 5, the field strength of the laser pulse has almost vanished so that the coupling and thus the dissociation probability is low.

The corresponding asymmetry parameter is shown in figure 5.17 for H_2 and in figure 5.18 for D_2. The asymmetry for the first maxima has a periodicity of 2π in the CEP in agreement with the experimental observations. For maximum 4 and 5, also a contribution with a π periodicity is observed, which is probably caused by the interference of dissociation channels which differ in more than one photon as shown in section 5.3. As the dissociation probability for these two maxima is low, this asymmetry structure does not significantly contribute to the total asymmetry.

The total probability distributions $|\Psi_{tot}|^2$ are obtained by adding up the ADK-weighted probability distributions of the five field maxima and are shown in figure 5.15 (f) and (l). The summation has to be incoherent, since the electron is not considered in the calculation and therefore the

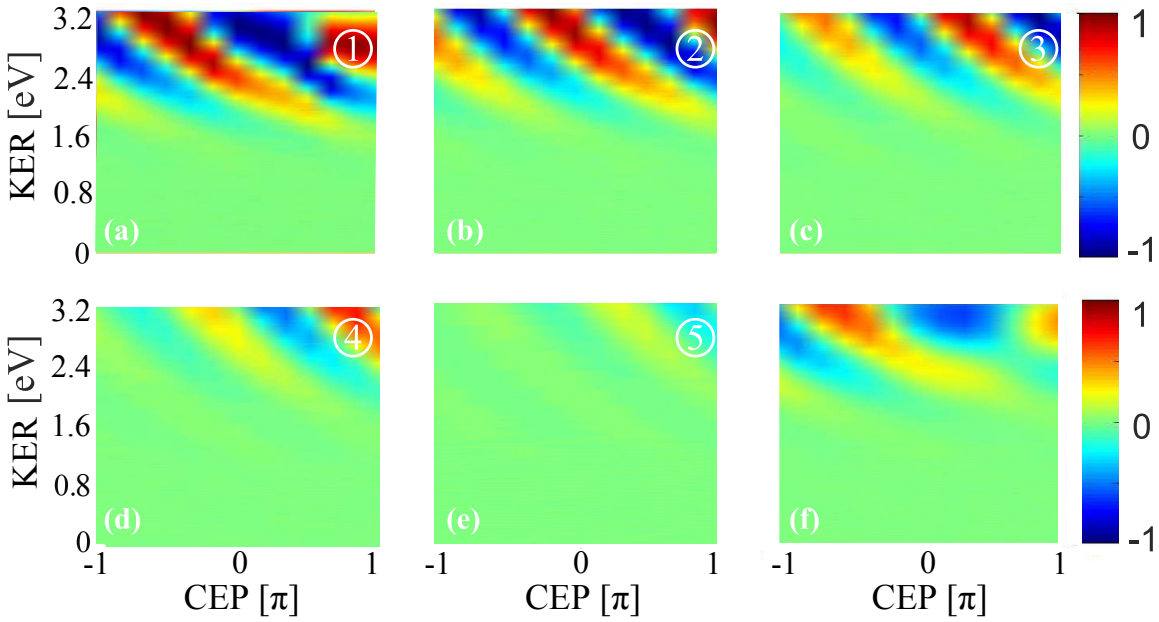

Figure 5.18: The phase and energy dependent asymmetry parameter for each of the five field maxima is shown for D_2. The asymmetry parameter was calculated from the probability distributions shown in figure 5.16, images (a-e) and (g-k). The asymmetry parameter for the total dissociation probability is shown in image e (calculated from figure 5.15 images (f) and (l)).

phases of the nuclear wave functions are not known.
The asymmetry parameter calculated from the total probability distributions is shown in figure 5.19 (a). In figure 5.19 (b), the asymmetry parameter obtained for D_2 for the same pulse parameters is shown. The structure of the asymmetry is in good agreement with the experimental results shown above. The contrast of the asymmetry is higher than in the experiment. The reason is that no focal volume averaging was performed in the calculation.

5.5 Interpretation and discussion

The results of the wave packet simulations are in good agreement with the experimental findings, which confirms the validity of the theoretical model presented in section 5.2.2.
Only the coupling between the gerade $1s\sigma_g$ and the ungerade $2p\sigma_u$ states seems to be responsible for the electron localization. Although a CEP dependent asymmetry in the direction of the emitted electron is observed, it is much smaller than the asymmetry in the proton emission and depends neither on the energy of the electrons, nor on the KER of the protons. Besides that, the simulations reproduce the asymmetry observed in the experiment very well. In these calculations, the electrons were not considered explicitly. An influence of the electron emission direction in the ionization step can thus be excluded from the experimental observations as well as from theory.

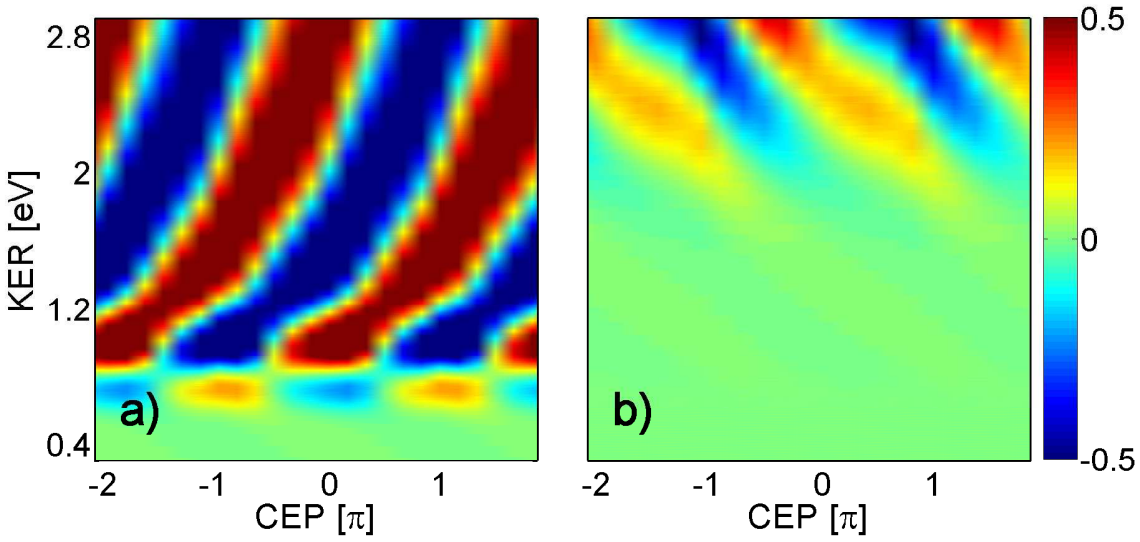

Figure 5.19: Asymmetry parameter obtained from the wave packet simulations for a) H_2 and b) D_2 dependent on CEP and KER.

This means, that the initial asymmetry, i.e. the asymmetry directly after the ionization step, is not responsible for the asymmetry observed in the proton emission. By contrast, for recollision induced dissociation the ionization step was found in [GI07] to play an important role. Here it was shown that the recolliding electron pushes the bound electron to one of the nuclei and thus induces an initial asymmetry. This initial localization of the bound electron is then maintained by the laser field of the pulse during the dissociation process.
The difference between H_2 and D_2 can be also explained within the theoretical model. Due to the larger mass of D_2^+ the wave packet propagates slower and reaches the area of strong coupling later than the wave packet in H_2^+. The nuclear wave packet in H_2^+ needs about $10\,fs$ to reach the $1\,\omega$ crossing. A laser pulse with a peak intensity of $0.44\,PW/cm^2$ and a duration of $6\,fs$ has then decreased to $0.014\,PW/cm^2$. The D_2^+ wave packet needs about $14\,fs$ to reach this internuclear distance. In this case, the laser field has decreased to about $0.003\,PW/cm^2$. The coupling strength for D_2^+ is therefore significantly lower than for H_2^+. Thus, only the high energetic part of the wave packet is fast enough to reach the coupling area when the field strength is still sufficiently high to induce an efficient coupling.
From this model it also becomes clear why there was almost no asymmetry observed for low energetic deuterons in the experiment of Kling et al., who used pulses with a duration of about $5\,fs$ and a lower intensity of $0.1\,PW/cm^2$. In the experiment of Kling et al., the laser pulse has already almost vanished at the time when the wave packet reaches the area, where the laser field can induce efficient coupling so that the dipole coupling is weak. By contrast, a wave packet, which was projected onto the $2p\sigma_u$ curve by recollision, slides down the potential curve in only about $5\,fs$. Therefore, it experiences a sufficient coupling by the laser pulse, which leads to the observed asymmetry for high KERs.
In the calculations carried out in the course of this thesis, the wave packets launched at the

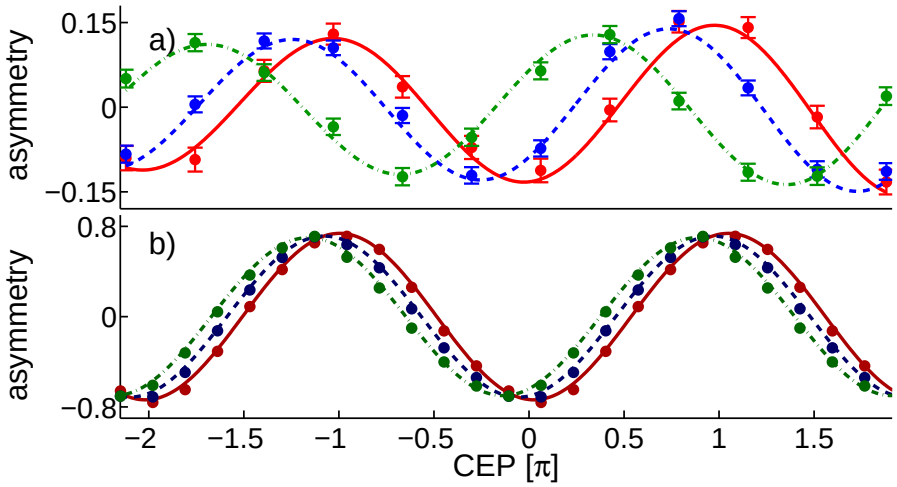

Figure 5.20: a) Measured asymmetry parameter in the KER range between 1.4 and 1.6 eV (range marked by dashed white lines in figure 5.3 (c) for an emission angle α of $0° - 10°$ (red solid line), $10° - 20°$ (blue dashed line) and $20° - 30°$ (green dashed-dotted line). b) Asymmetry parameter obtained from the wave packet simulations for a peak intensity of $I = 0.44\,PW/cm^2$ (red solid line), $I = 0.41\,PW/cm^2$ (blue dashed line) and $I = 0.36\,PW/cm^2$ (green dashed-dotted line). The phase scale for the experimental data was chosen such that the asymmetry between $0°-10°$ agrees with the one of the simulations for $I = 0.44\,PW/cm^2$.

different field maxima of the laser pulse were added up incoherently. An incoherent summation was necessary as the wave function of the emitted electron was not considered so that its phase and therefore also the phase of the nuclear wave packets is not known[2]. This simplification is justified by the good agreement between theory and experiment and the fact that there is no connection between the proton asymmetry and the momentum of the electron.
In the experimental results, a shift of the asymmetry with the emission angle of the protons was observed. Since the coupling strength between the gerade and ungerade state is dependent on the component of the electric field parallel to the molecular axis, the effective coupling strength in case of an angle α between the molecular axis and the polarization direction is proportional to $\mathcal{E}_{eff}(t) = \mathcal{E}(t)\,cos(\alpha)$. This means that the effective intensity for an angle α is $I_{eff} = I_0\,cos^2(\alpha)$. In figure 5.20 (b), the asymmetry calculated for an effective intensity of $0.41\,PW/cm^2$ ($\alpha = 15°$) and $0.36\,PW/cm^2$ ($\alpha = 25°$) is shown. A shift of the asymmetry dependent on the effective intensity is observed, which is qualitatively in accordance with the shift observed in the experiment for the corresponding angles shown in figure 5.20 (a). The slight decrease of the asymmetry can be attributed to the decrease of the effective coupling strength with increasing angle. The reason for the quantitative difference in the shift of the asymmetry is probably the negligence of the

[2] The phase of the electron can generally not be determined from its momentum as was shown in a recent experiment [GSM+09, Gop09]. The probability of measuring a certain electron momentum can be interpreted as an interference between at least two wave packets, which were launched at two different times, which are symmetric to a zero crossing of the field.

molecular rotation in the simulations. It was already shown in earlier measurements that not only a vibrational, but also a rotational wave packet is created in H_2^+ [Erg06]. In classical terms, the laser pulse imparts a 'kick' to the molecule, which leads to a rotation of the molecular axis towards the laser polarization axis [SS03]. This causes the measured angular distribution to be more narrow than the actual one during interaction with the laser pulse [ACE09]. So, the real effective emission angles may be smaller than the angles considered in the calculation. In order to clarify this point, a calculation including the rotational dynamics is necessary. The calculated shift of the asymmetry is also in qualitative agreement with the intensity dependent shift observed in the experiment, but as already explained, a quantitative comparison is not possible.
The phase and energy dependence of the asymmetry can be interpreted within the Floquet representation of Hua and Esry [HE09] presented in section 5.3. The 2π periodicity of the asymmetry indicates that mainly dissociation channels which differ by the net absorption of one photon contribute to the asymmetry. The tilt of the asymmetry stripes can be attributed to the energy dependence of the relative phase of the interfering wave packets. The latter will be discussed in more detail in the next chapter.
By comparing the results of the wave packet simulations to the predictions by Hua and Esry [HE09], one can see that the shape of the asymmetry stripes slightly differs, which is probably caused by the differences in the regarded systems. An interesting question which arises is, which role coherence plays for electron localization. Unfortunately, a quantitative comparison of the asymmetry contrast between the calculations of Hua and Esry, which assume an incoherent wave packet, and the simulations for a coherent one is not possible due to differences in the normalization. The role of coherence can be investigated by two-pulse measurements in the wave packet revival and the dephasing region, which are presented in the following chapter.

Chapter 6

Phase-stable two-pulse measurements

In the previous chapter, it was shown that the electronic motion in dissociating H_2^+ can be steered by the carrier-envelope phase such that the electron remains predominantly localized at one of the protons after the dissociation. This can be observed in the experiment as a CEP dependent asymmetry in the emission direction of the proton.
In these experiments, the creation of the nuclear wave packet and the CEP dependent localization of the electron are both induced by the same laser pulse. Thus, the question arises whether more control can be achieved by separating these two steps by using a two-pulse scheme. The first 'pump' pulse ionizes the H_2 molecule and thereby creates a nuclear wave packet in H_2^+, which then evolves in the ground state potential well. As shown in section 1.5, the wave packet undergoes dephasings and revivals during its evolution. A second CEP-stabilized 'control' pulse applied after a variable time delay induces dissociation and electron localization. If the second laser pulse is applied in the revival, the dependency of the asymmetry on the motion of the nuclear wave packet can be analyzed. Furthermore, by comparing the asymmetry in the revival, where the nuclear wave packet is well localized, with the asymmetry in the dephasing, where the nuclear wave packet is spread over the potential well, the role of coherence can be studied.
In the framework of this thesis, the first pump-control measurements of that kind have been performed demonstrating that the shape and the motion of the nuclear wave packet can be used as further control parameters for electron localization. Wave packet simulations were carried out and the results were compared to the experimental data. This made it possible to relate the observed delay dependent asymmetry to the shape and dynamics of the nuclear wave packet.
In the course of this chapter, atomic units are used unless otherwise noted.

6.1 Measurement of the wave packet evolution in H_2^+

The evolution of the nuclear wave packet in H_2^+ can be investigated by using two ultrashort laser pulses. Such a pump-probe scheme is illustrated schematically in figure 6.1. The first pulse ionizes the neutral H_2 molecule and creates a wave packet in H_2^+. The wave packet is probed by a second laser pulse, which is applied after a variable time delay and induces dissociation or double ionization. The energy spectrum of the fragments reveals information on the wave packet at the time the probe pulse is applied. Some important features and results of the two-pulse measurements on electron localization presented in this chapter can be understood on the basis

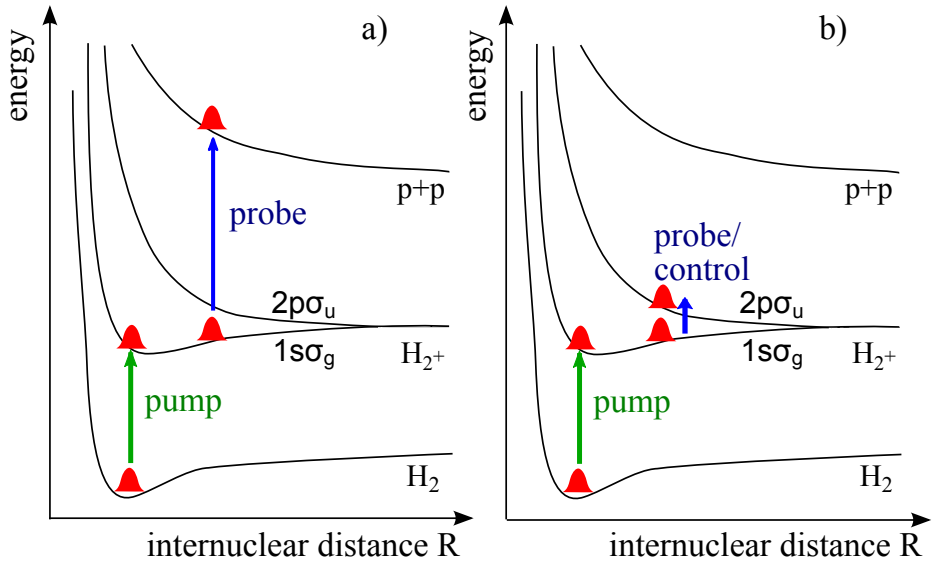

Figure 6.1: Schematic illustration of the pump-probe scheme. A first pump pulse ionizes the neutral H_2 molecule and creates a wave packet in H_2^+. A second laser pulse, which is applied after a variable time delay, induces either Coulomb explosion as shown in a) or dissociation as illustrated in b). Both fragmentation channels can be used to probe the wave packet evolution. The scheme shown in b) is also used in the pump-control measurements, where the CEP-stabilized control pulse induces dissociation and additionally a CEP dependent electron localization.

of pump-probe measurements on H_2.
In this section, some general features of pump-probe measurements are discussed. Information on the wave packet can be gained from the fragments, which originate from dissociation in the second pulse or the ones emerging from Coulomb explosion in the second pulse. These two fragmentation channels are discussed afterwards. Finally, the time of flight spectrum obtained for perpendicular polarization of the two laser pulses is presented. In this case, it is possible to distinguish between the fragments dissociating in the first and in the second pulse as is required for the measurements on electron localization.

6.1.1 General considerations

The temporal resolution of pump-probe measurements is mainly determined by the duration of the probe pulse. For measuring the oscillation of the bound wave packet in H_2^+, which has a vibrational period of about $17\,fs$, a good resolution can be achieved by using pulses with a duration of about $6\,fs$ [ERF$^+$05, ERF$^+$06a, ERF$^+$06b]. The length of the pump pulse also plays an important role as it determines the time window, in which the creation of the wave packet in H_2^+ can occur. In figure 6.2 (a), the temporal evolution of the probability density of the bound wave packet obtained by a wave packet calculation is shown. In this calculation, the wave packet was created by projecting the ground state wave function of H_2 onto the ground state potential of H_2^+ in an instantaneous step. In an experiment, however, the creation of the wave packet can

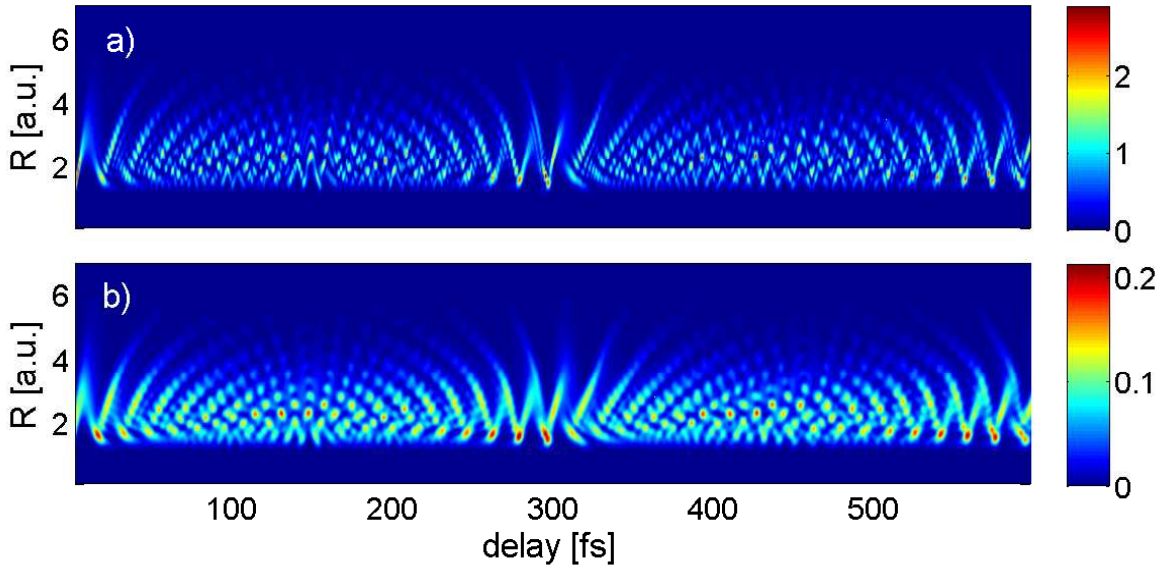

Figure 6.2: a) Calculated probability density of the bound nuclear wave packet in H_2^+ as a function of time after generation of the wave packet and internuclear distance. b) In order to illustrate the effect of the different possible ionization times in the probe pulse, the probability density from a) was weighted with the ADK-rate calculated for the five most pronounced maxima of a $6\,fs$ laser pulse. The obtained spectra were added incoherently with a shift relative to each other corresponding to the time difference between the field maxima.

occur at all times when the intensity of the laser pulse is high enough to ionize the H_2 molecule. The effect of a finite length of the pump pulse on the temporal evolution is illustrated in figure 6.2 (b). Here it was assumed that ionization can occur at the five most prominent field maxima of a $6\,fs$ pump pulse (see also section 5.4.1). The probability density distributions for the five maxima weighted by the corresponding ADK-rates were summed up incoherently[1]. One can see that fine structures of the probability density are washed out. Simulations performed by considering a fixed ionization time therefore might contain more structure than can be observed in the experiment. For this reason, in the simulations presented in this chapter, different possible start times were considered in order to improve the agreement between theory and experiment.
The revival times measured by pump-probe experiments were shown to deviate from the ones predicted by the simulations shown in figure 6.2 [REF$^+$06]. One reason for this discrepancy is that in the calculation the population of the vibrational states was assumed to be Franck-Condon like. However, the R dependence of the ionization probability leads to a stronger weighting of the lower lying vibrational states as discussed in section 1.3. In wave packet simulations for D_2 [Nie07], the time of the half-revival was shown to shift from $560\,fs$ for a Franck-Condon distribution to $540\,fs$ for assuming an R dependent ionization probability[2]. The revival time measured

[1]The summation is incoherent as the phases of the electronic part of the wave functions are not known.
[2]Calculation performed for a $6\,fs$ pulse with a peak intensity of $0.3\,PW/cm^2$.

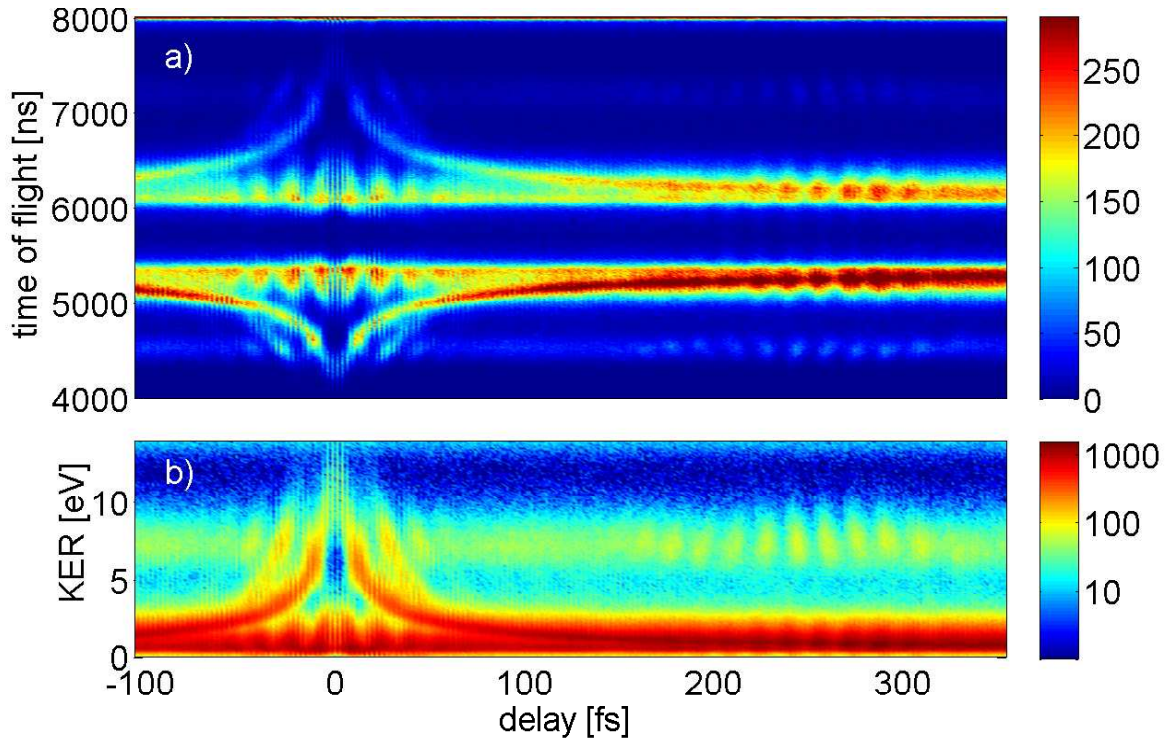

Figure 6.3: a) Proton spectrum obtained from a pump-probe measurement on H_2 with two $6\,fs$ laser pulses with equal intensity of about $0.4\,PW/cm^2$. The polarization axis of both pulses was parallel to the spectrometer axis. The time of flight of the protons is plotted versus the time delay between the two laser pulses. b) Corresponding delay dependent energy spectrum.

in experiments may be also influenced by post-pulses or a pedestal of the probe pulse. For example, a long pedestal was shown to shift the half-revival of D_2 further towards smaller times [Nie07]. As the pulse shape may vary after each realignment of the laser system, the observed revival time can change between different measurements. This effect is observed in the two-pulse measurements presented in this chapter.

6.1.2 Probing by Coulomb explosion

The wave packet evolution in H_2^+ can be probed by Coulomb explosion as illustrated in figure 6.1 (a). The first pulse ionizes the H_2 molecule and thereby launches a wave packet in the $1s\sigma_g$ state of H_2^+. After a variable time delay τ, the H_2^+ molecule is further ionized by the probe pulse. Thereby, the wave packet is projected in a vertical transition onto the repulsive Coulomb curve (see figure 6.1 (a)). The kinetic energy release of the protons is composed of the kinetic energy of the bound or dissociating wave packet E_{kin} at the moment of explosion and the Coulomb energy. The latter depends on the internuclear distance at the time τ. The kinetic energy release E_k is

given by

$$E_k(\tau) = E_{kin} + \frac{1}{R(\tau)}. \tag{6.1}$$

Thus, from the kinetic energy release of the fragments at the time delay τ the internuclear distance, where the nuclear wave packet is localized, can be reconstructed[3]. This allows for a mapping of the temporal evolution of the wave packet.
If the probe pulse is sufficiently strong, the whole wave packet is transferred to the Coulomb curve. Probing the wave packet by Coulomb explosion therefore, in principle, allows for the mapping of the whole wave packet. A high intensity of the probe pulse, however, increases the effective ionization window and thus lowers the temporal resolution. Besides that, it leads to a large amount of fragments which are created by double ionization in the probe pulse alone. They provide a delay independent background reducing the contrast of the measurement. Therefore, in pump-probe measurements often the intensity of the second pulse is chosen to be the same or only moderately stronger than the intensity of the first pulse [REF$^+$06].
For moderate intensities, the R dependence of the ionization probability plays an important role. As already discussed in section 1.3, the ionization probability depends on the ionization potential $I_p(R)$. Therefore, the probability for Coulomb explosion is significantly reduced for small R compared to large R. Thus, the contribution of the inner region of the potential well and thus of high energetic protons to the energy spectra is strongly suppressed.
In figure 6.3 (a), the time of flight spectrum of protons dependent on the delay is shown for a pump-probe measurement with two pulses, both having an intensity of $0.4\,PW/cm^2$. The polarization of the two pulses was parallel to the spectrometer axis. The spectrum is approximately mirror symmetric relative to a time of flight of $t_0 = 5700\,ns$, which corresponds to the time of flight for protons with zero initial energy. Protons with $t < t_0$ were emitted towards the ion detector, those with $t > t_0$ away from the ion detector.
The corresponding energy spectrum is shown in figure 6.3 (b). The KER of the protons created by Coulomb explosion lies between approximately 5 and $12\,eV$. A band can be observed, which ranges up to $12\,eV$ at zero delay and decreases to low energies for increasing delay. This band originates from delayed ionization. Hereby, the neutral H_2 is ionized in the first pulse and the created H_2^+ ion dissociates due to bond softening, i.e. the wave packet propagates towards large R. Therefore, with increasing delay the internuclear distance, at which the wave packet is projected onto the Coulomb curve by the second pulse, increases. Thus, the Coulomb energy decreases with the delay and the energy of the protons converges to the dissociation energy (see equation (6.1)).
At larger delays in figure 6.3, further structure can be observed in the Coulomb explosion channel. This structure originates from the wave packet, that remains bound after the creation of H_2^+ in the first pulse and is probed in the second pulse. The observed stripes occur at a distance of about $17\,fs$ and reflect the oscillation of the bound wave packet in H_2^+. They reach from high to low energies, which corresponds to the motion of the wave packet from small towards large R (see figure 6.1). The motion from large to small R cannot be observed. This can be explained by the anharmonicity of the potential, which introduces dispersion and thus influences the rel-

[3]For a bound wave packet, the energy E_{kin} is not known. For a reconstruction of the wave packet dynamics, it is sufficient to consider only the Coulomb energy as it is significantly larger than E_{kin}. In case of a dissociating wave packet, the energy E_{kin} corresponds to the dissociation energy, which can be obtained from single-pulse measurements.

ative phase of the vibrational states. At each reflection on the potential wall, the wave packet experiences dispersion due to the anharmonicity. As compared to a harmonic potential, the $1s\sigma_g$ potential is steeper at the inner turning point and more flat at the outer turning point. Therefore, compared to a harmonic potential, the upper vibrational states are reflected at the outer turning point later and at the inner turning point earlier than the lower ones [Erg06]. Thus, the upper states experience a negative phase shift at the inner turning point and a positive phase shift at the outer turning point relative to the lower vibrational states. Reflection at the outer turning point leads to a broadening of the wave packet, which is partially compensated after reflection at the inner turning point. As the count rate is determined by the convolution of the ionization probability and the density of the wave packet, the motion from the outer to the inner turning point cannot be observed in the measurement. The phase shifts at the inner and outer turning point do not compensate each other completely, which leads to the dephasing of the wave packet with increasing delay resulting in a washing out and finally vanishing of the stripes. After about $270\,fs$, the stripes appear again, but with inverted slope. With increasing delay, the slope of the stripes slowly reverses. The reason is that the relative phase between the vibrational states is more and more shifted in one direction until the wave packet dephases. The phase keeps shifting in the same direction when the wave packet is re-built, which can be regarded as a time reversal. Therefore, at the beginning of the revival, the wave packet is localized during its inward motion. After some time, the tilt of the stripes reverses and the wave packet dephases again.

6.1.3 Probing by dissociation

For the laser intensities used in the measurements presented in this chapter, dissociation dominates over Coulomb explosion. Dissociation can be also used to probe the wave packet dynamics. Thereby, the H_2 molecule is ionized in the pump pulse and the probe pulse induces dissociation of H_2^+ by coupling the $1s\sigma_g$ to the $2p\sigma_u$ state. The strength of the coupling is proportional to the square root of the intensity and can occur across the whole spectral bandwidth of the laser pulse (see section 1.4.1). If the coupling is sufficiently strong, a part of the wave packet is transferred to the $2p\sigma_u$ state, from which it can dissociate. A part of the population can be transferred back to the $1s\sigma_g$ state and can dissociate along this potential curve in case it has gained enough energy by sliding down the $2p\sigma_u$ before being transferred back (see also section 5.2.2). The dissociation process can be also understood in terms of the Floquet model as bond softening (see section 1.4). The dissociation can occur either via the 1ω or the 2ω channel.
The kinetic energy release depends on the number and wavelength of the absorbed photons as well as on the energy of the vibrational states (see equation 1.28). As the coupling between the $1s\sigma_g$ and the $2p\sigma_u$ state is efficient only at large internuclear distances, only the part of the wave packet near the outer turning point can be probed by dissociation. In the energy spectrum shown in figure 6.3, the protons emerging from dissociation are observed between 0 and $3\,eV$. At small delays, a strong variation of the count rate with the delay can be observed. It results from the oscillatory motion of the wave packet launched in the first pulse and probed in the second pulse. This fragmentation channel leads also to the modulation of the dissociation rate in the revival.

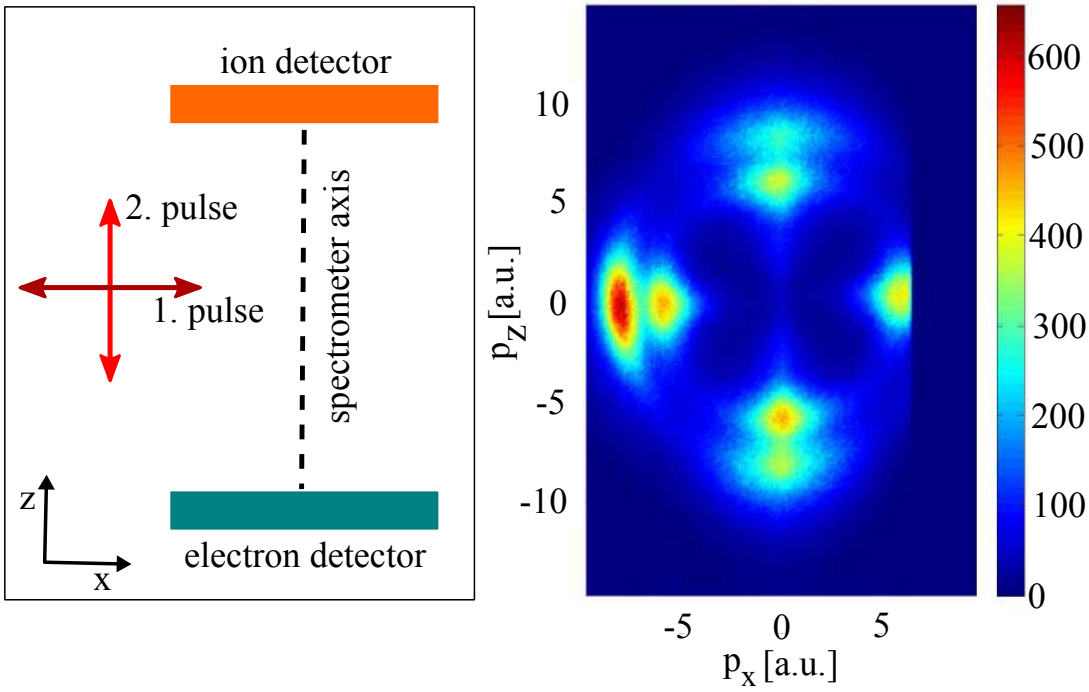

Figure 6.4: Left: In order to separate the protons emerging from dissociation in the first and in the second laser pulse, the two laser pulses were polarized perpendicular to each other. The first pulse is polarized perpendicular and the second pulse parallel to the spectrometer axis. Right: Momentum of the protons in the plane spanned by the polarization axes of the laser pulses. Only the protons emitted parallel to the spectrometer axis, i.e. in z-direction, are of interest in the measurements on electron localization as they emerge from dissociation in the second pulse. (The momentum distribution corresponds to the measurement presented in section 6.2.1. The momentum distribution is cut at the right side as not all protons emitted perpendicular to the spectrometer axis hit the detector.)

6.1.4 Pulses with perpendicular polarization

In the measurements presented in this chapter, the dependence of electron localization on the wave packet dynamics was investigated. Therefore, the first pulse should only induce ionization and dissociation should occur via the second pulse. A significant fraction of the molecules, however, dissociates already in the first pulse. For parallel polarization of the laser pulses, the fragments from the first and the second pulse cannot be separated from each other, which reduces the contrast of delay dependent processes.
As discussed in section 1.4.4, the protons emerging from dissociation are mainly emitted with a small angle relative to the laser polarization axis. In order to be able to separate the dissociation fragments from the first and the second pulse from each other, it is therefore useful to use laser pulses with perpendicular polarization [CBNW09].
The polarization axis of the first pulse was set perpendicular to the spectrometer axis as illustrated on the left side of figure 6.4 by using a half-wave plate. The polarization axis of the second

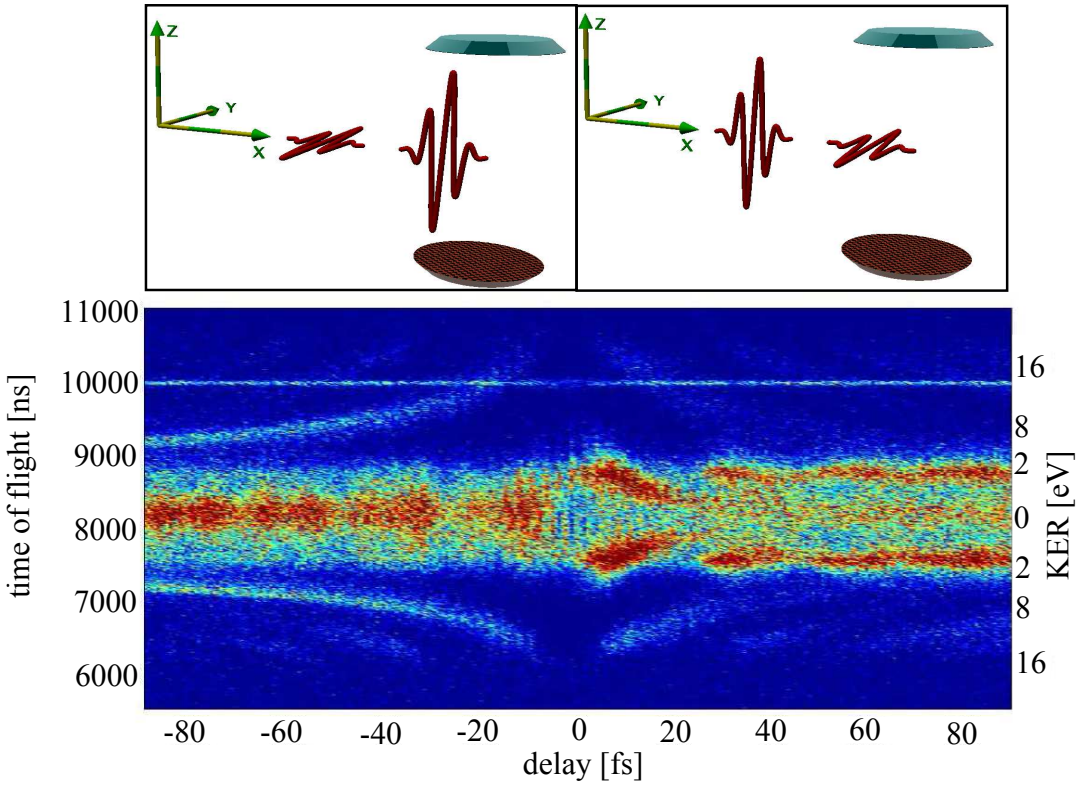

Figure 6.5: Time of flight spectrum for perpendicularly polarized laser pulses, both with an intensity of about $0.4\,PW/cm^2$. For positive delays, the second pulse is polarized parallel and for negative delays it is polarized perpendicular to the spectrometer axis. On the right side, the corresponding energy scale for fragments, which have zero initial momentum perpendicular to the spectrometer axis, is shown. For the measurement, D_2 was used as the temporal evolution can be observed somewhat more clear than for H_2. (The line at a time of flight of about $10000\,ns$ is formed by H_2^+, which originates from the residual gas.)

pulse was kept parallel to the spectrometer axis.
On the right side of figure 6.4 a typical momentum distribution of the protons in the plane spanned by the polarization axes of the laser pulses is shown. The protons from dissociation in the first and the second pulse are emitted perpendicular to each other and can therefore be easily separated by setting a condition on the emission angle. For the measurements on electron localization, ionization should occur in the first and dissociation in the second pulse. The protons created by this fragmentation channel originate from molecules, for which the molecular axis has a small angle relative to the polarization axis of the second pulse. The reason is that single ionization is rather independent of the molecular orientation, whereas dissociation is strongly angle dependent (see section 1.4.4). The rotation of the molecule during the delay between the first pulse and the second pulse can be neglected for the measurements presented here [ACE09].
In figure 6.5, the time of flight spectrum for perpendicularly polarized laser pulses is shown. On the left side of the spectrum (negative delays), the first laser pulse was polarized parallel and the second pulse perpendicular to the spectrometer axis (opposite case as in figure 6.4). For the high

energetic protons emerging from Coulomb explosion, delayed ionization can be observed. Here the first pulse ionizes the molecule and induces dissociation, whereby the dissociation fragments propagate parallel to the spectrometer axis. The second pulse further ionizes the H_2^+ ion, which leads to Coulomb explosion. The vibrational motion of the bound wave packet can be observed, too. Thereby, the first pulse launches a wave packet in H_2^+ and the second pulse probes the wave packet by further ionization. At low energies around a time of flight of about $7500\,ns$ and $8500\,ns$, the protons created by dissociation in the first pulse and thus emitted parallel to the spectrometer axis can be observed. The protons which are created by dissociation in the second pulse are emitted perpendicular to the spectrometer axis. Their momentum parallel to the spectrometer axis is around zero so that they contribute to the stripe at $8100\,ns$.
For positive delays, the pulse perpendicular to the spectrometer axis comes first (see also figure 6.4). Delayed ionization cannot be observed as the protons, which dissociate in the first pulse, are emitted perpendicular to the spectrometer axis and thus contribute to the stripe around $8100\,ns$. The vibrational motion of the bound wave packet, however, can be observed in the Coulomb explosion channel as the single ionization step is only weakly depending on the polarization direction. For dissociation in the first pulse, the protons are emitted perpendicular to the spectrometer axis and thus contribute to the stripe at $8100\,ns$. The protons created by ionization in the first and dissociation in the second pulse are emitted parallel to the spectrometer axis and can be observed around $1.5\,eV$ (7500 and $8500\,eV$). In this channel, a delay dependent modulation of the count rate can be observed, which originates from the vibrational motion of the bound wave packet. Those are the protons, which are of interest in the measurements presented in the following section. The intensities of the pulses were chosen to be similar to each other, with the first pulse being slightly stronger than the second one. In this way, the count rate in the desired channel was optimized and at the same time the probability for ionization and dissociation in the second pulse alone was reduced.

6.2 Pump-control measurements on H_2

For analyzing the dependence of electron localization on the dynamics and shape of the nuclear wave packet, a two-pulse scheme with two CEP-stabilized laser pulses was used. The first 'pump' pulse ionizes the neutral H_2 molecule and the second CEP-stabilized 'control' pulse induces dissociation[4] and electron localization after a variable time delay. In order to separate the dissociation events in the first and the second pulse, the two laser pulses were polarized perpendicular to each other as shown in figure 6.4.
The carrier-envelope phase of the laser pulses was stabilized as described in chapter 3. The CEP-stabilized laser pulses were split into two identical copies by using the Mach-Zehnder interferometer described in section 2.3. The intensities of the pump and the control pulse were adjusted independently from each other by apertures, which were placed in the two interferometer arms. The polarization axis in one interferometer arm was rotated by 90° by using a half-wave plate. Only the protons with an emission angle between 0° and 30° relative to the spectrometer axis were considered in the data analysis, which are the protons created by dissociation in the control pulse. The intensities of the two laser pulses were optimized such that the probability

[4]Coulomb explosion is not considered further in this chapter as here two protons are emitted so that no CEP or delay dependent asymmetry can be observed.

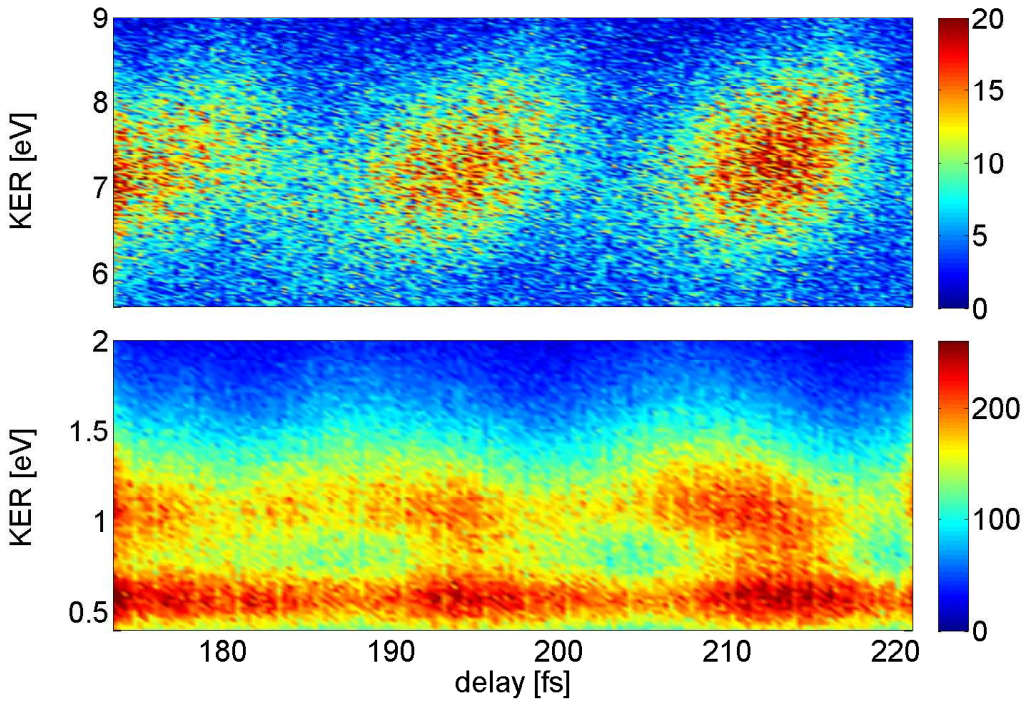

Figure 6.6: Proton count rate as a function of the kinetic energy release and the delay for the pump-control measurement in the revival. Only the protons emitted between 0 and 30° relative to the spectrometer axis are shown. In the lower image, the protons emerging from bond softening and in the upper image the protons created by Coulomb explosion are shown. In both fragmentation channels, a pronounced delay dependence can be observed.

for the desired fragmentation channel, i.e. ionization in the first and dissociation in the second pulse, was maximized. The intensity of the first pulse was chosen to be about $0.42\,PW/cm^2$ and of the second pulse to be about $0.4\,PW/cm^2$.
The carrier-envelope phase was scanned many times over a range of approximately 4π and at the same time the delay between the two laser pulses was scanned back and forth. In this way, possible temporal drifts of the laser pulse properties could not manifest in a systematic phase or delay dependence.
Such measurements are experimentally very challenging as not only the CEP, but also the delay is scanned. Therefore, for achieving sufficient statistics, long measurement times are required. In the course of this thesis, the stability of the laser system and the phase-stabilization could be significantly enhanced. The scans over a delay of about $100\,fs$, for example, required measurement times of about one day, which reaches the limit of what is possible with the current phase-stabilization methods. Therefore, in order to analyze the dependence of the asymmetry on the wave packet evolution, independent measurements in three delay regions were performed in the revival[5], the dephasing and the transition region between them. The results of these

[5]For the pump-control measurements and simulations presented in this chapter, the term revival refers to the half-revival of H_2^+.

measurements are presented in the following.

6.2.1 Revival

In the revival region, the nuclear wave packet is well localized and oscillates in the $1s\sigma_g$ potential of the H_2^+ molecule. Here the influence of the position and momentum of the wave packet on electron localization can be analyzed. A measurement at the beginning of the wave packet evolution, where the wave packet has not yet dephased, is less suited as the two laser pulses temporally overlap.
In figure 6.6, the proton count rate for the measurement in the revival is shown as a function of KER and delay. Only the protons emitted with an emission angle between 0° and 30° relative to the polarization axis of the control pulse are considered. In the upper image, the high energetic protons emerging from Coulomb explosion are shown. Here the spectrum reveals a typical structure resulting from the oscillatory motion of the wave packet close to the center of the revival. Note that the delay, at which the revival occurs, is not the same as in figure 6.3 due to differences in the pulse properties (see section 6.1.1).
In the bond softening regime shown in the lower image of figure 6.3, two energy ranges can be distinguished, the one centered at about $0.6\,eV$ corresponding to the $1\,\omega$ and the one around $1\,eV$ to the $2\,\omega$ dissociation channel. Note that the energy ranges of the two dissociation channels overlap as discussed in section 1.4.1 and 5.1. In both dissociation channels, a modulation of the dissociation rate with a periodicity of about $17\,fs$ can be observed, which can be attributed to the vibrational motion of the wave packet.
In order to determine the delay dependent asymmetry parameter, the delay range was divided into slices of $3\,fs$. For each of these slices, the KER and CEP dependent count rate for protons being emitted to the left $N_l(KER, CEP)$ and to the right $N_r(KER, CEP)$ with an emission angle between 0° and 30° relative to the spectrometer axis was determined. Thereby, a bin size of $0.2\,eV$ along the KER axis and a bin size of about $0.7\,rad$ along the CEP axis was chosen. For each KER-CEP-bin, the asymmetry parameter was calculated by using equation (5.1). A sinusoidal function of the form $f = a\sin(\varphi_{CE} + \phi)$ was fitted on the experimentally observed asymmetry for each KER range. The amplitude a and the position along the CEP axis ϕ were the fit parameters. This was done in order to enhance the visibility[6] of the asymmetry structure. Examples of the obtained KER and CEP dependent asymmetry for different delays are shown in figure 6.7. For all delays, a KER dependent asymmetry pattern can be observed, which reveals a 2π-periodicity in the CEP. For some delay ranges, like for example 189-192 fs or 210-213 fs, the asymmetry above $1\,eV$ reveals a similar strength and KER dependence as in the single-pulse measurements. Below $1\,eV$, the asymmetry becomes significantly weaker and the tilt of the asymmetry stripes, i.e. the KER dependence, reverses its direction. This indicates that the strength and shape of the asymmetry depends on whether the 1ω or the 2ω dissociation channel dominates.
By comparing the images in figure 6.7, one can see that the strength as well as the KER dependence of the asymmetry reveals a strong delay dependence. The variation of the asymmetry strength with the delay is most pronounced for intermediate KERs around $1.2\,eV$. For a delay

[6]For the two-pulse measurements, the asymmetry has to be considered in different delay ranges (compare also figure 6.8 with figure 6.9). Due to the limited measurement time, for each delay range, the achievable statistics is thus lower than for single-pulse measurements.

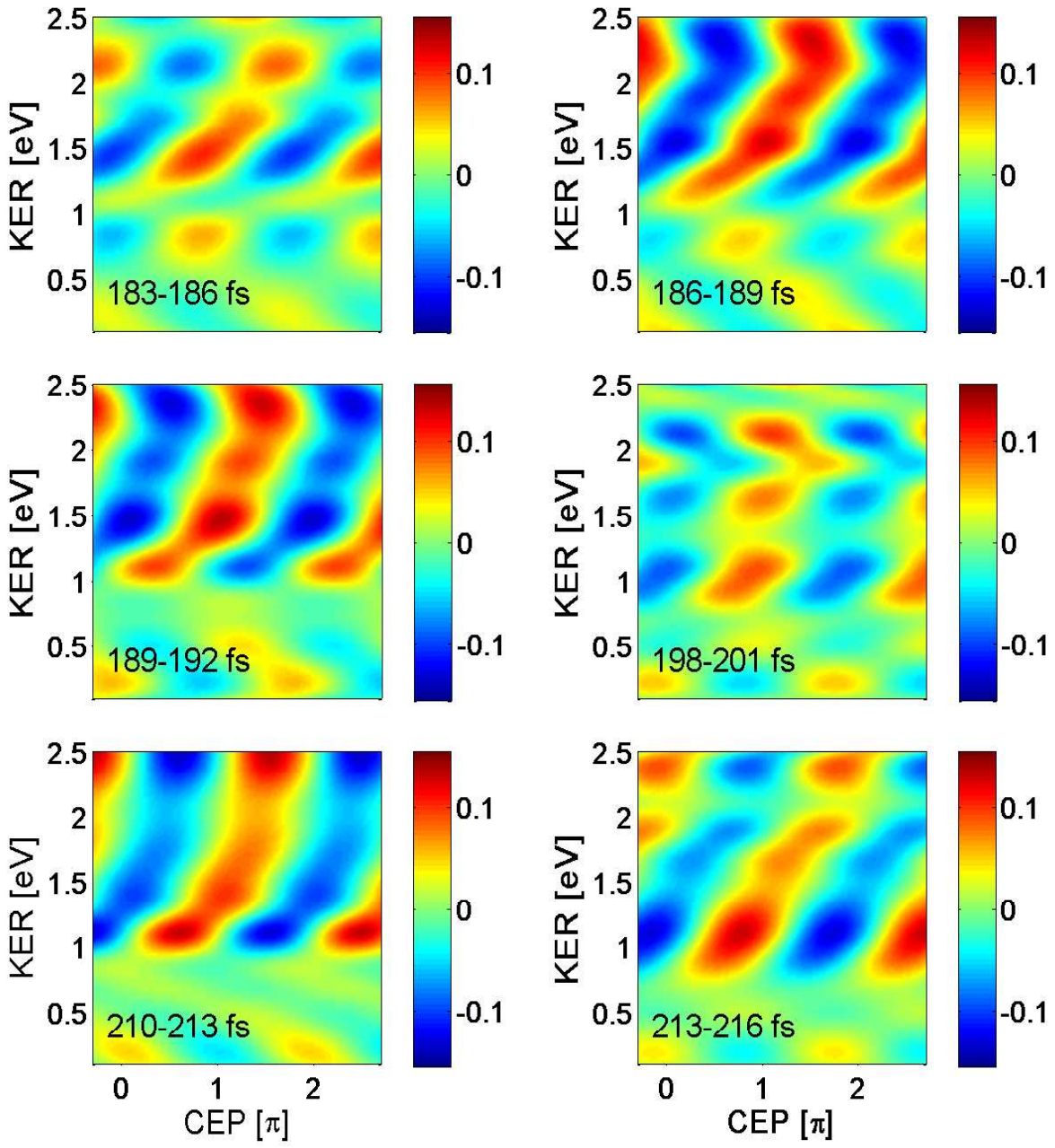

Figure 6.7: Measured asymmetry as a function of the KER and the CEP for different delay ranges in the revival. A pronounced delay dependence can be observed especially for intermediate KERs around $1.2\,eV$. Note that the CEP-scale is not absolute. It was chosen to match approximately the results of the wave packet simulations presented later in this chapter.

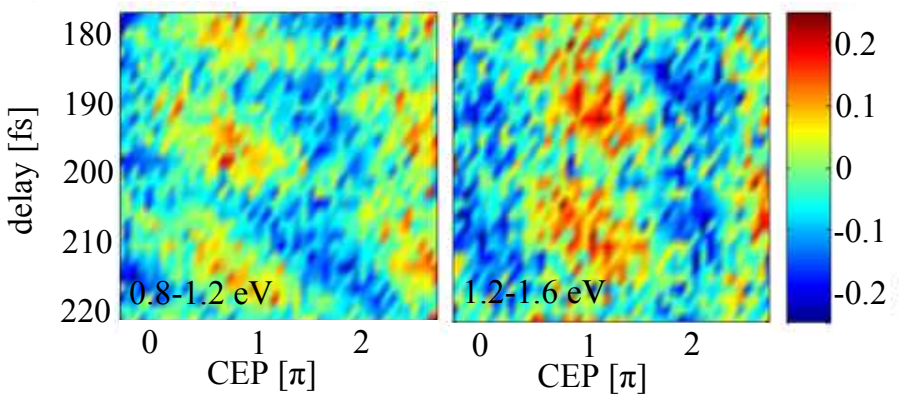

Figure 6.8: Asymmetry parameter measured in the revival region for two different KER ranges. In order to enhance the visibility, the asymmetry was fitted with a sinusodial function. The obtained result is shown in figure 6.9.

range of 182-186 fs, for example, the asymmetry between 0.8 eV and 1.2 eV has a minimum, whereas for a delay of 213-216 eV it is strongly pronounced in that energy range.
The delay dependence can also be seen in the left images of figure 6.9, where the asymmetry is shown as a function of the CEP and the delay for different KER ranges. For each KER range, the asymmetry parameter was calculated for a bin size of 0.7 rad for the CEP and 3 fs for the delay. For each delay range, the obtained asymmetry parameter was fitted along the CEP axis by a sinusoidal function as explained above. For a comparison with the unfitted data see figure 6.8.
In the right images in figure 6.9, the corresponding CEP and delay dependent proton count rates, i.e. the sum of N_r and N_l, are shown. For a KER between 0.8 eV and 1.2 eV, the strength of the asymmetry reveals a pronounced delay dependence with a periodicity of approximately 17 fs, which corresponds to the vibrational period of the bound nuclear wave packet. One can see that the corresponding dissociation yield is high where the asymmetry is high and vice versa. The asymmetry strength thereby strongly decreases in the minima. Between consecutive minima, the asymmetry stripes are tilted, i.e. the CEP dependence of the asymmetry changes with the delay. This structure also repeats with a periodicity of about 17 fs. A modulation of the dissociation yield with the CEP can be also observed, which, however, contains artifacts due to the measurement procedure[7] so that it could not be analyzed reliably.
The asymmetry for a KER range between 1.2 eV and 1.6 eV reveals a similar structure. However, the tilt of the asymmetry stripes is smaller than for a KER range of 0.8 eV-1.2 eV. For higher KERs between 1.6 eV and 2.0 eV, the asymmetry reveals only a weak delay dependence. Pronounced minima or a tilt of the asymmetry stripes cannot be observed anymore.
For KERs above 2 eV and below 0.8 eV, the signal to noise ratio is low so that a reliable analysis of the delay dependence is difficult. Therefore, only the intermediate KER range between 0.8 eV and 2.0 eV is analyzed in the remainder of this chapter.

[7]The carrier-envelope phase and the delay were scanned simultaneously so that some CEP-delay combinations were accessed more often than others. Therefore, when plotting the count rate as a function of the delay and CEP, modulations of the count rate caused by the scanning process occur additionally to modulations due to the phase and delay dependence of the ionization probability.

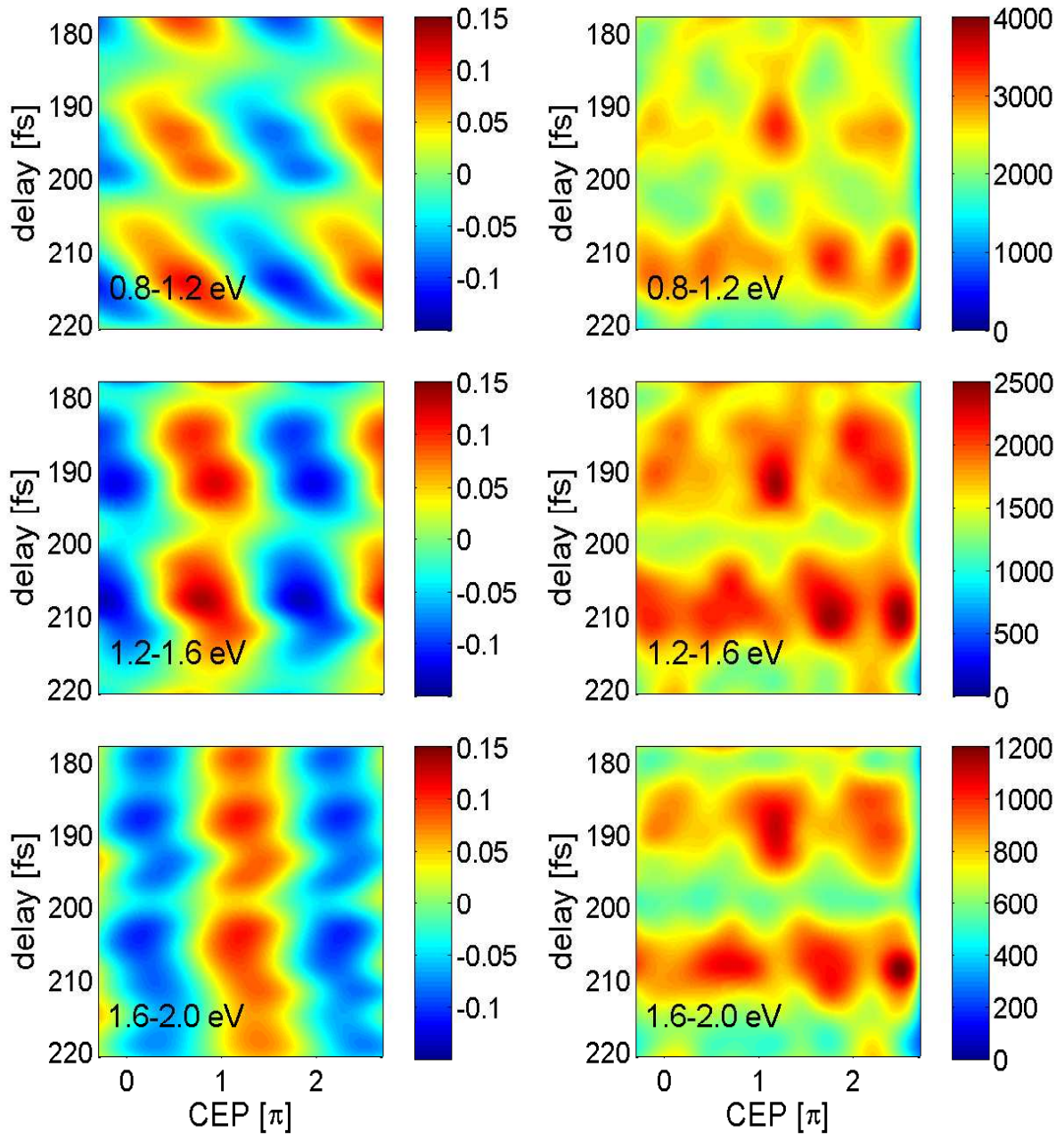

Figure 6.9: Left: Asymmetry parameter dependent on the delay and the CEP for the measurement in the revival. The asymmetry is shown for different KER ranges. It reveals a strong delay dependence, which decreases with increasing KER. Right: Corresponding dissociation yield for the different KER ranges. A high dissociation yield correlates with a high asymmetry and vice versa.

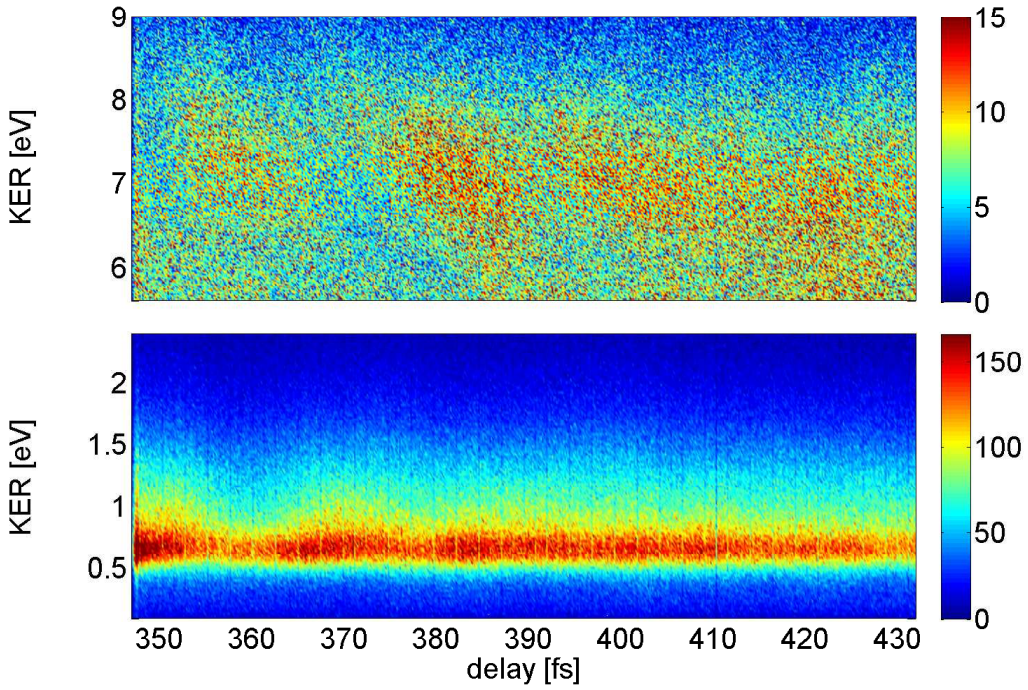

Figure 6.10: Proton count rate as a function of the delay for the pump-control measurement in the dephasing. The count rate in the dissociation (lower image) and the Coulomb explosion channel (upper image) is almost independent of the delay. Only for small delays, where the transition to the revival begins, a weak modulation can be observed.

The results in the revival region demonstrate that the asymmetry depends on the motion of the nuclear wave packet. The strength of the asymmetry, and thus the degree of electron localization, can be steered by the delay between pump and control pulse.

6.2.2 Dephasing

In the dephasing, the nuclear wave packet is spread over the $1s\sigma_g$ potential well. It therefore resembles an incoherent population of the vibrational states, for which electron localization was predicted by theory as discussed in section 5.3 in the previous chapter.
In this section, a measurement of the asymmetry in the dephasing is presented. It was carried out in the same way as the measurement in the revival.
The proton count rate as a function of the KER and the delay for the measurement in the dephasing is shown in figure 6.10 for Coulomb explosion (upper image) and dissociation (lower image). Again only the protons emitted within 30° relative to the polarization axis of the second pulse were considered. The count rate is almost independent of the delay. Only at small delays, where the transition to the revival begins, a slight variation of the count rate can be observed. Note that in this measurement the 1ω and the 2ω peak cannot be as clearly separated as for the measurement in the revival. This can be attributed to the strong dependence of the shape of these peaks on the details of the pulse shape.

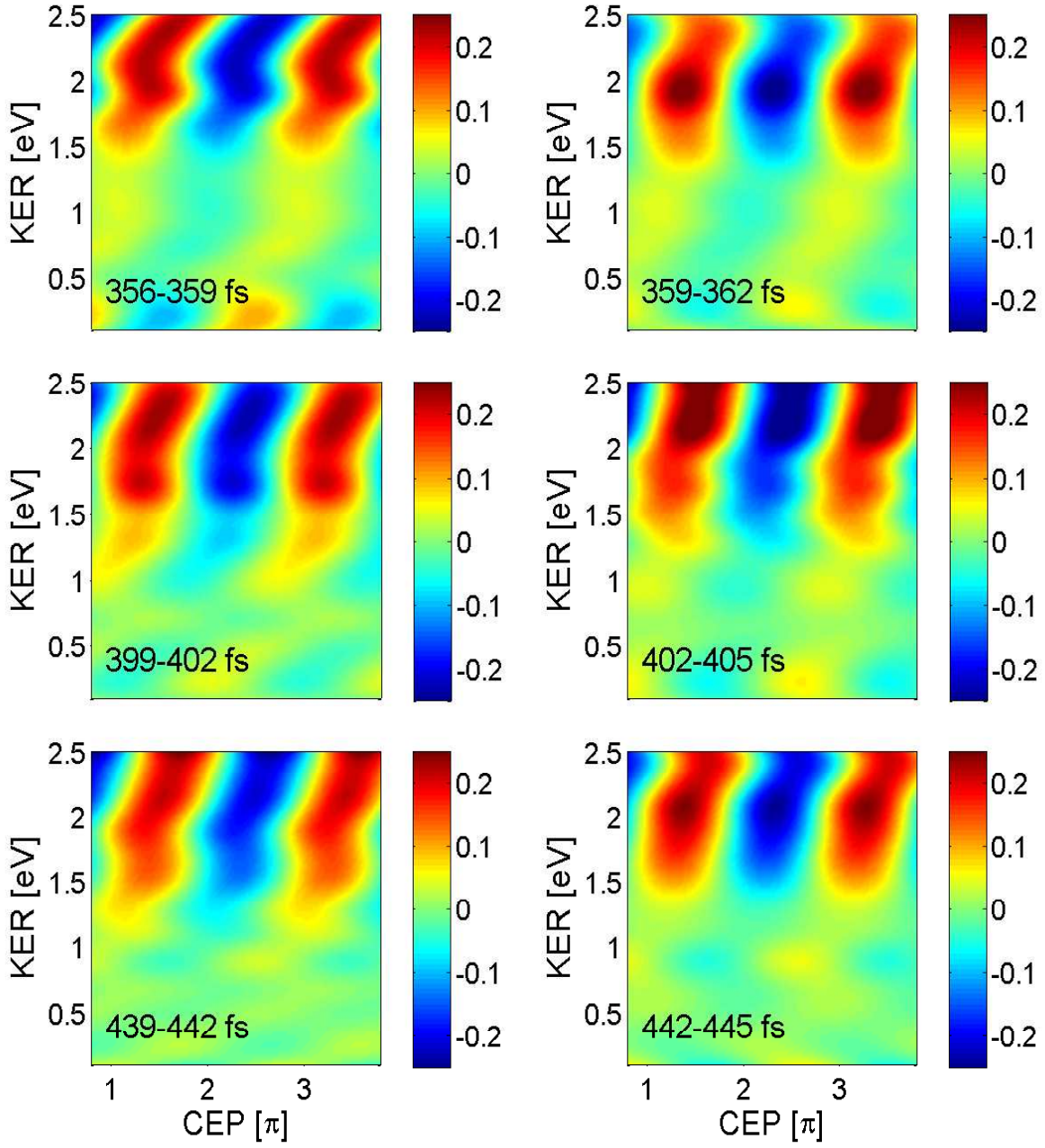

Figure 6.11: Measured asymmetry parameter for different delay ranges in the dephasing. The asymmetry is strongly pronounced only for high KERs and reveals only a weak dependence on the delay.

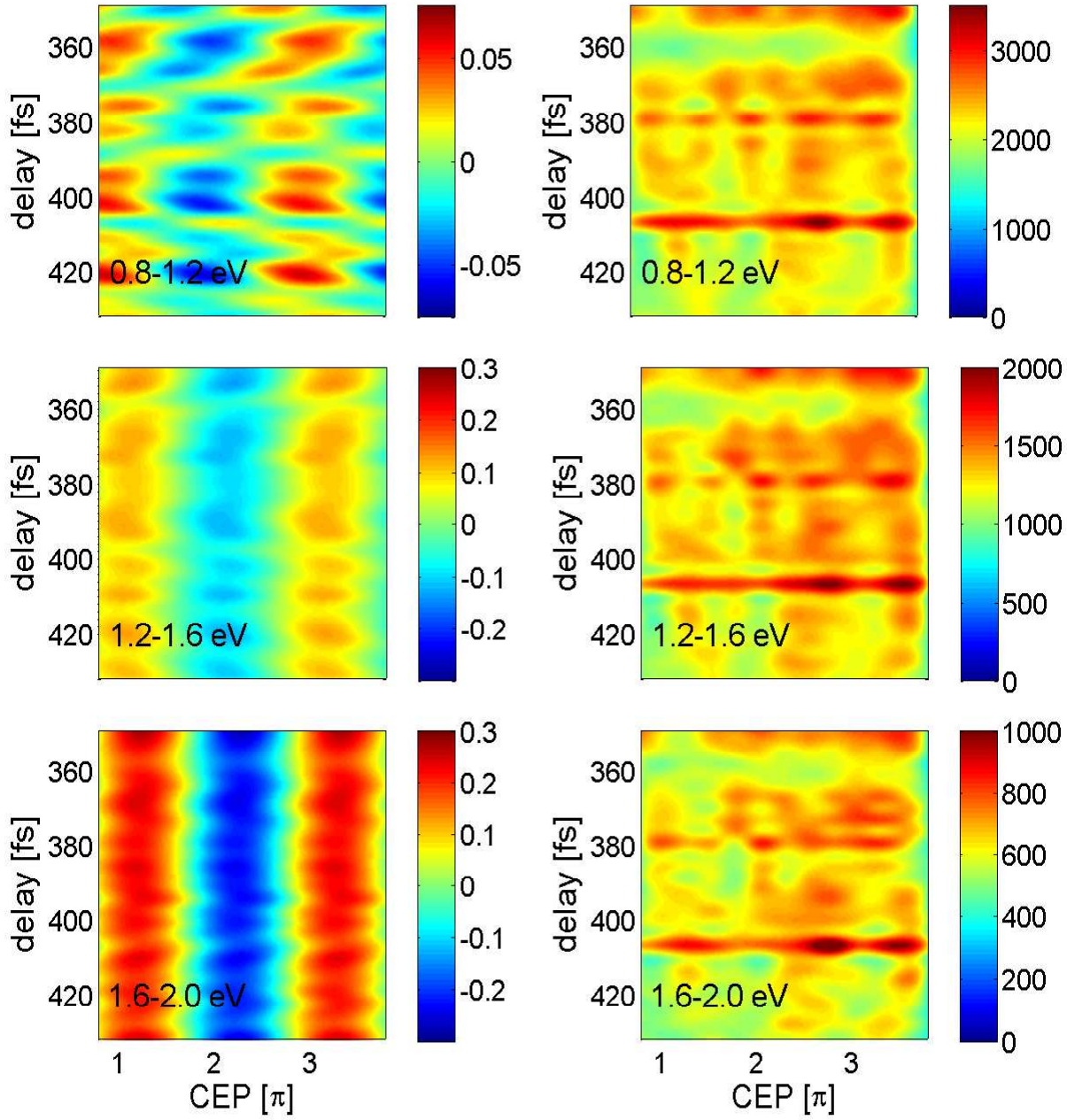

Figure 6.12: Measured asymmetry parameter (left) and corresponding dissociation yield (right) as a function of delay and CEP for the measurement in the dephasing region. Almost no delay dependence of the asymmetry can be observed for KERs above $1.2\,eV$. For lower KERs, the asymmetry strength is modulated with the delay, but the asymmetry is weak. Right: The proton count rate for the different KER ranges depends only weakly on the delay. (The maximum in the count rate at about $405\,fs$ is caused by a short dropout of the delay stage.)

The CEP and KER dependent asymmetry parameter determined in the same way as explained above is shown for different delays in figure 6.11. For all delays, a strong asymmetry can be observed for KERs above about $1.4\,eV$, which reveals only a weak dependence on the delay. For lower KERs, the asymmetry is significantly weaker. Often the asymmetry stripes in this energy range are tilted more strongly and in the opposite direction as for higher KERs. For some delays, the tilt of the asymmetry stripes changes the direction also close to $0.8\,eV$ similar to the measurement in the revival.
The asymmetry as a function of delay and CEP is shown in figure 6.12 for different KER ranges. For KERs between $0.8\,eV$ and $1.2\,eV$, the asymmetry is weak, but reveals a delay dependence in its strength. The CEP dependence of the asymmetry changes only weakly with the delay. Only for delays smaller than $360\,fs$, where the transition to the revival starts, a small tilt of the asymmetry can be observed. For higher KERs, the asymmetry strength and structure is almost independent of the delay. The dissociation rate for the regarded energy ranges also shows only a very weak dependence on the delay, which becomes slightly more pronounced only for small delays.
These results demonstrate that also in the dephasing a strong asymmetry can be obtained, at least for high KERs. Note that the strength of the asymmetry depends on the details of the pulse shape (see section 5.1.2). Therefore, the absolute value of the asymmetry for the three measurements presented here cannot be compared to each other. In order to be able to compare the strength of the asymmetry in the dephasing and the revival, a measurement in the transition region was performed. This results are presented in the following subsection.

6.2.3 Transition region

The delay dependent proton count rate for the measurement in the transition region is shown in figure 6.13. For small delays, clear maxima and minima can be observed in the dissociation yield, which smear out with increasing delay.
The KER and CEP dependent asymmetry for different delays is shown in figure 6.14. Again the asymmetry is most strongly pronounced for KERs above about $1.4\,eV$. The asymmetry for lower KER values is weak and reveals a similar structure as for the measurement in the dephasing, with changes in the slope and direction of the asymmetry stripes.
The asymmetry dependent on delay and CEP for different KER ranges is plotted in figure 6.15. Between $0.8\,eV$ and $1.2\,eV$, the asymmetry is weak and reveals a delay dependent modulation in its strength. The change of the CEP dependence with the delay is rather weak for delays larger than $330\,fs$. Around $330\,fs$, however, a shift of the asymmetry stripes, i.e. the CEP dependence, can be observed. For smaller delays, especially below $300\,fs$, indications of tilted asymmetry stripes are seen. The corresponding count rate also reveals a stronger modulation with the delay for delays smaller than $300\,fs$.
A change of the asymmetry structure with the delay can be also observed for a KER range between 1.2 and $1.6\,eV$. For large delays, the asymmetry structure is rather independent of the delay, but with increasing delays a transition to slightly tilted asymmetry stripes takes place. Besides that, the strength of the asymmetry slightly increases for delays smaller than $330\,fs$. For a KER range between $0.8\,eV$ and $1\,eV$, the dependence of the asymmetry on the delay is less pronounced, but a slight increase of the asymmetry strength with the delay is observable.

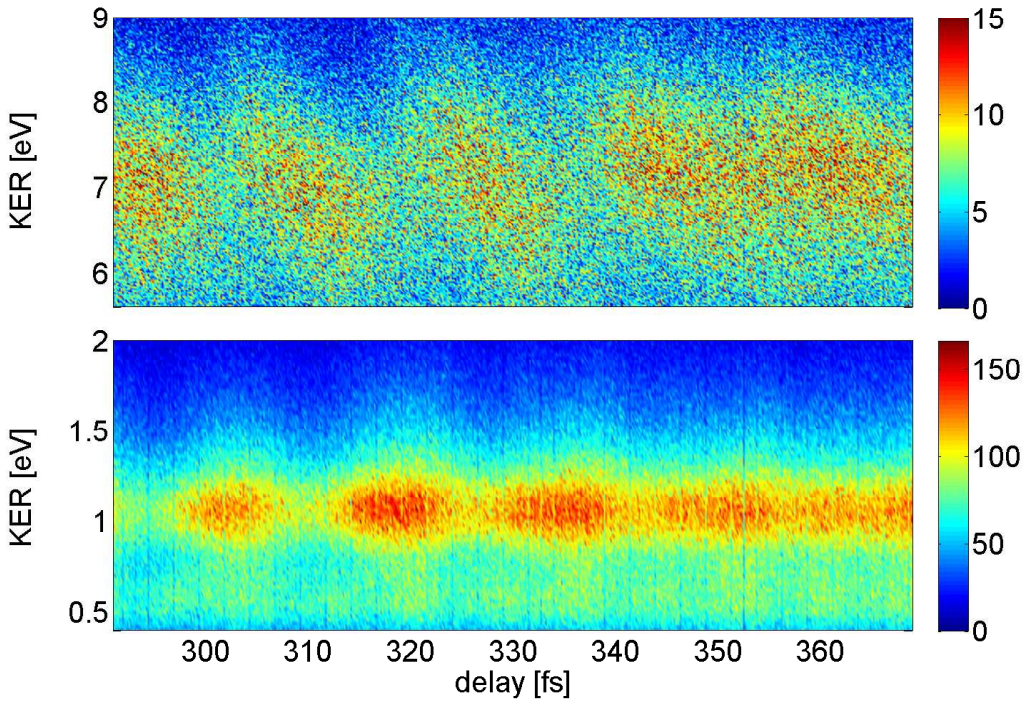

Figure 6.13: Delay dependent proton count rate for the measurement in the transition region between revival and dephasing. A modulation of the count rate can be observed in the dissociation (lower image) as well as in the Coulomb explosion channel (upper image), which smears out with increasing delay.

6.3 Theoretical calculations

The experimental results presented above demonstrate that the dynamics and the shape of the nuclear wave packet determine the strength and the structure of the observed asymmetry. This means that the degree and the KER dependence of electron localization is influenced by the nuclear wave packet. In order to gain a better understanding of the underlying physical mechanisms, wave packet calculations were performed, which are described in this section. The obtained results are presented and compared to the experimental data.

6.3.1 Calculation procedure

The calculations were based on the software package used also for the simulations of the single-pulse measurements [FER+07, TNF08, NT08] (see section 5.4).
The wave function in the H_2 ground state was calculated by propagation in imaginary time [LTE07] and set in an instantaneous step into the $1s\sigma_g$ potential. The created nuclear wave packet was then propagated in the potential well by solving the Schrödinger equation with the Crank-Nicholson split-operator method (see section 5.4 and appendix B). As long as no laser

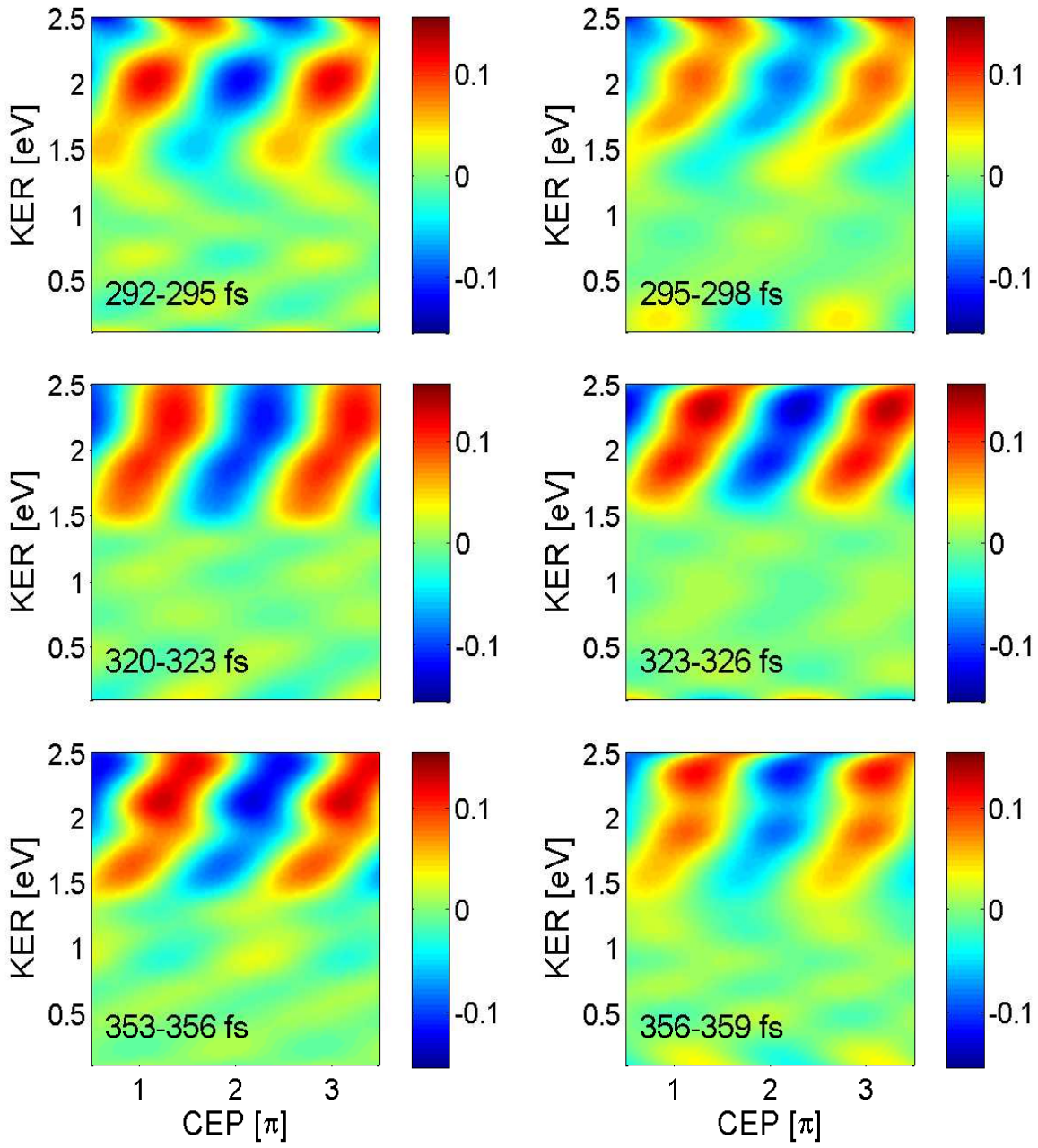

Figure 6.14: Measured symmetry parameter dependent on the KER and CEP for different delays in the transition region. Similar to the measurement in the dephasing, the asymmetry is most pronounced for high KER.

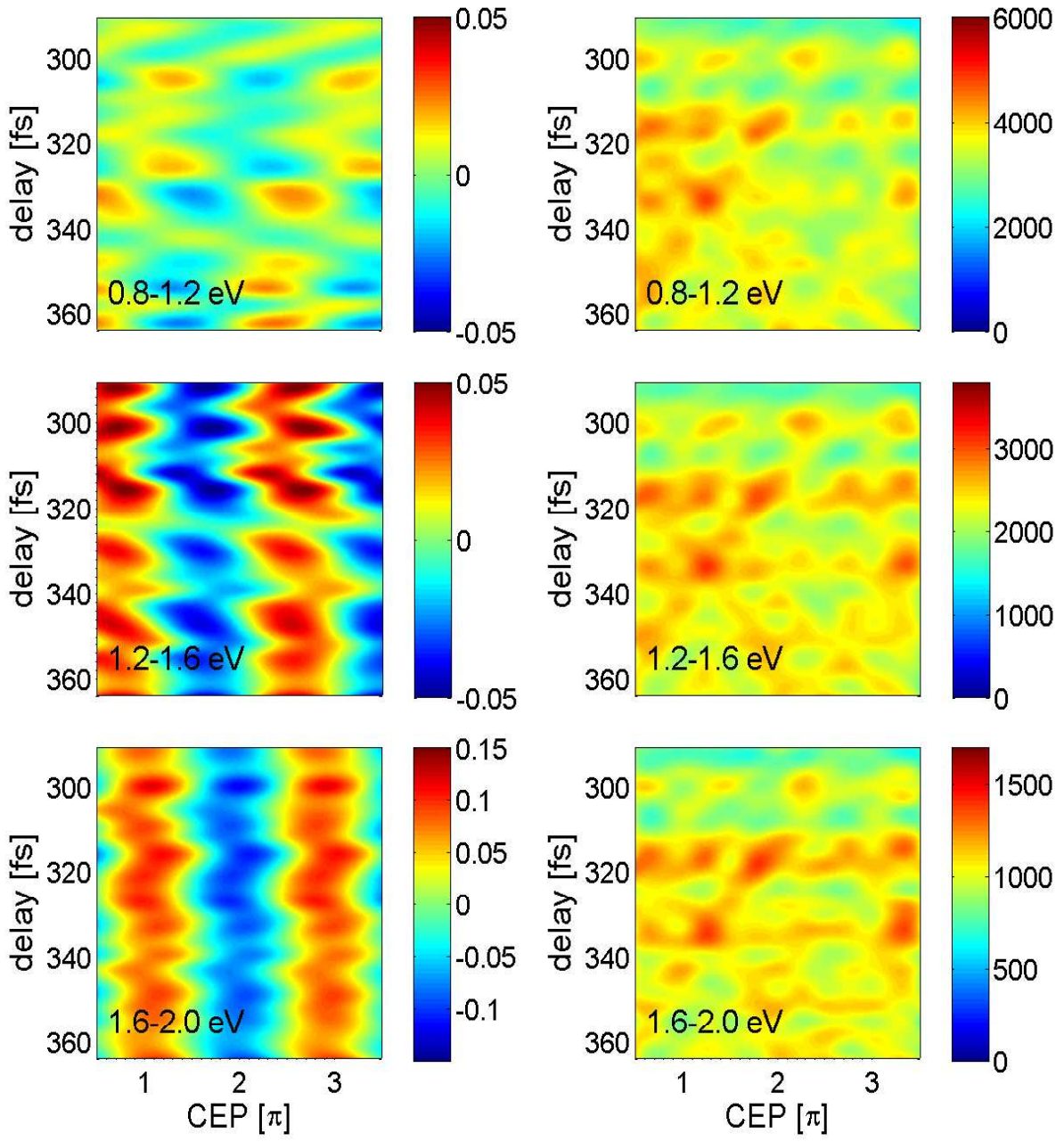

Figure 6.15: Delay and CEP dependent asymmetry (left) for the measurement in the transition region and the corresponding dissociation yield (right). For small delays, a delay dependence can be observed in the asymmetry and the proton count rate. With increasing delay, the modulation becomes weaker and the asymmetry strength slightly decreases.

pulse is applied, the propagation of the wave packet requires only a small numerical grid as the wave packet remains bound in the potential well. After a time delay τ, a laser pulse was applied inducing the coupling between the $1s\sigma_g$ and the $2p\sigma_u$ potential as described in section 5.4.
For calculating the full momentum distribution of the dissociating part of the wave packet, a long propagation time and a large numerical grid is required. The reason is that the finite width of the momentum distribution of the wave packet introduces a significant dispersion. Therefore, a rather long time is required until the dissociation process is completed, i.e. until the small momentum components have reached the continuum. The fast components of the dissociating wave packet have already propagated over a large distance during that time. Calculating the momentum distribution in this way for many different delays thus requires a long computation time.
For reducing the computation time, a so-called virtual detector [FT03] was applied. Here the momentum distribution is calculated from the time dependence of the wave function at a fixed position in coordinate space. This method requires only a small numerical grid and significantly reduces the computation time. For more details, see appendix B.3.
In the experiment, the pump pulse and the control pulse were polarized perpendicular to each other. Thus, for the protons emitted parallel to the control pulse, the pump pulse can be assumed to induce only single ionization of the neutral H_2 molecule and to have no further influence on the nuclear wave packet. The electric field of the pump pulse was therefore not explicitly considered in the simulations. However, as discussed in section 6.1.1, the finite length of the pump pulse plays an important role. It was considered in the calculation by assuming that ionization can occur in the five most intense field maxima of the pump pulse (see section 5.4). In order to determine the asymmetry for a certain delay τ and a certain CEP, the calculation was performed for each of the five possible ionization times, that means for the corresponding five effective delays τ_{eff} between the ionization step and the temporal center of the control pulse. Thereby, $\tau_{eff} = \tau + \Delta t$ is determined by the time Δt between the center of the pump pulse and the considered field maximum. Note that Δt depends on the carrier-envelope phase of the pump pulse, which was assumed to be the same as the CEP of the control pulse. This assumption well describes the experimental conditions[8]. For each considered value of the CEP and delay τ, the energy distributions obtained for the five ionization times were added incoherently, weighted by the corresponding ADK-rates as explained in section 5.4. A coherent summation of the wave packets was not possible as their relative phases were not known. From the obtained energy distributions of the wave packet emitted to the left $|\Psi_l(KER, CEP, \tau)|^2$ and to the right $|\Psi_r(KER, CEP, \tau)|^2$, for each value of the CEP and the delay the asymmetry parameter was determined by using equation (5.27). The delay was varied over $600\,fs$ in steps of $1\,fs$ and the CEP over 180° in steps of 30°.

6.3.2 Results

The calculations were performed for a $6\,fs$ control pulse with an intensity of $0.4\,PW/cm^2$. Examples of the obtained asymmetry parameter for different delays as a function of the CEP and the KER are shown in figure 6.16. Similar to the measurements, the asymmetry has a periodicity of 2π in the CEP and is dependent on the KER. For some delays, like for example in the revival

[8]Even if the CEP of the pump and the control pulse in the experiment differ from each other, the relative phase between the two pulses remains constant when scanning the phase.

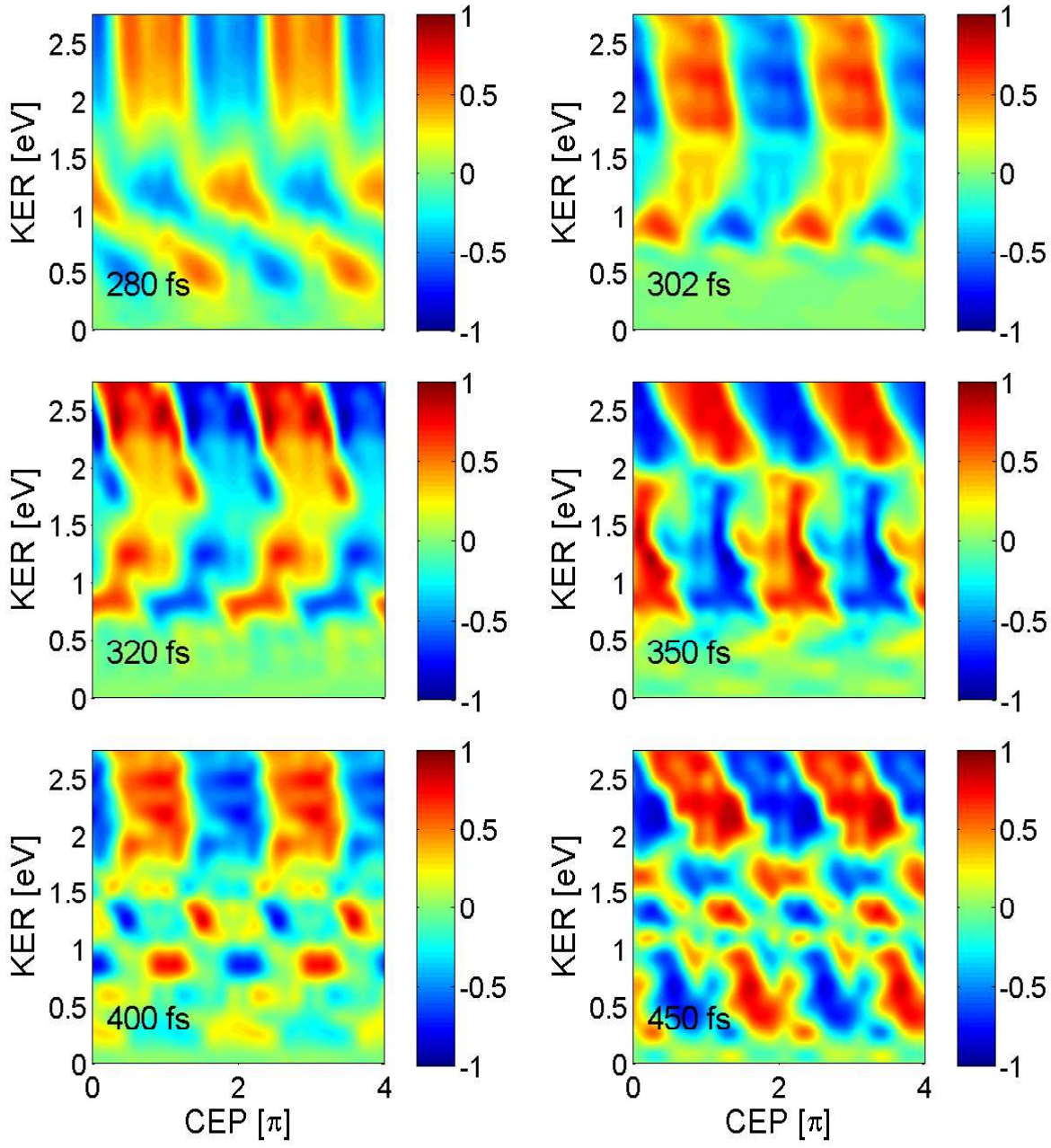

Figure 6.16: Asymmetry parameter obtained from the wave packet simulations dependent on the KER and CEP for different delays. The asymmetry reveals a stronger dependence on the delay and has generally a more structured KER dependence than in the measurements.

at $302\,fs$, the asymmetry reveals a similar KER dependence as observed in the experimental results (compare with figure 6.7). Generally, however, the asymmetry pattern is more structured and reveals a stronger delay dependence than the measurements. Note that the delays in the simulations and the experimental data cannot directly be assigned to each other as the revival times differ as explained in section 6.1.1.
In order to compare the results of the simulations with the experimental data, the delay regions in the simulations, which correspond best to the ones in the measurements, were selected.
The results of the simulation for the revival are shown in figure 6.17. In the left images, the asymmetry parameter and in the right images the corresponding dissociation yields are shown for the three KER ranges regarded in the measurement (compare figure 6.9). Tilted asymmetry stripes, similar to the ones in the experimental data, can be observed for a KER range between $0.8\,eV$-$1.2\,eV$, which occur with a periodicity of about $17\,fs$. The dissociation yield also reveals a strong delay dependent modulation with the same periodicity, which is in good agreement with the experimental observations (compare figure 6.9). For the KER range between $1.2\,eV$ and $1.6\,eV$, for small delays also tilted asymmetry stripes can be observed for small delays. For longer delays, however, the asymmetry is more structured than in the experiment. A good agreement with the measurement is also obtained for KERs between $1.6\,eV$ and $2\,eV$, where the asymmetry stripes are rather straight.
The results of the simulation for the dephasing is shown in figure 6.18. Contrary to the experimental results shown in figure 6.12, the asymmetry for KERs between $0.8\,eV$ and $1.2\,eV$ is not significantly weaker than for higher KERs. The structure of the asymmetry, however, is similar, with a periodicity of about $17\,fs$ in the asymmetry strength and almost no change of the CEP dependence with the delay. For KERs between $1.2\,eV$ and $1.6\,eV$, the asymmetry structure also remains rather constant over the whole delay range. A good agreement with the experimental data is given for KERs between $1.6\,eV$ and $2\,eV$. Despite some fast modulations, straight asymmetry stripes similar to the ones in the measurement can be observed. Contrary to the measurements shown in figure 6.12, a delay dependent modulation of the dissociation yield can be observed for all KER ranges. This modulation is, however, much less pronounced than in the revival.
In figure 6.19, the results of the calculation for the transition region are shown. In a KER range between $0.8\,eV$ and $1.2\,eV$, a similar structure as in the experiment shown in figure 6.15 is obtained. For KERs between $1.6\,eV$ and $2\,eV$, a transition from tilted to straight asymmetry stripes takes place, resembling the transition observed in the measurement between $1.2\,eV$ and $1.6\,eV$. The strength of the asymmetry slightly decreases over the regarded delay range and reveals fast modulations with the delay. In the dissociation yield, also a modulation with the delay can be observed.

6.3.3 Comparison with the experimental data

The results of the wave packet simulations reproduce qualitatively the main features of the experimental data. In general, however, the asymmetry in the theoretical results reveals more structure and a stronger delay dependence. This is also true for the dissociation yield. In the dephasing region, for example, the calculated dissociation yield still reveals a dependence on the delay, whereas in the experimental results no delay dependent modulation can be observed. There are several reasons for such discrepancies.

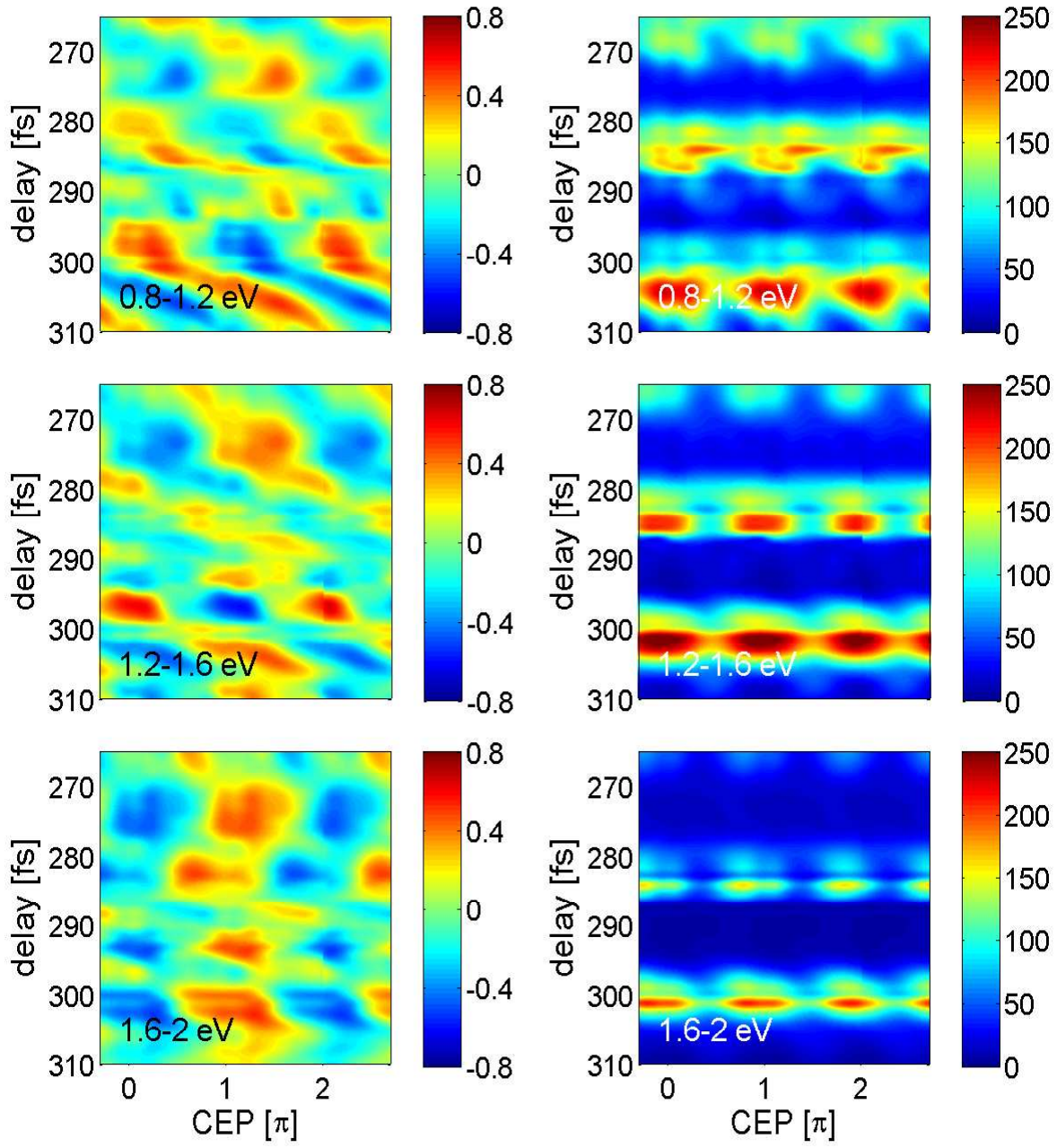

Figure 6.17: Left: Delay and CEP dependent asymmetry for a delay range in the revival. In agreement with the experiment (compare with figure 6.9), tilted asymmetry stripes are obtained for small KERs, whereas for high KERs the asymmetry does almost not shift with the delay. Right: The corresponding dissociation yield reveals a strong modulation with the delay, but only a slight modulation with the CEP.

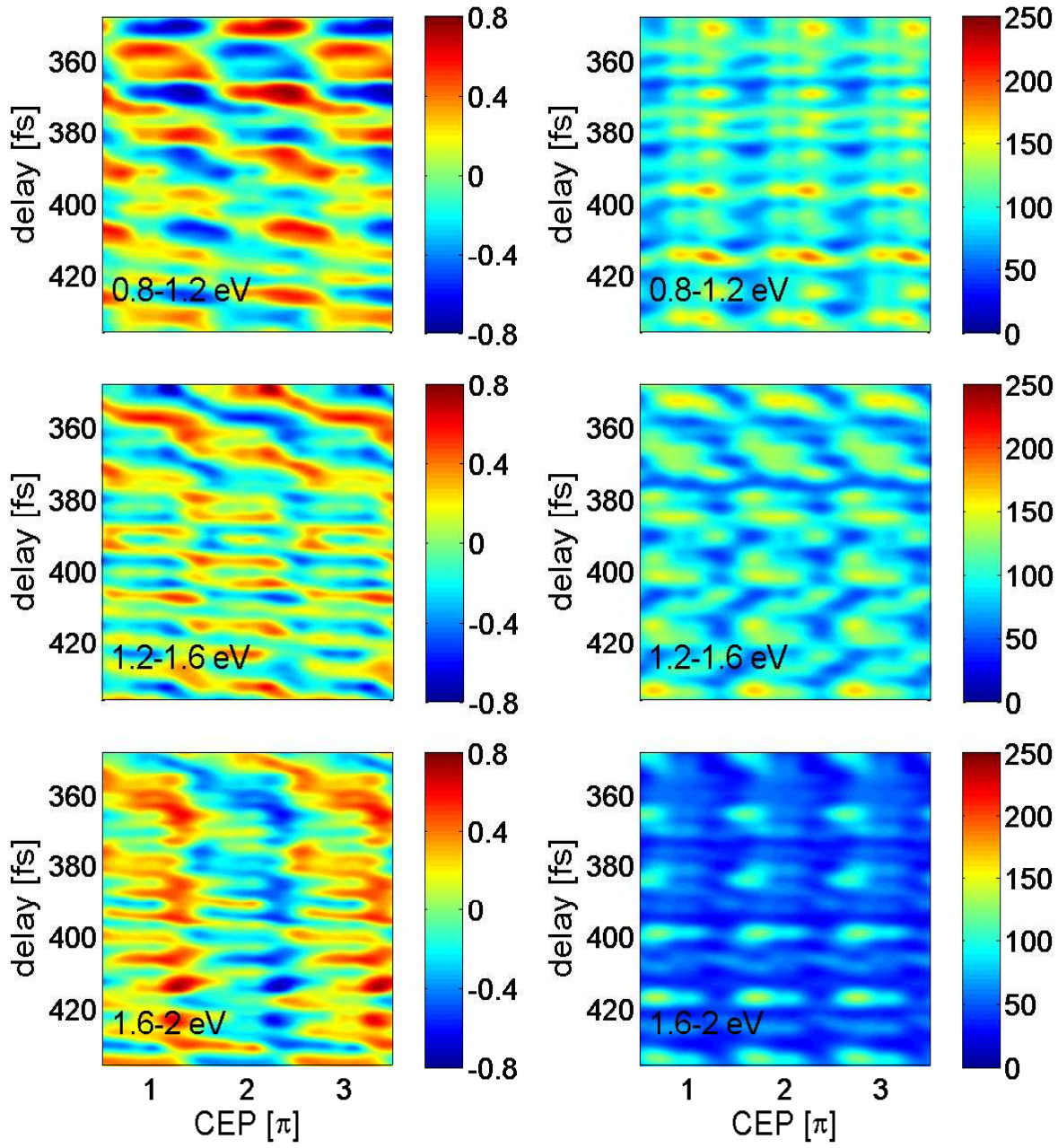

Figure 6.18: Calculated delay and CEP dependent asymmetry (left) and corresponding dissociation yield (right) for the dephasing region (compare with figure 6.12). The delay dependence of the asymmetry and dissociation yield is less pronounced than in the revival.

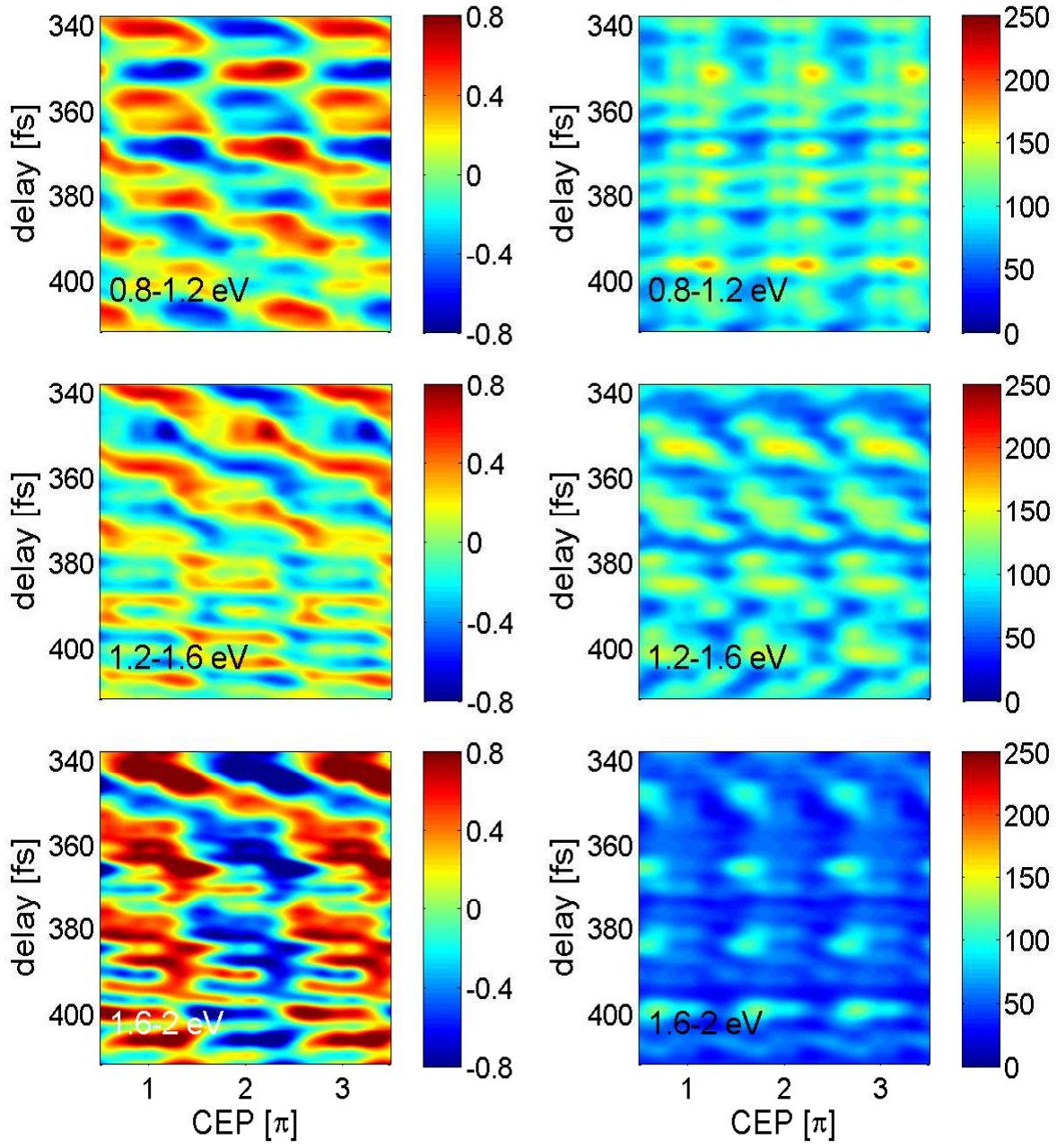

Figure 6.19: Calculated delay and CEP dependent asymmetry (left) and dissociation yield (right) for a delay range in the transition region between dephasing and revival (compare figure 6.15).

One of these reasons is that in the experiment the pulse intensity varies throughout the laser focus so that different intensities contribute to the experimental results. This effect was not considered in the calculation, which was performed for a fixed peak intensity. For estimating the effect of the focal volume, the calculation was also performed for $0.3\,PW/cm^2$, $0.2\,PW/cm^2$ and $0.1\,PW/cm^2$ for a small delay range in the revival. The obtained probability distributions were added incoherently, with the high intensities being weighted more strongly than the lower ones. This simple focal volume averaging was shown to wash out some details of the asymmetry structure, the overall features of the delay dependence, however, are maintained. This indicates, that the averaging over different intensities in the laser focus can, to some extend, explain some of the differences between theory and experiment. A detailed analysis of this effect is, however, beyond the scope of this thesis.
The averaging over different intensities leads also to a lowering of the asymmetry strength, which is one of the reasons why the asymmetry for the simulations is stronger than in the experimental data. Another reason is that the asymmetry stripes shift with the emission angle of the proton as shown in the previous chapter. Due to this shift, the asymmetry is reduced when all protons emitted within 30° relative to the laser polarization axis are considered. In the calculation, the molecular axis was assumed to be fixed parallel to the laser polarization axis so that the effect of the molecular orientation was not taken into account.
Differences between experiment and theory are, of course, also caused by the experimental conditions. The experimental parameters, like the carrier-envelope phase, have experimental errors and are therefore not as exactly defined as in the calculation. Besides that, details of the pulse shape, like a pedestal or satellite pulses, can influence the experimental results.
In the experiment, the ionization step, which induces the wave packet evolution, and the localization of the electron cannot be separated as clearly as in the theoretical calculation. In the experiment, ionization and dissociation can occur both in the control pulse. This channel cannot be separated from the case, where ionization occurs in the first and dissociation in the second pulse. Therefore, it leads to a delay independent background in the dissociation yield and the asymmetry. The background provides an asymmetry structure, which varies as a function of the CEP with a periodicity of 2π, but is independent of the delay. This provides a delay independent offset to the delay dependence of the asymmetry. This offset explains, for example, the differences between experiment and theory for the asymmetry in the dephasing for a KER of 0.8-1.2 eV (figures 6.12 and 6.18). For a fixed CEP, in the simulations the asymmetry changes from positive to negative values, whereby the magnitude is about the same for both signs. When adding a delay independent offset, one would obtain an asymmetry structure similar to the one observed in the experiment, with stripes for which the asymmetry is mainly positive and stripes for which it is mainly negative.
Despite the differences mentioned above, the simulations well reproduce the main experimental observations. Although some features of the experimental results are influenced by experimental conditions, which are not considered in the calculation, the main results of theory and experiment are in good agreement with each other. Therefore, the theoretical simulations provide a good basis for gaining a better understanding of the underlying physical mechanisms.
Experiment and theory clearly demonstrate that the asymmetry, i.e. the localization of the electron, depends on the shape and the dynamics of the nuclear wave packet. The strength, i.e. the degree of electron localization, as well as the structure of the asymmetry can be steered by the delay between the pump and the control pulse, which determines the properties of the nuclear

wave packet.

6.4 Theoretical model

The results of the wave packet simulations are in good qualitative agreement with the experimental data. The simulations can therefore be used to develop an intuitive model of how the shape and dynamics of the nuclear wave packet influence the localization of the electron. For this purpose, the calculated asymmetry was compared with the position and momentum distribution of the bound nuclear wave packet at the time the second laser pulse is applied.
The asymmetry obtained from the simulations is shown in figure 6.20 (a) for a delay range around the half-revival. Although the asymmetry was calculated for the entire KER range of the protons, it still reveals a pronounced delay dependence. A shortcoming of the normalized asymmetry is that it can become large when the dissociation yield is negligibly small. This can be avoided by using the absolute asymmetry instead, which is defined as the non-normalized difference of the number of protons emitted to the left and to the right

$$A_{abs} = N_l - N_r. \tag{6.2}$$

The absolute asymmetry is only large when the asymmetry as well as the dissociation yield is high. The absolute asymmetry and the dissociation yield for the regarded delay range are shown in figure 6.20 (b) and (c), respectively.
The evolution of the bound nuclear wave packet in this delay range is shown in figure 6.20 (d) in coordinate and in (e) in momentum space. One can see that the asymmetry as well as the dissociation yield are not determined by the momentum or position distribution alone, but by the combination of both. It is therefore useful to visualize the wave packet evolution in phase space. This was done by making use of the Wigner and Husimi distribution as explained in the following subsection. Afterwards, the influence of the WKB[9] phase of the dissociating wave packets on the asymmetry is analyzed. Finally, the theoretical model developed from the obtained results is presented.

6.4.1 Wigner and Husimi distribution

The asymmetry depends on the position as well as on the momentum of the bound nuclear wave packet. It is therefore desirable to display the probability distribution for the position and the momentum simultaneously. However, due to the uncertainty principle, in quantum mechanics it is not possible to find a probability distribution in phase space. Nevertheless, one can define a quasi-probability distribution in phase space by the so-called Wigner function [Wig32, Cas08], which is defined as

$$W(x,p) = 2\pi \int e^{-ipx'} \psi(x + x'/2)\psi^*(x - x'/2)dx'. \tag{6.3}$$

Here $\psi(x)$ is the wave function in coordinate space and p is the momentum. The projection of the Wigner function onto the p axis provides the probability distribution in coordinate space $|\psi(x)|^2$

$$\int W(x,p)dp = \psi(x)\psi^*(x), \tag{6.4}$$

[9] Wentzel-Kramers-Brillouin

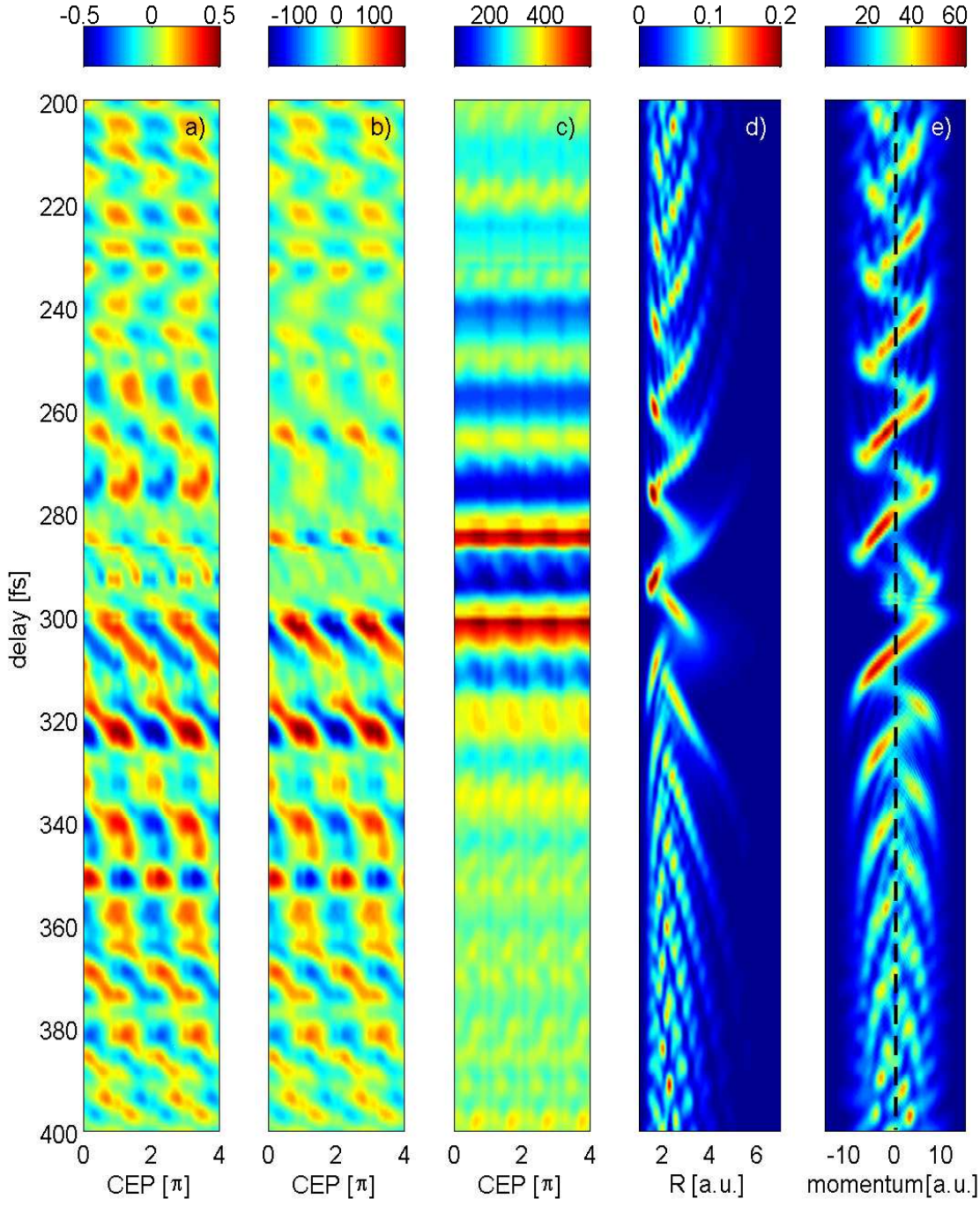

Figure 6.20: Comparison of the asymmetry and dissociation yield with the dynamics of the bound nuclear wave packet for a delay range around the half- revival. In a) the normalized asymmetry, in b) the absolute asymmetry and in c) the dissociation yield are shown for the entire KER range of the protons. The corresponding probability distribution of the bound wave packet is shown in d) dependent on R and in e) dependent on the momentum.

and the projection onto the x axis provides the probability distribution in momentum space $|\varphi(p)|^2$

$$\int W(x,p)dx = \varphi(p)\varphi^*(p). \tag{6.5}$$

The Wigner function is real and normalized. Contrary to a conventional probability distribution, however, there can be regions in phase space, where the Wigner function has negative values. This is the case for states, which have no classical analogy, and is caused by quantum mechanical interferences.

A more illustrative representation of the wave packet dynamics can be obtained by using the Husimi function [Hus40, TKC+08, HF09], which provides a semi-classical probability distribution in phase space. It is obtained by smoothing the Wigner function such that the distribution has only positive values. This is done by a convolution of the Wigner function with a Gaussian. The Husimi function is defined as

$$H(x,p,\kappa) = 2\int\int_{-\infty}^{\infty} dx'dp'W(x',p')exp\left(-\kappa(x'-x)^2 - \frac{(p'-p)^2}{\kappa}\right), \tag{6.6}$$

with $\kappa > 0$. The parameter κ determines the relative resolution in x and p and was chosen to be $\kappa = 1$.

The Husimi distribution of the bound nuclear wave packet in H_2^+ was calculated for a delay range of 600 fs. Examples of the obtained distributions for different delays are shown in the left column of figure 6.21. The KER and CEP dependent dissociation yield for these delays is displayed in the second column, the normalized asymmetry parameter in the third and the absolute asymmetry in the fourth column.

For zero delay, the wave packet is well localized and located at the minimum of the potential well. The momentum distribution is centered symmetrically around zero. Here the asymmetry as well as the dissociation yield is small. At a delay of 4 fs, the momentum is mainly distributed at positive momentum values. The wave packet can thus be regarded to move outwards, i.e. towards large R. Its probability distribution in R is located around the 3ω crossing at 3.3 $a.u.$ (marked by the dashed white line in figure 6.21). At this delay, the dissociation yield as well as the asymmetry is high.

In the dephasing region, the probability distribution has a large spread in momentum and in position and reveals a rather complex structure. This can be seen in figure 6.21 for a delay of 50 fs and of 180 fs. Due to this complexity, a comparison of the probability distribution with the asymmetry and dissociation yield is difficult for the dephasing.

The wave packet is again well localized in the revival. The Husimi distribution for different delays in the revival is shown in figure 6.22. For a delay of 290 fs, the wave packet is located at a large internuclear distance, i.e. around the 1ω and 3ω crossing, but has a negative momentum. The asymmetry as well as the dissociation yield are small in this case. The dissociation yield and total asymmetry are minimal somewhat later at 294 fs, when the wave packet moves inwards and is located close to the inner turning point of the potential well. Here, however, the normalized asymmetry is high. A high dissociation yield and asymmetry is obtained when the wave packet is located at a large internuclear distance and has a positive momentum as can be seen, for example, for a delay of 304 fs. Thereby, the total dissociation yield is highest when the wave packet is best localized. For delays after the center of the revival, the spread of the wave packet increases. Here the asymmetry and the dissociation yield become high when a part of the wave packet is at

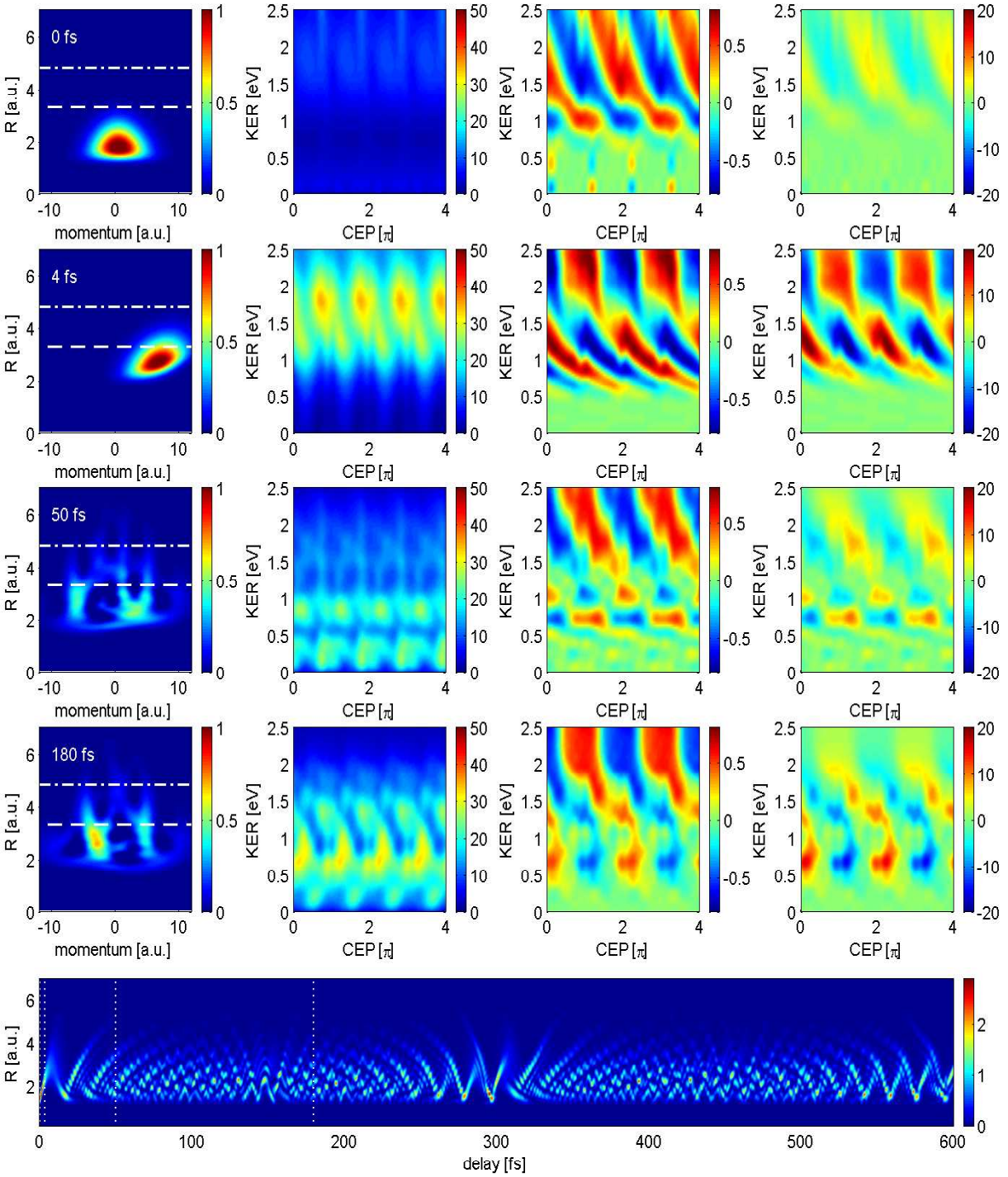

Figure 6.21: Comparison of the asymmetry and dissociation yield with the distribution of the bound nuclear wave packet in phase space for different delays. In the left column, the Husimi distribution of the bound wave packet is shown. The 3ω crossing is marked by the dashed line and the 1ω crossing by the dashed-dotted line. In the second column, the corresponding dissociation yield, in the third column the normalized asymmetry and in the fourth column the absolute asymmetry are shown as a function of the KER and the CEP. The regarded delays are marked with white dotted lines in the lowest image, where the wave packet evolution as a function of R and the delay is shown.

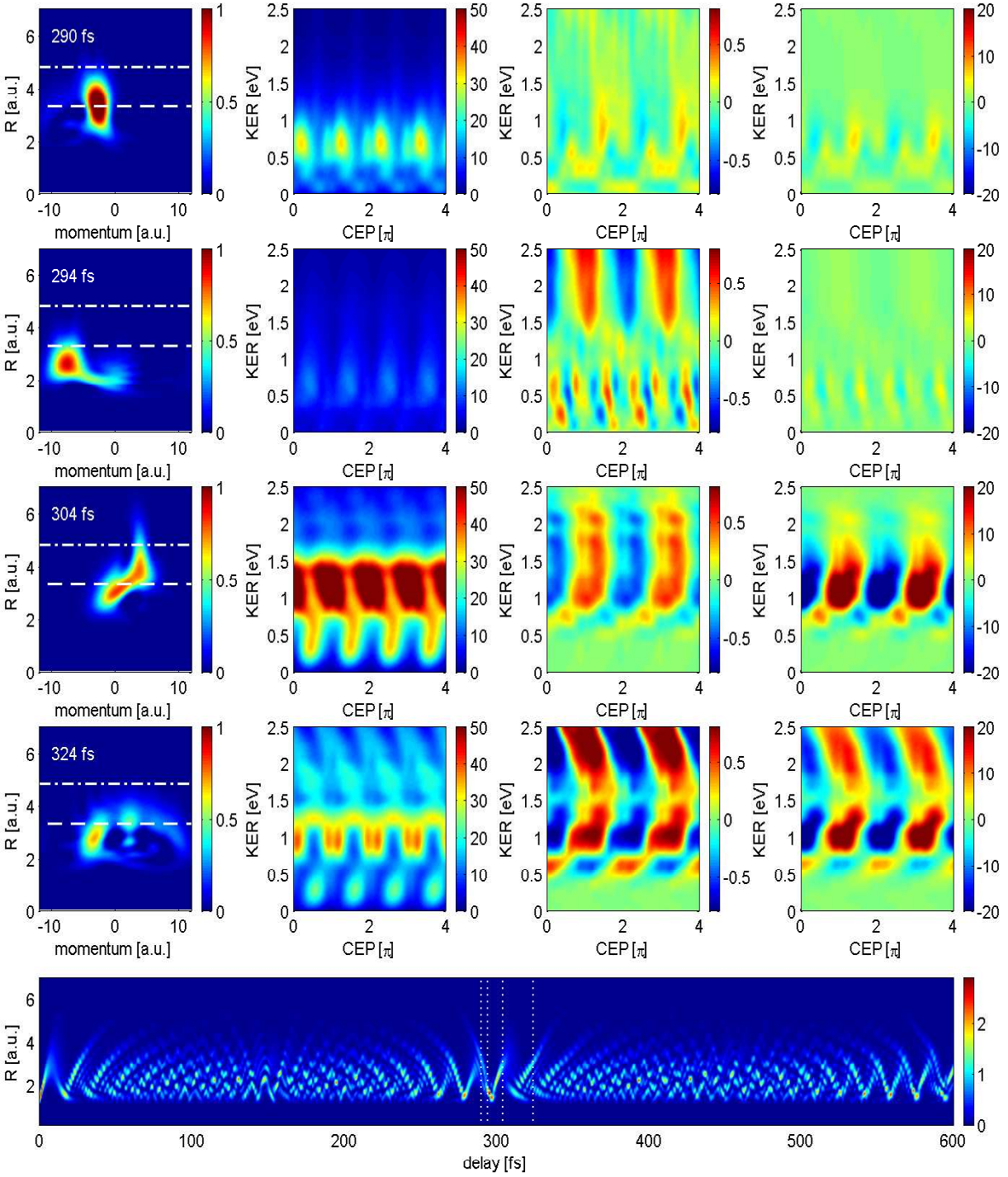

Figure 6.22: Same as figure 6.21, but for delays in the half-revival.

large R and has a positive momentum.
The comparison with the Husimi distribution reveals how the asymmetry strength depends on the wave packet dynamics. In the following subsection, the delay dependent shift of the asymmetry is analyzed.

6.4.2 WKB phase

The results presented above provide an insight into the connection between the strength of the asymmetry and the properties of the nuclear wave packet. In the revival, not only a delay dependent change of the asymmetry strength, but also a tilt of the asymmetry stripes, i.e. a shift of the CEP dependence of the asymmetry (see figures 6.9 and 6.17), is observed .
The origin of this shift can be explained by regarding the theoretical model presented in section 5.3 of the previous chapter. Here it was shown that the asymmetry can be interpreted as an interference between dissociation from the $2p\sigma_u$ state with the net absorption of an odd number of photons n, and dissociation from the $1s\sigma_g$ potential curve with the net absorption of an even number of photons n'. As can be seen from equation (5.24), the periodicity in the CEP dependence of the asymmetry is determined by $n - n'$, whereby $n - n' = 1$ for a periodicity of 2π as observed here. The positions of the maxima and minima of the asymmetry relative to the CEP axis is determined by the relative phase of the interfering wave packets[10]. Hence, the shift of the asymmetry with the KER and the delay can be attributed to a KER and delay dependence of this relative phase.
In order to obtain a simple picture of the KER dependent shift of the asymmetry, the phases of the interfering wave packets were approximated by the corresponding WKB[11] phases. The WKB method [Wen26, Kra26, Bri26, Dun32] is a semi-classical approximation of the solution of a one-dimensional stationary Schrödinger equation. The approximate solution for a potential $V(x)$, which can be regarded as constant over the de Broglie wavelength, is given by

$$\psi(x,t) = \left(\frac{constant}{[E - V(x)]^{1/4}}\right) exp\left(\pm i\, m \int dx' \sqrt{2m\,[E - V(x')]} - iEt\right), \tag{6.7}$$

where m is the mass and E the energy. The phase of a wave packet propagating along the potential $V(x)$ can thus be approximated by the exponent in equation (6.7). To obtain the relative phase of the interfering wave packets, it is sufficient to solve the integral $\int dx' \sqrt{2m\,[V(x') - E]}$. The term iEt does not contribute to the relative phase as interference occurs only if the dissociation channels contribute to the same energy E.
For calculating the relative phase, it was assumed that a part of the wave packet is launched to the $2p\sigma_u$ state at a certain internuclear distance R_s. The WKB phase was then obtained by numerically solving the integral $\int_{R_s}^{\infty} dx' \sqrt{2m\,[V(x') - E]}$ for the ungerade and the gerade potential curve. The relative phase is then given by the difference of the obtained results. It is shown in figure 6.23 as a function of the KER for $R_s = 4.8\,a.u.$, which corresponds to the 1ω crossing. One can see, that the relative phase becomes more and more KER independent with increasing KER. Thus, the shift of the asymmetry relative to the CEP axis is expected to be less pronounced for

[10] In equation (5.24), $\delta_u - \delta_g$ can be regarded as this relative phase. In [HE09], it is shown that also the amplitudes $\langle (g,u), E_k | \Psi_n \rangle$ provide a small energy dependent phase shift.
[11] Wentzel-Kramers-Brillouin

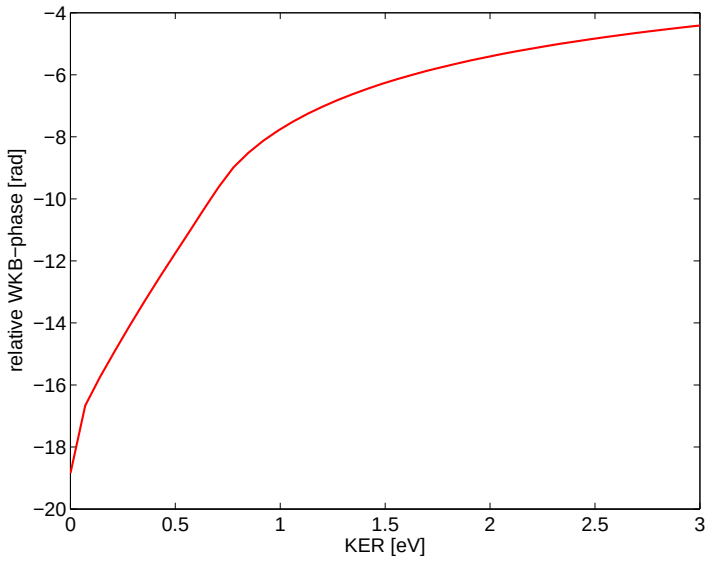

Figure 6.23: Relative WKB phase of the interfering wave packets as a function of the KER. The phase was calculated for the propagation along the gerade and the ungerade potential curve starting from an internuclear distance of $R_s = 4.8 a.u.$.

higher KER. This is indeed observed in the single-pulse measurements and calculations, where the asymmetry stripes become more straight with increasing KER (see figures 5.5 and 5.19).
A shift of the asymmetry relative to the CEP axis is observed in the revival also as a function of the delay, resulting in the tilt of the asymmetry stripes observed in figure 6.9 and 6.17. This shift has the same periodicity as the oscillation of the bound wave packet and occurs only in the revival, i.e. when the wave packet is well localized. This indicates that the motion of the bound wave packet influences the relative phase of the dissociation channels. The tilt of the asymmetry stripes was shown to decrease with increasing KER, which means that the influence of the wave packet motion is smaller for high KER. This can be understood by regarding the KER dependence of the WKB phase. For low KER, the relative phase reveals a strong KER dependence, indicating that the phase accumulated during the propagation along the potential curves plays an important role. For high KER, the relative phase becomes rather constant. This means that the phase accumulated during the propagation along the potential curves becomes less important. Therefore, the relative phase is less sensitive to the dynamics of the nuclear wave packet.

6.4.3 Theoretical interpretation

With the results presented in this section, a simple model regarding the interplay between the motion of the nuclear wave packet and the asymmetry can be developed.
In the revival, the wave packet is well localized and oscillates in the $1s\sigma_g$ potential. The dissociation yield as well as the asymmetry strength depends on the momentum and the position of the nuclear wave packet at the time the control pulse is applied. The coupling between the $1s\sigma_g$ and the $2p\sigma_u$ state by the laser field is thereby strong at large R, whereas at small R the energy gap

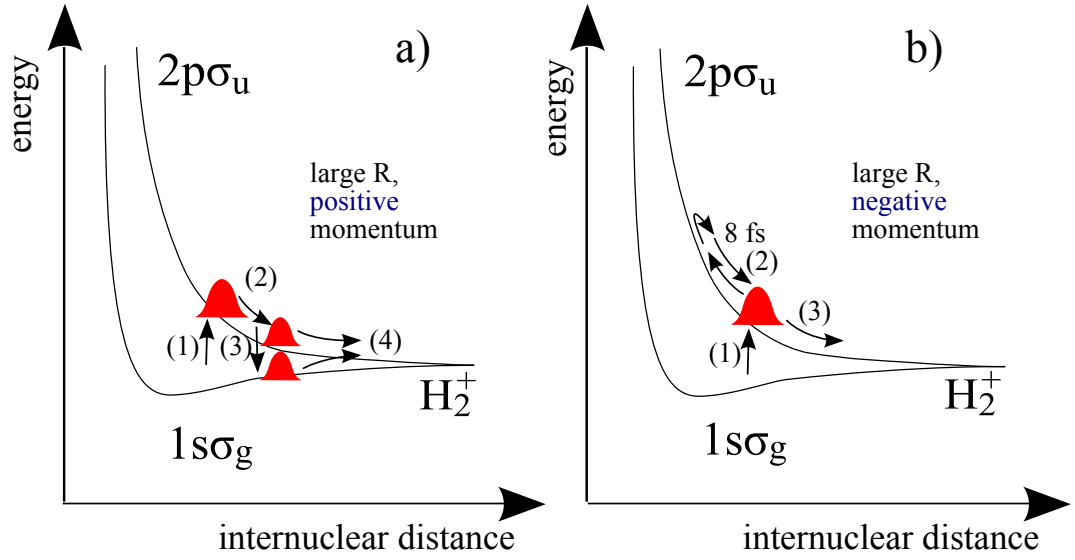

Figure 6.24: Schematic illustration of the dependence of electron localization on the wave packet dynamics. a) The nuclear wave packet is located at large R when the control pulse is applied, and has a positive momentum. The laser field of the pulse can efficiently couple the two electronic states. Population is thereby transfered to the $2p\sigma_u$ state (1) and slides down the potential curve (2). A part of the population is transfered back to the $1s\sigma_g$ state (3). It has gained enough energy, to overcome the potential barrier so that dissociation occurs from both, the $1s\sigma_g$ and the $2p\sigma_u$ curve (4). The two dissociation channels interfere and a pronounced asymmetry is obtained. b) The nuclear wave packet is located at large R and has a negative momentum. The coupling by the laser field is efficient such that population is transfered to the $2p\sigma_u$ curve (1). Due to its negative momentum, the population first moves towards small R (2) before it slides down the potential curve and dissociates (3). It requires about $8\,fs$ to return to the region of strong coupling. The laser field has almost vanished at that time so that there is no population transfer back to the $1s\sigma_g$ state. In this case, no interference and thus no asymmetry can occur.

to the $2p\sigma_u$ state is too high for the laser field to induce a significant coupling. For a population transfer between the $1s\sigma_g$ and the $2p\sigma_u$ state, the nuclear wave packet (or a part of it) has to be located at large R when the laser field is strong enough to induce an efficient coupling.
The population transfer is small when the wave packet is located at small R and has a negative momentum, i.e. moves towards small R. In this case, the wave packet reaches a large internuclear distance only when the laser field has mostly vanished. Thus, no efficient population transfer can occur so that the dissociation yield and the total asymmetry are small. This was observed, for example, at a delay of $294\,fs$ in figure 6.22. For this delay, however, the normalized asymmetry is high, which can be attributed to the small fraction of the wave packet moving outwards. This can be understood by considering that the asymmetry is caused by an interference between two dissociation channels, which lead to the same KER. If dissociation occurs via only one of the two channels, no asymmetry is obtained, whereas the asymmetry is maximal when the dissociating population is the same for the two interfering channels. Thus, even if the dissociation yield is

very small, the relative population of the interfering dissociation channels can be such that a high normalized asymmetry is obtained.
The dissociation yield and the asymmetry increase again when the wave packet has a positive momentum, i.e. moves towards large R, as in this case an efficient population transfer can occur. Thereby, the dissociation yield as well as the asymmetry is maximal when the wave packet is located at large R as there the coupling is very efficient (see figure 6.24 (a)).
Note that the maximum of the dissociation yield in figures 6.21 and 6.22 depends on the position of the wave packet. When the wave packet is located at small R, the dissociation yield has a maximum at large KER and vice versa. The total asymmetry reveals a similar behavior. The reason is that the KER, the wave packet gains by sliding down the potential curve, depends on the value of R, at which the transition to the $2p\sigma_u$ state occurs, whereby it decreases with increasing R.
When the wave packet is still at large R, but has a negative momentum, the dissociation yield and the absolute asymmetry decrease strongly as can be seen, for example, at a delay of $290\,fs$. In this case, the normalized asymmetry becomes minimal, which indicates that the interference between different dissociation channels is weak. This can be understood by regarding the motion of the dissociating wave packets on the potential curves illustrated in figure 6.24. The initial momentum of the population, which is transferred to the $2p\sigma_u$ state ((1) in figure 6.24), is negative so that the wave packet moves first towards small R before it slides down the potential curve (2). The time, the wave packet needs to return to large R, was estimated by assuming that the wave packet is set to the $1s\sigma_g$ state at the 3ω crossing with a negative initial momentum. The time required to return to that point was found to be approximately $8\,fs$ for a momentum of $-5\,a.u.$ and about $10\,fs$ for a momentum of $-10\,a.u.$. This means that for a $6\,fs$ laser pulse the laser field has already mostly vanished when the wave packet returns to large R so that no efficient population transfer to the $1s\sigma_g$ state can occur. For dissociation from the $1s\sigma_g$, however, such a transfer of population is necessary as the population remaining bound in the $1s\sigma_g$ state cannot overcome the potential barrier. Therefore, there is only dissociation from the $2p\sigma_u$ state (3), so that no interference and thus no electron localization can occur.
With this intuitive model the dependence of the asymmetry strength can be well understood in the revival, where the wave packet is localized. When the wave packet dephases, the situation becomes less clear as the wave packet is spread in phase space. However, also in the dephasing the wave packet reveals some structure, which changes with the delay so that the asymmetry does not become entirely delay independent.
When regarding figure 6.20, one can see that the delay dependence of the asymmetry is not mirror symmetric to the center of the revival, but is more pronounced after the center. The reason for this is probably that after the revival center the bound wave packet is better localized during its outward motion, whereas before the revival it is better localized during the inward motion (see also section 6.1.1).
The WKB phase was shown to provide a qualitative explanation for the tilt of the asymmetry stripes, i.e. the delay dependent shift of the asymmetry relative to the CEP axis, observed in the revival. This shift indicates that the motion of the wave packet manifests in a shift of the relative phase of the interfering dissociation channels. For an estimation of this shift, the simple semi-classical model presented here is, however, not sufficient. It does, for example, not include effects caused by a time dependent change of the potential caused by the laser field, which can affect the motion of the dissociating wave packets. The WKB phase can, however, provide a

qualitative understanding of the KER dependence of the relative phase. For intermediate energies, the relative phase is strongly dependent on the KER. Here the relative phase is sensitive to the evolution of the wave packet on the potential curves. For high energies, however, the WKB phase is mainly determined by the total energy. Thus, the phase accumulated during the propagation along the different dissociation pathways becomes less important so that the phase difference between the interfering dissociation channels is only weakly affected by the dynamics of the nuclear wave packet.

6.4.4 Comparison with other theoretical predictions

A similar control scheme for electron localization as presented in this chapter was proposed by Calvert et al. [CRW$^+$10]. There it was analyzed how a two-pulse scheme can be used to enhance the absolute asymmetry for dissociating D_2, i.e. to maximize the degree of electron localization and the dissociation yield simultaneously.
In these calculations, a nuclear wave packet is launched in the $2p\sigma_u$ potential of D_2^+. Contrary to the calculations presented in this thesis, a fixed ionization time is assumed so that the effect of a finite length of the pump pulse is not considered. After a variable time delay, an IR laser pulse with a duration of $7\,fs$ and $0.2\,PW/cm^2$ is applied, which induces dissociation and electron localization.
The obtained absolute asymmetry as a function of the delay and the CEP of the second laser pulse is shown in figure 6.25 for a delay range around the half-revival of D_2^+, which is centered around $550\,fs$. Hereby, the asymmetry was integrated over the entire KER range of the deuterons.
In the revival, the absolute asymmetry strongly depends on the delay. Thereby, the asymmetry is pronounced only for small delay ranges, which repeat with a periodicity of about $25\,fs$. It almost vanishes for the delays in between. The asymmetry exhibits tilted stripes, i.e. the asymmetry shifts relative to the CEP axis with the delay. The maxima of the asymmetry are correlated with a high dissociation yield. The asymmetry is high when the wave packet moves outwards and drops to a minimum when the wave packet is close to the inner turning point. The most pronounced asymmetry is observed for a delay around $570\,fs$ and $600\,fs$. Here the nuclear wave packet is more localized when moving towards large internuclear distances than for any other delays.
The results of Calvert et al. demonstrate that the absolute asymmetry can be maximized by choosing the value of the delay and the CEP appropriately. The strongest asymmetry is achieved, when the wave packet is well localized and moves outwards, which is in good agreement with the results of the simulations presented in this chapter.
The results of Calvert et al., however, cannot be directly compared to the results presented here as the calculations were performed for D_2 and for other pulse parameters. Besides that, in the calculations of Calvert et al. the influence of the finite length of the pump pulse is not considered. In the simulations and calculations presented in this chapter, however, the nuclear wave packet is launched at different start times for each value of the delay. Thereby, the start times are correlated with the CEP as the pump and the control pulse have the same phase. This influence of the different possible start times was shown to be crucial for obtaining a good agreement of the theoretical calculations with the experiment.

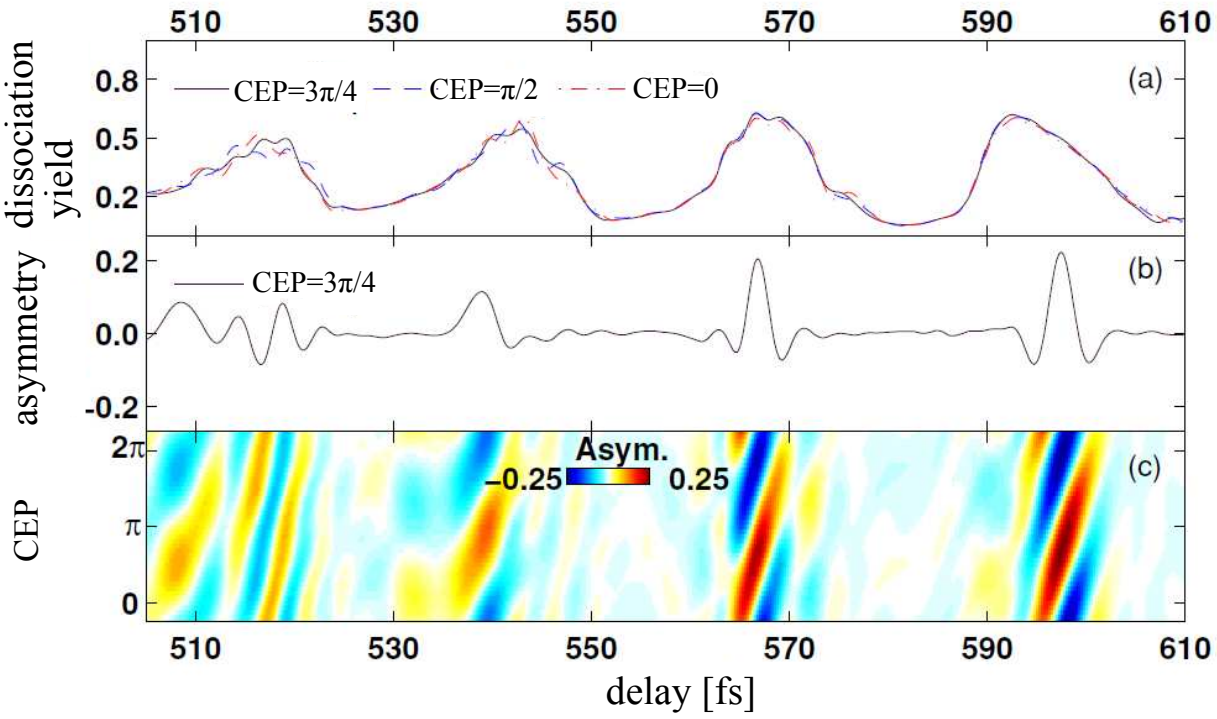

Figure 6.25: Theoretical predictions by Calvert et al. [CRW+10] for a pump-control scheme applied for D_2 in the half-revival. The calculation was performed for a control pulse with a duration of $7\,fs$ and a peak intensity of $0.2\,PW/cm^2$. a) Dissociation yield as a function of the delay between pump and control pulse for different values of the CEP. b) Absolute asymmetry as a function of the delay for a CEP of $3\pi/4$. c) Absolute asymmetry as a function of the delay and the CEP.

6.5 Conclusions

In this chapter, the first experimental realization of a pump-control scheme for steering electron localization in dissociating H_2^+ was presented. The results demonstrate the ability to control the electronic motion by the shape and motion of the bound nuclear wave packet. Thereby, the time delay between the pump and the control pulse determines the properties of the nuclear wave packet. The most pronounced delay dependence of the asymmetry is observed in the revival, where the wave packet is localized and oscillates in the ground state potential of H_2^+.

The delay dependence of the asymmetry for the measurement in the revival is illustrated in figure 6.26 (b). Here the maximal amplitude[12] of the asymmetry is shown as a function of the KER and the delay. The amplitude reveals clear maxima and minima for intermediate KERs, which demonstrates the ability to control to what extent the molecule is susceptible to electron

[12]For each delay and KER range, the measured asymmetry was fitted along the CEP axis by a sinusoidal function (see section 6.2.1). The amplitude of this function represents the maximal asymmetry that can be obtained for each KER and delay range.

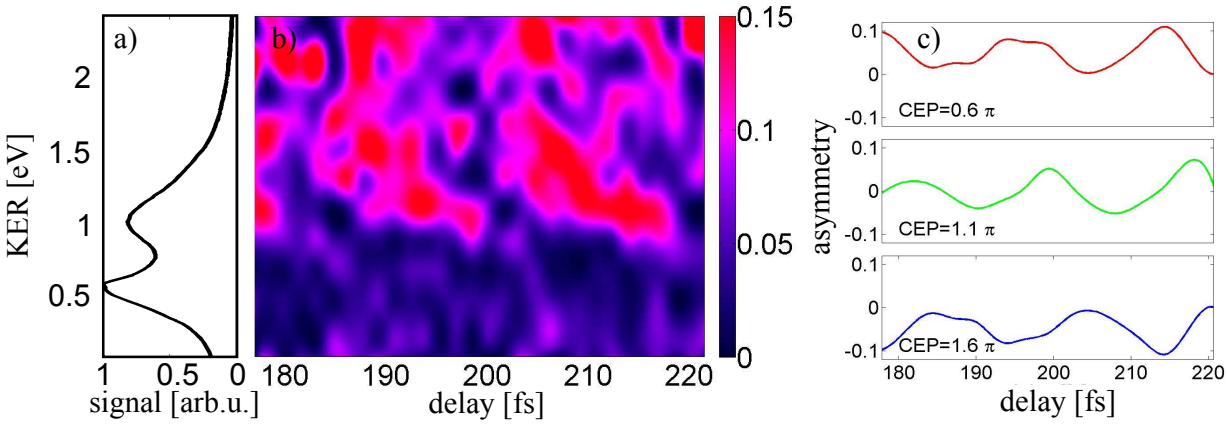

Figure 6.26: Illustration of the ability to control electron localization by the delay on the basis of the measurement in the revival (see figure 6.9). a) KER dependent dissociation yield integrated over all CEP and delay values. b) Maximal (normalized) asymmetry that can be achieved as a function of the delay and the KER. Above $2\,eV$ the asymmetry contains artifacts. Here the signal to noise ratio is low due to the small count rate. c) Normalized asymmetry as a function of the delay for different values of the CEP.

localization. As the amplitude of the asymmetry, i.e. the degree of electron localization, depends on the proportion of dissociation along the $1s\sigma_g$ and the $2p\sigma_u$ potential curve, the control of the asymmetry strength is directly related to the ability to control the dissociation pathway of the nuclear wave packet by the time delay of the pulses [MMC+07].
The strength of the asymmetry can be steered by choosing the value of the CEP and the delay. This is illustrated in figure 6.26 (c) for the measurement in the revival. Here the asymmetry for a KER range between $0.8\,eV$ and $1.2\,eV$ is shown as a function of the delay for three different values of the CEP (compare figure 6.9). For a CEP of $1.6\,\pi$, the asymmetry is negative, i.e. the electron is predominantly localized at one of the two protons over the entire delay range. The degree of localization at this proton can be maximized or minimized by the delay. The same can be done for the localization at the other proton for a CEP of $0.6\,\pi$. When choosing a CEP of $1.1\,\pi$ the asymmetry changes from positive to negative values as a function of the delay. In this case, the delay determines at which of the two protons the electron remains predominantly localized.
In the dephasing region and the transition region, experiments and simulations reveal a strong normalized asymmetry, at least for high KER. The normalized asymmetry thereby reflects the relative population of the interfering dissociation channels. These results indicate, that for obtaining a high asymmetry, a localized wave packet is not a prerequisite. However, the dissociation yield and thus the absolute asymmetry has pronounced maxima only when the wave packet is localized. Thus, in order to maximize the absolute asymmetry a delay in the revival, where the wave packet is well localized, has to be chosen (see figure 6.20).
The experimental results are in good qualitative agreement with wave packet simulations, which reproduce the main features of the measured delay dependence of the asymmetry. The results of the calculation could therefore be used to develop an illustrative semi-classical model regarding the interplay between the dynamics of the nuclear wave packet and the localization of the

electron. With this simple model, the main features of the delay dependence in the revival as well as the difference between revival and dephasing can be explained qualitatively. Even though the electron and its motion was not considered explicitly in the wave packet simulations, its final localization is well reproduced.

Summary and outlook

The advent of intense laser pulses was a breakthrough towards the goal to actively control chemical reactions, i.e. to selectively steer the making and breaking of molecular bonds. For achieving such control, understanding the interaction of intense laser fields with molecules is of profound importance. A prototype reaction for such investigations is the dissociation of the most fundamental molecular system, H_2^+ (D_2^+).

In the framework of this thesis, the possibility to steer the localization of the electron at one of the protons in the dissociation of H_2^+ by using ultrashort laser pulses with a stabilized carrier-envelope phase (CEP) was demonstrated experimentally. In single pulse measurements, the CEP dependence of electron localization was investigated. The use of a reaction microscope as detector allowed to analyze details of the fragmentation process not accessible by other detection techniques. In this way, the electron localization mechanism could be clarified. By the application of a pump-control scheme with two time-delayed phase-stabilized laser pulses, the degree of control was significantly enhanced. In these experiments, the ability to steer electron localization by the shape and dynamics of the nuclear wave packet was demonstrated experimentally for the first time.

The long term stabilization of the carrier-envelope phase required for these measurements represents a major experimental challenge. In the course of this thesis, an already existing laser system was CEP-stabilized and optimized for long term phase-stability. The laser pulses were generated in a titanium:sapphire oscillator and amplified by chirped pulse amplification in a multipass amplifier system. By spectral broadening in a gas filled hollow fiber in combination with a chirped mirror compressor, laser pulses with a duration of $6\,fs$ and a peak intensity up to $10^{15}\,W/cm^2$ were obtained. The CEP in the oscillator was stabilized by using an f-0f interferometer and after the fiber compressor by using an f-2f interferometer, both in combination with a feedback loop. For the two-pulse measurements, the CEP was additionally independently monitored by a stereo-ATI spectrometer. By this means, phase drifts could be detected and corrected, which allowed to further increase the measurement time.

By using a reaction microscope, the three-dimensional momentum vectors of all charged reaction fragments could be reconstructed so that fully differential data of the fragmentation process were obtained. Furthermore, the possibility to measure particles in coincidence allowed to investigate the relation between the electron and proton emission, which allowed to clarify the electron localization mechanism.

The measured asymmetry in the proton emission for a single-pulse measurement is shown in figure S1 for two different ranges of the emission angle. A clear CEP dependent asymmetry in the emission direction of the protons can be observed in a kinetic energy release (KER) range between 0 and $3\,eV$. The asymmetry stripes are tilted, i.e. the asymmetry reveals a KER de-

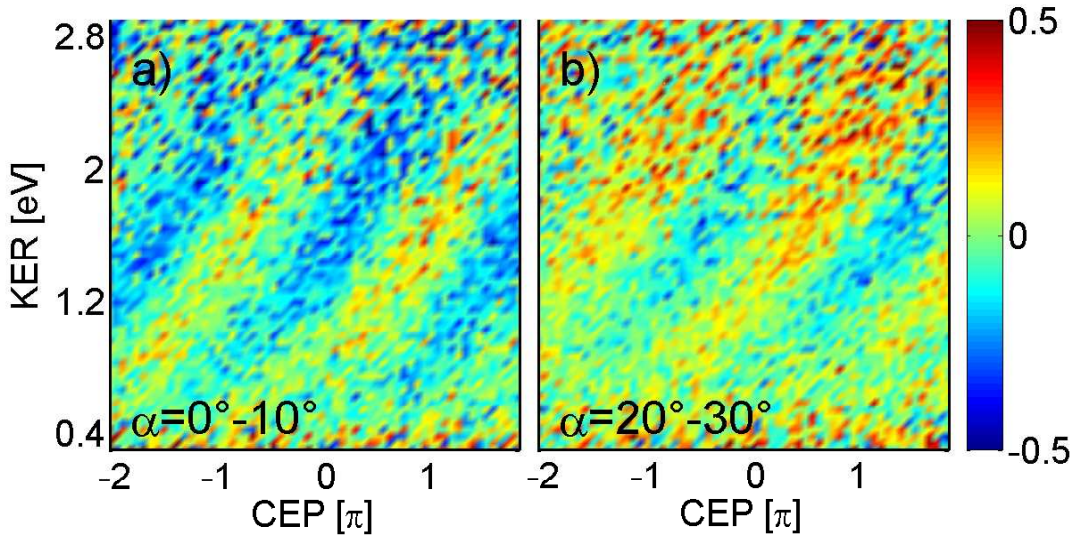

Figure S1: Experimental results of a single pulse measurement on H_2 with CEP-stabilized laser pulses. The asymmetry in the emission direction of the proton is shown in dependence of the carrier-envelope phase and the kinetic energy release.

pendent shift. Furthermore, a shift of the asymmetry in dependence of the emission angle of the protons is observed. The electrons detected in coincidence with the protons also reveal a CEP dependent asymmetry, which is, however, much weaker than that of the protons.
In this regime of kinetic energy release, dissociation can be attributed to bond-softening, i.e. to the formation of light induced states. No recollision mechanism is involved in this process, so that the experimental results cannot be explained by the model presented in [KSV$^+$06].
In order to gain more insight into the localization mechanism for the bond softening regime, wave packet simulations were performed. In these calculations, the nuclear wave packet was propagated on the $1s\sigma_g$ and the $2p\sigma_u$ potential curves. Dissociation and electron localization were induced by the laser field via a dipole coupling between the two electronic states. By these simulations, the main features of the experimental results could be well reproduced.
On the basis of the experimental and the theoretical results, a simple model for explaining the localization mechanism was developed: The neutral H_2 molecule is singly ionized in the laser pulse, whereby a vibrational wave packet is created in the electronic ground state $1s\sigma_g$ of H_2^+. The wave packet moves towards a large internuclear distance R. When it reaches the internuclear distance, where the energy gap between the $1s\sigma_g$ and the first excited electronic state $2p\sigma_u$ matches approximately the photon energy, the electric field in the tail of the laser pulse can efficiently couple these two states. Due to the gerade and the ungerade parity of the coupled electronic states, electron localization at one of the nuclei is achieved.
In this model, the asymmetry is caused solely by the coupling of the $1s\sigma_g$ and the $2p\sigma_u$ states by the laser field. The initial asymmetry induced by the ionization step, i.e. the asymmetry caused by removing the first electron from one of the nuclei, does not play a role. This assumption was experimentally proven by the asymmetry of the electron, which was detected in coincidence

with the proton. Although a clear CEP dependent asymmetry is found, it is much weaker than the asymmetry of the protons. Besides that, the asymmetry of the electron does not depend on the electron energy, whereas the proton asymmetry reveals a pronounced KER dependence. Furthermore, the electron asymmetry is independent of the KER of the protons. These findings indicate that there is no, or only a very weak connection between the emission direction of the proton and the electron. The initial electron localization can thus be ruled out to be the reason for the asymmetry in the proton emission.
With this simple model, also the results for measurements on D_2 could be explained. Here almost no asymmetry was observed for KERs below $1.5\,eV$, which can be attributed to an isotope effect: Due to the higher mass, the wave packet in D_2^+ propagates slower such that it reaches a large internuclear distance when the laser field has already mostly vanished. Only the high energetic part of the wave packet is fast enough to reach this region when the field is still sufficiently strong to induce a significant coupling.
The angle dependence of the asymmetry could be also explained qualitatively with the simple model presented above. As only the field component parallel to the internuclear axis contributes to the coupling, for an increasing angle between the molecular axis and the laser polarization axis, the coupling is reduced. In order to simulate this effect, the calculation was repeated for lower intensities, which would correspond to the effective intensities experienced for different angles. The calculated asymmetry reveales a shift with increasing angle in qualitative agreement with the experimental observations. The shift is, however, smaller than the one observed in the experiment. This difference can be probably attributed to the creation of a rotational wave packet in H_2^+. Due to the rotation of the molecule, the measured emission angle can be smaller than the angle between molecular axis and polarization axis at the time of the interaction with the laser pulse [ACE09].
For electron localization as observed in the experiments described in this thesis, the nuclear wave packet has to reach a large internuclear distance, when the laser field is sufficiently high to couple the gerade and the ungerade state. This suggests to enhance the control by the application of a second laser pulse. For this purpose, a pump-control scheme was applied by using two CEP-stabilized laser pulses. The first pump pulse ionizes the neutral H_2 molecule and launches a localized wave packet in the gerade state of H_2^+. A second control pulse is applied after a variable time delay inducing dissociation and localization of the electron. Investigating the delay dependent asymmetry in the revival region, where the nuclear wave packet is localized and oscillates in the potential well, allows to analyze the influence of the wave packet dynamics on electron localization. By comparing the asymmetry in the revival with the asymmetry in the dephasing region, where the wave packet is spread over the potential well, information on the role of coherence can be obtained.

The polarization axes of the two laser pulses were chosen to be perpendicular to each other. Due to the strong angle dependence of the dissociation probability, protons from dissociation in the first and the second pulse could be distinguished by their emission angle. In this way, events could be excluded, where the dissociation was already initialized by the pump pulse.
The delay dependent asymmetry for the measurements in the revival region is shown in figure S2 for two different KER ranges. For intermediate KERs around $1\,eV$, the strength of the asymmetry varies strongly with the delay with a periodicity of $17\,fs$, which corresponds to the vibrational period of the bound wave packet. Additionally, a delay dependent shift of the asymmetry relative to the CEP axis is observed, which reveals the same periodicity. The delay dependence becomes

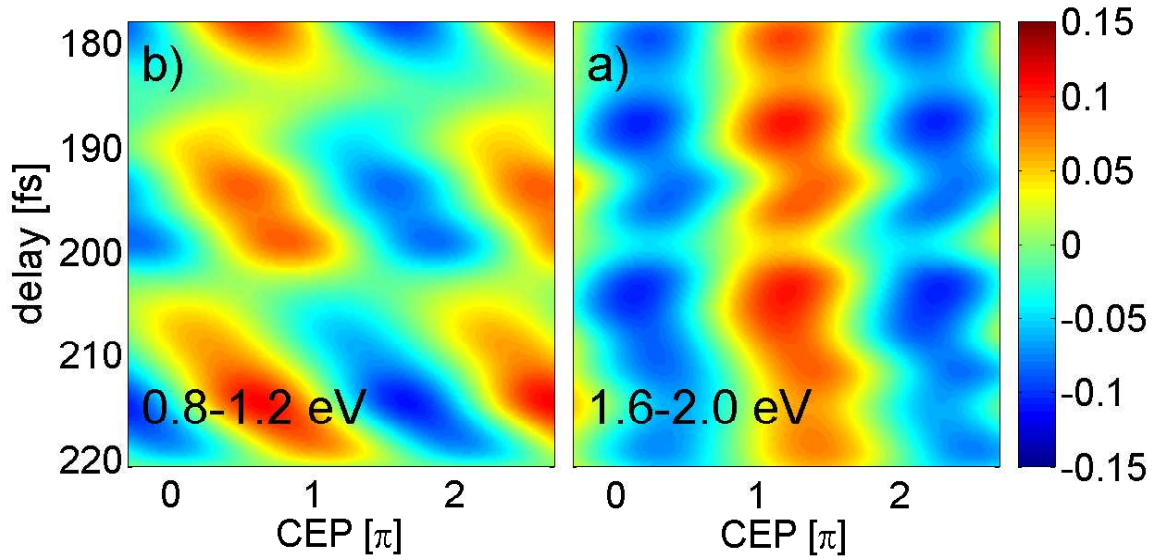

Figure S2: Experimental results of a pump-control measurement on H_2 in the revival region. The asymmetry is shown as a function of the delay for two different KER ranges.

less pronounced with increasing KER. In the dephasing region, the asymmetry was shown to be rather independent of the delay. Only for intermediate KERs, a modulation of the asymmetry strength with the delay can be observed.
In order to gain a better understanding of the experimental observations, wave packet simulations were performed similar to those for the single-pulse measurements. The results of the calculations qualitatively reproduce the main features of the experimentally observed delay dependence. The calculated asymmetry was compared to the dynamics of the bound nuclear wave packet at the time the control pulse was applied. In this way, a simple and intuitive model for explaining the results in the revival region could be developed: For electron localization to occur, population dissociating from the $2p\sigma_u$ state has to interfere with population dissociating from the $1s\sigma_g$ state. Therefore, the nuclear wave packet has to be located at large R when the laser field is strong enough to induce an efficient population transfer between these two states. If the nuclear wave packet moves towards large R when the control pulse is applied, the laser field can efficiently couple the two electronic states so that the asymmetry as well as the dissociation probability is high. The coupling is thereby most efficient when the wave packet is located at large R. If the wave packet reverses its direction, however, the asymmetry decreases. In this case, the wave packet launched to the $2p\sigma_u$ state first moves towards small R, before it slides down the potential curve and dissociates. When it returns back to large R, the laser field of the pulse has already mostly vanished. Hence, no efficient population transfer back to the $1s\sigma_g$ state can take place and thus almost no dissociation occurs along the $1s\sigma_g$ curve. The dissociation probability and the asymmetry drop to a minimum when the wave packet moves inwards and is localized at small R as in this case an efficient coupling by the laser field is not possible.
The delay dependent shift of the asymmetry relative to the CEP axis could be also qualitatively

explained by a simple model. The position of the maxima and the minima relative to the CEP axis depend on the relative phase of the interfering wave packets. The delay dependent shift in the revival thus indicates that the dynamics of the bound nuclear wave packet imprints a relative phase to the interfering wave packets. An estimation of this relative phase by using the WKB approximation revealed that the energy dependence of the relative phase decreases for large KER. This means that for high KER the relative phase is less dependent on the dynamics of the bound wave packet, which is in good agreement with the experimental observations.
In the dephasing region, the bound wave packet is spread over the potential well such that almost no delay dependent shift of the relative phase occurs. The delay dependence of the asymmetry strength does, however, not completely vanish, which can be attributed to substructures of the bound wave packet.
These results demonstrate the possibility to control electron localization by the shape and dynamics of the bound nuclear wave packet. With the presented pump-control scheme the asymmetry can thus be steered by two parameters, the carrier-envelope phase and the delay, so that a high degree of control can be achieved.
The experimental results presented in this thesis, revealed detailed insight into the electron localization mechanism for bond softening. The combination of ultrashort phase-stable laser pulses with the advantages of the reaction microscope will allow to investigate electron localization also for other molecular systems. Of great interest is, for example, the role of the first ionization step in electron localization involving a recollision process, like for example for CO molecules [ZvdHZ$^+$09].
The CEP-effects in recollision processes are, however, strongly dependent on the pulse length. For observing pronounced phase effects for such processes, the pulse length has to be reduced. For this purpose, one can make use of the fact, that recollision can occur only if the laser field is linearly polarized. The effective pulse duration can therefore be reduced if the pulse is linearly polarized for a time shorter than the pulse duration. This can be realized by using a so-called polarization gating [SME$^+$nt, OSDV05]: A linearly polarized laser pulse passes through a multiple-order quarter wave plate. Thereby, it splits into two linearly polarized pulses with perpendicular polarization. The pulses are shifted relative to each other by a time delay, which is shorter than the pulse duration. At the times when the two pulses temporally overlap and have the same amplitude, the resulting electric field is circularly polarized. The outgoing laser pulse is then circularly polarized in the center and linearly polarized at the beginning and the end. This pulse passes through a further quarter wave plate such that the linear field is turned into a circular one and vice versa. Thereby, a pulse is created, which is linearly polarized only in the pulse center. By this means, the time window, in which a recollision process can occur, can be significantly reduced. The achieved enhancement of the CEP-effects together with the increased measurement time will allow for a detailed analysis of the phase dependence in recollision processes.
The pump-control measurements presented in this thesis clearly demonstrate that the properties of the nuclear wave packet can be used as further control parameter for electron localization. Further insights into the relation between electron localization and the wave packet properties would be gained by measuring the asymmetry over a long delay range. In this way, the different stages of the wave packet evolution as well as the transition between them could be further analyzed. Furthermore, by long term measurements, the statistics would be improved so that the delay dependence could be investigated with a better temporal resolution. Such a pump-control

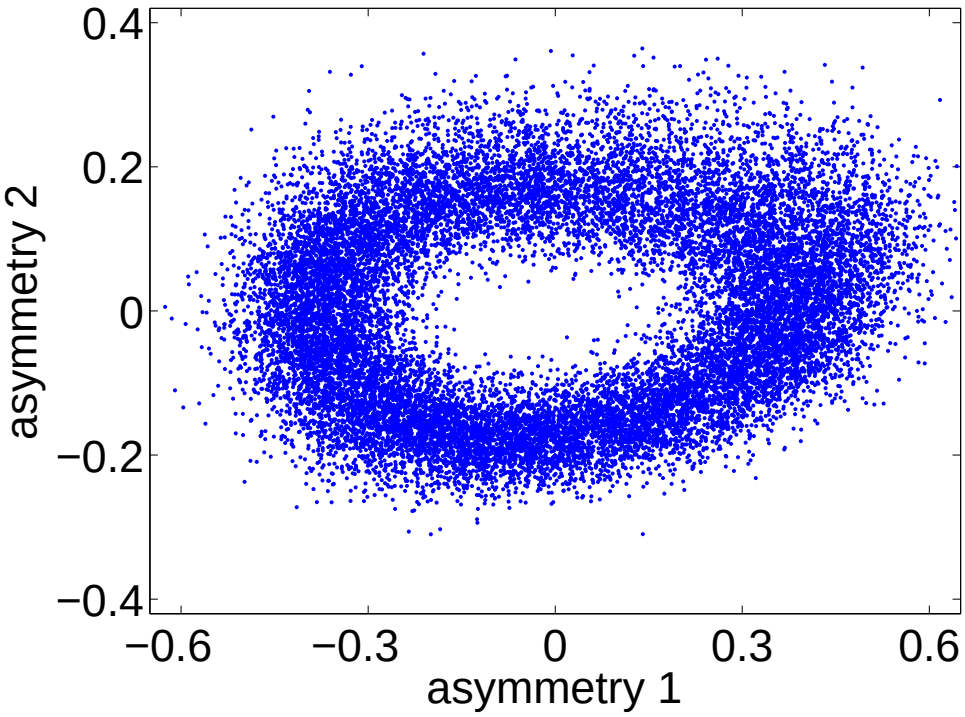

Figure S3: Single-shot measurement of the phase ellipse by the stereo-ATI spectrometer. The asymmetry for high energetic electrons for two different energy regions is plotted versus each other. Each position on the phase ellipse can be assigned to a CEP value. In this way, the CEP of each single laser pulse can be determined.

scheme could be applied also to other molecular systems. The properties of the nuclear wave packet could be steered additionally by the application of a further laser pulse or by tuning the pulse properties via a pulse-shaper.
So far, experiments of this kind were restricted by the limited time a stabilization of the carrier-envelope phase can be achieved. A stabilization of the phase would, however, become obsolete if the CEP of each laser pulse could be measured. For this purpose, the setup of the stereo-ATI spectrometer was improved. The signal to noise ratio was significantly enhanced so that single-shot measurements of the CEP are now possible.

A phase ellipse obtained in such a single-shot measurement is shown in figure S3 (compare section 3.4). Here the asymmetry of the high energetic electrons for two energy ranges is plotted versus each other. By using the simple theoretical model developed in [Hof09], each position on the phase ellipse can be assigned to a certain CEP value. In future measurements, the signal of the stereo-ATI spectrometer will be monitored for each single pulse. Hence, no phase stabilization will be required as the data measured in the reaction microscope can be sorted in dependence of the CEP. By this method, the measurement time will be extended to several days[13]. In this way, long term measurements with good statistics will become possible.
In the near future, pump-probe experiments on atoms are planned, which will allow to reveal

[13]The measurements carried out in the course of this thesis required measurement times up to one day

the full electronic level structure of the analyzed system. The feasibility of this spectroscopic scheme was demonstrated in recent analytical and numerical calculations [ORP10]. An intense pump pulse thereby excites a coherent superposition of bound as well as continuum electronic states. By a second laser pulse, these states are projected onto common continuum states. As the transitions in the pump and the probe pulse are nonlinear, there are no restrictions by dipole selection rules. Thus, all energetically allowed transitions can be accessed. The ejected photo-electrons are then detected with the reaction microscope. During the time between the pump and the probe pulse, the intermediate states evolve field free and accumulate different phases due to their different energies. These phase differences result in an interference pattern in the energy spectrum of the photo electrons, which reveals the energy level spacing of the analyzed atom. This pump-probe scheme thus represents a new spectroscopic method, which allows to reveal the complete electronic structure of atoms.

Appendix A

Atomic units

In atomic physics, the use of *atomic units* is customary. The base units of this system are related to the dimensions of the hydrogen atom.

Base units and natural constants

$r_e = 1a.u. = 5.2918 \cdot 10^{-11}m$	Bohr radius of the K-shell of hydrogen
$m_e = 1a.u. = 9.1095 \cdot 10^{-31}kg$	rest mass of the electron
$q_e = e = 1a.u. = 1.6022 \cdot 10^{-19}As$	charge of the electron
$\hbar = m_e v_e r_e = 1a.u.$	reduced Planck constant
$c = e^2/(\hbar\alpha) = 137a.u.$	speed of light

The conversion factors to other common units are:

Conversion factors

energy	$E[eV] = 27.2 \cdot E[a.u.]$
momentum	$p[Ns] = 1.995 \cdot 10^{-24} \cdot p[a.u.]$
time	$t[s] = 4.134 \cdot 10^{16} \cdot t[a.u.]$
velocity	$v_e = 1a.u. = 2.1877 \cdot 10^6 m/s$
max. el. field strength in a laser pulse	$1a.u. \hat{=} 35.1 \cdot 10^{15} W/cm^2$

Appendix B

Details of the wave packet simulations

In this chapter, the basic concepts of the wave packet simulations for calculating the CEP dependent asymmetry in the dissociation of H_2 and D_2 are presented. A more detailed description of the used program package can be found in [Nie07].

B.1 Crank-Nicholson split-operator propagation

The time evolution of a wave function $\Psi(x,t)$ is described by the time dependent Schrödinger equation, which is given by

$$i\frac{\mathrm{d}}{\mathrm{d}t}\Psi(x,t) = \hat{\mathcal{H}}\Psi(x,t). \tag{B.1}$$

For a time independent Hamiltonian, the solution of this equation is

$$\Psi(x,t) = \mathrm{e}^{-i\hat{\mathcal{H}}(t-t_0)}\Psi(x,t_0). \tag{B.2}$$

In case of a time dependent Hamiltonian, one can regard a time step Δt, in which the Hamiltonian is approximately constant. The wave function after this time step can then be approximated as

$$\Psi(x,t+\Delta t) = \mathrm{e}^{-i\hat{\mathcal{H}}\Delta t}\Psi(x,t). \tag{B.3}$$

For a particle in an external potential $\hat{\mathcal{V}}$, the Hamiltonian is given by

$$\hat{\mathcal{H}} = \hat{\mathcal{T}} + \hat{\mathcal{V}}, \tag{B.4}$$

where $\hat{\mathcal{T}}$ is the operator of the kinetic energy. Since the operator of the potential and the operator of the kinetic energy do not commute, the time propagation operator can not be written as a product of two exponential functions, one containing only $\hat{\mathcal{V}}$ and one only $\hat{\mathcal{T}}$. Therefore the *Baker-Campbell-Hausdorff-formula* is applied which gives

$$\mathrm{e}^{-i(\hat{\mathcal{T}}+\hat{\mathcal{V}})\Delta t} = \mathrm{e}^{-i\hat{\mathcal{V}}\Delta t/2}\mathrm{e}^{-i\hat{\mathcal{T}}\Delta t}\mathrm{e}^{-i\hat{\mathcal{V}}\Delta t/2} + \mathcal{O}\left(\Delta t^3\right). \tag{B.5}$$

This so-called split-operator method is accurate up to Δt^3. Such a splitting is useful as then, for the kinetic energy operator, free propagation can be applied and since the potential is diagonal

on the spatial lattice, the propagation of the potential reduces to a multiplication of the wave function with a scalar function in the exponential.
The Crank-Nicholson method makes use of the so-called Cayley-approximation for the time propagator

$$\mathrm{e}^{-i\hat{\mathcal{H}}\Delta t} = \frac{\hat{1} - i\hat{\mathcal{H}}\Delta t/2}{\hat{1} + i\hat{\mathcal{H}}\Delta t/2}. \tag{B.6}$$

This involves the inversion of a matrix

$$\underline{\underline{A}}^{-1} \equiv \left(\hat{1} + i\hat{\mathcal{H}}\Delta t/2\right)^{-1} \tag{B.7}$$

which is numerically demanding. It can be avoided by defining a wave function Φ which fulfills the equation

$$\Phi(t) = 2\left(\hat{1} + i\hat{\mathcal{H}}\Delta t/2\right)^{-1}\Psi(t). \tag{B.8}$$

Φ can be determined by solving the equations

$$\frac{1}{2}\left(\hat{1} + i\hat{\mathcal{H}}\Delta t/2\right)\Phi(t) = \Psi(t). \tag{B.9}$$

The propagated wave function $\Psi(t+\Delta t)$ can then be obtained by

$$\begin{aligned}\Psi(t+\Delta t) &= \frac{\hat{1} - i\hat{\mathcal{H}}\Delta t/2}{\hat{1} + i\hat{\mathcal{H}}\Delta t/2}\Psi(t) \\ &= \left(2\left(\hat{1} + i\hat{\mathcal{H}}\Delta t/2\right)^{-1} - \hat{1}\right)\Psi(t) \\ &= \Phi(t) - \Psi(t).\end{aligned} \tag{B.10}$$

For the short-time propagation, therefore only a linear set of equations (B.9) has to be solved. The computational effort is further reduced by using a three point formula for the second derivative

$$\frac{\mathrm{d}^2}{\mathrm{d}x^2}\Psi(x,t) = \frac{\Psi(x-\Delta x,t) - 2\Psi(x,t) + \Psi(x+\Delta x,t)}{\Delta x^2}. \tag{B.11}$$

The operator for the kinetic energy $\exp\{-i\hat{T}\Delta t\}$ has then a tridiagonal form, whereby the upper and lower diagonal contains only the constants $-i\Delta t/(4\Delta x^2)$. Thus only the elements of the main diagonal have to be calculated for each time step Δt.

B.2 Coupled channel propagation

For the independent propagation of two wave functions $\Psi_g(x,t)$ and $\Psi_u(x,t)$ on two different potential curves, the Crank-Nicholson propagation presented in the previous section can be applied. In the calculations carried out in the framework of this thesis, a nuclear wave packet was propagated on the $1s\sigma_g$ and the $2p\sigma_u$ potential curves of the H_2^+ (D_2^+) molecule. A transition between these two dissociation channels was introduced by a dipole coupling. The Schrödinger equation of such a system can be written as

$$i\frac{\mathrm{d}}{\mathrm{d}t}\begin{pmatrix}\Psi_g(t)\\ \Psi_u(t)\end{pmatrix} = \left(\hat{\mathcal{H}}_0 + \hat{\mathcal{H}}_c\right)\begin{pmatrix}\Psi_g(t)\\ \Psi_u(t)\end{pmatrix}, \tag{B.12}$$

where $\hat{\mathcal{H}}_0 = \hat{\mathcal{T}} + \hat{\mathcal{V}}$ is the Hamiltonian of the uncoupled system and $\hat{\mathcal{H}}_c$ describes the coupling between the two wave functions.

As described in the previous section, the Hamiltonian of the uncoupled system is given by a tridiagonal matrix. The total Hamiltonian of the coupled system is therefore given by a block matrix, where the diagonal blocks are tridiagonal and the off-diagonal blocks, which introduce the coupling, are diagonal

$$\hat{\mathcal{H}} = \hat{\mathcal{H}}_0 + \hat{\mathcal{H}}_c$$

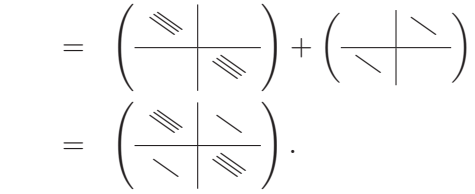

(B.13)

The propagation of the wave functions is performed by applying the split operator method

$$\mathrm{e}^{-i\hat{\mathcal{H}}\Delta t} = \mathrm{e}^{-i\hat{\mathcal{H}}_c\Delta t/2}\mathrm{e}^{-i\hat{\mathcal{H}}_0\Delta t}\mathrm{e}^{-i\hat{\mathcal{H}}_c\Delta t/2} + \mathcal{O}\left(\Delta t^3\right). \tag{B.14}$$

The action of the uncoupled Hamiltonian is calculated by independent Crank-Nicholson propagations. The dipole coupling elements dependent on the internuclear distance were already determined in a previous calculation so that the calculation of the coupling reduces to a multiplication.

B.3 Virtual detector

For calculating the CEP dependent asymmetry by wave packet propagation, a large numerical grid is required. The simulation of the delay dependent asymmetry described in chapter 6 therefore requires long computation times. The time necessary to obtain the energy and momentum distribution can be reduced significantly by using a so-called virtual detector [FT03]. Here the momentum distribution is obtained from the time dependence of the wave function at a fixed position in coordinate space.
As an ansatz the wave function is written as

$$\Psi(r,t) = A(r,t)\exp(i\phi(r,t)) \tag{B.15}$$

with a real phase $\phi(r,t)$ and real amplitude $A(r,t)$. The probability current density at a position r_d of outgoing particles with mass μ is given by

$$j(r_d,t) = \frac{\rho(r_d,t)}{\mu}\nabla\phi(r_d,t). \tag{B.16}$$

It is a product of the probability density $\rho(r_d,t) = |A(r,t)|^2$ and a velocity v at position r, which is related to the momentum by

$$k(r_d,t) = \mu v = \nabla\phi(r_d,t). \tag{B.17}$$

Thus the momentum at each time can be obtained from the gradient of the phase $\phi(r_d, t)$ at a fixed position r.
In the simulation presented in chapter 6, only one dimension is considered. For the wave packet propagation, the numerical methods described above are used. At each time step, the momentum is calculated at the position $x_d = 20\,a.u.$, where the virtual detector is located. The determined momenta are then combined to a histogram. The probability for finding ΔN events with momenta k within a small momentum interval Δk around the momentum value k_j is thereby given by

$$\Delta N(k_j) = \Delta k \int dt\, j(x_d, t) \begin{cases} 1 & \text{for } k \in \left[k_j - \frac{\Delta k}{2},\, k_j + \frac{\Delta k}{2}\right] \\ 0 & \text{else.} \end{cases}$$

Bibliography

[ACE09] F. Anis, T. Cackowski, and B.D. Esry, *Rotational dynamics of dissociating H_2^+ in a short intense laser pulse*, J. Phys. B **42** (2009), no. 9, 091001. 91, 100, 137

[ADK86] M.V. Ammosov, N.B Delone, and N.B. Krainov, *Tunnel ionization of complex atoms and of atomic ions in an alternating electromagnetic field*, Soviet Physics JETP **64** (1986), no. 6, 1191. 11

[AFM+79] P. Agostini, F. Fabre, G. Mainfray, G. Petite, and N.K. Rahman, *Free-free transitions following six-photon ionization of xenon atoms*, Phys. Rev. Lett. **42** (1979), no. 17, 1127. 10

[AS91] S.W. Allendorf and A. Szöke, *High-intensity multiphoton ionization of H_2*, Phys. Rev. A **44** (1991), no. 1, 518. 21

[AT55] S.H. Autler and C.H. Townes, *Stark effect in rapidly varying fields*, Phys. Rev. **100** (1955), no. 2, 703. 18

[BDM05] A. Becker, R. Dörner, and R. Moshammer, *Multiple fragmentation of atoms in femtosecond laser pulses*, J. Phys. B **38** (2005), S753. 12

[BJ67] F.W. Byron and C.J. Joachain, *Multiple ionization processes in helium*, Phys. Rev. **164** (1967), no. 1, 1. 12

[BKP+04] T. Brixner, G. Krampert, T. Pfeifer, R Selle, G. Gerber, M. Wollenhaupt, O. Graefe, C. Horn, D. Liese, and T. Baumert, *Quantum control by fast polarization shaping*, Phys. Rev. Lett. **92** (2004), no. 20, 208301. 4

[BLR04] P. Baum, S. Lochbrunner, and E. Riedle, *Zero-additional-phase spider: full characterization of visible and sub-20 fs ultraviolet pulses*, Opt. Lett. **29** (2004), 210. 40

[BPG+05] T. Brixner, T. Pfeifer, G. Gerber, M. Wollenhaupt, and T. Baumert, *Optimal control of atomic, molecular and electron dynamics with tailored femtosecond laser pulses*, Springer Verlag, Femtosecond Laser Photoelectron Spectroscopy, 2005. 5

[BR05] P. Baum and E. Riedle, *Design and calibration of zero-additional-phase spider*, J. Opt. Soc. Am. B **22** (2005), 1875. 40

[Bri26] L. Brillouin, *La mécanique ondulatoire de Schrödinger; une méthode générale de resolution par approximations successives*, Comptes rendus **183** (1926), 24. 126

[Bri03] Brixner, T. and Gerber, G., *Quantum control of gas-phase and liquid-phase femtochemistry*, ChemPhysChem **4** (2003), 418. 4

[BS86] P. Brumer and M. Shapiro, *Control of unimolecular reactions using coherent light*, Chem. Phys. Lett. **126** (1986), 541. 4

[BUU+03] A. Baltuska, Th. Udem, M. Uiberacker, M. Hentschel, E. Goulielmakis, Ch Gohle, R. Holzwarth, V. S. Yakovlev, A. Scrinzi, T. W. Hansch, and F. Krausz, *Attosecond control of electronic processes by intense light fields*, Nature **421** (2003), no. 6923, 611. 6, 47

[BZ77] P.R. Berman and J. Ziegler, *Generalized dressed-atom aproach to atom-strong-field interactions – application to the theory of lasers and Bloch-Siegert shifts*, Phys. Rev. A **15** (1977), no. 5, 2042. 18

[BZMS90] P.H. Bucksbaum, A. Zavriyev, H.G. Muller, and D.W. Schumacher, *Softening of the H_2^+ molecular bond in intense laser fields*, Phys. Rev. Lett. **64** (1990), no. 16, 1883. 20

[Cas08] W. B. Case, *Wigner functions and Weyl transforms for pedestrians*, Am. J. Phys **76** (2008), 937. 121

[CBNW09] C. R. Calvert, W. A. Bryan, W. R. Newell, and I. D. Williams, *Time-resolved studies of ultrafast wavepacket dynamics in hydrogen molecules*, Physics Reports **doi:10.1016/j.physrep.2009.12.004** (2009). 22, 99

[Chu81] S.-I. Chu, *Floquet theory and complex quasivibrational energy formalism for intense field molecular photodissociation*, J. Chem. Phys. **75** (1981), no. 5, 2215. 17

[Cor93] P. B. Corkum, *Plasma perspective on strong field multiphoton ionization*, Phys. Rev. Lett. **71** (1993), no. 13, 1994. 12

[CRW+10] C R Calvert, R B King, W A Bryan, W R Newell, J F McCann, J B Greenwood, and I D Williams, *Multi-pulse scheme for enhancing electron localization through vibrational wavepacket manipulation*, Journal of Physics B **43** (2010), no. 1, 011001. 130, 131

[DAL+04] P Dombi, A Apolonski, Ch Lemell, G G Paulus, M Kakehata, R Holzwarth, Th Udem, K Torizuka, J Burgdorfer, T W Hansch, and F Krausz, *Direct measurement and analysis of the carrier-envelope phase in light pulses approaching the single-cycle regime*, New Journal of Physics **6** (2004), 39. 47

[dJFZ+06] V.L.B. de Jesus, B. Feuerstein, K. Zrost, D. Fischer, A. Rudenko, F. Afaneh, C.D. Schröter, R. Moshammer, and J. Ullrich, *Atomic structure dependence of nonsequential double ionization of He, Ne and Ar in strong laser fields*, J. Phys. B **37** (2006). 13

[dJRF+04] V.L.B. de Jesus, A. Rudenko, B. Feuerstein, K. Zrost, C.D. Schröter, R. Moshammer, and J. Ullrich, *Reaction microscopes applied to study atomic and molecular fragmentation in intense laser fields: non-sequential double ionization of helium*, J. electron spectroscopy and related phenomena **141** (2004), 127. 59

[DK91] N.B Delone and N.B. Krainov, *Energy and angular electron spectrum for the tunnel ionization of atoms by strong low-frequency radiation*, J. Opt. Soc. Am. B **8** (1991), no. 6, 1207. 11

[DMJ+00] R. Dörner, V. Mergel, O. Jagutzki, L. Spielberger, J. Ullrich, R. Moshammer, and H. Schmidt-Böcking, *Cold target recoil ion momentum spectroscopy: A 'momentum microscope' to view atomic collision dynamics*, Physics Reports **95** (2000), 330. 57

[DR06a] J. Diels and W. Rudolph, *Ultrashort laser pulse phenomena*, Academic Press, 2006. 29, 31, 33, 37

[Dür06b] M. Dürr, *Electron induced break-up of helium: Benchmark experiments on a dynamical four-body coulomb system*, Ph.D. thesis, 2006. 62

[Dun32] J. L. Dunham, *The Wentzel-Brillouin-Kramers method of solving the wave equation*, Phys. Rev. **41** (1932), no. 6, 713. 126

[DWW+02] R. Dörner, Th. Weber, M. Weckenbrock, A. Staudte, M. Hattass, R. Moshammer, J. Ullrich, and H. Schmidt-Böcking, *Multiple ionization in strong laser fields*, Adv. At. Mol. Opt. Phys. **48** (2002), 1. 12

[EP97] A.T.J.B. Eppink and D.H. Parker, *Velocity map imaging of ions and electrons using electrostatic lenses: Application in photoelectron and photofragment ion imaging of molecular oxygen*, Rev. Sci. Instrum. **68** (1997), 3477. 7

[ERF+05] Th. Ergler, A. Rudenko, B. Feuerstein, K. Zrost, C.D. Schröter, R. Moshammer, and J. Ullrich, *Time-resolved imaging and manipulation of H_2 fragmentation in intense laser fields*, Phys. Rev. Lett. **95** (2005), 093001. 2, 3, 25, 94

[ERF+06a] Th. Ergler, A. Rudenko, B. Feuerstein, K. Zrost, C.D. Schröter, R. Moshammer, and J. Ullrich, *Ultrafast mapping of H_2^+ (D_2^+) nuclear wave packets using time-resolved Coulomb explosion imaging*, J. Phys. B **39** (2006), S493. 2, 3, 25, 94

[ERF+06b] Th. Ergler, A. Rudenko, B. Feuerstein, K. Zrost, C. D. Schröter, R. Moshammer, and J. Ullrich, *Spatiotemporal imaging of ultrafast molecular motion: Collapse and revival of the D_2^+ nuclear wave packet*, Physical Review Letters **97** (2006), no. 19, 193001. 2, 94

[Erg06] Th. Ergler, *Zeitaufgelöste Untersuchungen zur Fragmentationsdynamik von H_2 (D_2) in ultra-kurzen Laserpulsen*, Ph.D. thesis, Ruprecht-Karls-Universität Heidelberg, 2006. 17, 25, 26, 36, 37, 91, 98

[ESW+06] B. D. Esry, A. M. Sayler, P. Q. Wang, K. D. Carnes, and I. Ben-Itzhak, *Above threshold coulomb explosion of molecules in intense laser pulses*, Phys. Rev. Lett. **97** (2006), 013003. 21

[FBM+87] R.R. Freeman, P.H. Bucksbaum, H. Milchberg, S. Darack, D. Schumacher, and M.E. Geusic, *Above-threshold ionization with subpicosecond laser pulses*, Phys. Rev. Lett. **59** (1987), no. 10, 1092. 10

[FER+07] B. Feuerstein, Th. Ergler, A. Rudenko, K. Zrost, C.D. Schröter, R. Moshammer, J. Ullrich, T. Niederhausen, and U. Thumm, *Complete characterization of molecular dynamics in ultrashort laser fields*, Phys. Rev. Lett. **99** (2007), no. 15, 153002. 82, 111

[FGS81] R. L. Fork, B. Greene, and C. Shank, *Generation of optical pulses shorter than 0.1 psec by colliding pulse mode-locking.*, Appl. Phys. Lett. **38** (1981), 679. 1

[Fis03] D. Fischer, *Mehr-Teilchen-Dynamik in der Einfach- und Doppelionisation von Helium durch geladene Projektile*, Ph.D. thesis, Ruprecht-Karls-Universität Heidelberg, 2003. 64

[FMF+01] B. Feuerstein, R. Moshammer, D. Fischer, A. Dorn, C. D. Schröter, J. Deipenwisch, J. R. Crespo Lopez-Urrutia, C. Höhr, P. Neumayer, J. Ullrich, H. Rottke, C. Trump, M. Wittmann, G. Korn, and W. Sandner, *Separation of recollision mechanisms in nonsequential strong field double ionization of Ar: The role of excitation tunneling*, Phys. Rev. Lett. **87** (2001), no. 4, 043003. 13

[FMG84] R. L. Fork, O. E. Martinez, and J. P. Gordon, *Negative dispersion using pairs of prisms*, Optics letters **9** (1984), no. 5, 150. 33

[FMU00] B. Feuerstein, R. Moshammer, and J. Ullrich, *Nonsequential multiple ionization in intense laser pulses: interpretation of ion momentum distributions within the classical 'rescattering' model*, J. Phys. B **33** (2000), no. 21, L823. 12

[FPAC82] F. Fabre, G. Petite, P. Agostini, and M. Clement, *Multiphoton above-threshold ionisation of xenon at 0.53 and 1.06μm*, J. Phys. B **15** (1982), 1353. 10

[FPPC99] L.J. Frasinski, J.H. Posthumus, J. Plumridge, and K. Codling, *Manipulation of bond hardening in H_2^+ by chirping of intense femtosecond laser pulses*, Phys. Rev. Lett. **83** (1999), no. 18, 3625. 21

[FRA+05] T. Fuji, J. Rauschenberger, A. Apolonski, V. S. Yakovlev, G. Tempea, T. Udem, C. Gohle, T. W. Hänsch, W. Lehnert, M. Scherer, and F. Krausz, *Monolithic carrier-envelope phase-stabilization scheme*, Optics letters **30** (2005), no. 3, 332. 49

[FT03] B. Feuerstein and U. Thumm, *On the computation of momentum distributions within wavepacket propagation calculations.*, J. Phys. B **36** (2003), 707. 114, 147

[GI07] S. Graefe and M.Y. Ivanov, *Effective fields in laser-driven electron recollision and charge localization*, Phys. Rev. Lett. **99** (2007), no. 16, 163603. 89

[Gim06] H. Gimpel, *Erzeugung und Anwendung intensiver ultrakurzer Lichtpulse mit stabiler Träger-Einhüllenden-Phase*, Ph.D. thesis, Ruprecht-Karls-Universität Heidelberg, 2006. 52, 60

[Gop09] R. Gopal, *Electron wave packet interferences in ionization with few-cycle laser pulses and the dissociative photoionization of D_2 with ultrashort extreme ultraviolet pulses*, Ph.D. thesis, Ruprecht-Karls-Universität Heidelberg, 2009. 90

[Gou90] L. G. Gouy, *Sur une propriete nouvelle des ondes lumineuses.*, C. R. Acad. Sci. Paris **110** (1890), 1251. 59

[GSM+09] R. Gopal, K. Simeonidis, R. Moshammer, Th. Ergler, M. Dürr, M. Kurka, K.-U. Kühnel, S. Tschuch, C.D. Schröter, D. Bauer, J. Ullrich, A. Rudenko, O. Herrwerth, Th. Uphues, M. Schultze, E. Goulielmakis, M. Uiberacker, M. Lezius, and M. Kling, *Electron wavepacket interferences pointing towards holographic imaging in few-cycle pulses*, Phys. Rev. Lett. **103** (2009), 053001. 6, 90

[GSMD+95] A. Giusti-Suzor, F.H. Mies, L.F. DiMauro, E. Charron, and B. Yang, *Dynamics of H_2^+ in intense laser fields*, J. Phys. B **28** (1995), no. 3, 309. 20

[Hal06] J.L. Hall, *Nobel lecture: Defining and measuring optical frequencies*, Rev. Mod. Phys. **78** (2006), 1279. 44

[HE09] J.J. Hua and B.D. Esry, *The role of mass in the carrier-envelope phase effect for H_2^+ dissociation*, J. Phys. B **42** (2009), 085601. 7, 78, 79, 80, 81, 91, 126

[HF09] L.-Y. Hu and H.-Y. Fan, *Wavelet transformation and Wigner-Husimi distribution function*, Int. J. Theor. Phys. **48** (2009), 1539. 123

[Hän06] T.W. Hänsch, *Nobel lecture: Passion for precision*, Rev. Mod. Phys. **78** (2006), 1297. 6, 44

[Hof09] C. Hofrichter, *A stereo electron spectrometer for carrier-envelope phase measurements of few-cycle laser pulses*, Diploma thesis, Ruprecht-Karls-Universität Heidelberg, 2009. 52, 140

[Hus40] K. Husimi, *Some formal properties of the density matrix*, Proc. Phys. Math. Soc. Jpn. **22** (1940), 264. 123

[Isa11] W. Isaacson, *The biotech century*, Time magazine, 1999.01.11. 1

[IW98] C. Iaconis and I.A. Walmsley, *Spectral phase interferometry for direct electric-field reconstruction of ultrashort optical pulses*, Optics letters **23** (1998), no. 10, 792. 40

[JDR+00] D. J. Jones, S. A. Diddams, J. K. Ranka, A. Stentz, R. S. Windeler, J. L. Hall, and S. T. Cundiff, *Carrier–envelope phase control of femtosecond mode–locked lasers and direct optical frequency synthesis*, Science **288** (2000), no. 5466, 635. 45

[Kel64] L.V. Keldysh, *Ionization in the field of a strong electromagnetic wave*, Soviet Physics JETP **20** (1964), 1307. 9

[KFF+09] M. Kremer, B. Fischer, B. Feuerstein, V. L. B. de Jesus, V. Sharma, C. Hofrichter, A. Rudenko, U. Thumm, C. D Schröter, R. Moshammer, and J. Ullrich, *Electron localization in molecular fragmentation of H_2 by carrier-envelope phase stabilized laser pulses*, Phys. Rev. Lett. **103** (2009), no. 21, 213003. 7, 65, 67, 76

[KGU+04] R. Kienberger, E. Goulielmakis, M. Uiberacker, A. Baltuska, V. Yakovlev, F. Bammer, A. Scrinzi, Th Westerwalbesloh, U. Kleineberg, U. Heinzmann, M. Drescher, and F. Krausz, *Atomic transient recorder*, Nature **427** (2004), no. 6977, 817. 6

[Khe01] A. Kheifets, *On different mechanisms of the two-electron atomic photoionization*, J. Phys. B **34** (2001), no. 8, L247. 12

[KLT+06] M. Kresz, T. Loffler, M. D. Thomson, R. Dorner, H. Gimpel, K. Zrost, T. Ergler, R. Moshammer, U. Morgner, J. Ullrich, and H. G. Roskos, *Determination of the carrier-envelope phase of few-cycle laser pulses with terahertz-emission spectroscopy*, Nat Phys **2** (2006), 327. 6

[Kra26] H. A. Kramers, *Wellenmechanik und halbzahlige Quantisierung*, Zeits. f. Physik **39** (1926), 828. 126

[Kre09] M. Kremer, *Einfluß der Träger-Einhüllenden-Phase auf die Wechselwirkung ultrakurzer Laserpulse mit Molekülen*, Ph.D. thesis, Ruprecht-Karls-Universität Heidelberg, 2009. 8, 43, 60, 65

[KS08] F.K. Kneubühl and M.W. Sigrist, *Laser*, Vieweg + Teubner, 2008. 29

[KSV+06] M.F. Kling, Ch. Siedschlag, A.J. Verhoef, J.I. Khan, M. Schultze, Th. Uphues, Y. Ni, M. Uiberacker, M. Drescher, F. Krausz, and M.J.J. Vrakking, *Control of electron localization in molecular dissociation*, Science **312** (2006), 246. 6, 65, 67, 73, 75, 136

[KSZ+08] M.F. Kling, Ch. Siedschlag, I. Znakovskaya, A.J. Verhoef, S. Zherebtsov, F. Krausz, M. Lezius, and M.J.J. Vrakking, *Strong-field control of electron localisation during molecular dissociation*, Mol. Phys. **106:2** (2008), 455. 71, 73, 75

[KTK+01] M. Kakehata, H. Takada, Y. Kobayashi, K. Torizuka, Y. Fujihira, T. Homma, and H. Takahashi, *Single-shot measurement of carrier-envelope phase changes by spectral interferometry*, Opt. Lett. **26** (2001), no. 18, 1436. 47

[Kuc87] M.Y. Kuchiev, *Atomic antenna*, JETP **45** (1987), no. 7, 404. 12

[Lau77] A.M.F. Lau, *Radiative-dressed molecules: Ab initio theory and single/multiphoton dissociation with electronic transitions*, Phys. Rev. A **16** (1977), no. 4, 1535. 18

[LPW+04] F. Lindner, G. G. Paulus, H. Walther, A. Baltuška, E. Goulielmakis, M. Lezius, and F. Krausz, *Gouy phase shift for few-cycle laser pulses*, Phys. Rev. Lett. **92** (2004), no. 11, 113001. 59, 60

[LRE+04] X. Liu, H. Rottke, E. Eremina, W. Sandner, E. Goulielmakis, K. O. Keeffe, M. Lezius, F. Krausz, F. Lindner, M. G. Schätzel, G. G. Paulus, and H. Walther, *Nonsequential double ionization at the single-optical-cycle limit*, Phys. Rev. Lett. **93** (2004), no. 26, 263001. 6

[LTC98] S. Larochelle, A. Talebpour, and S.L. Chin, *Non-sequential multiple ionization of rare gas atoms in a Ti:Sapphire laser field*, J. Phys. B **31** (1998), 1201. 12

[LTE07] L. Lehtovaara, J. Toivanen, and J. Eloranta, *Solution of time-independent Schrödinger equation by the imaginary time propagation method.*, J. Comp. Phys **221** (2007), 148. 82, 111

[MBT+92] E. Mevel, P. Breger, R. Trainham, G. Petite, P. Agostini, J.-P. Chambaret, A. Migus, and A. Antonetti, *Contrasted behaviour of stark-induced resonances in multiphoton ionization of krypton*, J. Phys. B **28** (1992), L401. 10

[MBT+93] E. Mevel, P. Breger, R. Trainham, G. Petite, P. Agostini, A. Migus, J.-P. Chambaret, and A. Antonetti, *Atoms in strong optical fields: Evolution from multiphoton to tunnel ionization*, Phys. Rev. Lett. **70** (1993), no. 4, 406. 10

[MFS+00] R. Moshammer, B. Feuerstein, W. Schmitt, A. Dorn, C. D. Schröter, J. Ullrich, H. Rottke, C. Trump, M. Wittmann, G. Korn, K. Hoffmann, and W. Sandner, *Momentum distributions of Ne^{n+} ions created by an intense ultrashort laser pulse*, Phys. Rev. Lett. **84** (2000), no. 3, 447. 12

[Mil88] R. Miller, *Atomic and molecular beam methods*, Oxford University Press, 1988. 58

[MMC+07] D S Murphy, J McKenna, C R Calvert, W A Bryan, E M L English, J Wood, I C E Turcu, W R Newell, I D Williams, and J F McCann, *Controlling dissociation processes in the d_2^+ molecular ion using high-intensity, ultrashort laser pulses*, Journal of Physics B: Atomic, Molecular and Optical Physics **40** (2007), no. 11, S359. 132

[MSA+08] J. McKenna, A. M. Sayler, F. Anis, B. Gaire, Nora G. Johnson, E. Parke, J. J. Hua, H. Mashiko, C. M. Nakamura, E. Moon, Z. Chang, K. D. Carnes, B. D. Esry, and I. Ben-Itzhak, *Enhancing high-order above-threshold dissociation of h_2^+ beams with few-cycle paser pulses*, Phys. Rev. Lett. **100** (2008), no. 13, 133001. 21

[MWWZ07] H. Ma, C. Wan, A. Wu, and A. H. Zewail, *DNA folding and melting in real time: Observed collapsed structures redefine the energy landscape*, Proc. Natl. Acad. Sci. **104** (2007), 712. 1

[MWZ06] H. Ma, C. Wan, and A. H. Zewail, *Ultrafast t-jump in water: Studies of conformation and reaction dynamics at the thermal limit*, J. Am. Chem. Soc. **128** (2006), 6338. 1

[NDSS96] M. Nisoli, S. De Silvestri, and O. Svelto, *Generation of high energy 10 fs pulses by a new pulse compression technique*, Appl. Phys. Lett. **68** (1996), 2793. 35

[Nie07] T. Niederhausen, *Quantum Dynamics in Laser-Assisted Collisions, Laser-Molecule Interactions, and Particle-Surface Scattering*, Ph.D. thesis, Kansas State University, Manhattan, Kansas, 2007. 71, 95, 96, 145

[NT08] T. Niederhausen and U. Thumm, *Controlled vibrational quenching of nuclear wave packets in D_2^+*, Phys. Rev. A **77** (2008), no. 1, 013407. 82, 111

[ORP10] C. Ott, P. Raith, and T. Pfeifer, *Bound- and continuum-state electronic wavepacket interference in strong-field few-cycle pump-probe experiments*, n.n. (2010). 141

[OSDV05] D. Oron, Y. Silberberg, N. Dudovich, and D. M. Villeneuve, *Efficient polarization gating of high-order harmonic generation by polarization-shaped ultrashort pulses*, Phys. Rev. A **72** (2005), no. 6, 063816. 139

[Pav04] D. Pavicic, *Coulomb Explosion and Intense-Field Photodissociation of Ion-Beam H_2^+ und D_2^+*, Ph.D. thesis, Ludwig-Maximilians-Universität München, 2004. 17, 20

[PBNW94] G. G. Paulus, W. Becker, W. Nicklich, and H. Walther, *Rescattering effects in above-threshold ionization: a classical model.*, Journal of Physics B **21** (1994), L703. 12

[PDMT03] L. Peng, D. Dundas, J. F. McCann, and K. T. Taylor, *Dynamic tunnelling ionization of H_2^+ in intense fields.*, J. Phys. B **36** (2003), L295. 26

[PLW+03] G.G. Paulus, F. Lindner, H. Walther, A. Baltuška, E. Goulielmakis, M. Lezius, and F. Krausz, *Measurement of the phase of few-cycle laser pulses*, Phys.Rev. Lett. **91** (2003), 253004. 54

[PLW+05] G. G. Paulus, F. Lindner, H. Walther, A. Baltuska, and F. Krausz, *Measurement of the phase of few-cycle laser pulses*, J. Mod. Opt. **52** (2005), 221. 48

[PM96] M. Plummer and J. F. McCann, *Field-ionization rates of the hydrogen molecular ion*, J. Phys. B **29** (1996), 4625. 26

[Pos04] J. H. Posthumus, *The dynamics of small molecules in intense laser fields*, Rep. Prog. Phys. **67** (2004), no. 5, 623. 22

[PSR03] T. Pattard, T. Schneider, and J.M. Rost, *On the role of shake-off in single-photon double ionization*, J. Phys. B **36** (2003), no. 12, L189. 12

[Rau07] J. Rauschenberger, *Phase-stabilized ultrashort laser systems for spectroscopy*, Ph.D. thesis, Ludwig-Maximilians-Universität München, 2007. 55

[RE07a] V. Roudnev and B. D. Esry, *General theory of carrier-envelope phase effects*, Phys. Rev. Lett. **99** (2007), no. 22, 220406. 21

[RE07b] V. Roudnev and B.D. Esry, *HD^+ in a short strong laser pulse: Practical consideration of the observability of carrier-envelope phase effects*, Phys. Rev. A **76** (2007), 023403. 7, 65, 78, 81, 82

[REF+06] A. Rudenko, Th. Ergler, B. Feuerstein, K. Zrost, C. D. Schröter, R. Moshammer, and J. Ullrich, *Real-time observation of vibrational revival in the fastest molecular system*, Chemical Physics **329** (2006), 193. 95, 97

[Rob04] R.W. Robinett, *Quantum wave packet revivals*, Phys. Rep. **392** (2004), no. 1-2, 1. 22, 24

[Sae00] A. Saenz, *On the influence of vibrational motion on strong-field ionization rates in molecules*, J. Phys. B **33** (2000), no. 20, 4365. 15, 17

[Sam90] J. A. R. Samson, *Proportionality of electron-impact ionization to double photoionization*, Phys. Rev. Lett. **65** (1990), no. 23, 2861. 12

[SBC+06] G. Sansone, E. Benedetti, F. Calegari, C. Vozzi, L. Avaldi, R. Flammini, L. Poletto, P. Villoresi, C. Altucci, R. Velotta, S. Stagira, S. De Silvestri, and M. Nisoli, *Isolated single-cycle attosecond pulses*, Science **314** (2006), no. 5798, 443. 6

[Sch09] M. Schürholz, *Pump-Probe Experimente an Molekülen mit intensiven Laserpulsen*, Diploma thesis, Ruprecht-Karls-Universität Heidelberg, 2009. 63

[SFSK94] R. Szipöcs, K. Ferencz, Ch. Spielmann, and F. Krausz, *Chirped multilayer coatings for broadband dispersion control in femtosecond lasers*, Opt. Lett. **19** (1994), 201. 32

[Shi65] J.H. Shirley, *Solution of the Schrödinger equation with a Hamiltonian periodic in time*, Phys. Rev. **138** (1965), no. 4B, B979. 17

[SJD+95] L. Spielberger, O. Jagutzki, R. Dörner, J. Ullrich, U. Meyer, V. Mergel, M. Unverzagt, M. Damrau, T. Vogt, I. Ali, Kh. Khayyat, D. Bahr, H. G. Schmidt, R. Frahm, and H. Schmidt-Böcking, *Separation of photoabsorption and compton scattering contributionsto he single and double ionization*, Phys. Rev. Lett. **74** (1995), no. 23, 4615. 12

[SKS91] D. E. Spence, P. N. Kean, and W. Sibbett, *60–fsec pulse generation from a self–mode–locked ti:sapphire laser*, Opt. Lett. **16** (1991), no. 1, 42. 37

[SLS+95] A. Stingl, M. Lenzner, Ch. Spielmann, R. Szipöcs, and F. Krausz, *Sub-10-fs mirror-dispersion-controlled ti:sapphire laser*, Opt. Lett. **20** (1995), 602. 33

[SM85] D. Strickland and G. Mourou, *Compression of amplified chirped optical pulses.*, Opt. Comm. **56** (1985), 219. 1, 33

[SME+nt] I. J. Sola, E. Mevel, L. Elouga, E. Constant, V. Strelkov, L. Poletto, P. Villoresi, E. Benedetti, J. P Caumes, S. Stagira, C. Vozzi, G. Sansone, and M. Nisoli, *Controlling attosecond electron dynamics by phase-stabilized polarization gating*, Nat Phys **2** (2006/05//print), no. 5, 319. 139

[SS03] H. Stapelfeldt and T. Seideman, *Colloquium: Aligning molecules with strong laser pulses*, Rev. Mod. Phys. **75** (2003), no. 2, 543. 91

[Sta05] A. Staudte, *Subfemtosecond electron dynamics of H_2 in strong fields or the quest for the molecular clock*, Ph.D. thesis, Johann Wolfgang Goethe-Universität, Frankfurt, 2005. 10

[SYDK93] K. J. Schafer, Baorui Yang, L. F. DiMauro, and K. C. Kulander, *Above threshold ionization beyond the high harmonic cutoff*, Phys. Rev. Lett. **70** (1993), no. 11, 1599. 12

[SZW+08] L. Song, C. Zhang, J. Wang, Y. Leng, and R. Li, *Accurate measurement of carrier-envelope phase drift for infrared femtosecond laser pulses*, Opt. Express **16** (2008), no. 26, 21383. 47

[Tar07] P. Tarantilis, *Aufbau und Inbetriebnahme einer Apparatur zur Charakterisierung der spektralen Phase und des zeitlichen Profils von ultrakurzen Lichtimpulsen, ZAP-SPIDER*, Diploma thesis, Ruprecht-Karls-Universität Heidelberg, 2007. 40

[TDF+97] R. Trebino, K. W. DeLong, D. N. Fittinghoff, J. N. Sweetser, M. A. Krumbügel, B.A. Richmann, and D.J. Kane, *Measuring ultrashort laser pulses in the time-frequency domain using frequency-resolved optical gating*, Review of Scientific Instruments **68** (1997), no. 9, 3277. 40

[TFJRG+05] T. Takao Fuji, J. Jens Rauschenberger, Ch. Gohle, A. Alexander Apolonski, T. Thomas Udem, V. S. Yakovlev, G. Tempea, Th. W. Hänsch, and F. Krausz, *Attosecond control of optical waveforms*, New Journal of Physics **7** (2005), 116. 50

[TGB99] G. Tempea, M. Geissler, and T. Brabec, *Phase sensitivity of high-order harmonic generation with few-cycle laser pulses*, J. Opt. Soc. Am. B **16** (1999), no. 4, 669. 12

[TIK82] M. Takeda, H. Ina, and S. Kobayashi, *Fourier-transform method of fringe-pattern analysis for computer based topography and interferometry*, J. Opt. Soc. Am. **72** (1982), 156. 41

[TKC+08] F. Toscano, A. Kenfack, A. R. R. Carvalho, J. M. Rost, and A. M. O. Ozorio de Almeida, *Husimi-Wigner representation of chaotic eigenstates*, Proc. R. Soc. A-Math. Phys. Eng. Sci. **464** (2008), no. 2094, 1503. 123

[TKR86] D. J. Tannor, R. Kosloff, and S. A. Rice, *Coherent pulse sequence induced control of selectivity of reactions: Exact quantum mechanical calculations*, J. Chem. Phys. **85** (1986), 5805. 4

[TNF08] U. Thumm, T. Niederhausen, and B. Feuerstein, *Time-series analysis of vibrational nuclear wave-packet dynamics in D_2^+*, Phys. Rev. A **77** (2008), no. 6, 063401. 82, 111

[UFSC+04] X. Urbain, B. Fabre, E. M. Staicu-Casagrande, N. de Ruette, V. M. Andrianarijaona, J. Jureta, J. H. Posthumus, A. Saenz, E. Baldit, and C. Cornaggia, *Intense-laser-field ionization of molecular hydrogen in the tunneling regime and its effect on the vibrational excitation of H_2^+*, Phys. Rev. Lett. **92** (2004), no. 16, 163004. 14, 16, 17

[UMD+03] J. Ullrich, R. Moshammer, A. Dorn, R. Dörner, L.Ph.H. Schmidt, and H. Schmidt-Böcking, *Recoil-ion and electron momentum spectroscopy: Reaction Microscopes*, Rep. Prog. Phys **9** (2003), 1463. 57, 59

[US03] J. Ullrich and V.P. Shevelko, *Many-particle quantum dynamics in atomic and molecular fragmentation*, Springer, Berlin, 2003. 57, 58

[vBD72] F. von Busch and G. H. Dunn, *Photodissociation of H_2^+ and D_2^+: Experiment*, Phys. Rev. A **5** (1972), no. 4, 1726. 14

[Ver06] A. Verhoef, *Absoulte phase control of intense few-cycle pulses and steering the atomic-scale motion of electrons*, Ph.D. thesis, Ludwig-Maximilians-Universität München, 2006. 55

[VFG85] J. A. Valdmanis, R. L. Fork, and J. P. Gordon, *Generation of optical pulses as short as 27 femtoseconds directly from a laser balancing selfphase modulation, group-velocity dispersion, saturable absorbtion, and saturable gain.*, Opt. Lett. **10** (1985), 131. 1

[VVS96] M.J.J. Vrakking, D.M. Villeneuve, and A. Stolow, *Observation of fractional revivals of a molecular wave packet*, Phys. Rev. A **54** (1996), no. 1, R37. 24

[VVU93] S.I. Vetchinkin, A.S. Vetchinkin, and I.M. Umanskii, *Gaussian wavepacket dynamics in an anharmonic system*, Chem. Phys. Lett. **215** (1993), no. 1,2,3, 11. 24

[WBK+07] M Wollenhaupt, T. Bayer, M. Krug, C. C. Sarpe-Tudoran, and T. T Baumert, *Coherent control of electrons, atoms and molecules with intense shaped light pulses*, Journal of Physics: Conference Series **88** (2007), 012053. 4

[WEB05] M. Wollenhaupt, V. Engel, and T. Baumert, *Femtosecond laser photoelectron spectroscopy on atoms and small molecules: Prototype studies in quantum control*, Annual Review of Physical Chemistry **56** (2005), 25. 5

[Wen26] G. Wentzel, *Eine Verallgemeinerung der Quantenbedingungen für die Zwecke der Wellenmechanik*, Zeits. f. Physik **38** (1926), 518. 126

[WGW+00] Th. Weber, H. Giessen, M. Weckenbrock, G. Urbasch, A. Staudte, L. Spielberger, O. Jagutzki, V. Mergel, M. Vollmer, and R. Dörner, *Correlated electron emission in multiphoton double ionization*, Nature **405** (2000), 658. 12

[WHH+09] M. Wittmann, B. Horvath, W. Helml, M.G. Schätzel, X. Gu, A.L. Cavalieri, G.G. Paulus, and R. Kienberger, *Single-shot carrier-envelope phase measurement of few-cycle laser pulses*, Nature Physics **5** (2009), 357. 52, 54

[Wie07] U. Wiedemann, *Zeitaufgelöste Experimente zur Fragmentationsdynamik von CH_4 in intensiven, ultra-kurzen Laserpulsen*, Diploma thesis, Ruprecht-Karls-Universität Heidelberg, 2007. 63

[Wig32] E. P. Wigner, *On the quantum correction for thermodynamic equilibrium*, Phys. Rev. **40** (1932), 749. 121

[WSD+94] B. Walker, B. Sheehy, L.F. DiMauro, P. Agostini, K.J. Schafer, and K.C. Kulander, *Precision measurement of strong field double ionization of helium*, Phys. Rev. Lett. **73** (1994), no. 9, 1227. 12

[WT96] I.A. Walmsley and R. Trebino, *Measuring fast pulses with slow detectors*, Opt. Phot. News **7** (1996), 23. 40

[WWS+00a] Th. Weber, M. Weckenbrock, A. Staudte, L. Spielberger, O. Jagutzki, V. Mergel, F. Afaneh, G. Urbasch, M. Vollmer, H. Giessen, and R. Dörner, *Recoil-ion momentum distributions for single and double ionization of helium in strong laser fields*, Phys. Rev. Lett. **84** (2000), no. 3, 443. 12

[WWS+00b] Th. Weber, M. Weckenbrock, A. Staudte, L. Spielberger, O. Jagutzki, V. Mergel, F. Afaneh, G. Urbasch, M. Vollmer, H. Giessen, and R. Dörner, *Sequential and nonsequential contributions to double ionization in strong laser fields*, J. Phys. B **33** (2000), no. 4, L127. 12

[XSP+96] L. Xu, Ch. Spielmann, A. Poppe, T. Brabec, F. Krausz, and T. W. Hansch, *Route to phase control of ultrashort light pulses*, Optics letters **21** (1996), no. 24, 2008. 37, 45

[YC05] J. Ye and S. T. Cundiff, *Femtosecond optical frequency comb technology: Principle, operation and application*, Springer, 2005. 44, 47

[ZB93] A. Zavriyev and P.H. Bucksbaum, *Light-induced vibrational structure in H_2^+ and D_2^+ in intense laser fields*, Phys. Rev. Lett. **70** (1993), no. 8, 1077. 21

[ZB95] T. Zuo and A. D. Bandrauk, *Charge-resonance-enhanced ionization of diatomic molecular ions by intense lasers*, Phys. Rev. A **52** (1995), R2511. 26

[ZBMS90] A. Zavriyev, P.H. Bucksbaum, H.G. Muller, and D.W. Schumacher, *Ionization and dissociation of H_2 in intense laser fields at $1.064\mu m$, $532nm$, and $355nm$*, Phys. Rev. A **42** (1990), no. 9, 5500. 20, 22

[Zew88] A.H. Zewail, *Laser Femtochemistry*, Science **242** (1988), no. 4886, 1645. 1

[Zew91] A.H. Zewail, *Femtosecond transition-state dynamics*, Faraday Discuss. Chem. Soc. **91** (1991), 207. 1

[Zew95] A.H. Zewail, *Coherence - a powerful concept in the studies of structures and dynamics*, Laser Physics **5** (1995), 417. 1

[Zew96] A.H. Zewail, *Femtochemistry: Recent progress in studies of dynamics and control of reactions and their transition states*, J. Phys. Chem. **100** (1996), 12701. 1

[Zew00a] A.H. Zewail, *Femtochemistry: Atomic-scale dynamics of the chemical bond*, J. Phys. Chem. A **104** (2000), 5660. 1

[Zew00b] A.H. Zewail, *Femtochemistry: Atomic-Scale dynamics of the chemical bond using ultrafast lasers (Nobel Lecture)*, Angew. Chem. Int. Ed. Engl. **39** (2000), 2586. 2

[Zro05] K. Zrost, *Wechselwirkung von Atomen und kleinen Molekülen mit intensiven, ultrakurzen Laserpulsen*, Ph.D. thesis, Ruprecht-Karls-Universität Heidelberg, 2005. 10, 35, 39

[ZvdHZ+09] I. Znakovskaya, P. von den Hoff, S. Zherebtsov, A. Wirth, O. Herrwerth, M. J. J. Vrakking, R. de Vivie-Riedle, and M. F. Kling, *Attosecond control of electron dynamics in carbon monoxide*, Phys. Rev. Lett. **103** (2009), no. 10, 103002. 139

Acknowledgements

I wish to express my gratitude to all the people, who supported me during my PhD thesis. Foremost, I wish to thank my supervisor, Robert Moshammer, for his support over the years and help in physics and technical issues and also for his practical support in the lab. During my time in the group I learned from him a lot about an exciting research area and also about working as an experimentalist.
I wish to express my appreciation to Joachim Ullrich for giving me the opportunity to work in his group, which is outstanding in research as well as in the excellent working atmosphere. I also thank him for his support and helpful discussions and for giving his precious time to everyone despite of being involved in many projects and experiments.
Manuel Kremer, with whom I worked together during the whole period of my PhD, I thank for being a supportive colleague and a very great friend.
A special thanks to Bernold Feuerstein for his support in doing the theoretical simulations, the help for the interpretation of the results as well as for helpful and inspiring discussions inside and outside of physics.
I wish to thank Thomas Pfeifer for helpful suggestions and interesting discussions concerning physics as well as technical issues in the laser lab. My special thanks goes also to Artem Rudenko, who introduced me to the work on the Reaction microscope and to the research area.
Furthermore, I like to say 'obrigada' to Vitor de Jesus for the nice time of working together, for the good friendship and for bringing a Brazilian touch into the group.
My appreciation goes also to Vandana Sharma and Siva Rama Krishnan for the good time in the lab and for the support and the friendship. I thank the former Diploma students, Olliver Herrwerth, Andreas Achtelik, Markus Schürholz and Christian Hofrichter for the nice time of working together.
All my roommates, especially Thomas Pflüger, I thank for the pleasant atmosphere in the office. Thanks also to Renate Hubele for having some chocolate for encouragement and for a good time together.
Not least I would like to thank Helga Krieger, Bernd Knape and Claus Dieter Schröter, whose support and knowledge in technical issues is essential for the work in the laboratories.
I am grateful to all my colleagues in the working group for plenty of nice discussions and a very good time at the institute.
To all my friends I wish to express my gratitude for the beautiful time together and for their support. Thanks also to Andreas Trenkwalder for proofreading my thesis.
Last but not least I wish to thank my family, who has always been there for me during all phases of life.